A STUDY ON RHODIUM AND PALLADIUM MIXED-MEDIA SOLS

THE UNIVERSITY OF
WAIKATO
Te Whare Wānanga o Waikato

A thesis
submitted in partial fulfilment
of the requirements for the degree
of

Master of Science in Chemistry

at

The University of Waikato

by

JACOB E. JAINE

The University of Waikato
2011

Abstract

Historically the majority of precious metal sols have been prepared in an aqueous medium, while a much smaller proportion have been prepared in various non-aqueous solvents. Few however have been prepared in mixtures of the two, this paucity being the *raison d'être* of this study. The goal therefore was to perform a systematic investigation of the changes in the properties of rhodium and palladium sols generated in mixtures of water and another organic cosolvent across a range of volumetric compositions.

Six cosolvents were investigated: methanol, dimethylsulfoxide, acetonitrile, N,N-dimethylformamide, acetone, and tetrahydrofuran. To stabilise the resulting sols against aggregation four protecting agents were used: poly(vinyl pyrrolidone), poly(vinyl alcohol), poly(acrylic acid), and arabinogalactan, which was a newly-available polysaccharide extracted from the Western Larch tree. To reduce the metals from their precursor salts, sodium borohydride and hydrazine hydrate were used. The resulting colloids were analysed by Transmission Electron Microscopy (TEM), Photon Correlation Spectroscopy (PCS) and Ultraviolet/Visible Spectrophotometry.

The size of the primary particles in the resulting sols was shown by TEM to be inversely proportional to the proportion of cosolvent in which they were generated. A theory was postulated to account for these changes based on temporary stabilisation of the metal nuclei by adsorption of cosolvent molecules.

The characteristics of the aggregates observed in the TEM micrographs were shown to be independent of the cosolvent proportion, changing

progressively but unpredictably across the composition ranges studied for most systems. This behaviour was believed to be caused by changes in the conformations of the protecting agents, which depended nonlinearly on the composition of the dispersion medium in which they were used.

The measurements collected *in-situ* by both PCS and UV/Vis were considered to be good indicators of the levels of aggregation observed in the sols *ex-situ* by TEM, with any disparities between the two sets of measurements rationalised with relative ease. PCS measurements gave average hydrodynamic diameters of approximately 20 nm – 80 nm for sols generated in purely aqueous dispersion media, depending on the metal and protecting agent used.

Infrared spectra were collected of carbon monoxide adsorbed to the surface of the particles of the sols in mixed-media to determine the effect of the cosolvent proportion on $\nu(CO)_{ads}$. Sols generated for the aforementioned work were found to be of insufficient density for this purpose, so a series of high-density sols were synthesised especially. Adsorbed CO was successfully detected on rhodium sols in mixtures of water and either MeOH, DMF, DMSO or MeCN. In these cases $\upsilon(CO)_{ads}$ and its intensity decreased as the cosolvent proportion was increased. This behaviour was rationalised by competitive adsorption of the cosolvent molecules onto the surface of the colloidal particles, precluding the adsorption of CO molecules. The consequent decrease in surface coverage was presumed to have lead to a loss of dipolar coupling, affecting the stretching frequency. These data were used to support the theory postulated for the decrease in the average particle size of the sols generated in mixed-media.

Acknowledgements

There have been a multitude of people who have helped me through this undertaking over the last two years, each in different capacities but each playing important roles. In no particular order, thanks to the following people:

Firstly, an emphatic thank you to my supervisor, Dr. Michael Mucalo, without whom I could not have come this far. His ability to put up with my crazy colloid plans is unsurpassed.

Thanks to my family for their unwavering support, despite my occasional lack of communication. I appreciate everything you have done for me.

Thanks to all my friends who have had to put up with me blithering about colloids for hours at a time, but who have continued to stick by me.

Thanks to my girlfriend, who has been subjected to my insanity for periods in vast excess of what is healthy for a single person.

Thanks to all those involved in the frequently frustrating TEM experience. Special thanks go to Helen Turner and Steve Hardy for their help and comic relief throughout the ordeal. Thanks also go to staff from the Engineering Department who have helped along the way, and to Dr. Sato from the University of Canterbury for his very helpful training.

Thanks to all the lab technicians I have perpetually pestered with requests for chemicals and equipment. These include but are not limited to Wendy Jackson, Pat Gread, and Annie Barker.

Thanks to all the other students in C.3.11, with whom I have shared the trials and tribulations of a variety of projects.

Lastly I would like to thank Balázs Rózsa, whose work has been a constant inspiration to me and helped me through many of the slower days.

Table of Contents

List of Figures

List of Tables

List of Terms and Abbreviations

Instrumental Techniques

TEM	Transmission Electron Microscope
SEM	Scanning Electron Microscope
DLS	Dynamic Light Scattering
QELS	Quasi-Elastic Light Scattering
PCS	Photon Correlation Spectroscopy
ELS	Electrophoretic Light Scattering
FTIR	Fourier Transform Infrared Spectroscopy
ESI-MS	Electrospray Ionisation Mass Spectrometry
UV/Vis	Ultraviolet Visible Spectrophotometry

Chemicals

DMSO	Dimethylsulfoxide
DMF	N,N-dimethylformamide
THF	Tetrahydrofuran
MeCN	Acetonitrile
PVP	Poly(vinyl pyrrolidone)
PAA	Poly(acrylic acid)

PAAH	Poly(acrylic acid hydrazide)
PVA	Poly(vinyl alcohol)
ARG	Arabinogalactan

Physical Properties and Quantities

kT	Thermal temperature scale
m/z	Mass to charge ratio
ϕ_{abc}	Volume fraction of 'abc' in a mixture.
px	Pixel
EDL	Electrical double layer
IHP	Inner Helmholtz Plane
OHP	Outer Helmholtz Plane
CCD	Charge-Coupled Device
η	Viscosity
RI	Refractive Index

Statistical Terms

PSD	Particle Size Distribution
D[1,0]	Number PSD
$\bar{x}$	Number mean of a PSD obtained by TEM

σ	Number standard deviation of a PSD obtained by TEM
x_{PCS}	Number mean of PSD obtained by PCS

Miscellaneous

IUPAC	International Union of Pure and Applied Chemistry

Chapter 1: Introduction

1.1 Definitions

A colloidal system is defined by the International Union of Pure and Applied Chemistry (IUPAC) as:

> "*..a state of subdivision, implying that the molecules or polymolecular particles dispersed in a medium have at least in one direction a dimension roughly between 1 nm and 1 μm, or that in a system discontinuities are found at distances of that order*" [1].

This effectively means that a colloidal system is dispersion of fine particles throughout a medium which appears to be homogeneous macroscopically, although on the microscopic scale the particles and their dispersion medium represent discrete thermodynamic phases.

In a colloidal system the dispersed particles are referred to as the *dispersed phase*, and the medium that they are dispersed in is referred to as either the *dispersion medium* or the *continuous phase*. Either of these may be a gas, a solid, or a liquid [2]. The eight possible combinations of these give rise to a variety of different classes of colloidal systems, many of which are recognisable from every-day life, as shown in Table 1.

With the advent of the 'nanoscience revolution' around the turn of the second millennium, there has been an increasing shift toward the use of the '*nano*' prefix to describe colloidal systems; '*nanoparticles*' being a commonly used synonym for 'colloid' in the scientific vernacular. While IUPAC has no official definition of the word nanoparticle, they are generally taken to be particles in *any* form, not necessarily in dispersion, with sizes in the order of nanometres. Colloidal particles on the other

hand may occupy any size range within the approximate aforementioned limits, so long as they remain stable for an appreciable period of time.

Of most interest to the colloid scientist is the class referred to as *sols*, where solid particles are dispersed in a liquid medium. These can be divided into two broad classes based on the nature of the interactions between the particles and their dispersion medium. *Lyophobic* sols exhibit little interaction between the two, resulting in a sol whose physical properties are approximately the same as the dispersion medium. The opposite is *lyophilic* sols, where interactions such as solvation contribute significantly to changes in the physical property of the sol compared to its dispersion medium [3]. Lyophobic sols, the focus of a significant proportion of research on colloidal systems, can be further divided based on their dispersion medium. For example, the classical water-based sols are referred to as *hydrosols*, whereas sols with organic dispersion media are referred to as *organosols*.

		Continuous phase		
		Gas	Liquid	Solid
Dispersed phase	Gas	None, all gasses are miscible	*Foam* (shaving cream)	*Solid foam* (polystyrene cup)
	Liquid	*Liquid aerosol* (fog, mist)	*Emulsion* (mayonnaise, milk)	*Gel* (gelatin)
	Solid	*Solid aerosol* (dust, smoke)	*Sol* (paint, mud)	*Solid sol* (stained glass)

Table 1: Classification of types of colloids based on their dispersed and continuous phases [4-6]. The name of the class of the dispersion is italicised, examples given in parentheses directly below.

1.2 History

The history of colloid science is both long and rich. While it is not within the scope of this thesis to summarise it extensively, there are some landmark events and studies which have contributed significantly to the development of the field.

Colloidal systems have been known to chemists for centuries, although largely without recognition as such. The earliest recorded colloidal systems were gold sols, produced by various alchemists. "Potable Gold" was purported throughout the middle ages to be the 'Elixir of Life', an all-healing solution for the treatment of a variety of ailments [7-8]. Similar gold sols have been used extensively to colour stained glass, such as the "Purple of Cassius" in 1665.

It was not until 1774 that it was hypothesised by Macquer [2] that these sols were actually heterogeneous dispersions of small particles, not homogeneous solutions. These results were published in his *Dictionnaire de Chymie* in 1776.

A number of studies then appeared from a variety of scientists categorising various colloid preparations and phenomena. Scheele discovered colloidal manganese, Berzelius produced various sulphide sols, as well as various other studies by the likes of Nägeli, Bütschli, Quincke and Selmi throughout the 1800s.

In 1857 Faraday published an extremely important paper on gold colloids and their properties, entitled "*Experimental relations of gold (and other metals) to light*". This was one of the first extensive and systematic studies of colloids, illustrating their difference from bulk materials or solutions. It also explained the variation of colour in terms of particle size,

the first known example of quantum size effects [9]. This is considered by many as the 'birth of nanotechnology'.

The term 'colloid' (from the Greek '*kolos*', for glue) was coined by Graham in 1861, who used it to explain the differences in the diffusion rates of colloids and crystalloids across a semi-permeable membrane. He also coined the terms 'hydrogel' and 'hydrosol'; nomenclature which remains in use to this day. As a consequence, his collective works over the surrounding years are also considered of vital importance to the field.

Svedberg also published an important body of work beginning in 1905, dealing with the synthesis of organosols of over 30 various metals. During this work he invented the ultracentrifuge, and for these works '*on dispersed systems*' he was awarded the Nobel Prize in Chemistry in 1926 [10].

Concurrent with Svedberg, Zsigmondy also published a body of work on colloids and developed the ultramicroscope, which allowed colloid scientists to directly visualise colloidal particles for the first time. He was awarded the (delayed) 1925 Nobel Prize in Chemistry in 1926, along with Svedberg [11].

With colloid science coming into the limelight to the extent that multiple Nobel Prizes were being awarded for its development, condensation of the collective knowledge was becoming increasingly necessary. It was to this end that Weiser published the excellent series of Inorganic Colloid Chemistry books [12-14], detailing the development of the field thus far. They are both voluminous and elaborate, and their review is not necessary here.

Arguably the most important 'modern' paper on colloid chemistry was published in 1951 by Turkevich *et al.* [15], detailing the synthesis and growth processes of colloidal gold. Many of their syntheses are used to

this day. This point may be considered the starting point of the near-exponential increase in colloid research, giving rise to the massive body of knowledge we know contemporarily as 'colloid chemistry'.

The majority of this classic literature pertains to hydrosols; comparatively there has been much less work done on organosols. In spite of this disparity, the sum of this work is still far too great to wholly summarise here. Instead, the reader is referred to any other number of review on the topic such as the Weiser works [12-14]. There are, however, three major classes of precious metal organosols which are deserving of mention.

The first of these is the polyol method, a technique widely used for the production of metal sols in alcoholic media [16-18]. The precursor materials are suspended or dissolved in a poly-alcohol such as ethylene glycol which is gently heated, causing the precursor to become reduced to a colloidal form. The oxidised polyol molecules then adsorb to the surface of the particles generated to provide them with steric stabilisation. The second although very similar class of organosols are those which are generated in small reducing alcohols containing α-hydrogens, such as methanol or ethanol [19-21]. The third class of organosols are those which are prepared in some arbitrary fashion but *extracted* into an organic solvent [22-24]. While these techniques are all used frequently in modern times for the production of various precious metal sols and many of them require water to work, in no cases that the author is aware of are systematic studies presented of the effects of the solvent composition of the dispersion medium on the size and morphology of the resulting particles. Consequently, this will be one of the aims of the current research, as described in Section 1.4.

1.3 Properties, Characteristics and Theory of Colloids

In order to understand many of the observations of the properties of a colloidal system, it is necessary to understand the physical concepts which underlie their behaviour. The following section is devoted to a brief discussion of these concepts.

1.3.1 Brownian Motion

Brownian motion is the phenomenon which causes colloidal particles to be held in suspension in their dispersion medium. In much the same way as a volleyball is held in the air by being repeatedly hit by its players, a particle may be held in suspension by continuously being 'hit' by the molecules comprising its dispersion medium.

When solvent molecules collide with a colloidal particle, there is a transfer of momentum between the two which results in alteration of their paths. This causes the particle to follow an apparently "random walk" in solution, known as *Brownian motion*. An example of the Brownian motion of three colloidal particles is shown in Figure 1.

If the particles are relatively small, the momentum gleaned from the collisions will be sufficient to overcome the force of gravity, and they will be held in suspension indefinitely. As the particle size increases, this balance slowly shifts until the Brownian motion is in a net downward direction, causing the particle to *sediment* from suspension. Analogously if one attempts to play volleyball with too heavier a ball, it will not be possible to hold the ball in suspension, and it will eventually fall to the floor. This is ultimately the cause of instability of any colloidal system.

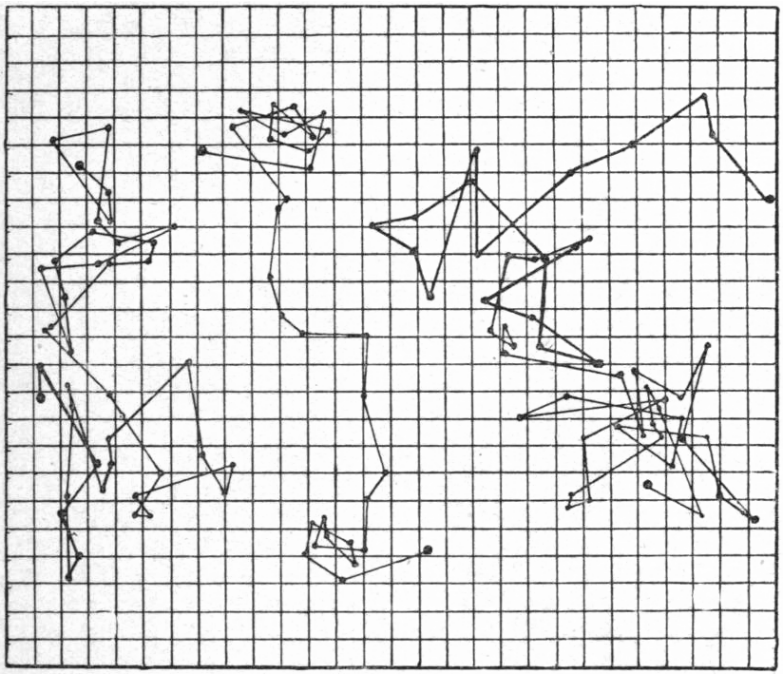

Figure 1: Map of the positions of three 530 nm colloidal particles on a Cartesian grid at 30-second intervals. Each square represents 3.125 μm. Reproduced from Les Atoms [25].

The nature of the Brownian motion of a colloidal particle is affected by a number of factors. Firstly, and as previously mentioned, is the size of the particle. Larger particles are not 'kicked' as far in a given collision, consequently their motion is more sluggish than small particles, making them more susceptible to sedimentation. Smaller particles are 'kicked' further during collisions, so their motion is 'quicker' and they are more resistant to sedimentation. An illustration of the difference between these two cases is shown in Figure 2. Note that technically it is the *inertia* of the particle which controls this factor, as the inertia represents the mass, and the mass is related to the size of the particle by the density. Therefore the critical size at which extremely dense colloidal particles will sediment (for example colloidal osmium particles) may be much smaller than less dense colloidal particles (such as colloidal magnesium particles).

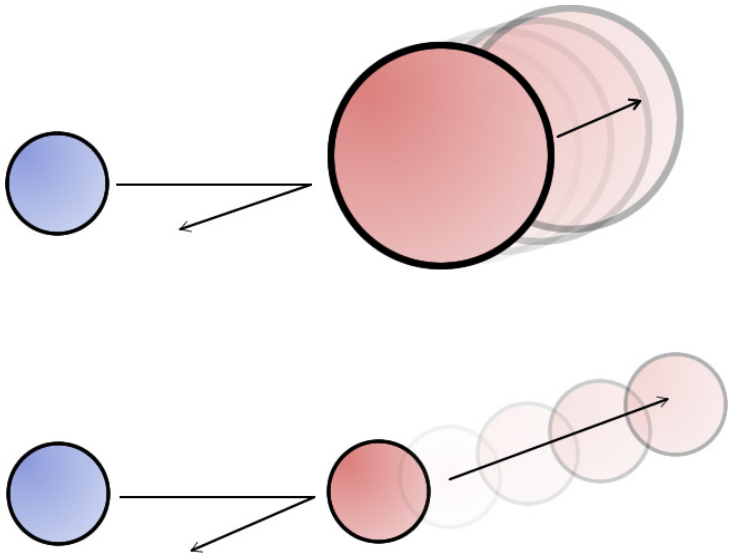

Figure 2: Illustration of the differences in a collision between a solvent molecule (blue) and large or small colloidal particles (red).

The second factor which can alter the characteristics of the Brownian motion is temperature. This has the effect of giving the molecules in the dispersion medium more kinetic energy, which causes them to move faster. The resulting collisions are more energetic, causing the colloidal particles to be 'kicked' further. If these collisions become too energetic, particles may stick together and sediment, destabilising the dispersion (see section 1.3.2). On the other hand, if the temperature is too low the particles will have little motion and will sediment under their own weights. Only at 'intermediate' temperatures (such as in a fridge) are many dispersions at their optimal stability.

A third factor which can influence Brownian motion is the viscosity of the dispersion medium. Particles dispersed in a 'thick' viscous solvent such as DMSO will, other factors aside, be more stable than one dispersed in a 'thin' non-viscous solvent such as MeOH.

1.3.2 Stabilisation Mechanisms

The progression from a stable colloidal system to total macroscopic separation of the dispersed and continuous phases can occur via a number of processes. *Aggregation* (also called *flocculation*, *agglomeration*) is the process where a number of smaller particles adhere to one another to form a single larger particle called an *aggregate*, *floc* or *agglomerate*. When these aggregates reach a critical size determined by the nature of the dispersion medium they will sediment, as discussed in Section 1.3.1, ultimately leading to phase separation. These processes are illustrated in Figure 3.

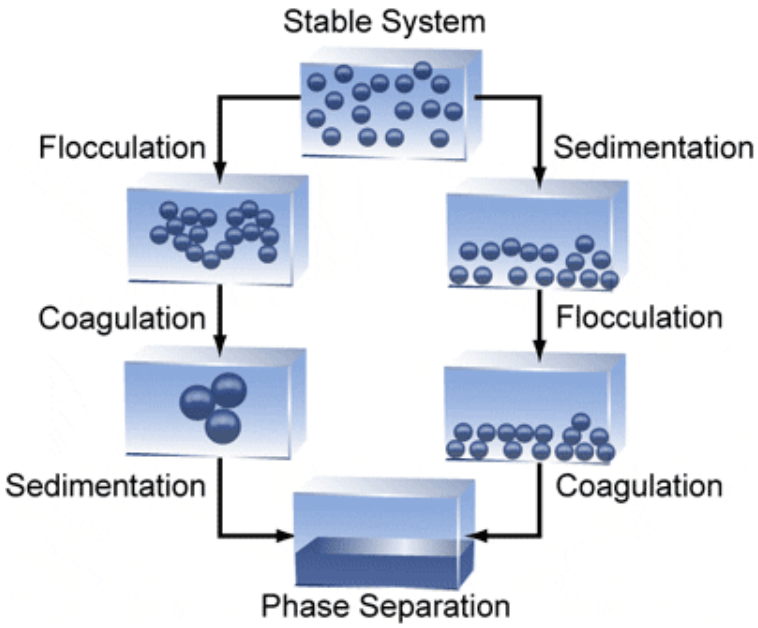

Figure 3: Illustration of the various destabilisation pathways available in a colloidal system [26].

One of the desired features of a colloidal system is that it exhibits long-term stability, *viz*., the particles do not fall out of suspension after a given time period. No exact definitions exist on how to label a colloid as "stable" or "unstable"; the difference between the two often being a matter of judgement. The lines are further blurred by the possible existence of weakly-bound secondary aggregates which may be redispersed with

mechanical agitation. Often the distinction is an easy one to make though, with the majority of colloidal systems either aggregating extremely fast or extremely slowly.

A dispersion of fine particles will naturally aggregate due to the attractive Van der Waals forces between particles, causing it to eventually sediment. To prevent this process, particles must possess a force which mutually repels them, preventing them from coming into close enough contact to aggregate with one another. The origin of the aggregation derives from the shape of the potential energy curve, where ΔG is positive at large particle separations and negative at low particle separations (see DLVO theory, Section 1.3.3). There are two general mechanisms to prevent this aggregation, as follows.

1.3.2.1 Electrostatic Stabilisation: the Electrical Double Layer

Electrostatic stabilisation is the 'natural' mechanism of colloid stabilisation, which occurs for particles which possess a sufficient surface charge. The surface charge attracts ions from the dispersion medium to form an *electrical double layer* (EDL) surrounding the particles, which causes the particles to mutually repel one another. Because the particles are prevented from coming within proximity of each other, they cannot aggregate, so the system is stable.

Over the years there have been a variety of models proposed for the structure of the electrical double layer existing at charged interfaces such as colloidal particles [27]. The earliest model was attributed to Helmholtz in 1853 [28]. It is the simplest model for the EDL, giving a potential which decreases linearly from a plane of charge in the electrode known as the *Inner Helmholtz Plane* (IHP) to a rigid plane of solution ions known as the *Outer Helmholtz Plane* (OHP). Around 1910 this model was improved upon

by Gouy [29-30] and Chapman [31], who replaced Helmholtz's model with a diffuse layer of ions to account for thermal motion, where the potential decreases exponentially from the electrode through the EDL. A combination of these two models was put forward by Stern in 1924 [32], where the charge falls off linearly for a short period, accounting for the tightly-bound surface ions, then decreases linearly into solution.

Since these early models, further progress has been made in regards to the structure of the EDL, with the most accurate model having been proposed in an IUPAC technical report in 2005 [33], being a combination of the three aforementioned models. A diagram of the structure is shown in Figure 4.

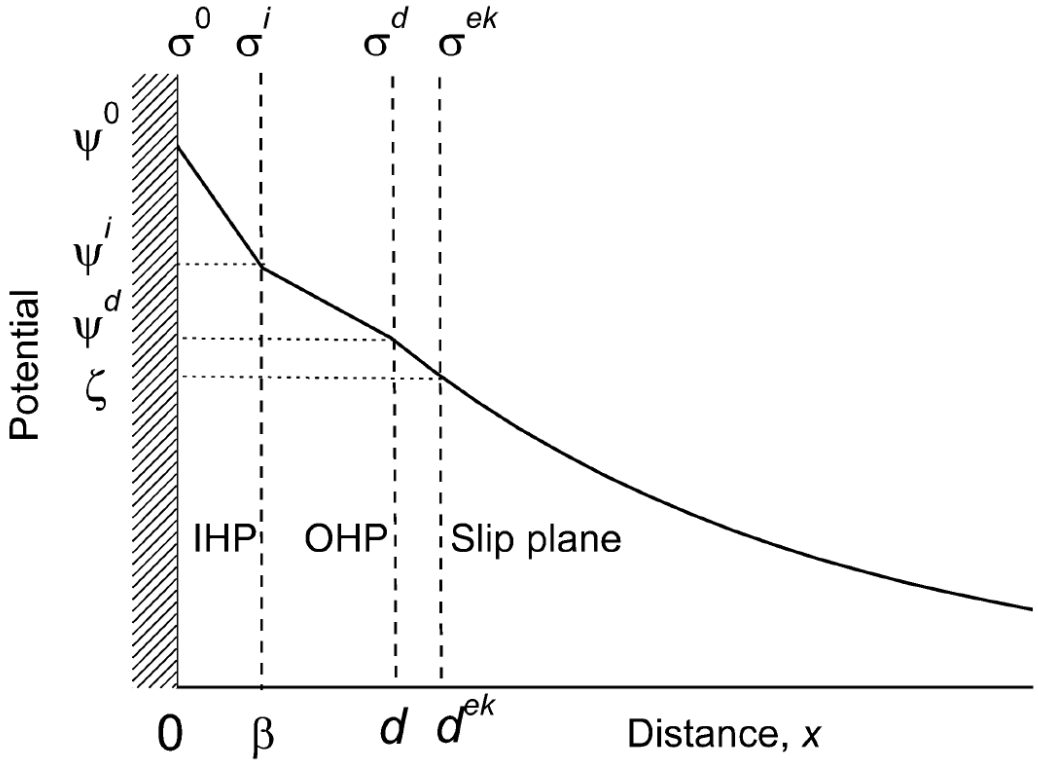

Figure 4: Illustration of the structure of the electrical double layer extending into solution from the surface of a charged plane or particle. Potential is illustrated on the ordinate axis and distance from the surface on the abscissa [33].

The IHP is the locus of adsorption for hydrated counter-ions, between the surface and which there is a region of zero charge density. This is known as the *Stern layer*. The OHP at $x = d$ defines the start of the diffuse layer, which is characterised by an exponential decrease in potential with distance. At a short distance into the diffuse layer is the slipping plane, located at $x = d^{ek}$, which is the point closest to the surface where ions will migrate with a particle. It is at this point that the zeta potential, ζ, is measured (see Section 2.3) [33].

1.3.2.2 Steric Stabilisation

In the absence of sufficient electrostatic stabilisation, steric stabilisation may be used to stabilise a colloidal dispersion. This arises from the adsorption of bulky molecules or polymers referred to as '*protecting agents*' to the surfaces of particles. Provided that these adsorbed molecules are large enough, any two given particles will not be able to approach one another closely enough to aggregate.

The ability of these protecting agents to maintain the colloidal state of dispersed particles by steric repulsion has been known to chemists for a long time. Synthesis of colloids in the presence of biopolymers and macromolecules such as gelatin, tannin, gum arabic, casein, albumin, or starch have been widely exhibited to impart stability upon otherwise unstable systems [12]. In modern times the use of polymers such as poly(vinyl pyrrolidone) or surfactants such as cetyl trimethylammonium bromide are preferred.

There are two main factors which give rise to effective steric stabilisation. The first is the size of the adsorbed molecules. Larger molecules (such as polymers) are generally more effective than smaller molecules (such as the citrate ion) as their larger size makes it more

difficult for particles to approach closely enough to one another to aggregate. This effect is referred to as *excluded volume repulsion*. The second criterion is the strength of binding. The stronger the protecting agent is bound to the surface of the particles, the more effective the resulting steric protection is.

Other than the direct physical preclusion of the ability for particles to approach one another, there are two other effects which give rise to effective steric protection by surface adsorption of molecules. If one considers two particles coated in long alkyl chains in the immediate vicinity of one another, overlap of these chains will decrease their number of available configurations, thus resulting in an unfavourable decrease in entropy which drives particles apart. This is referred to as the *entropic effect*. Secondly, an overlap of these chains results in an increase in 'chain concentration' in the interparticulate region, which is osmotically counteracted by the particles separating. This is referred to as the *osmotic effect* [34].

Also of importance with regards to protecting agents is their conformation in solution, which directly affects their ability to impart stability to a dispersion. The conformation of a polymer is influenced by the nature of its solvent – when dissolved by a 'good' solvent the polymer adopts a 'random coil' conformation, in which case the steric protection is effective. This is referred to as the "*θ-point*", or use of a "*θ-solvent*", and results from a balance of the chain-chain and chain-solvent interactions. When dissolved by a 'bad' solvent where chain-chain interactions are more favourable than chain-solvent interactions, a polymer will tend to 'curl up'. This compression of the adsorbed polymer layer will affect the distance to which particles can approach one another, which in turn affects the stability of the system [35-36], an issue pertinent to this study.

1.3.3 Derjaguin-Landau-Verwey-Overbeek (DLVO) Theory

DLVO theory describes the stability of a colloidal system in terms of the total of its interparticulate forces. It was developed independently by Derjaguin and Landau [37] and Verwey and Overbeek [38] in the 1940s. It ascribes the stability of a colloidal system to the nature of its potential energy curve as a function of particle separation [2]. The shape of the free energy curve is determined by the sum of the Van der Waals attraction between particles and the repulsions between particles arising from either the EDL or adsorbed molecules:

$$V_T = V_A + V_R$$

Where V_T is the total free energy of the system, V_A is the energy of attraction and V_R is the energy of repulsion. The attractive term is given as:

$$V_A = -A/12\pi D^2$$

Where A is the Hamaker constant, and D is the distance between the particles. The repulsive term is given as:

$$V_R = 2\pi\varepsilon a\zeta^2 \mathrm{e}^{-\kappa \mathrm{D}}$$

Where a is the particle radius, ε is the relative static permeability of the solvent, κ is a function of the ionic composition and ζ is the zeta potential [39].

Plotting the summation of these interaction terms gives a diagram which is indicative of the stability of a dispersion, and can be reconciled with its physical properties. A highly stable dispersion will exhibit a curve in which the potential energy increases as the particle separation is decreased, until at very small separations an inversion is reached, and the free energy falls to a primary minimum. A semi-stable dispersion may exhibit a weak secondary energy minimum at larger separations before

the primary minimum, and an unstable dispersion will have no barrier to aggregation at all. Each of these scenarios is illustrated in Figure 5.

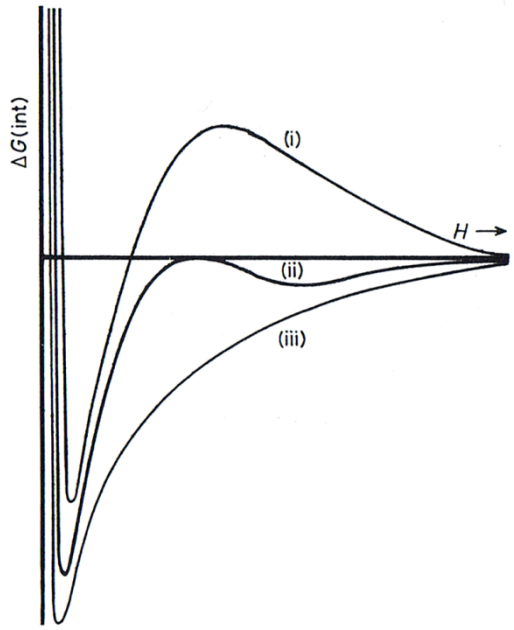

Figure 5: Energy diagram illustrating the variation of free energy of a colloidal system with particle separation. Plot (i) represents a stable colloid, (ii) a weakly stable colloid, and (iii) an unstable colloid [2].

1.3.4 Light Scattering

One of the earliest observations that alerted chemists to the potential differences between molecular or ionic solutions and colloidal systems was the observation that colloidal systems scattered light. This phenomenon still finds importance in modern colloid science studies as it is the basis of all light scattering techniques, such as Photon Correlation Spectroscopy.

When a beam of collimated coherent light is passed through a regular solution it will emerge with approximately the same intensity as it entered with. With a colloidal dispersion, a proportion of the light is adsorbed and reemitted at different angles from the incident beam, *i.e.,* it is 'scattered'. As a consequence the beam can be observed passing through solution, just

as rays of sunlight may be seen passing between clouds under certain atmospheric conditions.

For particles which are small compared to the illumination wavelength the scattering is anisotropic, that is, light is scattered with equal intensity in all directions. This is known as Rayleigh scattering [40]. For larger particles whose diameters are comparable to the illumination wavelength the scattering becomes isotropic, that is, an angular dependence is observed. This is known as Mie scattering [41]. An example of the complex patterns formed for 'large' particles is shown in Figure 6.

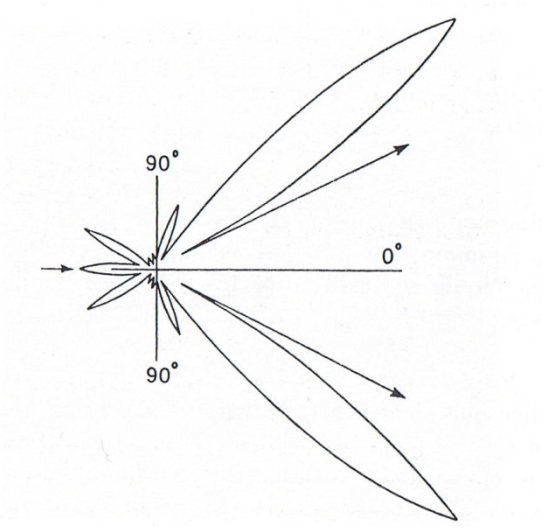

Figure 6: Scattering pattern for a 'large' particle. The intensity at an arbitrary angle is given by the distance from the origin to the perimeter [2].

Whether a particle is 'large' or 'small' compared to the wavelength is determined by its size parameter, α. If α is much smaller than unity, the particle is considered 'small'. The size parameter is calculated by:

$$\alpha = \frac{2\pi r}{\lambda}$$

Where α is the size parameter, r is the particle radius and λ is the wavelength of illumination.

The intensity of the scattered light for 'small' particles is given as:

$$I = I_0 \frac{1 + cos^2\theta}{2R^2} \left(\frac{2\pi}{\lambda}\right)^4 \left(\frac{n^2 - 1}{n^2 + 2}\right)^2 \left(\frac{d}{2}\right)^6$$

Where I is the scattering intensity, I_0 is the incident intensity, θ is the scattering angle, λ is the wavelength, n is the refractive index of the particle, and d is the particle diameter.

When the particles are large or nonspherical the calculation becomes nontrivial, and will not be dealt with in this introductory section. An elementary understanding of these concepts allows one to perform calculations to test experimental observations, as in Section 4.3.

1.3.5 Uses of Colloids and Nanoparticles

Nanoparticles and colloids are purported to have a wide variety of uses in many fields of technology, a fact which is only beginning to be realised since the '*nanotechnology boom*' around the turn of the second millennium. The principles of colloid science as a whole contribute to the development of technology in many fields, such as materials sciences, cosmetics, cleaning products, paints, catalysis, electronics, biomedics, environmental remediations, energy capture, agriculture, food, and military technology [42-43]. A table displaying selected applications in these fields is shown below.

Field	Application
Materials Science	Modification of the properties of clays, tougher and stronger ceramics, nanofluids for improved heat transfer, ferrofluids for bearings, field visualisation, NMR tomography contrast enhancement, etc [44].
Cosmetics and	Sunscreens containing TiO_2 nanoparticles, makeups

Personal Care	containing nanosized pigments, starch-based dispersions [45]
Cleaning Products	Hydrophobic nanoparticulate coatings to repel dirt [46]
Paints	Paints containing less pigment, improved scratch resistivity, polishes with mildly abrasive nanoparticles [47]
Catalysis	Hydroformylation, hydrosilylation, photocatalysis, hydrogenation, etc [48].
Electronics	Improved laser sources and optical storage devices from quantum dots [49], increasing computing power by use of molecular and nanoelectronics [50].
Biomedics	"Nanobots" for the selective delivery of therapeutic agents, immunostaining [50], bandages and antibacterial cleansers containing silver nanoparticles [47].
Environmental	Water purification, sewage disposal [2], dispersion of radionuclides [51], oil/mineral extraction [6]
Energy Capture	More efficient solar cells, fuel cells.

Table 2: List of uses of nanoparticles and colloids.

1.3.6 Preparative Methods

There are two general approaches to making colloids. The first is the "top down" method, whereby bulk material is mechanically subdivided to form smaller particles. These called *dispersion* methods. The second approach are "bottom up" methods, where molecular precursors are joined together to form particles. These are called *condensation* methods. Colloids produced by condensation methods are generally smaller, more

monodisperse and more stable than those produced by dispersion methods [52]. Bottom-up techniques are usually more attractive to the chemist, as they can be performed easily in a laboratory with standard equipment. This brief review therefore will mainly cover such techniques.

1.3.6.1 Chemical Reduction Methods: "Bottoms Up"

The reduction of metal salts in aqueous solution is by far the most common technique for production of colloidal systems, indeed being the basis for many of the classic colloid studies [9, 15, 53]. It allows the greatest control of factors which influence the particle growth, and by careful selection of concentrations of reagents, additives, and reaction conditions, one can fine-tune the synthesis of a colloidal system to produce particles which are highly monodisperse [54-56] or possess novel morphologies [57-61]. A wide variety of colloidal metals have been produced in this fashion, with precious metals often used because of their nobility and favourable electrochemistry.

The chemical basis of the metal salt reduction method is based largely in redox chemistry, as indicated by the name. A metal salt in solution is reduced from a positive nonzero oxidation state by a reducing agent, resulting in singular zero-valent metal atoms. Once the dispersion medium becomes saturated with respect to metal atom concentration, particles begin to grow by aggregation of these atoms into primary particles. For example, the reduction of a gold(III) or palladium(II) salt by sodium borohydride. Shown below is the overall redox equation for reduction of the tetrachloroaurate(III) ion by borohydride, with spectator ions omitted:

$$Au^{III}Cl_{4(aq)}^{-} + BH_{4(aq)}^{-} + 2H_2O \rightarrow Au_{(coll)}^{0} + B(OH)_{4(aq)}^{-} + 4H_{2(g)}$$

Common precursors for metal salt reductions include metal halides ($RhCl_3$, $PdCl_2$), metal halide acids and salts (K_2PtCl_6, $HAuCl_4$), or other miscellaneous compounds such as nitrates ($AgNO_3$). A wide variety of reducing agents are commonly used in combination with these, each with their own set of required reaction conditions. Typically used are sodium borohydride (ice, 273 K), sodium citrate (reflux, 373 K), formates, alcohols, hydrazine, reducing sugars, etc. These may be used in combination with protecting agents (*e.g.* PVP, trioctylphosphine oxide, etc) or other additives (*e.g.* cetyl trimethylammonium bromide), which may adsorb to the outside of the particles or interact with the precursors in a way such that either the growth or stability of the resulting particles are influenced in some way.

While the reducing agents mentioned above are all available off-the-shelf for use in ambient conditions, there are a variety of new synthetic techniques emerging where the reducing agent is either created or activated under much less conventional conditions. These include sonolytic, microwave, radiolytic and photolytic methods.

1.3.6.1.1 Sonolytic Methods

It has been known for a long time that sonochemical methods can activate reaction pathways which are otherwise unavailable under standard conditions. Recently sonochemistry has seen application in colloid science to produce a variety of colloids, inducing reduction of metal precursor solutions [62-65]. The pathway is ascribed to acoustic cavitation, the explosive formation and collapse of air bubbles in the solution. The rate of formation and destruction of these bubbles is so high that it gives rise to extreme localisations of high temperature and pressure under which radical species are generated. These radicals act as the reducing agents which act upon the metal precursor to generate a colloidal dispersion.

1.3.6.1.2 Microwave Irradiation

Application of microwave radiation sources for the production of colloids has only gained ground in the last few years. Many syntheses use standard or lightly modified microwave ovens for elevated-temperature syntheses with good results. The homogenous nature of the heating of a solution by microwaving can aide in increasing monodispersity in otherwise difficult syntheses [52, 66-67].

1.3.6.1.3 Radiolytic Methods

Exposure of solutions of a metal precursor to γ-radiation sources with various additives has been shown by a variety of groups to produce colloidal metals [68-70]. As with sonolytic methods, the actual reducing agents are species such as hydrated electrons and organic radicals generated *in-situ*.

1.3.6.1.4 Photolytic Methods

A variety of photolytic methods exist for the synthesis of colloidal metals, such as laser photolysis [71] and UV irradiation [72]. Some of these methods even allow control of the morphology, producing particles such as nanorods [73-74].

1.3.6.2 Dispersion Methods: "Tops Down"

1.3.6.2.1 Thermal Decomposition

Thermal decomposition takes advantage of an unwanted side-effect common in inorganic and organometallic chemistry — the unwanted decomposition of compounds to form elemental (colloidal) metal. Unstable inorganic precursors such as acetates or cyclooctadiene complexes can be refluxed in high-boiling organic solvents for extended periods, yielding colloidal metal [75-76]. While this does not technically

represent subdivision of material, there is typically no change in oxidation state of the metal used, hence it fits with the dispersion methods.

1.3.6.2.2 Bredig's Arc

Bredig's arc is a classical vaporisation-condensation technique for the production of colloidal systems [77]. An unprotected DC arc is struck between two metal poles submerged in a dispersion medium (usually water), resulting in vaporisation of metal from the pole surfaces. Cooling of the metal vapour by the dispersion medium causes the atomic metal vapour to condense into colloidally-sized particles. It is no longer a widely used technique, due to the uncontrollable nature of the volatilisation and condensation, and the impurity of the resulting products [78].

1.3.7 Surface Adsorption of Carbon Monoxide

The chemistry of simple homoleptic metal carbonyls such as $Ni(CO)_4$ has been known since the 18th century [79], however it was not until later in the 20th century when it was realised that CO adsorb to the surface of colloidal metal particles.

The bonding of CO (and similar isoelectronic ligands) to the surface of colloidal particles can be considered analogous to the bonding in simple metal carbonyls, described as "synergic $p\pi$-$d\pi$ back-bonding". A σ-bond is formed by donation of the nonbonding electrons on the CO carbon to an empty orbital on the metal centre, followed by back-donation from the filled metal d-orbitals to a pair of π^* antibonding orbitals on the CO carbon. This creates an M-CO bond, but simultaneously weakens the C-O bond. This is illustrated below in Figure 7.

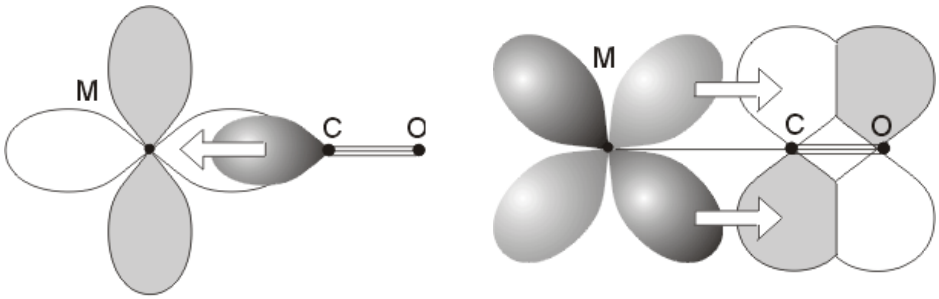

Figure 7: Bonding scheme for metal carbonyls. The formation of a σ bond is shown on the left, with synergic dπ-pπ back donation shown on the right [79].

The "strength" of this weakening is manifested in $\upsilon(CO)_{ads}$, which can be quickly and easily be measured by FTIR spectroscopy. The interest in this is two-fold. Firstly, adsorption and desorption of simple molecules such as CO is often an important step in catalytic processes, hence there is a variety of literature characterising its adsorption (and similar π-acceptor ligands) on supported colloidal catalysts [80-83]. Secondly, evaluation of $\upsilon(CO)_{ads}$ can be used easily as a spectroscopic probe to assess the surface chemistry of a variety of systems [24, 84-89].

1.4 Aims of the Present Study

As mentioned previously, the majority of studies on precious metal sols reported in the literature are based on hydrosols, while a relatively smaller number are based on organosols. To the author's best knowledge however, there is a dearth of systematic studies pertaining to sols generated in dispersion media composed of mixtures of aqueous and non-aqueous solvents. It was therefore of interest to investigate this area.

It is well known that altering the composition of a reaction medium can alter the way a reaction proceeds, in fact it is a sufficiently important field that there are entire books written solely about solvent effects. On these grounds it was predicted that synthesising precious metal sols in

alternative reaction media could possibly influence their particle size and morphology as well as their stability.

It was decided to generate sols in a mixture of water and an other organic cosolvent, the proportion of which (ϕ) was varied between 0% v/v and 90% v/v. The cosolvents chosen were methanol, N,N-dimethylformamide, dimethylsulfoxide, acetonitrile, tetrahydrofuran and acetone. All are dipolar aprotic solvents (except MeOH) with complete miscibility with water in all proportions. Their structures are shown in Figure 8.

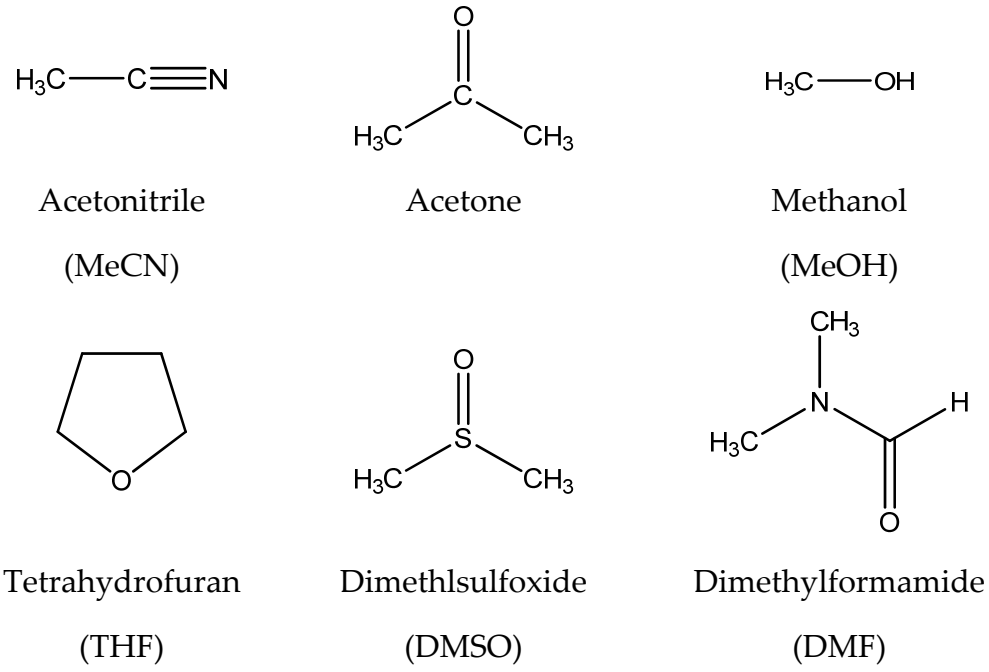

Figure 8: Structures of the solvents used in this study.

Palladium and rhodium were chosen as the metals to study, for three main reasons. Both are highly active catalysts for a variety of reactions [19, 48], so knowledge on their performance when dispersed colloidally in a variety of solvents is paramount. They have also been studied less relative to the other precious metals, based on the number of studies on

SciFinder®. Lastly both were readily available in the forms of $RhCl_3$ and $PdCl_2$.

Because colloidal dispersions of many precious metals (rhodium and palladium included) are inherently unstable without steric assistance, the effect of the addition of polymeric protecting agents prior to reduction was also investigated. Four polymeric protecting agents were chosen: poly(vinyl pyrrolidone), poly(vinyl alcohol), poly(acrylic acid) and arabinogalactan, referred to herein as PVP, PVA, PAA and ARG respectively. Three of their structures are given in Figure 9.

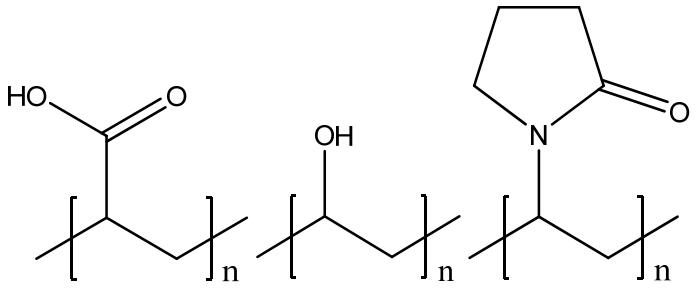

Figure 9: Structures of the protecting agents PAA (left), PVA (center), and PVP (right).

Whereas PVP, PVA and PAA are polymers in the traditional sense, arabinogalactan is a carbohydrate polymer. It is a newly purified and commercially available polysaccharide extracted from the Western Larch tree (*Larix occidentalis*), supplied by the American company Larex, Inc., which has since been acquired the Swiss Lonza group Ltd. The recent advent of its purification and commercial availability has lead to successful trials by Mucalo *et. al.* as a protecting agent for precious metal colloids [90]. Its backbone consists of β-(1→3) linked D-galactopyranose residues, 69% of which bear either one (23%) or two (46%) β-(1→6) linked D-galactopyranosyl residues, with smaller percentages of backbone residues bearing larger branches with terminal arabinose residues [90-92].

Ordinarily these protecting agents are all used in purely aqueous media, and their performance in organic or mixed-media is not widely known. As such, their use in mixed-media in this study pushed the usual boundaries of their usage. A variety of interesting effects were predicted to be elicited from this.

Two reducing agents were chosen to reduce the metal precursors to their metallic state, sodium borohydride and hydrazine hydrate, both of which are routinely used as reducing agents in colloid syntheses in aqueous solvents.

A variety of techniques were employed to characterise the resultant colloids. TEM was used to image particles *ex-situ*, which allowed direct observation of the particle morphologies as well as evaluation of the particle size distribution. This allowed the effect of the cosolvent concentration on the average particle size and polydispersity to be evaluated. Additionally information on the levels of aggregation and particle necklacing could be collected. Two *in-situ* techniques were also used to study the sols. The first was UV/Visible Spectrophotometry, which allowed information to be collected on the sol density (turbidity) and level of reduction in the sols. The second was PCS, which is a technique not often seen in colloid science. This allowed the average hydrodynamic size of the sols to be measured, which gave insights into their state in solution. The combination of these three techniques allowed a comprehensive view of the effect of the cosolvent proportion on the actual state of the dispersion of the generated sols. The use of mixed-media with these instrumental techniques also pushed the boundaries of their usual usage, and as such their effectiveness for characterising sols in mixed-media was unknown.

A second aim of the study was to investigate the effect of the cosolvent proportion (ϕ) on the FTIR spectra of carbon monoxide (CO) adsorbed to the surface of the particles in the sols. Because the stretching frequency of CO is sensitive to the electronic environment in which it exists, this allowed an insight into the chemistry occurring at the surface of the sols resulting from the use of mixed media, and also furthered the knowledge of the behaviour of surface-adsorbed CO.

Chapter 2: Instrumental Techniques

This chapter will serve to cover the basic design and operation of the instruments used in this study to investigate and characterise colloidal dispersions. Also presented is as a brief literature review of some of their other uses across the field of colloid science as a whole. Instruments to be covered include the Ultraviolet/Visible Spectrophotometer, Photon Correlation Spectrometer (Zetasizer), Transmission and Scanning Electron Microscopes, the Electrospray-Ionisation Mass-Spectrometer, the Nuclear Magnetic Resonance Spectrometer, and the Fourier Transform Infrared Spectrometer.

2.1 Ultraviolet/Visible Spectrophotometry

Ultraviolet/Visible spectrophotometry, commonly referred to as 'UV/Vis', is a widely-used analytical technique based on the absorption of ultraviolet and visible electromagnetic radiation (200 nm - 800 nm) by a chemical species. Its versatility and almost universal applicability makes it a very powerful technique, especially for the colloid chemist.

A wealth of information about a colloidal dispersion can be obtained from a simple UV/Vis spectrum. One of its most primitive uses is for determining whether or not a metal solution has been fully reduced to a colloidal dispersion, that is, '*how reduced*' a colloid is. The principle behind this technique is that the absorption spectra of the precursor metal salts usually have sufficiently different absorption profiles from the final colloid that when superimposed over one another, both can be observed simultaneously. The spectra of transition metal salts usually display intense electronic absorption transitions in their UV/Vis profiles in the visible region as reflected by their colours; $RhCl_3$ for example is rose-red,

the $[PtCl_6]^{2-}$ ion is bright orange, and the $[PdCl_4]^{2-}$ ion is brown. Conversely the spectrum of a monodisperse non-adsorbing isotropic colloidal dispersion frequently shows far less features, giving a curved profile which increases monotonically toward lower wavelengths.

There are of course exceptions to these very general rules; colloidal dispersions of gold, copper and silver for example display surface plasmon resonances which give them a variety of brilliant colours, arising from excitation of the "collective modes of motion of the electron gas" [49]. Other elements also display deviations from these general rules, and all elements display dependences on their particle size and on the dielectric constant of their dispersion medium [93].

A second use of UV/Vis spectrophotometry is turbidimetric particle size distribution determinations, that is, the determination of the particle size distribution of a colloidal system using UV/Vis spectrophotometry alone [94-100]. The principle behind the technique is based on the size-dependence of the scattering intensity for dispersed particles, as discussed in Section 1.3.4. It has since been surpassed by a variety of more user-friendly particle sizing techniques so is now more of a historical curiosity, although it is still of interest. Most determinations involve taking absorbance measurements of a dispersion at various wavelengths, converting from absorbance to dimensionless turbidity units, and calculation of the PSD using complex formulae in combination with known optical properties of the system. Numerous research groups have employed such an approach, with results obtained being generally in good agreement with particle size distributions obtained by 'classical' methods such as transmission electron microscopy. An example comparing PSDs obtained by turbidimetry and SEM is shown in Figure 10. In a similar way, it has been shown possible to determine the average

particle size of colloidal gold based on the position at which its surface plasmon resonance occurs [101].

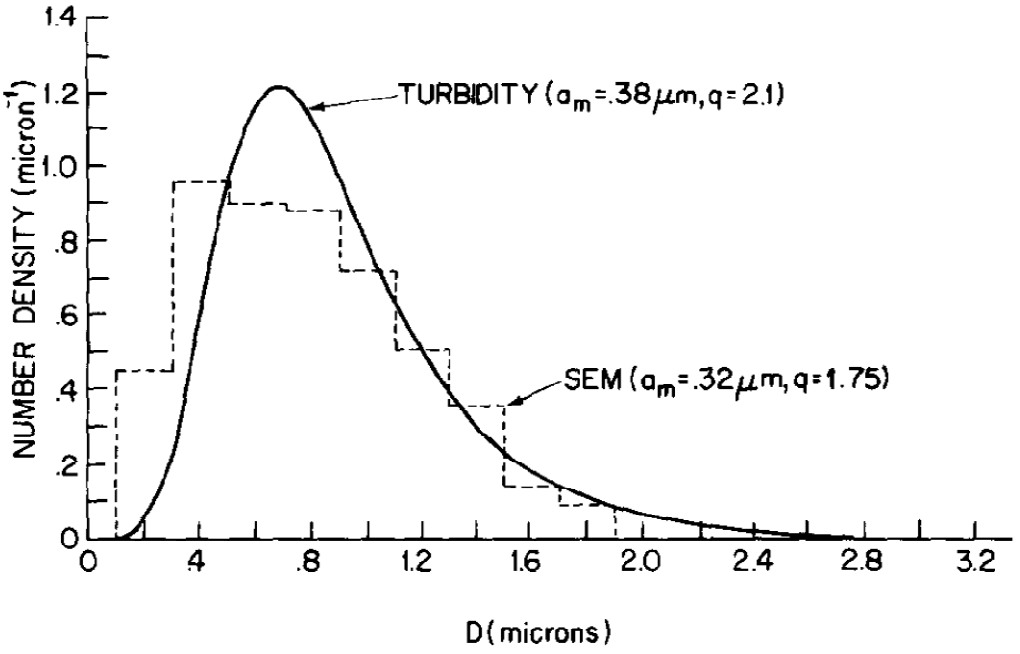

Figure 10: Comparison of a particle size distribution of a latex dispersion, collected by turbidimetry and scanning electron microscopy. Note the relatively close alignment of the two distributions [94].

Because the turbidity relates directly to the particle size, a third use of UV/Vis spectrophotometry is for following aggregation/flocculation processes *in-situ*. For example, Furlong *et al.* [102] have studied the UV/Vis spectra of colloidal platinum sols treated with gaseous hydrogen, finding that the aggregation caused by the treatment causes significant changes in the spectra. For example, the change in the absorbance at a fixed wavelength (A_{450}, for example) can be used to indicate whether or not the particle density has increased or decreased. Similarly, comparison of the A_{450} measurements between preparations can be used as a semi-quantitative estimate of the particle loading in a given dispersion, a technique which has been employed previously by Mucalo *et al.* [3, 90, 103].

2.2 Photon Correlation Spectroscopy

Photon Correlation Spectroscopy (PCS) is a light scattering technique used to elucidate the particle size distribution of colloidal systems *in-situ*. It is also commonly referred to as Dynamic Light Scattering (DLS), or sometimes Quasi-Elastic Light Scattering (QELS). Samples can often be measured as-received, which is advantageous over *ex-situ* techniques such as TEM where removal of the particles from their dispersion medium can cause changes in their properties.

As suggested by the name, PCS is an optical technique which relies on the interaction of light with the analyte. A monochromatic laser beam is shone through a cuvette containing the analyte suspension, which is scattered by the particles in the measurement volume. Particles which are small with respect to the wavelength ($\cong \lambda/10$) act as Rayleigh scatterers, scattering all light isotropically. For those particles whose size is approximately equal to the illumination wavelength, there is a strong angular dependence in the scatter intensity with respect to the detection angle, as described by Mie 'theory'. In either instance, the scattered photons mutually interfere giving a time-dependent fluctuation of scattering intensity, which is detected by an off-axis photodetector as a speckle pattern. The intensity data is passed through a software correlator, which compares the intensity of the signal to itself at various time intervals. If a scattering event occurs at time t, and the signal is correlated at $t + \Delta t$, there will be little correlation in the signal as the particle has shifted. However, if the signal is correlated at smaller intervals such as $t + \delta t$, a strong correlation will exist. For small particles the correlation coefficient will be less than for large particles and will last for a shorter period. A graph of the correlation coefficient versus the correlation time is

referred to as a correlogram. This processing is performed using an autocorrelation function such as below.

$$g^1(q;\tau) = \sum_{i=1}^{n} G_i\,(\Gamma_i) e^{(-\Gamma_i \tau)} = \int G(\Gamma) e^{(-\Gamma\tau) d\Gamma}$$

The correlation data is then processed by an algorithm such as "NNLS" or "CONTIN" which converts it into a particle size distribution. A diagram showing the fluctuation in scattering intensity, correlogram and PSD for "large" and "small" particles is shown in Figure 11.

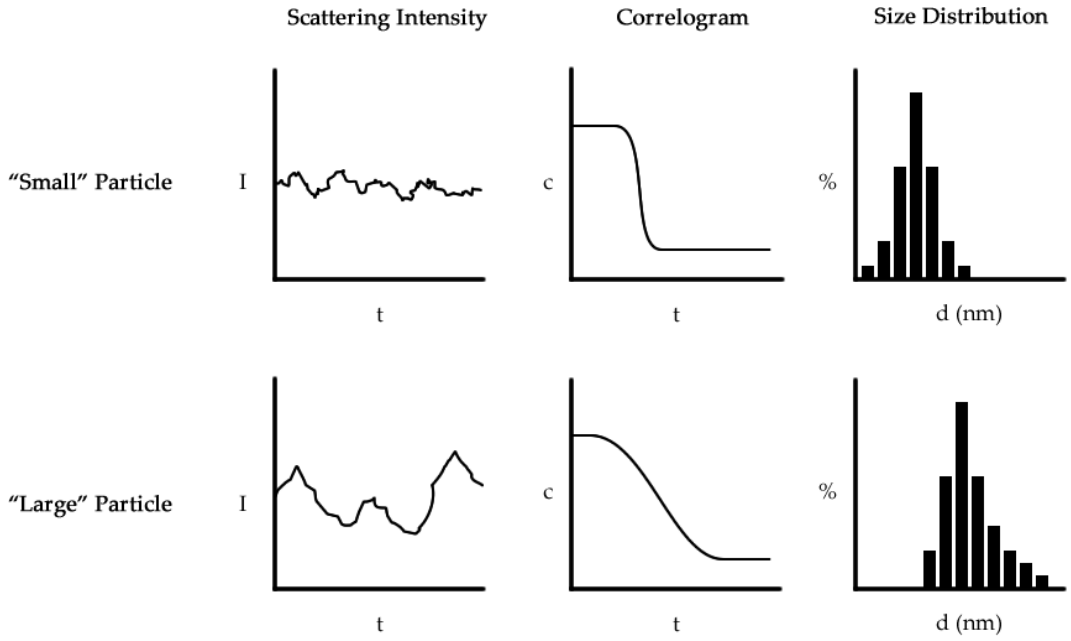

Figure 11: Comparison of the time-domain scattering intensity, correlogram and resulting particle size distribution for a "large" and a "small" colloidal system.

Because the mobility of the particles depends on their diffusion coefficient and not on their size, the data generated must then be converted into a hydrodynamic radius using the Stokes-Einstein equation, given below:

$$d(H) = \frac{kT}{3\pi\eta \mathrm{D}}$$

Where d(H) is the hydrodynamic radius, kT is the thermal temperature scale, η is the viscosity of the dispersion medium and D is the diffusion constant.

Because of the necessary use of the Stokes-Einstein equation, the PSD data generated using a technique such as this is not necessarily an indication of the 'particle size'; a fact which many seem to overlook. Rather it is a hydrodynamic radius, the size of a sphere with a diffusion coefficient equal to that of the sample. This means it may include in its sum the 'core' of the particle, any associated electrical double layer, and any adsorbed polymer molecules. It is most accurately considered to be an indication of the 'hydrodynamic state' of a colloidal dispersion.

2.3 Electrophoretic Light Scattering

Electrophoretic Light Scattering (ELS) is a technique used to measure the zeta potential (ζ) of colloidal particles, the potential at the slipping plane in the EDL. The ζ-potential of a colloidal system is an indicator of the repulsive force between particles due to the electrical double layer, and is generally a good indicator of a colloidal system's stability. Systems with $\zeta \geq |30|$ mV are generally considered to be adequately stable.

Both PCS and ELS measure the properties of particles based on the interference of photons with each other. However, where the motive force for the movement of particles in PCS Brownian motion, the motive force in ELS is an externally applied electrical field. This field causes charged particles to move in solution, called *electrophoresis*. A set of laser beams crossed over in the analysis volume gives rise to a set of interference fringes, from which the motion of the particles can be analysed. As the potential across the solution is rapidly reversed ('*Fast Field Reversal*'), the

acceleration of the particles is measured, which is proportional to their ζ-potential.

2.4 Transmission Electron Microscopy

Transmission Electron Microscopy (TEM) is a microscopy technique used widely in materials science for high-resolution imaging applications to visualise the fine structure of materials. It is capable of subatomic resolution, with the lattice structures of a variety of materials being routinely resolved. It is considered the *de facto* standard for characterisation of colloidal systems, playing an incredibly important part in colloid science and nanoscience as a whole.

The prime use of TEM for the colloid scientist is for evaluating the size and morphology of colloidal particles. Typically a large number of particles are imaged, their sizes measured, and a particle size distribution in the form of a histogram is generated. A wide range of samples can be characterised in this fashion [104]. Significant care must be taken in interpreting TEM micrographs, as it is an *ex-situ* technique, and the necessary dehydration of samples during their preparation means that some structures observed in micrographs are not necessarily present *in-situ*.

The first TEM was developed in the 1930's by Knoll and Ruska [105], and commercial instruments were available soon afterward. This meant that for the first time scientists could visualise colloidal particles, collecting information on both particle size and morphology. As is the case with many instruments initially the resolution was not particularly good, although continued development over the years has seen the production of TEMs capable of exhibiting spatial resolutions below 50 picometers (0.05 nm) at magnifications of up to 50,000,000 x [106-107]. Despite these

massive theoretical resolutions, a variety of imperfections in the electromagnetic lenses of TEM instruments called *aberrations* usually impinge on the imaging process. For the 'average' TEM user an increase of 10^3 – 10^4 in resolution is seen over optical microscopy, although this is still substantial.

The reason that TEM gives such a large increase in resolution over an optical microscope is that it uses a beam of electrons to image the sample rather than a beam of light. Electrons are subject to wave-particle duality, which because of their small mass gives them a very small de Broglie wavelength. Since the resolving power of a microscope depends directly on the wavelength of the source used, this means electrons are a much better source for high resolution work than visible light is. Further resolving power can be gained by increasing the accelerating voltage of the instrument, which has the effect of accelerating the electrons faster so they have a higher kinetic energy, which in turn gives them an even lower wavelength. Typical modern TEMs use accelerating voltages in the ranges of 100 kV – 300 kV.

The layout of a TEM is somewhat complex, although there are a variety of basic components worth mentioning. At the top of the column is the electron gun, usually a tungsten filament or a single LaB_6 crystal, which emits electrons when provided with sufficient current. These electrons are accelerated down the column, controlled by a variety of electromagnetic lenses (*cf.* glass lenses in optical microscopes), which focus the beam into a small spot on the sample. The majority of the electrons pass through the sample to a fluorescent screen in the viewing chamber on which the projected image of the sample is observed, but a significant portion is absorbed by the sample, providing the phase contrast in the resulting image. A schematic illustrating these components is given in Figure 12.

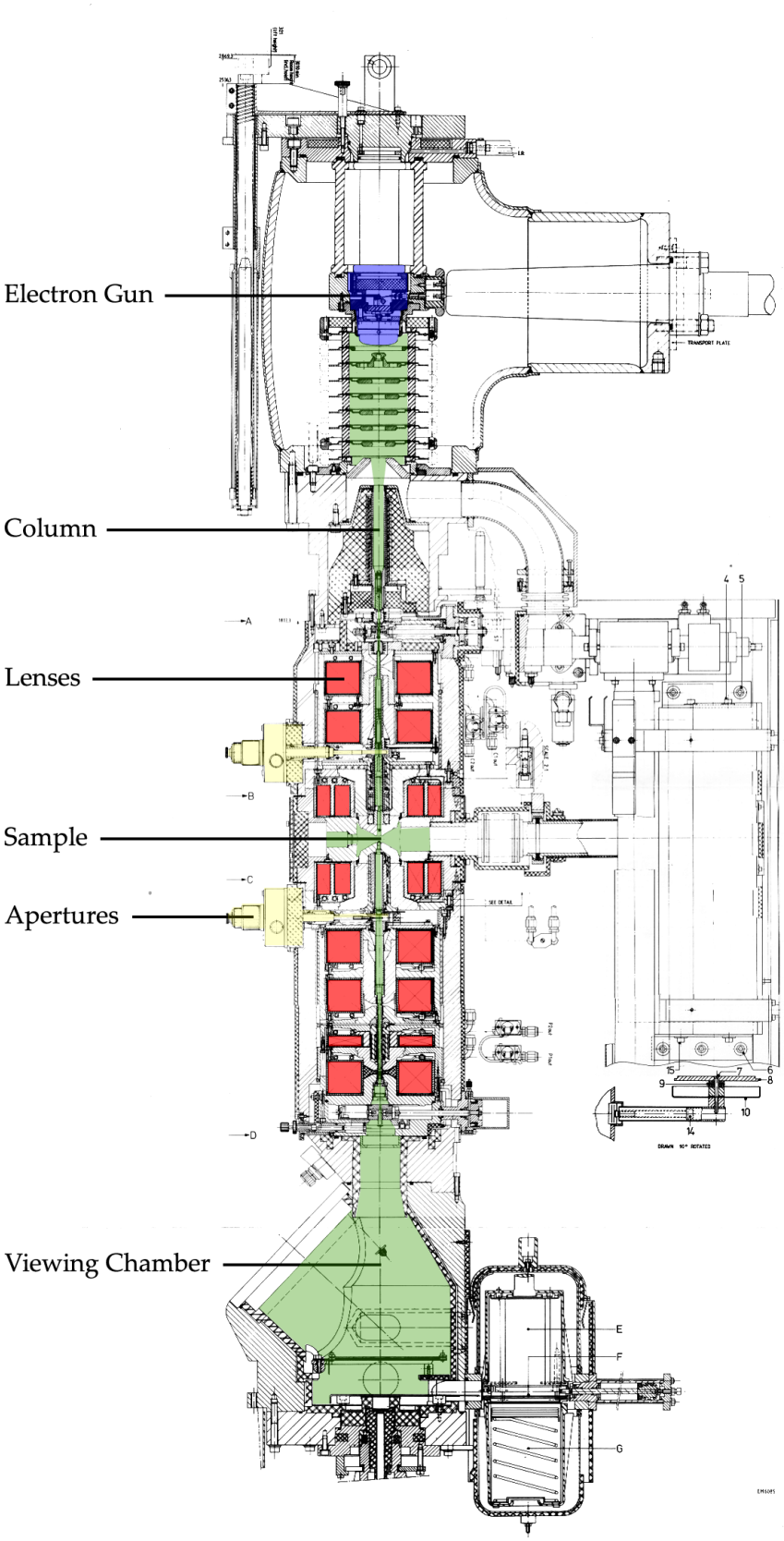

Figure 12: Cross-section through the Philips CM30 TEM column, with the core components labelled. Adapted from [108].

2.5 Scanning Electron Microscopy

Scanning Electron Microscopy (SEM) is an electron microscopy technique similar to TEM. Whereas images in TEM are formed by electrons which pass through the sample, images in SEM are formed from electrons which are backscattered from the sample and detected by a secondary electron detector. The advantage to this is that larger samples can be analysed three dimensionally, although the resolution is generally inferior to that of a TEM instrument. This can be useful for inspecting very large particles, substrates to which particles are adsorbed, or morphologies of objects. The characteristics of an SEM are otherwise similar to that of a TEM.

2.6 Electrospray Ionisation Mass Spectrometry

Electrospray Ionisation Mass spectrometry (ESI-MS) is an instrumental technique used in analytical chemistry to measure the mass to charge ratio (m/z) of chemical species in solution. Compared to other ionisation techniques electrospray is relatively soft, so large molecules can be observed with little fragmentation. Because of this, singly-charged or pseudomolecular ions are commonly observed, which can aid in identifying the species present in a solution by comparing the mass spectrum and isotopic ratios with likely candidates.

In ESI-MS, a sample to be analysed is dissolved in a mixture of volatile solvents (*e.g.* methanol or acetonitrile) and pumped through a capillary. When the correct potential is applied to the capillary, a stream of charged droplets is nebulised from its tip known as a taylor cone. As the charge density of the droplets approaches the maximum for the surface tension of the solvent, the droplets are destroyed either by a coulomb explosion or ion evaporation [109-110]. This process is often aided by a desolvation gas.

The spray of ions is passed through a set of skimmer cones, transitioning the pressure between atmospheric and the ultrahigh vacuum required for the operation of the rest of the instrument. The stream of ions then passes through a mass analyser such as a quadrupole or time-of-flight which separates them according to their mass to charge ratios, and then to a detector. The detector data is fed to a computer which converts the ion counts to a mass spectrum which is displayed on-screen.

2.7 Nuclear Magnetic Resonance Spectroscopy

Nuclear Magnetic Resonance (NMR) Spectroscopy is a technique used in chemistry to elucidate information about the chemical environment of the constituent atoms of an analyte, commonly leading to deduction of the analyte's structure. For a given nucleus to be NMR-active it must exhibit a nonzero spin, an intrinsic property of atomic nuclei given by the spin quantum number. This can be zero, an integer, or a range of simple fractions such as $^{5}/_{2}$. There are a wide range of NMR-active nuclei, including ^{1}H, ^{13}C, ^{31}P, ^{35}Cl, ^{103}Rh and ^{195}Pt. Several of the heavier nuclei commonly used in colloid preparations are NMR-active (such as Rh, Pt, Pd), allowing their observation. NMR of colloidal particles gives a broad signal, whose position is shifted from that of the bulk metal by a Knight Shift [111].

2.8 Fourier Transform Infrared Spectroscopy

Infrared Spectroscopy, also known as Vibrational Spectroscopy, is an analytical technique used to investigate the absorption of infrared radiation (approximately 4000 cm^{-1} - 400 cm^{-1}) by molecules. Absorption of radiation of this frequency gives rise to fundamental vibrations of the bonds in (and sometimes between) molecules. A plot of the absorbance versus the frequency of the radiation allows identification of the vibrating

species, allowing structural determination of the molecule. For example, υ(CO) usually occurs around 1700 cm^{-1}, and υ(OH) around 3500 cm^{-1}.

To generate an IR spectrum, the required wavelengths need be generated by a radiation source, passed through a sample of some form, and detected on the other side. Historically this required either the source or the detector to be scanned across the entire wavelength. Modern FTIR instruments however rely on the use of a Michelson interferometer, eliminating this need. A single beam is directed toward a half-silvered mirror, which splits the beam two ways. When the two beams then converge, an interference pattern is produced containing all the necessary information to compute the spectrum.

While FTIR spectroscopy may not seem like an inherently useful technique for the characterisation of colloids, it has been proven useful for the detection of surface-adsorbed species. Many studies on adsorbed species utilise FTIR [24, 81, 85-89, 112-115], as it is relatively fast and easy, and many laboratories are equipped with FTIR spectrometers. Indeed, it is the basis for the studies in this study concerning the surface adsorption of CO to colloidal particles.

Chapter 3: Materials and Methods

3.1 Materials

All chemicals were purchased and used as-received. Millipore distilled water (G = 18±0.2 μS) was used in all preparations. All glassware was acid washed with aqua regia prepared by mixing 3 parts hydrochloric acid (analytical reagent, 36%) and 1 part nitric acid (analytical reagent, 70%), both obtained from Ajax.

Rhodium trichloride hydrate (99%) and palladium dichloride (99%) were obtained from Aldrich Chem. Co. Further rhodium was obtained from Precious Metals Online, based at Monash University LPO, Melbourne, Australia (99%).

Sodium borohydride ("laboratory chemical" grade) was obtained from Asia Pacific Specialty Chemicals Ltd. Hydrazine hydrate (general purpose reagent, 99-100%) was obtained from BDH Chemicals Ltd.

PVA (99%, M_W 22,000) and PVP (99%, M_W 700,000) were both obtained from BDH Ltd. PAA (M_W 2,000) was obtained from Aldrich Chem. Co. Ltd. ARG (99%) was obtained from Larex, Inc.

Acetonitrile (analytical grade, 99.5% assay by gas chromatography), acetone (analytical grade, 99.5% assay by gas chromatography), *n*-heptane (99%), tetrahydrofuran (laboratory reagent, 99%) with 0.04% butylated hydroxytoluene and methanol (99.9%, spectrophotometric grade) were all obtained from Ajax. Dimethylsulfoxide (reagent grade, 99.9% assay by gas chromatography) was obtained from Scharlau.

Amberlite MB 6113 H^+/OH^- ion-exchange resin was obtained from Sigma. Whatman filter paper (540 hardened ashless) was used during filtration steps. Sodium azide was obtained from Ajax Finechem Pty Ltd. (reagent grade 99%). Deuterium oxide for NMR experiments was obtained from Aldrich (>99.6% deuterated). Latex particle size standards were obtained from SpheroTech Inc. (5% w/v solutions, nominal 70 nm and 2070 nm) and Duke Scientific. Carbon monoxide (99.999%, research grade) was obtained from BOC.

3.2 Methods

3.2.1 Reagent preparation

The general procedure for the synthesis of metal sols closely followed previous work by Mucalo et al. [90], with some minor modifications. 0.03 mol L^{-1} stock solutions of each metal salt were made by dissolving the salt in distilled water. For palladium, an additional 2 mole equivalents of NaCl were added to aid dissolution of the water-insoluble $PdCl_2$ as the soluble complex ion $[PdCl_4]^{2-}$. All metal salt solutions were produced in water.

5% w/v stock solutions of protecting agents (PVP, PAA, PVA, ARG) were used to impart stability by way of steric protection onto the otherwise inherently unstable rhodium and palladium colloids. Each was prepared by dissolution of 5.000 g of the respective solid polymer powder into a 100 mL volumetric flask with 0.100 g of NaN_3 added to deter bacterial and fungal growth. All protecting agent solutions were produced using water.

Fresh solutions of $NaBH_4$ (0.033 mol L^{-1}) were produced daily in water and used immediately, due to their instability which causes them to convert rapidly to borates in hydroxylic solvents [116].

3.2.2 Colloid preparation

3.2.2.1 Sols with No Cosolvent

The following procedure was used to produce the hydrosols generated in pure water. These were the 'control sols' against which the sols generated in mixed-media were compared.

1.00 mL of the 0.03 mol L^{-1} metal salt solution and 46.5 mL of water were placed in a scrupulously clean beaker with a magnetic stirring bar with 1.5 mL of a 5% w/v solution of a protecting agent. The solution was cooled to 0°C in an ice bath while being stirred. 1.75 mL of the reducing agent was added dropwise at a rate of *ca.* 1 drop per second. The resulting instantaneously formed pitch-black sol was stirred for an hour, then stirred for a further hour with *ca.* 0.1 g of ion-exchange resin to remove ionic impurities. Conductivity data is given in Section 5.1.2 to support the effectiveness of this resin.

The sols were gravity-filtered with Whatman filter paper, allowing passage of particles smaller than 8 μm. Significant darkening of the filter paper during this period was taken to indicate retention on the filter paper of aggregates larger than 8 μm, in which case the colloid was instead carefully decanted to accommodate for the collection of the full range of particle sizes. Samples were then stored at 5°C until analysis, usually within several days.

3.2.2.2 Sols in Mixed-Media

The preparation of the mixed-media sols was identical to the hydrosols described previously except for one factor. In these sols a portion of the water in the reaction mixture was replaced by an equal volume of cosolvent such that the final ratio of volumes in the reaction mixture, once the reducing agent was added, was equal to a value given in Table 3. This

method allowed the mixed-media sols to actually be generated in the mixed-media, so their actual growth was affected by the solvent composition.

Non-ideal effects, specifically non-additive volumes, were ignored.

Water volume replaced (mL)	Resulting organic concentration (% v/v)
5	10
15	30
25	50
35	70
45	90

Table 3: Amount of water replaced during synthesis of sols in mixed-media to achieve the desired final solvent composition.

3.2.3 CO Adsorption

Samples were prepared in a similar way to previous works by Mucalo *et al.* [24, 85, 87-88, 112-113] with some minor alterations. Whereas previous works used a specially designed gas bubbler, it was found equally as effective to use a pipette attached to the gas cylinder and submerged in *ca.* 1 mL of colloid solution in a 5 mL glass vial. A cold-trap using an acetone slush was used between the cylinder and the colloid to condense any $Fe(CO)_5$ (see Chapter 7). Plastic vials could not be used as they were dissolved by the organic solvents. CO was bubbled through the solution at a rate of *ca.* 25 mL min^{-1} (as measured by an inverted measuring cylinder under water), and an aliquot was withdrawn for analysis after 20 minutes.

3.3 Characterisation Methods

3.3.1 Ultraviolet/Visible Spectrophotometry

All spectra were recorded on a VARIAN Cary 100 Scan UV/Vis spectrophotometer using Cary WinUV Scan software, version 3.10(182). Samples were diluted 1:8 with a mixture identical to their dispersion medium and run in a pair of matched quartz cuvettes over the wavelengths 190 nm – 900 nm. For turbidity measurements, the absorbance at 450 nm was recorded and multiplied by the dilution factor to generate a dilution-independent absorbance number which was representative of the "density" of the colloid.

3.3.2 Photon Correlation Spectroscopy

Experiments were run on a Malvern Zetasizer 3000HS$_A$ using a 535 nm He-Ne laser with 90° detection. Analysis was performed in AUTO mode using the CONTIN algorithm. Disposable plastic fluorescence cuvettes of 1 cm pathlength were used for samples in water, and equivalent quartz cuvettes for samples containing organic solvents. Scans of each sample were recorded three times and averaged. All data collected was from the most intense peak in the "number" section in the sample summary table, which the researcher has found to be the most reliable way to collect data from the Zetasizer.

3.3.3 Transmission Electron Microscopy

Imaging was performed on a Philips CM30 TEM with the accelerating voltage set to 200 kV or 250 kV. Samples were deposited onto collodion-coated 400-mesh 3 mm copper grids prepared at the University of Auckland's Cell Biology Department. Two main methods were used for preparation of the samples. Ordinarily samples were prepared by

deposition of a single drop (*ca.* 30 μL) of the undiluted colloid onto a grid in a petri dish, and were left in a desiccator under vacuum overnight or until dry. For samples where this did not provide an adequately homogeneous dispersion for imaging, an N_2-driven nebuliser was used to spray the sample onto the grids. Individual grids were cut from their parafilm support medium and taped into a piece of filter paper in a petri dish to prevent them from being blown away during spraying. A schematic of the nebuliser is shown in Figure 13.

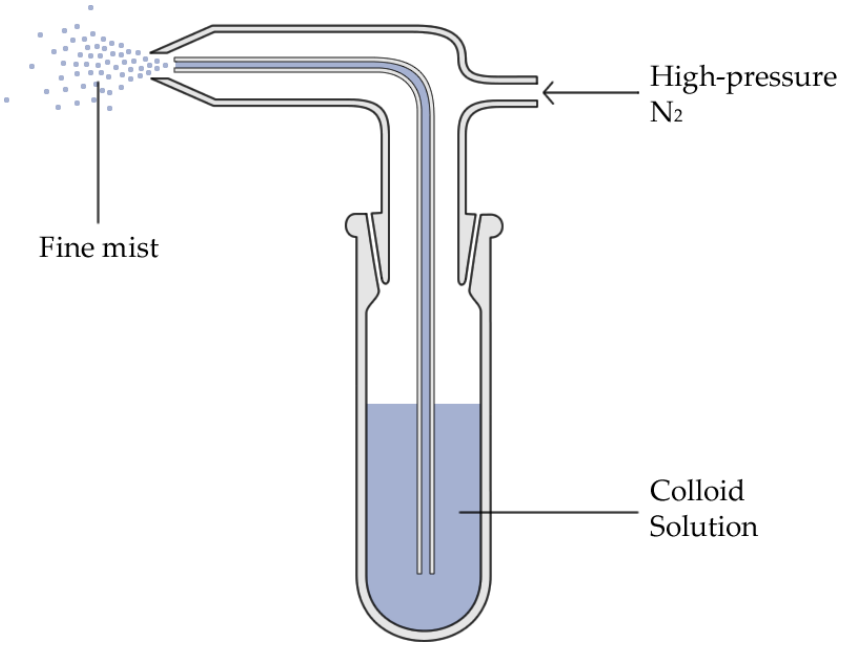

Figure 13: Schematic of the pneumatic nebuliser used for preparation of TEM samples.

Although the former method was deemed more crude, it was used more frequently due to its fast and easy nature. Samples prepared by this method generally tended to be of an acceptable quality for imaging, although sometimes their appreciable polymer content caused the particles to 'clump' into thick deposits on the grid. This effect contributed significantly to the blurriness encountered in imaging some preparations.

For colloids in prepared in mixtures of water and either DMSO, MeCN or DMF an additional "solvent extraction" step was performed before

application of the colloid to the grid. Approximately 1 mL of colloid solution was introduced into a clean glass vial with a volume of *n*-heptane approximately equal to twice the volume of cosolvent in the colloid to be extracted. For those sols generated in 90% v/v a small amount of water (*ca.* 0.5 ml) was added to aid extraction. The vial was shaken for several minutes, and a drop of colloid from the bottom (largely aqueous) layer was deposited onto the grids.

3.3.4 Scanning Electron Microscopy

All images were recorded on a Hitachi S4700 FE-SEM at 20 kV. 'Globs' of precipitated protecting agent were extracted from solution with tweezers and allowed to dry under ambient conditions. Once dehydrated, sections were cut and mounted to aluminium SEM stubs with double-sided carbon tape and sputtered with a thin coating of platinum.

3.3.5 Electrospray Ionisation Mass Spectrometry

All spectra were run on a Bruker MicrOTOF™ ESI-MS. Samples were run undiluted (≅ 0.0006 mol L^{-1}) in both positive and negative ion mode. The mass ranges investigated were 100 m/z – 2000 m/z. Capillary exit voltage was set to 100.0 V, skimmer cone voltages to 50.0 V and the reflector voltage to 1300 V.

3.3.6 Nuclear Magnetic Resonance Spectroscopy

^{103}Rh spectra were run on a Bruker Avance 300 MHz FT-NMR with TopSpin 1 hardware using a broadband probe tuned to its lowest possible frequency.

3.3.7 Fourier Transform Infrared Spectroscopy

Samples were run at 4 cm^{-1} resolution on a PerkinElmer Spectrum™ 400 FTIR spectrophotometer between 2200 cm^{-1} and 1800 cm^{-1} for 3 scans.

Samples were prepared by placing a drop of colloid solution between two circular Buck Scientific 3 mm x 32 mm CaF_2 windows held in a SpectraTech PresLok™ holder.

Chapter 4: Instrument Calibration, Issues, and Parameters

4.1 Issues Encountered with the PCS Technique

Relative to many other more established techniques such as TEM, PCS is relatively new and unknown. Theoretically it is perfectly suited to determining the particle size distributions of colloidal systems, however in practice it has many complications. Analysis of 'simple' systems such as monodisperse latex spheres and unprotected colloidal gold can be performed fast and easily, and high levels of confidence in the results can be assured by the Malvern quality control criterion. Real samples repeatedly proved to be much more difficult, with solvent choices and adsorption of macromolecules causing several issues which affected results.

4.1.1 Measurement Parameters

For samples containing an organic cosolvent, the viscosity and refractive index of the sample dispersion medium were required to be input manually. Several of the solvents used such as DMSO exhibited marked deviations from ideality in their properties upon mixing with water, depending nonlinearly on their fractional compositions. DMSO for example becomes almost twice as viscous with 33% water content than when neat [117]. If one assumes that that protecting agent polymer chains were entirely particle-bound, then their contribution to the viscosity of the dispersion medium would have been negligible. However, this assumption is not necessarily correct. Because the protecting agent was used in excess with respect to the particles, it was possible that some remained 'free' in the dispersion medium. Determining exactly what

contribution the free polymer chains made to the viscosity of the medium was deemed nontrivial, and beyond the scope of this project. Furthermore the viscosities of some polymer solutions such as PVA are known to depend on the level of hydration which is directly affected by the proportion of organic solvent used, and also dependent on the concentration dissolved salts present. As a consequence it was assumed that the major contribution to the viscosities of the dispersion media were simply the nature of the solvents used, the exact viscosities and refractive indexes of which were obtained from the literature [117-123] and converted to volume fractions (ϕ) as required. Refractive Indices (RI) also showed strong deviations from ideality in many cases. Graphs showing these deviations and the values used for PCS are shown below and overleaf.

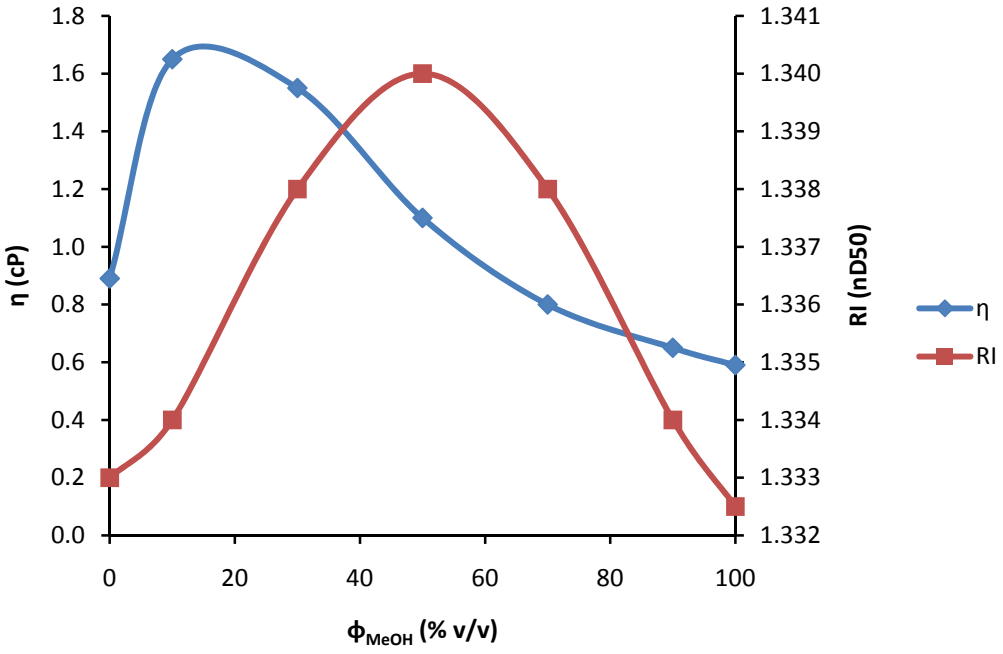

Figure 14: Viscosity and Refractive Index of binary MeOH-H_2O mixtures.

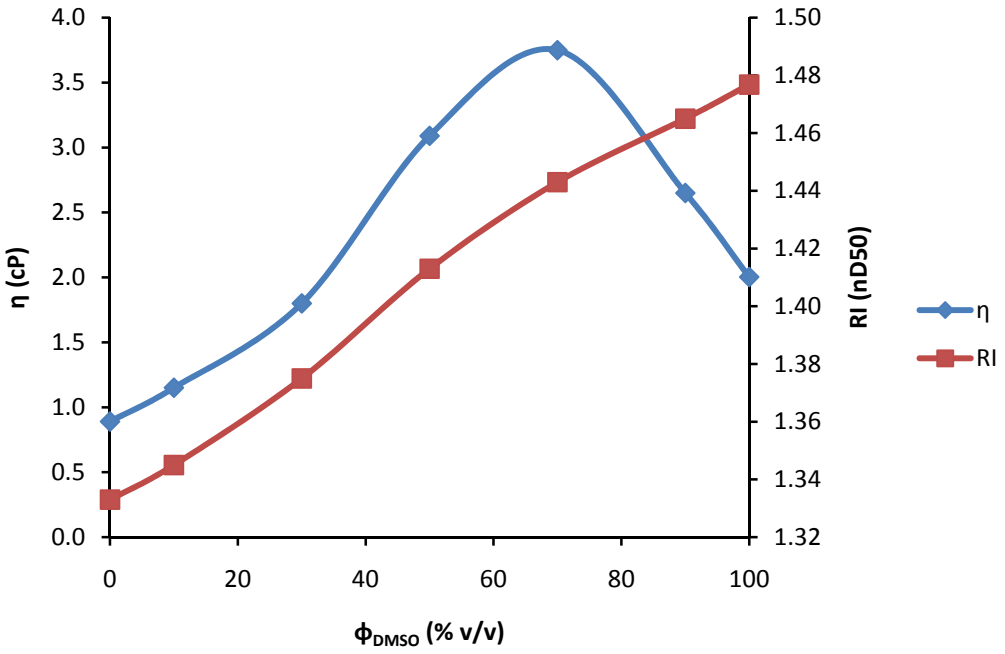

Figure 15: Viscosity and Refractive Index of binary DMSO-H_2O mixtures.

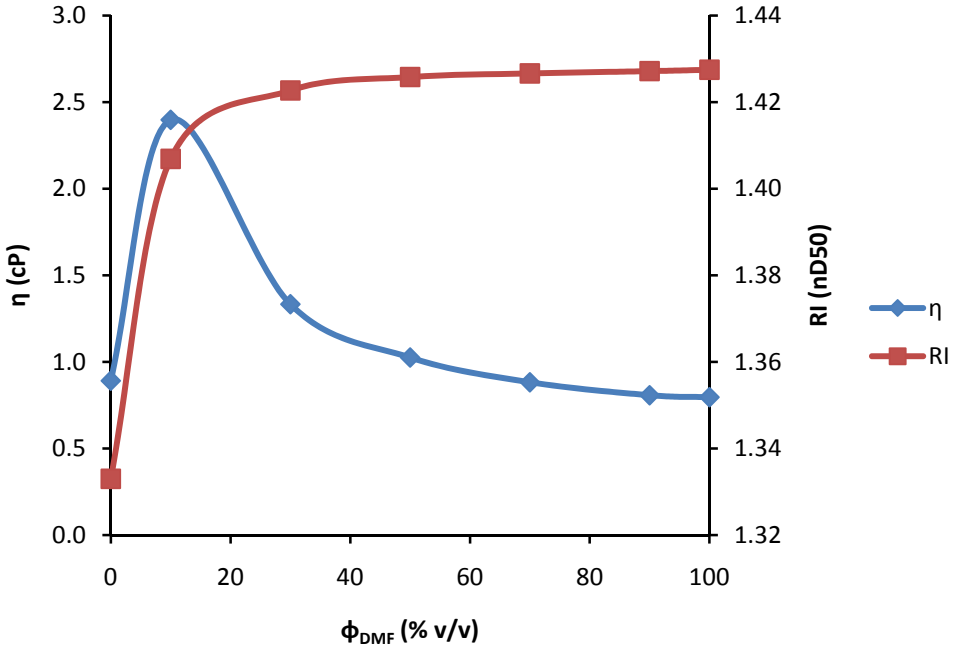

Figure 16: Viscosity and Refractive Index of binary DMF-H_2O mixtures.

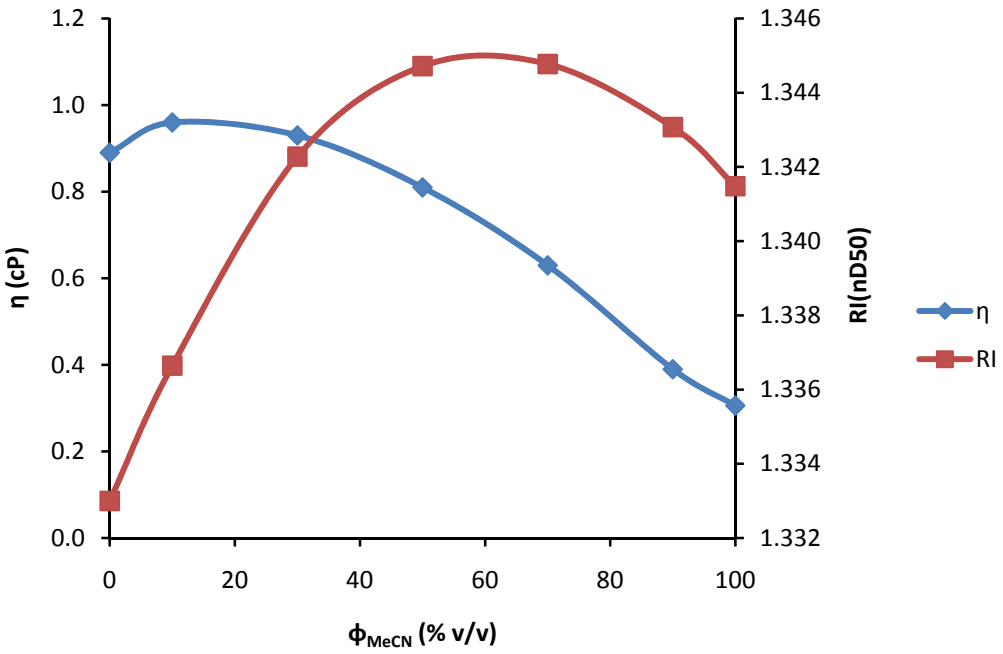

Figure 17: Viscosity and Refractive Index of binary MeCN-H_2O mixtures.

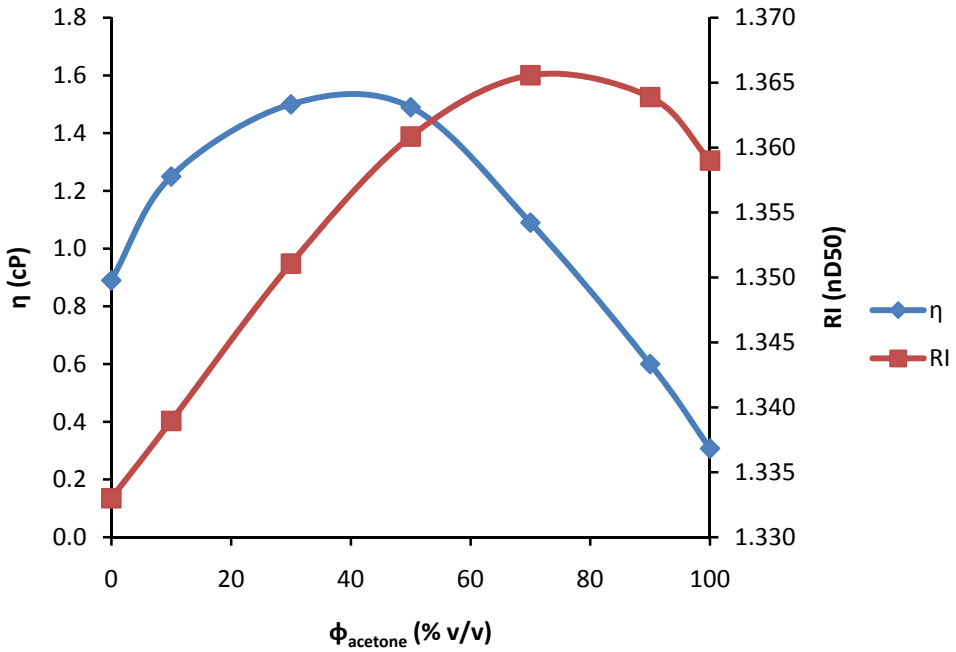

Figure 18: Viscosity and Refractive Index of binary acetone-H_2O mixtures.

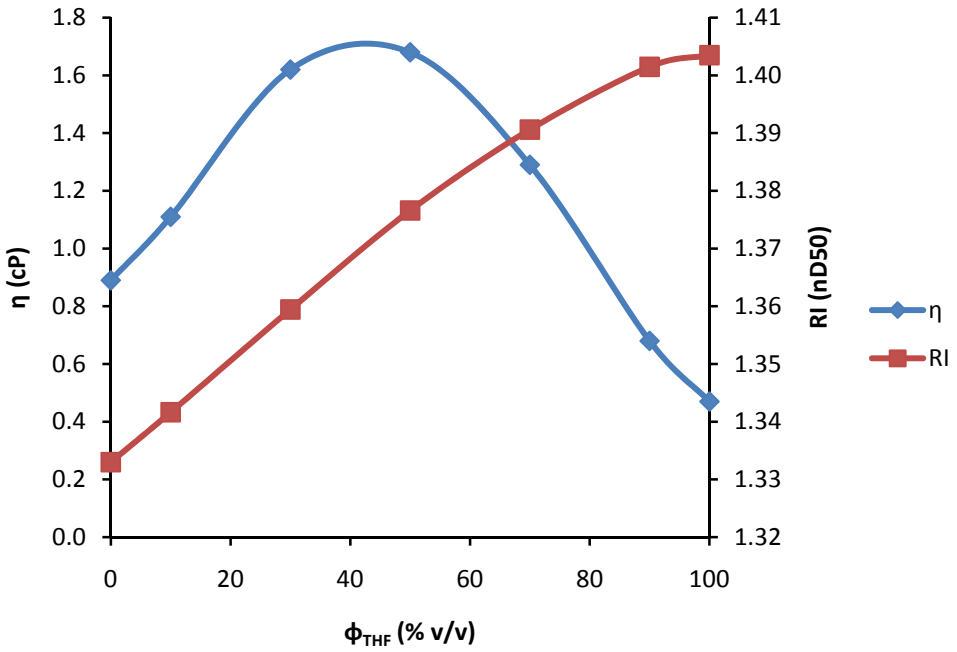

Figure 19: Viscosity and Refractive Index of binary THF-H_2O mixtures.

4.1.1.1 Attempts at Viscometry

Cursory attempts were made to determine the actual viscosities of the dispersion media of a variety of preparations, but were met with little success. It was hoped that accurate measurements of these viscosities could be used to improve the accuracy of results obtained from PCS, as the dispersion medium viscosity is a required measurements parameter, as mentioned previously.

An Anton Paar PV-1 P digital viscometer was used with a special low-viscosity spindle coupled to a thermostatted waterbath. Unfortunately the dynamic range of the instrument was too high to accurately measure the low viscosities encountered in this piece of research. Initially the accuracy of the instrument was investigated by running neat solvents, however the results were neither stable nor accurate nor precise enough. All future work was consequently abandoned.

4.1.2 Algorithm Choice

One of the first problems to be mindful of when using the Zetasizer was which algorithm to choose. The Malvern PCS software contains 5 algorithms for interpretation of scattering data and generation of PSDs: AUTO, CONTIN, NNLS, Multimodal and Monomodal/Cumulant. While it is purported that each of these has advantages for different sample types, there is little information available in the literature surrounding which algorithm is most appropriate for which types of samples, or what their differences are. Sample analysis under identical parameters but with changes only in the algorithm was shown to yield vastly different results. Table 4 shows the variability in the results produced by each algorithm, and PSDs are shown in Figure 20. The sample was a PVP-protected palladium sol reduced by borohydride in 10% v/v MeOH. Analysis by TEM showed the particle size to be 2.5 ± 0.6 nm, monomodal and monodisperse, and almost 3 times smaller than the lowest PCS estimate and 150 times smaller than the highest. Unfortunately the lowest estimate can only detect single peaks, so while it may be closest to the 'real' particle size, using it would present a real danger of missing legitimate peaks.

Algorithm	x_{PCS}	σ_{PCS}	Countrate
AUTO	8.8	4.4	16.3
NNLS	53.2	27.5	16.4
CONTIN	28.1	29.5	16.9
Multimodal	68.1	155.3	17.0
	393.1	209.4	
Cumulant	7.2	5.8	16.7

Table 4: Differences in PCS results for a single colloid using various data interpretation algorithms.

While all estimates are much higher than the 'true' value, the measured hydrodynamic size should be slightly larger than that obtained by TEM due to the presence of the EDL or adsorbed polymer layers. This is a valid explanation for small disparities between the two measurements, but not for those exhibited by, for example, the multimodal algorithm.

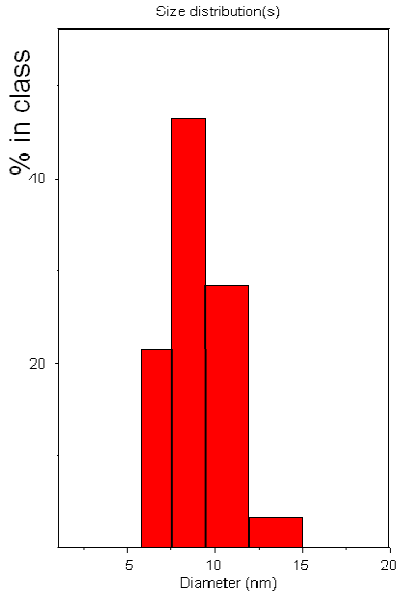

a)

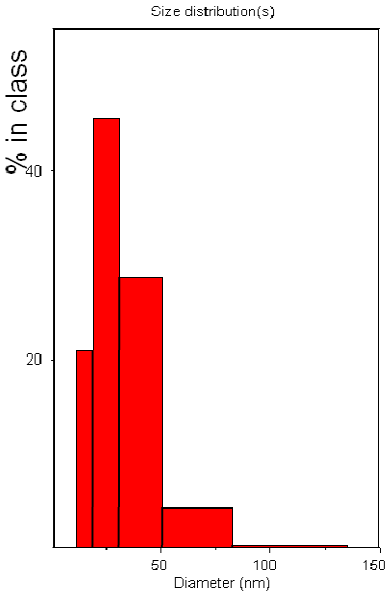

b)

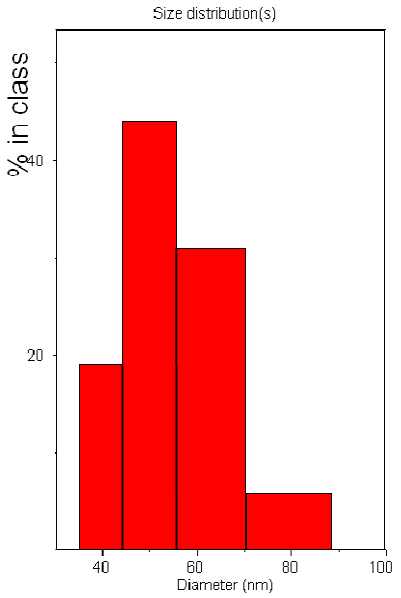

c)

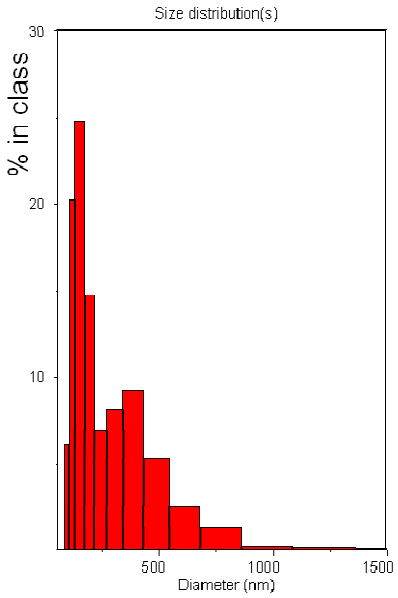

d)

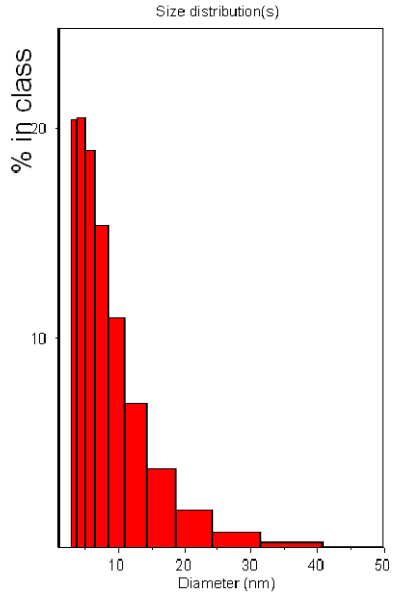

e)

Figure 20: PCS particle size distributions for a palladium colloid obtained under identical instrument parameters, varying only the data interpretation algorithm. Algorithms are a) AUTO, b) CONTIN, c) NNLS, d) Multimodal and e) Cumulant.

4.1.3 Influence of Protecting Agents on Resolution

If there is free (*i.e.* not particle-bound) polymer in the dispersion medium, the polymer macromolecules can scatter light which will be detected by the Zetasizer in addition to the light scattered by the particles. PCS scans revealed that the protecting agents used in this study proved to be particularly efficient light scatterers with widely varying hydrodynamic sizes. The results are shown in Table 5.

Protecting Agent	$\bar{x}$ (nm)	σ (nm)
PVP	7.4	4.2
PVA	618.3	320.4
PAA	42.0	10.7
ARG	812.1	446.4
Water	0	0

Table 5: Summary of the data obtained by PCS for diluted stock-solutions of the protecting agents used in this study.

If the hydrodynamic size of these polymer macromolecules (represented by the '*radius of gyration*') is significantly different to the size of the actual particles in the dispersion, then the resulting PSD will be bimodal, containing two peaks. Only one of these peaks will be the 'particle size', the other being 'fake' data from the free polymer. The result is that the Z_{ave} (the overall 'average particle size') becomes disproportionately high, and the quality control criteria (such as the polydispersity limit) can be unduly breached. Novice users must therefore be careful in their interpretation of such summary statistics.

A second problem which resulted from this scenario was that the resolution of the instrument was lowered by the presence of such undesired non-analyte species. The model of Zetasizer used has 64 channels over which it scans, which essentially means that the resulting PSD can be a maximum of 64 size classes in width. These channels are spread over whatever range is necessary to cover all observable light-scattering species in a given sample. For relatively monodisperse colloids such as those produced in this study, this is more than adequate resolution. However when the dispersion contains free polymer molecules which are much different in size, the 64 available channels must be spanned far enough across the size range to cover both the polymer and the particles. This widens the size classes, which means that the data collected for the actual analyte species (the particles) is less accurate. A diagram illustrating this point is shown in Figure 21; clearly the distribution for the 'no free polymer' case is more accurate.

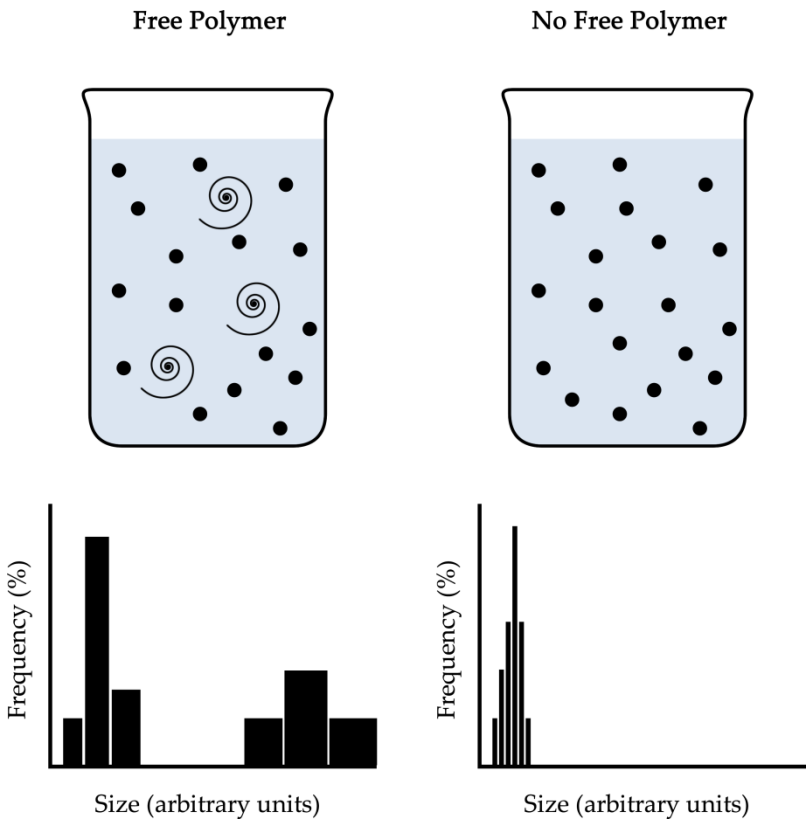

Figure 21: Schematic illustrating the effect on the PSD obtained by PCS when large 'free' macromolecules are present in solution. Black circles represent colloidal particles; spirals represent free polymer molecules.

To avoid the problem of having the light-scattering polymers detected in the first place, one may change the detection range. This could exclude any polymers or other light-scattering species, so long as their sizes fall outside the range of the analyte scatter(ers). This cannot be performed with the auto algorithm however, necessitating that it be changed to one of the others such as CONTIN or NNLS. As described before however, this can also lead to changes in the actual data, making the experiment of little use. Alternatively, higher peaks may simply be ignored and size data for the actual analyte species extracted from the data summary tables which the software provides. This is dangerous though, as without secondary data such as TEM one cannot assume these are not real particles, possibly negating the 'quick and easy' attraction that PCS has which attracts people to it in the first place.

4.1.4 Effects of Solution Agitation

In theory a sample should be well-mixed before being analysed by PCS to ensure that the small volume analysed is an accurate representation of the bulk solution. With the colloids such as those produced for this piece of research this presented a number of problems.

The first was that shaking the solution re-suspended large particles which had fallen to the bottom of the vessel. The scattering from these larger particles could swamp the scattering from smaller particles, decreasing the resolution of scan. If the sample was filtered, aggregates which were not big enough to sediment but were not small enough to pass through filter paper were be removed from the dispersion, so the scan results were not an accurate indication of the particle size distribution of the dispersion.

The second was that without shaking, significant de-mixing of the dispersion medium could occur with certain solvent mixtures. Water and DMSO for example are both mutually miscible, but when a mixture of the two is left to stand it will not remain completely homogeneous for extended lengths of time due to the formation of strong H-bonded solvent complexes, and will require re-mixing to homogenise. This was a concern as it could cause the polymer and particle fractions of the solution to partition differentially between two regions of solvent. This meant that the analysed portion of the sample may not necessarily be representative of the sample's bulk composition.

To balance these two factors, sample vials were swirled while being held against the surface of the desk, which agitated the dispersion medium to the extent that it was re-mixed, but also left large aggregated particles at

the bottom of the vessel. The colloidally stable supernatant was then analysed.

4.1.5 Ways to Describe a Particle Size Distribution

There are numerous ways to describe the distribution of the sizes of a set of particles, and the Zetasizer provides three: intensity, volume and number-weighted distributions. Number-weighted distributions are the easiest to understand and the most useful, however many assumptions are made in their derivation. They are calculated from the volume-weighted distribution, which is in turn calculated from the intensity-weighted distribution, which is essentially the raw data from the instrument. At each of these steps a number of assumptions are used, which means that the number-weighted distributions are frequently much less accurate than the other two. While this does not necessarily mean that the number-weighted distributions are wrong, it does mean that one must be wary of them, and that the instrument is not infallible.

4.2 Estimation of the Accuracy of TEM Measurements

Traditionally, measurements of the sizes of colloidal particles have been made from TEM micrographs on photographic paper. Many modern instruments however are equipped with digital cameras to record micrographs in a much faster and easier fashion. The downside to this is that a digital micrograph is of much lower resolution than an actual photograph. The AMT camera equipped to the CM30 TEM used for this research, for example, was limited to capture sizes of 1280x1024 pixels (1.3 megapixels in camera terms). Photographic film on the other hand is generally agreed to be a much higher resolution, as it is an ‘analog’ medium, and is not limited by the number of pixels or the size of the CCD. This means that to obtain as accurate a particle measurement with a digital

micrograph as one could obtain by measuring micrographs on photographic paper, the zoom must be increased to a much higher level. This is not convenient though, as increasing the zoom level also simultaneously decreases the number of measureable particles in a given micrograph.

Because digital micrographs are composed of a regular array of pixels, for a given digital micrograph each pixel will represent a certain distance across the sample, which will change depending on the magnification at which the micrograph is captured. For example, on the microscope used for this study at 53,000x zoom, each pixel represented 0.408 nm. Because the smallest distance one can measure is between two adjacent pixels, this distance corresponded to the minimum measurable particle size at that specific magnification range. The sizes of two measured particles are therefore not considered to be significantly different from one another unless the difference between them is greater than this value. A plot showing the change in 'pixel size' versus magnification is shown in Figure 22.

The size was found to obey exactly an exponential relation to the magnification, with one pixel equalling one nanometre at 21,954x zoom. Note that the magnification is the direct magnification, not the magnification at the camera, which is 11.4 times higher.

The error in the measurement of a particle can be calculated by dividing the pixel size, which represents the minimum measureable distance, by the size of the particle measured. For relatively large particles this error is not significant, as it represents a very small percentage of the overall size of the particle. For example a when a 500 nm particle is measured at 10,000x zoom, the size of a pixel corresponds to 2.19 nm, which is a 0.4%

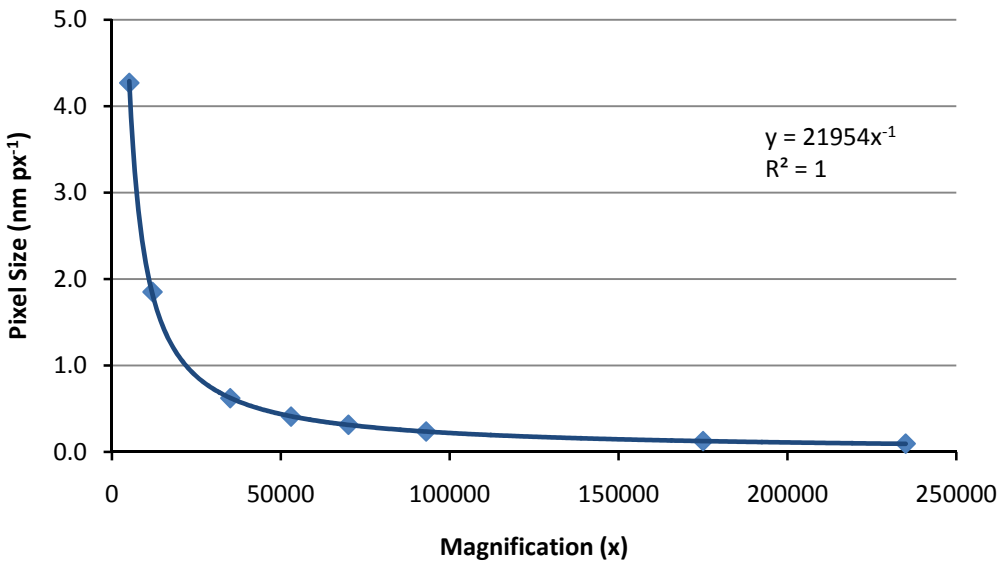

Figure 22: Pixel size for measurements taken from digital micrographs at various magnifications.

error. However, when the particle size decreases to below 10 nm such as the particles generated in this study, the error becomes significantly higher. For example when a 5 nm particle is measured at 10,000x zoom, the error is a massive 44%, which is unacceptably high. In order to reduce this, the magnification at which the particles are measured must be increased significantly. To bring the error down to below 5%, the magnification must be increased to over 87,000x. A plot showing the error in the measurement of variously sized particles versus magnification is shown in Figure 23.

At magnifications this high however the instrument must be well-aligned and calibrated to avoid degradation of the quality of the micrographs collected, which can lead to uncertainty in the measurement process. This was a significant issue for the specific TEM used for this study, as it suffered from a number of problems which were out of control of its operators such as HT instability, dirty apertures causing spherical aberration, incorrectable astigmatism, and a misaligned electron gun. The

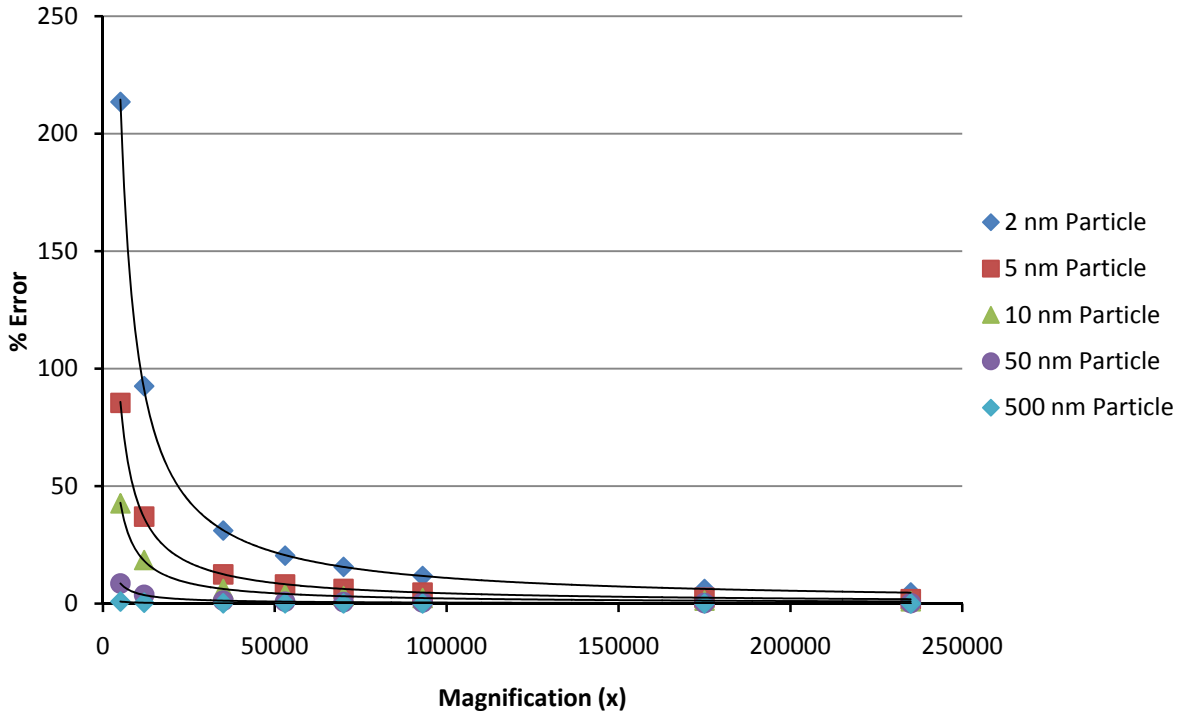

Figure 23: Percentage error in particle size measurements from digital micrographs of variously sized particles.

result of these problems was that many images collected were not of optimal quality, which sometimes led to blurring in the micrographs at the peripheries of the particles. Because of these problems, increasing the magnification to lower the error due to the pixel size only worked to a certain extent, after which the levels of blurring of the particles began to outweigh it, which varied depending on the condition of the TEM column at the time, and on the nature of the sample. This effect was investigated by measuring a number of particles at a 'low' magnification (*ca*. 32,000x) and re-measuring them at a higher magnification (*ca*. 125,000x). Differences of <0.1 nm were observed, less than the 5% measurement accuracy of TEM instruments, thus it was not considered to be a major issue.

The effect of the pixel error can be seen when measuring particles whose sizes appear to fall into 'groups'. This effect is overcome by measuring a

large enough number of particles. The usual 100 measurements per sample used for this project appeared to be enough to overcome this issue. Typically images were captured at a variety of magnifications, extending up to 225,000x for some samples, although approximately 70,000x was the average magnification used. At this magnification the difference between two measurements must be approximately 0.35 nm to be statistically significant, which was routinely realised.

The important point arising from these issues is that the error in particle size measurements was a dynamic quantity, and varied based on a variety of factors, which must be interpreted and considered constantly during analysis.

4.3 Estimation of the Relative Contributions to UV/Vis Measurements from Variation in the Particle Size and Dispersion Medium Dielectric Constant

As explained in Section 1.3.4, the intensity with which a particle scatters light depends on a variety of factors. The two which are most important with respect to the sols generated in this study are the particle size and the dielectric constant of the medium in which they are dispersed. Determining the influence these factors had on the UV/Vis spectra recorded was therefore of interest.

When one ignores multiple scattering, which is a reasonable assumption for dilute colloidal suspensions, the absorbance of the system is equal to the sum of the light scattered at 180° of each of the particles in the measurement volume. If the particles comprising the suspension are all relatively monodisperse, or the exact distribution of sizes can be specified, then one can model the absorbance spectrum of a colloidal suspension by analysing the scattering from only a single particle. Of course this is a

fairly coarse model, but it is useful none the less for predicting the effect of changes in the particle size and dielectric of the dispersion medium. Many pieces of software are available for this task, including MiePlot by Philip Laven [124].

The MiePlot program performs calculations for the scattering of light by spheres using Mie Theory and the Debye Series, based on established calculation methods. It has been used and referenced in a variety of published works [125-127] including many papers on colloids and/or nanoparticles [128-130]. In this study it was used to simulate the scattering intensity versus wavelength spectra of rhodium and palladium particles, which as mentioned previously may be considered complimentary to UV/Vis spectra. Calculations were performed between the wavelengths 200 nm - 900 nm at 1 nm resolution using unpolarised light and a 180° scattering angle, with the refractive index of each metal taken from the CRC Handbook [131]. Complex values of the refractive index were ignored. Because the plots of the refractive index of the metals versus λ were so complicated, a file containing the full tabulation of values was used rather than a 4-λ approximation. The plots showing the real values of the refractive index for both metals is given in Figure 24.

Using these values a series of theoretical spectra were calculated for particles of different sizes. Given in Figure 25 is a plot of the scattering intensity for a series of monodisperse rhodium particles over the approximate size range encountered in this study, from large (10 nm) down to extremely small (0.1 nm, the approximate size of an individual atom). Evidently, the absorbance at a given wavelength decreases dramatically as the size decreases, consistent with the r^6 scattering dependency. Figure 26 shows the variation in the I_{450} (the scattering

intensity at 450 nm) values with d, the particle diameter, as well as the

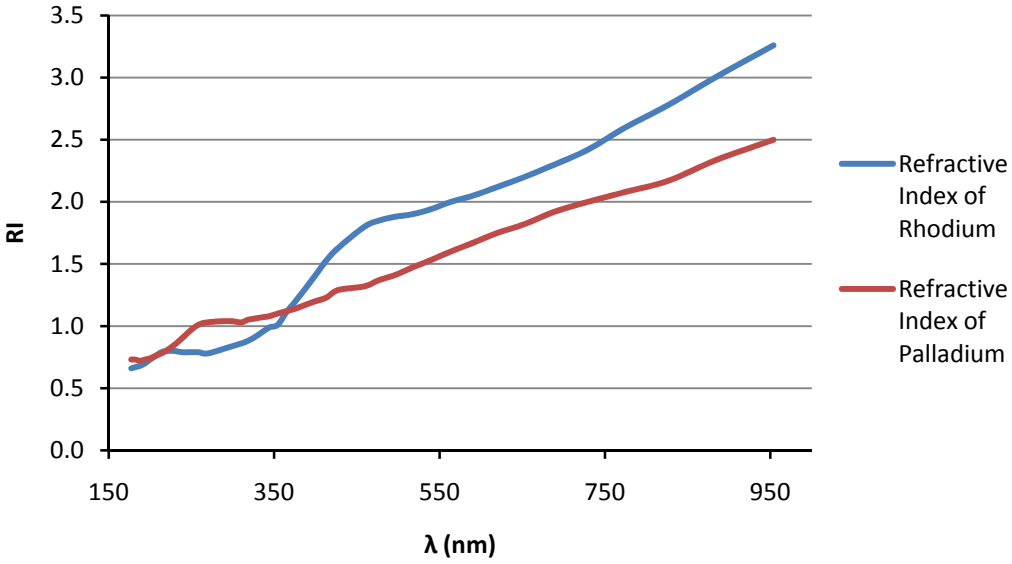

Figure 24: Real refractive index of rhodium and palladium metal.

percentage difference between adjacent values. We can see from this that the intensity decreases dramatically with particle size, with a 9 nm particle scattering light with only 54% of the intensity of a 10 nm particle, an 8 nm particle scattering light with only 50% of the intensity of a 9 nm particle and so-on. From this we can reasonably expect that the measured absorbance (A_{450}) values will decrease as the average particle size decreases, other factors aside. It must also be noted however that because a fixed amount of metal precursor is introduced into the system at the start, only a certain mass of particles can be produced. When the particles are larger less are formed; when they are smaller more are formed. Because the number increases as the size decreases, there are more particles available to scatter light, thus the absorbance will increase. Conversely when the particles are larger there are less of them to scatter light, and the absorbance will decrease. This 'number dependence' will

have the effect of 'flattening' the influence of the particle size, causing it to become less significant.

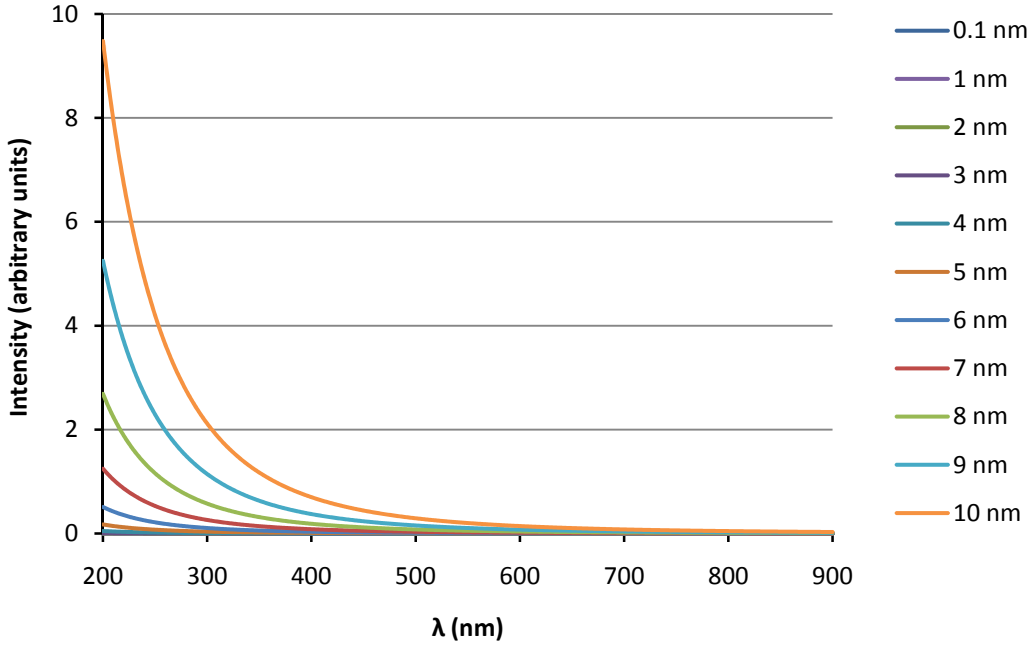

Figure 25: Simulated scattering spectra of variously sized rhodium particles, with sizes ranging from 0.1 nm – 10 nm.

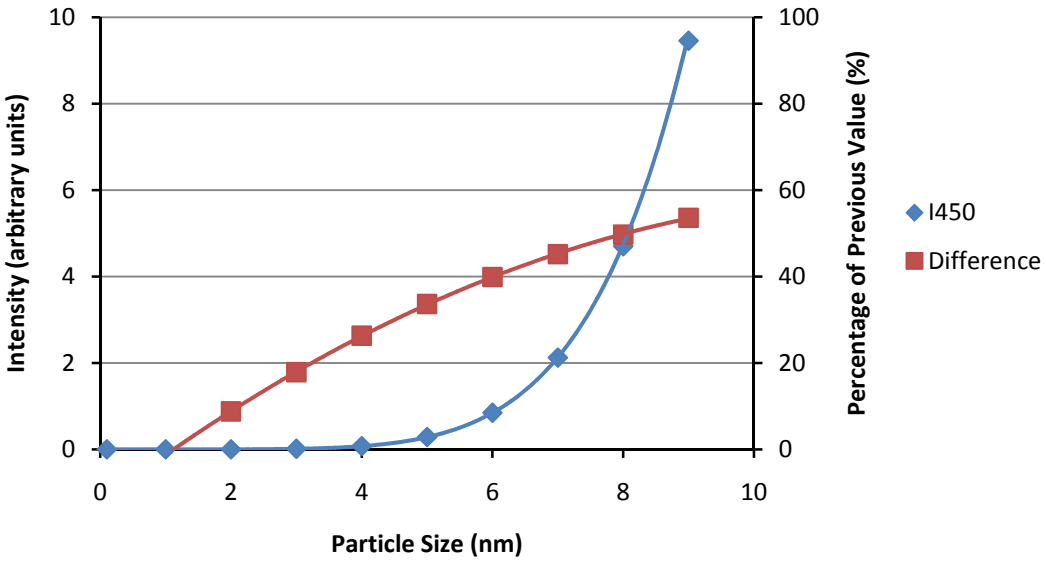

Figure 26: Plot of the I_{450} values from simulated spectra of variously sized rhodium particles, along with a plot showing the percentage size of each value compared to the previous.

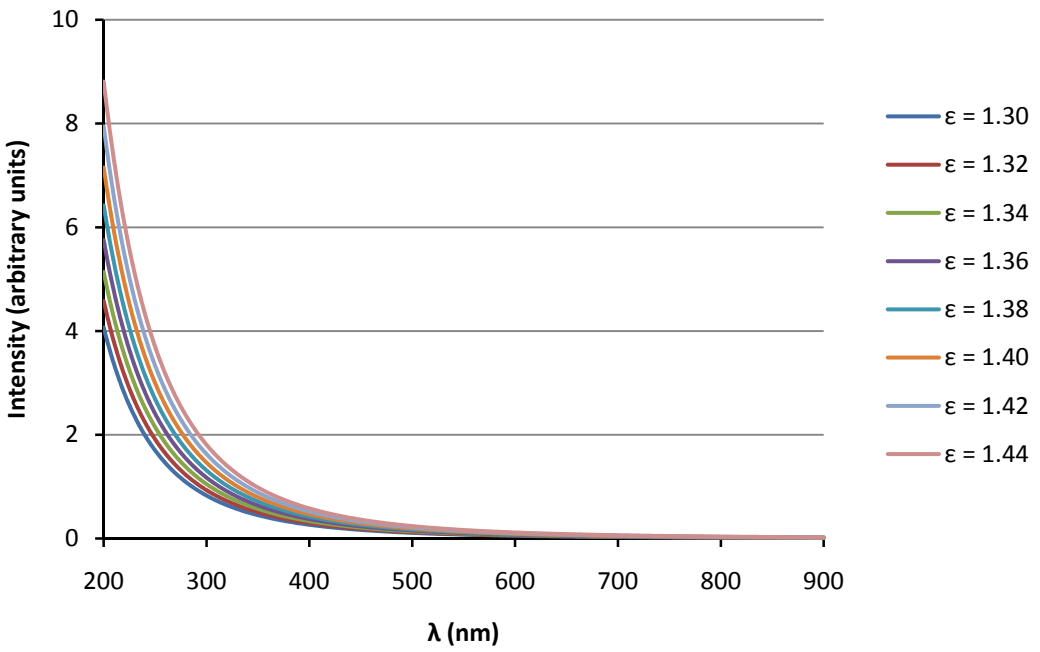

Figure 27: Simulated scattering spectra of monodisperse 5 nm rhodium particles where the dielectric constant of the dispersion medium is varied over a range of values.

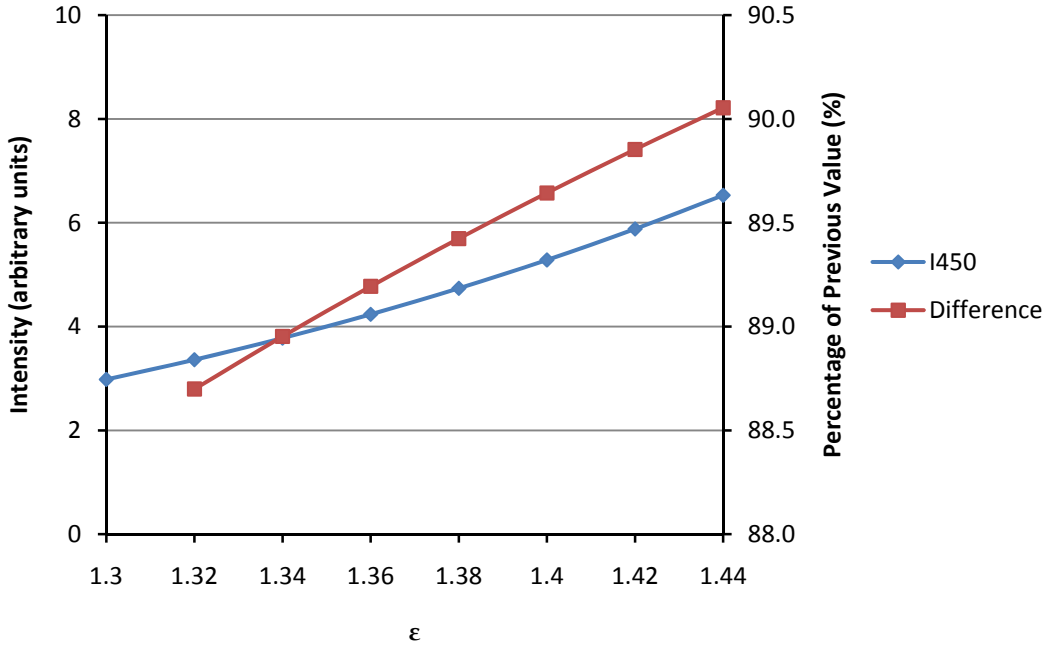

Figure 28: Plot of the I_{450} values from simulated scattering spectra of monodisperse 5 nm rhodium particles where the dielectric is varied over a range of values, along with a plot showing the percentage size of each value compared to the previous.

Compared to the dependence on particle size, the dependence of the scattering intensity on the dielectric constant of the dispersion medium is much less. Increasing ε increases the scattering intensity at a given wavelength, but only in the order of 0.02% per 0.02 at 450 nm. This is illustrated in Figure 27 and Figure 28. Therefore although it will make some contribution to the measured absorbance values, it is not likely to be of significance.

From the analysis of the data gleaned from these simulations we can see that the UV spectrum of a colloid is likely to be highly dependent on the size of the particles in the size range under consideration. It is of note therefore that for a set of sols with decreasing particle size, the A_{450} values should decrease correspondingly. Trends such as this are likely to only be valid for samples containing little or no aggregation however, as changes to the size and morphology of the particles would likely affect the way they scatter light. This effect was corroborated by the measurements taken— as ϕ was increased, the size of the primary particles and the A_{450} measurements (generally) decreased, in cases where little aggregation was present.

4.4 Verification of Instrument Calibration

4.4.1 PCS

In order to assess the accuracy of measurements collected by the Zetasizer, three particle sizing standards were analysed. The first was a suspension of polystyrene particles manufactured by the Duke Scientific Corporation, used for calibration of any particle sizing apparatus. The standard was traceable to the National Institute of Standards and Technology (NIST), but had expired at the time of use so was not technically valid. It was supplied as a 2% w/v dispersion of 200 nm

spheres dispersed in a dilute salt solution. It was prepared for analysis by diluting 40 μL of the sample to 4 mL using a 10 mM NaCl solution. The diluted sample was run 10 times on automatic mode with the algorithm set to monomodal. The results of these scans are given in Section 4.4.1.1.

Two standards from SpheroTech were also analysed. Both were supplied as 5% w/v solutions of polystyrene spheres, with nominal sizes of 70 nm and 2070 nm. There are referred to from here onward as the 'small' and 'large' standards respectively. While not officially NIST certified, their exact measurements were determined using instruments calibrated with NIST certified standards, so were good for comparative purposes.

The results generally showed that while the data measured by PCS was not identical to the specified values for each of the standards, the results obtained could be rationalised and the differences traced to a variety of effects. The accuracy was judged to be sufficient, thus the method is valid. A short discussion of each standard measured along with some results is given in the following sections.

4.4.1.1 Duke Standard

Given in Table 6 is the size data collected by PCS for the Duke Scientific particle sizing standard. The PSD is given in Figure 30. The measured size was in excess of the specified size by approximately 50%, at 302 nm compared to 200 nm. There are a variety of possible reasons for this. The first option is that since the standard was relatively old, its constituent particles had aggregated into small flocs, giving an average hydrodynamic radius in excess of the 'true' value.

The second and equally valid option is that because the particles were dispersed in a salt solution, the association of an EDL with the particle

	Specified (nm)	Measured (nm)	% Difference
x_{PCS}	200.0	302.0	+51%
σ_{PCS}	3.2	47.0	+1,370%

Table 6: Specified and measured particle size data of the 220 nm "Duke" latex sphere standard.

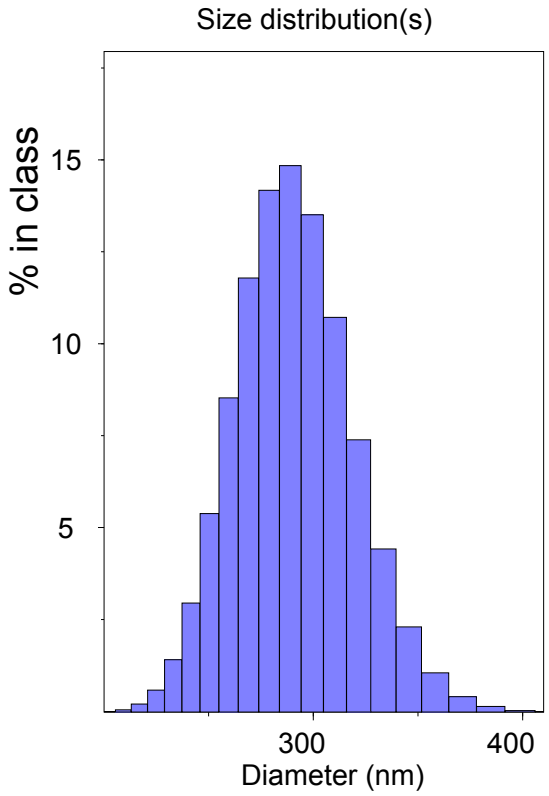

Figure 29: PCS particle size distribution of the 220 nm "Duke" latex sphere standard.

surface caused a decrease in their hydrodynamic mobility, which caused the apparent increase in their size. While using a 'concentrated' salt solution was meant to minimise this, it is a factor which could not be avoided. These possibilities easily account for the 51% difference in the average particle size observed, however they do not initially appear to account for the massive 1,370% difference in the standard deviation. It should be remembered that the specified values are obtained for the 'fresh' standard, where particles exist only as primary particles, hence the standard deviation supplied is only valid for differences between

individual primary particles. As soon as any significant level of aggregation occurs this value is dramatically increased due to the association between the particles. For example, if one takes three relatively monodisperse particles and joins two of them together, the average particle size would be increased by approximately 50%, but the standard deviation would increase to a far greater extent.

In order to determine if the differences in the size data were caused by the preparation of the standard, two factors were investigated. Firstly the concentration of the salt diluent was varied, and samples were measured using 0.1 mM, 1 mM and 10 mM NaCl. Over this composition range the results were found to vary to a negligible amount. A second variable investigated was the method with which the sample was dispersed. Samples were shaken by hand, shaken using a vortex mixer and placed into an ultrasonic bath for varying lengths of time. None of these procedures were found to induce any significant change in the PSD.

4.4.1.2 SpheroTech 'Large' Standard

The measurements collected for the "large" SpheroTech standard were much closer to the specified values than the Duke standard, giving only a 6% difference in the average particle size, although still giving a 900% difference in the standard deviation. The reasons for this were most likely to be the same as those described in the previous section, although lessened in severity as they were new samples with (probably) less aggregation. The size data is given in Table 7, and the PSD in Figure 30.

	Specified (nm)	Measured (nm)	% Difference
x_{PCS}	2070	2197	+6%
σ_{PCS}	50	450	+900%

Table 7: Specified and measured size data of the 2070 nm SpheroTech "large" latex sphere standard.

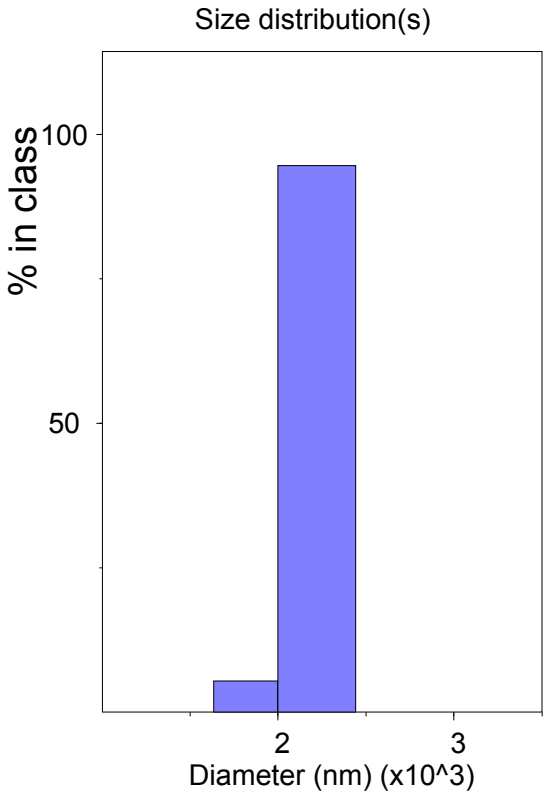

Figure 30: PCS particle size distribution of the 2070 nm "SpheroTech" latex sphere standard.

4.4.1.3 SpheroTech 'Small' Standard

The characteristics displayed by the SpheroTech 'small' standard were intermediate between the 'large' Spherotech standard and the Duke standard. The particle size as measured in this study was in excess of the supplied value by 30%, 90.8 nm compared to the specified 70 nm. While no standard deviation was supplied with the standard, an enquiry to the company at a later date yielded the actual PSD data obtained using their

procedures, which listed a standard deviation of 5.3 nm. This data is given in Appendix 2. Using this standard deviation the difference was +380%.

	Specified (nm)	Measured (nm)	% Difference
x_{PCS}	70	90.8	+30%
σ_{PCS}	5.3	20	+380%

Table 8: Specified and measured size data of the 70 nm SpheroTech "large" latex sphere standard.

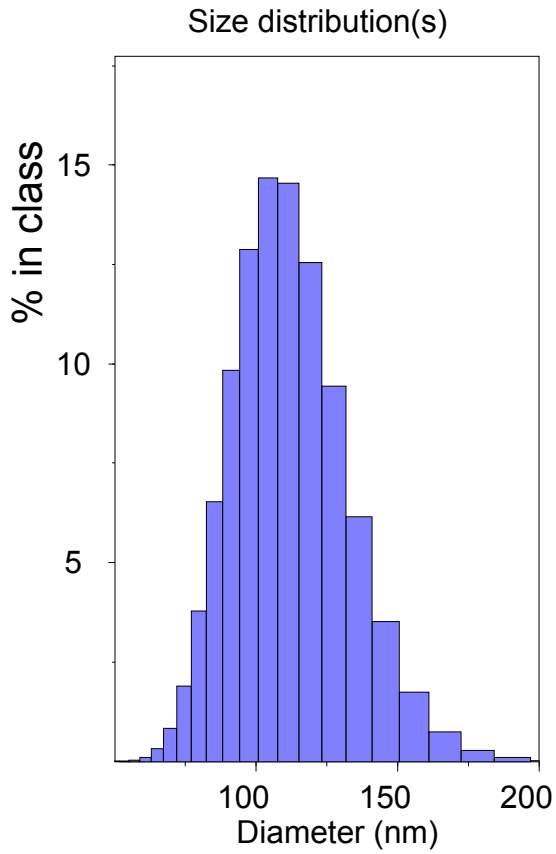

Figure 31: PCS particle size distribution of the 70 nm "SpheroTech" latex sphere standard.

4.4.2 TEM

In order to determine whether or not measurements collected from the TEM were accurate, the three latex particle size standards from the previous section were prepared and measured. Samples were prepared by addition of 1 drop of the standard (*ca.* 50 μL) into 5 mL of distilled water.

The solution was thoroughly stirred, and a drop was deposited onto a TEM grid and left to dry in a desiccator. The diameters of 100 particles of each standard were counted, with each particle measured twice at 90° separations.

The first standard used was the Duke Scientific NIST-certified standard used in the PCS method validation. Despite being expired, it was deemed unlikely the sizes of the primary particles had been significantly affected by prolonged storage. This was confirmed by the measurements, which compared favourably with those specified on the bottle. The other standards used were two SpheroTech standards used for the PCS validation, prepared and analysed in an identical fashion to the Duke standard. A summary of the data collected is given in Table 9.

	Duke	SpheroTech Large	SpheroTech Small
$\bar{x}$ (specified)	199 nm	2070 nm	70 nm
$\bar{x}$ (measured)	200 nm	2058 nm	72 nm
Difference	+1 nm	-12 nm	+2 nm
Difference (%)	0.5%	0.5%	2.8%
σ (specified)	3.4 nm	50 nm	Not supplied
σ (measured)	5.8 nm	26 nm	Not supplied
Difference	+2.4 nm	-24 nm	Not supplied
Difference (%)	41%	48%	-

Table 9: Measurements of three latex sphere standards by TEM and their corresponding differences to the specified values.

In the following sections micrographs of each standard are given, along with their PSDs and a short discussion of the results. Note that in the PSDs, "measured" refers to the distribution as measured by TEM; "simulated" refers to a normal distribution using the average and

deviation as measured by TEM, and "specified" indicated a normal distribution using the average and deviation as specified by the manufacturer.

Although there were minor differences in the results, they were generally in good agreement with those values supplied by the manufacturers, with any errors being explained relatively easily. From this we can conclude that particle measurements obtained from the TEM are sufficiently accurate representations of particle size. Further information about each standard is given in the following sections.

4.4.2.1 Duke Standard

The specifications provided by Duke Scientific for their latex standards are measured directly by electron microscopy, so the Duke standard was likely to be the most useful for validation of TEM measurements. The average diameter as measured in this study was only 1 nm higher than that provided by the manufacturer, corresponding to an error of only 0.5%, perfectly acceptable for the type of measurements needed for this research. The minor difference is easily attributed to the error associated with counting only 100 particles compared to the much larger numbers likely counted by the manufacturer. The standard deviation as measured exhibited a much higher difference, being nearly two-thirds higher than the provided σ. This is shown in the particle size distribution, with the "measured" and "simulated" PSDs being much wider than the "specified" PSD, as shown in Figure 32. The difference between the specified and measured standard deviation can be attributed to the difficulty in measuring between exact opposite sides of a two-dimensional sphere, resulting in some measurements being longer and some being shorter than the "correct" value. Despite these minor differences, the measurements

agree well with those provided. A micrograph of the standard is shown in Figure 33.

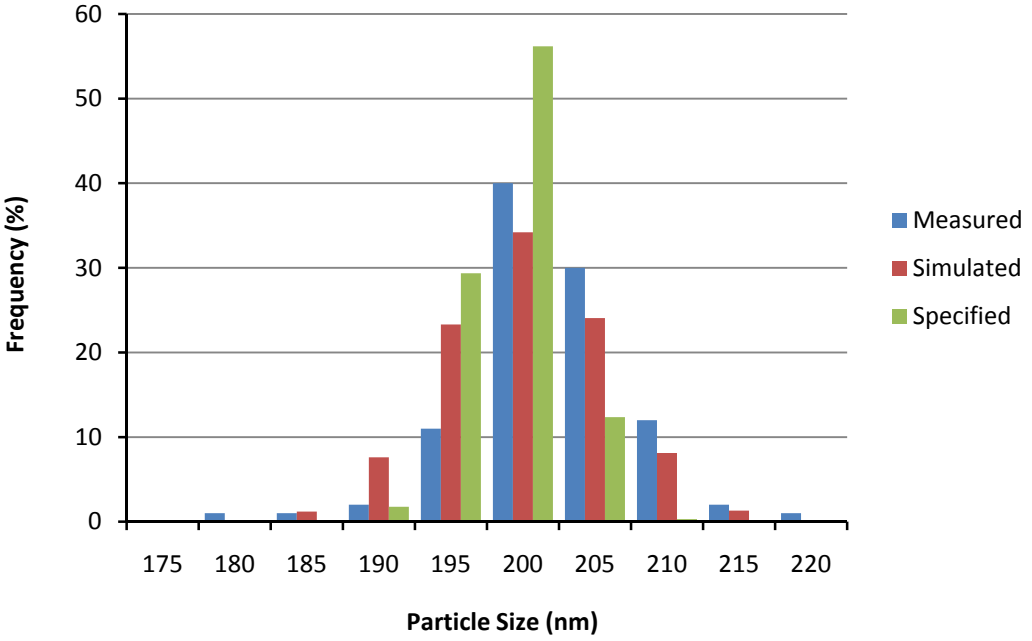

Figure 32: Particle size distributions of the "Duke" latex standard as measured by TEM (measured), simulated using the $\bar{x}$ and σ values obtained by TEM (simulated), and generated using the $\bar{x}$ and σ provided by the manufacturer (specified).

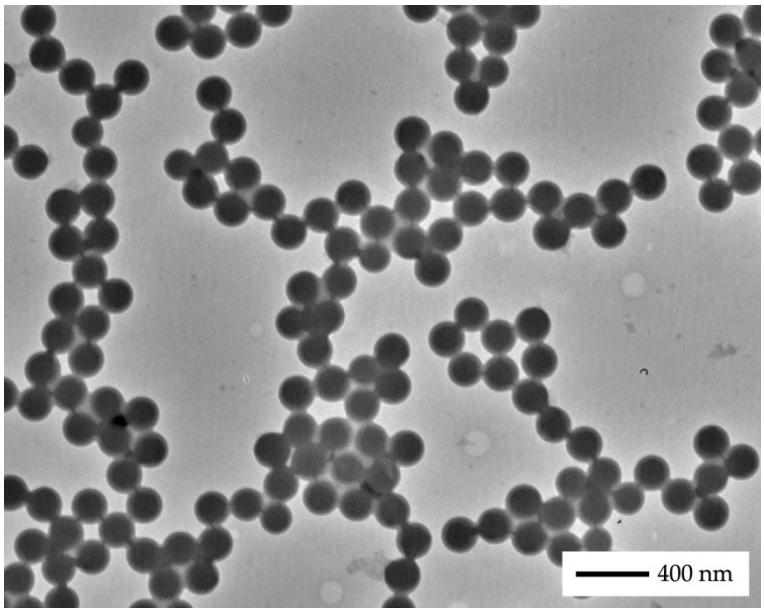

Figure 33: TEM micrograph of the "Duke" latex sphere standard.

4.4.2.2 SpheroTech 'Large' Standard

As the specified size for the standards by SpheroTech are measured by light-scattering techniques, the particle sizes as measured by electron microscopy were liable to be slightly smaller in absence of an electrical double layer. This certainly holds true for the "large" standard, with the measured size being 12 nm (0.5%) smaller than the supplied size, at 2058 nm and 2070 nm respectively. Looking at the actual distributions as shown in Figure 34, this may not make sense, as the "measured" distribution contains a maxima at 2070 nm. However, the long tail toward low diameters brought the average down significantly, as shown by the "simulated" distribution. These results indicate that the measurements are within acceptable error limits, with the measured and specified sizes agreeing well. A micrograph of the standard is shown in Figure 35.

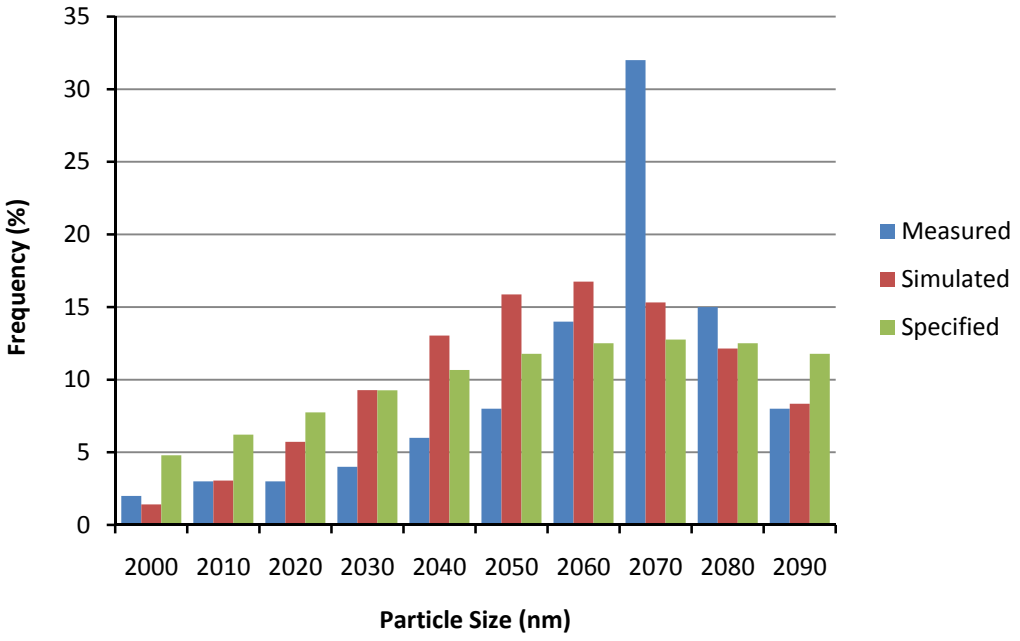

Figure 34: Particle size distributions of the "Spherotech" 2070 nm latex standard as measured by TEM (measured), simulated using the $\bar{x}$ and σ values obtained by TEM (simulated), and generated using the $\bar{x}$ and σ provided by the manufacturer (specified).

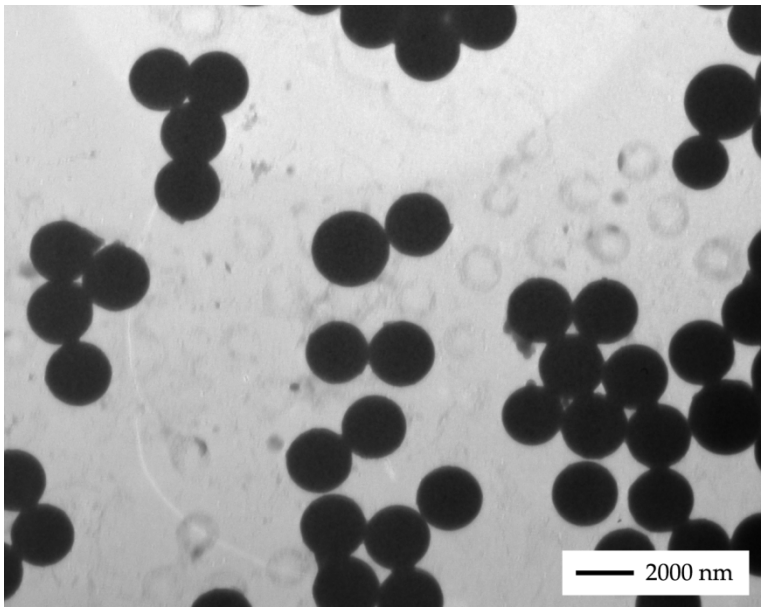

Figure 35: TEM micrograph of the "SpheroTech" 2070 nm latex standard.

4.4.2.3 SpheroTech 'Small' Standard

Theoretically the "small" standard should have suffered the same problems as the "large" one with respect to its measurements; however it appears this was not the case. Where the specified particle size was 70 nm, it was measured slightly larger at 72 nm, a difference of almost 3%. Despite having a slightly higher error than the previous standards it remained acceptably low, and was definitely considered to be an "acceptably accurate" measurement. The difference was likely to have arisen from measurement of the particles at a lower relative magnification, resulting in a higher overall error as described in Section 4.2. For some reason a standard deviation was not specified by the manufacturer; for this reason the "specified" distribution has been replaced by a single bar at the mean value in the PSD, shown in Figure 36. Note that it has been scaled to one-quarter size to retain the scale of the other distributions, although it represents 100% of the sample. A micrograph of the standard is shown in Figure 37.

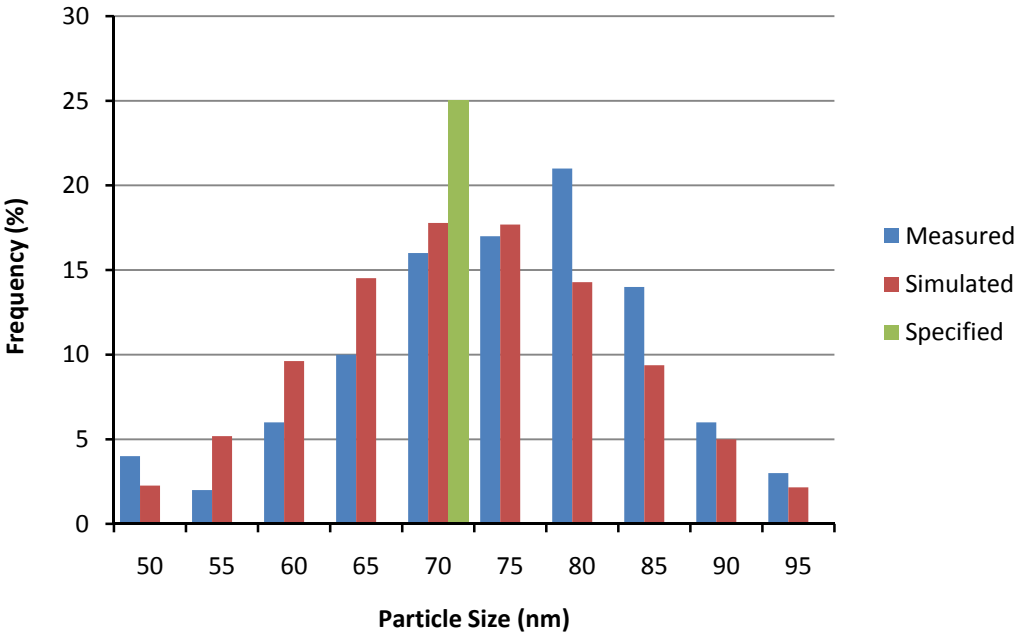

Figure 36: Particle size distributions of the "SpheroTech" 70 nm latex standard as measured by TEM (measured), simulated using the $\bar{x}$ and σ values obtained by TEM (simulated), and generated using the $\bar{x}$ and σ provided by the manufacturer (specified).

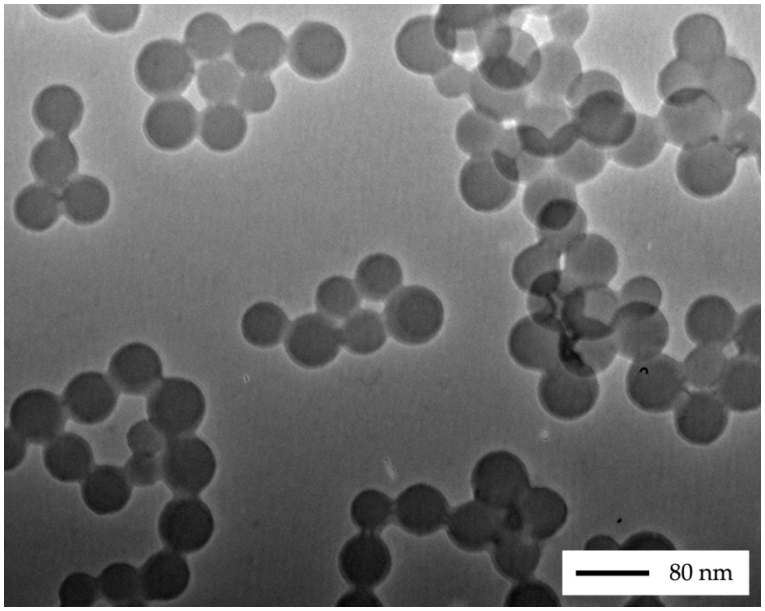

Figure 37: TEM micrograph of the "SpheroTech" 70 nm latex standard.

Chapter 5: Rhodium Mixed-Media Sols

When rhodium sols were generated in mixtures of water and an organic cosolvent, approximately half of the syntheses resulted successfully in the production of colloidal rhodium. Of the syntheses which were successful, the use of an organic cosolvent had a clear influence on the particle size and morphology of the resulting sols. For all characterised sols the average particle size as measured by TEM, $\bar{x}$, was shown to be inversely proportional to the cosolvent proportion, ϕ. There was generally relatively little change in the morphology of the primary particles, although there were often unpredictable changes in the levels of aggregation. Changes were also observed in the levels of necklacing, the process whereby primary particles become physically fused together.

Three prime phenomena were observed which thwarted otherwise successful syntheses. The first of these was the spontaneous formation of strong solvent complexes with the precursor material. This occurred when reduction was attempted in mixtures of water and a coordinating solvent such as DMSO and MeCN, where the presence of a vast excess of the solvent with respect to the concentration of metal precursor resulted presumably in the stabilisation of the +1 oxidation state, preventing the precursor from being reduced to its elemental form, which is a widely documented phenomenon [132].

The second factor contributing to the failure of some syntheses was the observed insolubility of the protecting agents in mixed-media solvents using cosolvents of low polarities such as THF. This problem was frequently encountered, and resulted in the protecting agent and adsorbed particles or precursor being precipitated from solution.

The third factor was the observed inability for hydrazine to spontaneously reduced rhodium, compared to palladium (see Chapter 6) for which the reduction was feasible at room-temperature.

In the following sections of this chapter, details are given fully describing the exact characteristics of the Rh sols generated, both in mixed-media and in pure water for comparison's sake.

5.1 Hydrosols

5.1.1 General Remarks

Five rhodium sols were produced in pure water as control experiments against which the sols generated in mixed-media were compared. A photograph of these sols is shown in Figure 38.

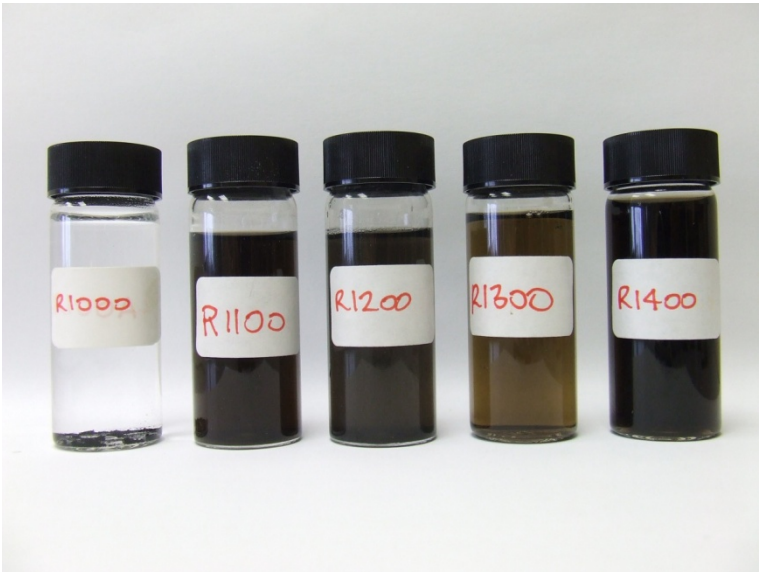

Figure 38: A photograph of five borohydride-reduced rhodium hydrosols with different protecting agents. From left to right: no protecting agent, PVP, PVA, PAA, ARG. The labels on the vials refer to their conditions of synthesis, as described in Appendix 1.

When sols were synthesised in the absence of a protecting agent, addition of aqueous borohydride to the dilute solution of $RhCl_3$ resulted instantly in a swirl of black particles, indicating the reduction from Rh^{III} to

Rh^0. The resulting sol was unstable and completely precipitated to the bottom of the reaction vessel within minutes of synthesis.

In contrast, when sols were synthesised in the presence of a protecting agent (PVP, PVA, PAA or ARG) an excellent level of stability was imparted, and the resulting sols showed no signs of precipitation after several months. All four protecting agents showed the same initial level of stability. During their synthesis it was observed that addition of the protecting agent to the dilute $RhCl_3$ solution caused the solution to darken slightly from rose-red, presumably due to coordination of the protecting agents to the metal precursor salt. This interaction has been shown previously to be an important step in generating stable and monodisperse sols [133]. Addition of the reducing agent then caused the solutions to darken slowly with time, indicating a slower and more controlled growth relative to the unprotected sols. A summary of the data collected for these sols is given in Table 10.

	TEM		PCS	UV/Vis
Protecting Agent	$\bar{x}$ (nm)	σ (nm)	x_{PCS} (nm)	A_{450}
PVP	5.0	1.3	19.4	2.87
PVA	2.7	0.7	61.6	1.86
PAA	2.5	0.6	40.0	1.55
ARG	3.2	1.1	7.3	4.41

Table 10: Summary of the mean and standard deviations in the particle size for control experiments.

When synthesised, rhodium sols protected with PVP and ARG were black, while those protected by PVA and PAA were dark and light brown respectively. This colour difference was later discovered to be indicative of their relative particle sizes, with lighter coloured sols possessing smaller particle sizes.

Reduction of $RhCl_3$ by hydrazine was found not to occur spontaneously, as addition of a solution of hydrazine to the rose-red solution of $RhCl_3$ caused no apparent change in colour. Even after addition of large volumes of undiluted hydrazine no changes were observed. Curiously, several works exist which suggest that hydrazine-reduction of $RhCl_3$ is possible, with one [134] suggesting that it is not spontaneous as it is with palladium, but requires the presence of alkali and heat, a fact which the author was unaware of whilst the work for this study was being conducted. Regardless, in the researcher's experience the particle size would generally be much harder to control had heat been applied to such a preparation, resulting in more polydisperse sols. As such, preparative methods such as this would fall outside the scope and aims of this project.

5.1.2 TEM Data

TEM was used to determine both the particle size distributions and the morphologies of the particles generated. Micrographs with magnifications of between 30 kx – 90 kx were routinely obtained, although depending on the nature of the sample this was sometimes higher or lower than these general limits. Magnifications as little as 3 kx were required to be used for imaging large aggregates, and as high as 255 kx for 'ideal' samples where the particles were small and non-aggregated. Despite the theoretical high-resolution capabilities of the Philips CM30 TEM used, magnifications higher than these often could not be obtained due to the sub-optimal operating condition of the TEM column at the time of use. Consequently no high-resolution micrographs were able to be collected during this study.

Despite these limitations, large numbers of micrographs were collected of sufficiently high resolution to obtain accurate PSDs and make definitive judgements on particle morphologies. Frequently particles were observed

to be embedded in deposits of a relatively thin homogeneous material, which provided little contrast in the collected micrographs. This electron-transparency indicated that the layer was comprised of lower atomic weight elements, so was assumed to be the dehydrated polymeric protecting agent. This added layer made locating particle-rich areas easy, although the extra distance through which the electron beam had to travel caused in some cases a notable decrease in resolution.

In no cases were any salt crystals caused by ionic impurities observed in the micrographs, which attested to the effectiveness of the ion-exchange resin used after preparation of the colloids. A plot showing the conductivity of a PVP-protected sol with time while exposed to ion-exchange resin is shown in Figure 39. All four sols showed similar behaviour, with initial conductivities in the region of 900 μS - 1200 μS, which fell to approximately 50% of the initial value within 15 minutes, before ceasing to decrease further after approximately 50 minutes. Because of the reliability of this trend, the conductivity of future sols was not measured while ion exchanging.

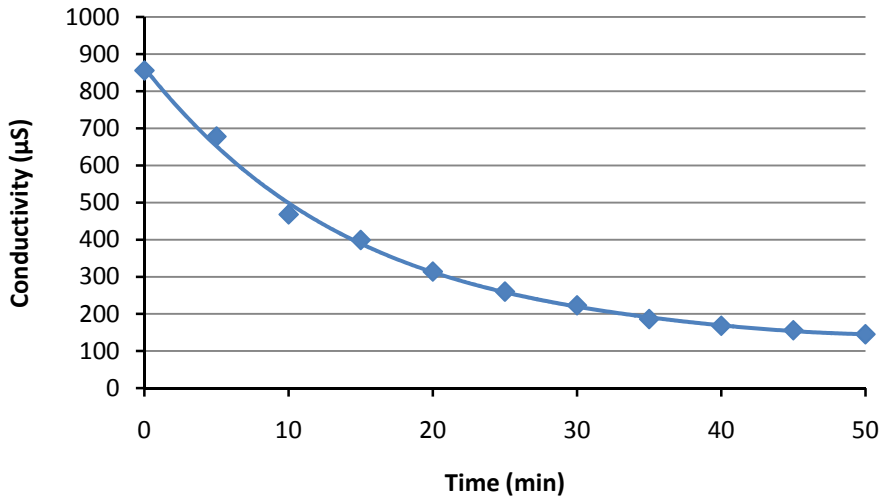

Figure 39: Plot of conductivity versus time for a PVP-protected rhodium hydrosol being ion-exchanged.

5.1.2.1 PVP-Protected Sols

The macroscopic stability of the PVP-protected rhodium hydrosol reduced by borohydride in water was vastly higher than sols which were unprotected, remaining stable for the length of the study, compared to aggregating instantaneously. This is consistent with its reportedly high protective ability [135] and its preponderance in the literature as an effective protecting agent. TEM micrographs revealed that approximately half of the primary particles existed on their own as discrete entities, and the other half existed in small aggregates of 2 – 5 particles. Generally primary particles were well-rounded, with little deviation from being spherical. PVP-protected sols exhibited the highest polydispersity and particle size, with an average particle size of 5.0 nm and a standard deviation of 1.3 nm. A typical micrograph is shown in Figure 40.

Despite these observations, the micrographs indicated that it was actually the *least* effective of all the protecting agents used in this study. This is possibly due to the massive size of the PVP chains used (700,000 g mol^{-1}, corresponding to approximately 6300 monomer units per chain), which may have given rise to bridging flocculation where two or more particles become attached to the same chain and they become aggregated.

5.1.2.2 PVA-Protected Sols

PVA-protected sols exhibited only large three-dimensional aggregates, often in the order of several microns in size and similar to those reported previously [112]. These were assumed to be an artefact of the dehydration arising from the sample preparation procedure, as aggregates of this size would have been too large to remain in suspension, a theory which was supported by the apparent stability of the dispersion macroscopically.

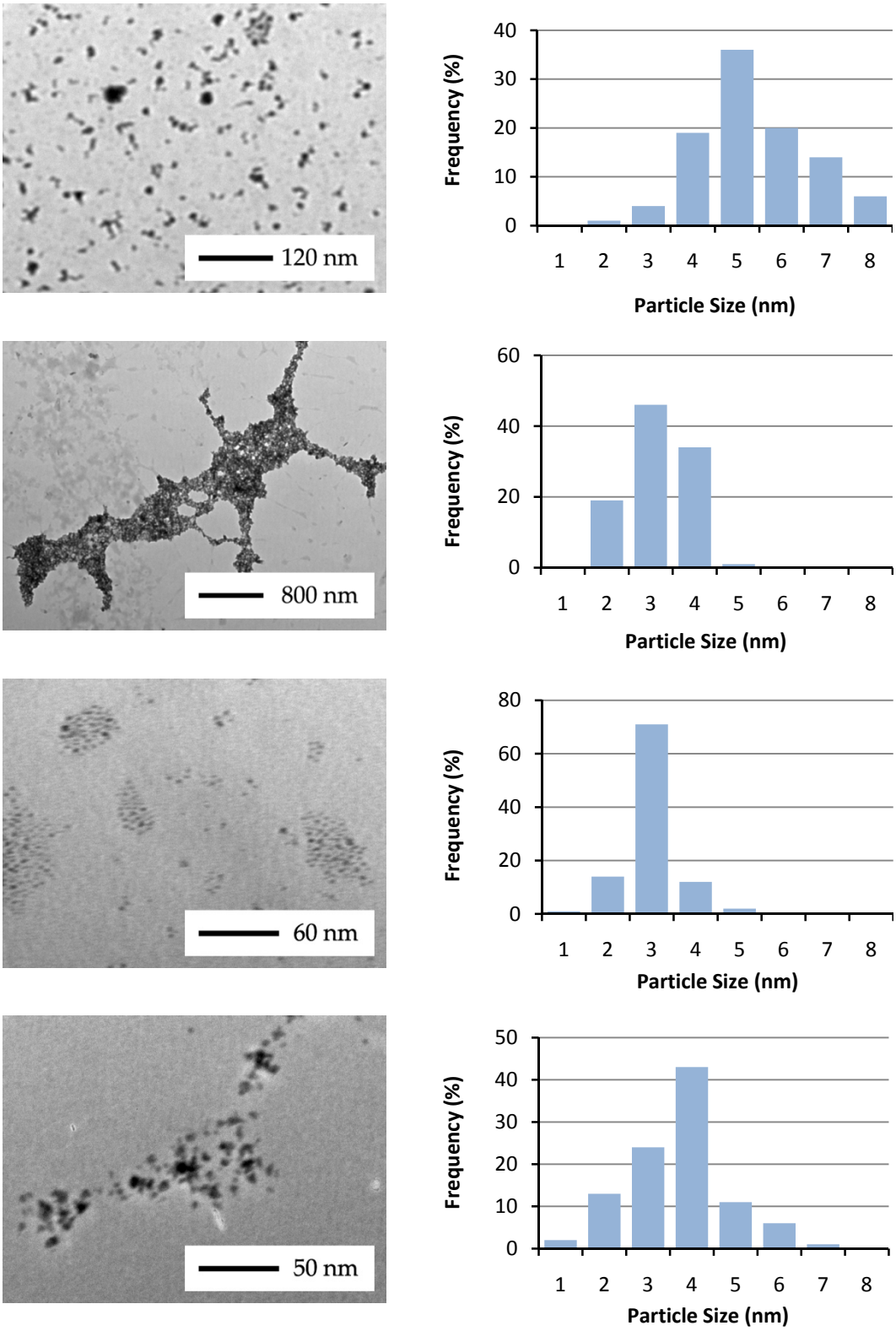

Figure 40: TEM micrographs and accompanying PSDs for rhodium hydrosols protected by PVP (top), PVA, PAA, ARG (bottom).

This was further supported by PCS data which suggested a much smaller particle size *in-situ* than the size of the aggregates measured by TEM. Analysis of the edges of the aggregates allowed imaging of individual primary particles, which generally appeared to be relatively spherical with little necklacing. The average particle size was 2.7 nm with a standard deviation of 0.7 nm, the second smallest size in the control group. A typical micrograph is shown in Figure 41.

5.1.2.3 PAA-Protected Sols

PAA-protected sols showed small clusters of primary particles, ranging in size from 2 - 50 particles. In no cases were they sufficiently tightly packed to indicate that they existed as associated units in solution, rather they had probably self-assembled by formation of H-bond networks during dehydration, in a similar fashion to those reported with gold [129]. As with PVA, this theory was supported by the UV/Vis and PCS data collected. Particles were all nearly spherical, with no deviations from this morphology and no particle necklacing. The average particle size was 2.5 nm and the standard deviation was 0.6 nm, both the lowest of the control groups. This was reflective of the colour of the sol, brown, indicating that there was an observable size-dependence on the colour at this concentration below approximately 3 nm. This was later observed with other rhodium sols with similar or smaller particle sizes. A typical micrograph is shown in Figure 41.

5.1.2.4 ARG-Protected Sols

Preparations of rhodium sols using ARG as a protecting agent have never been synthesised or imaged before in the scientific literature, therefore are of special interest. Dispersions were easily imaged, with discrete primary particles occurring together in small branched groups, with a small

number of small aggregates. Frequently there was short-range necklacing observed between small numbers of particles, forming irregular and 'lumpy' primary particles, although non-neckaced primary particles existed simultaneously. In both cases, the average particle size was 3.2 nm and the standard deviation of 1.1 nm, values intermediate between PVP-protected and PAA/PVA-protected sols. TEM micrographs showing the typical particle morphology is shown in Figure 40 and Figure 41.

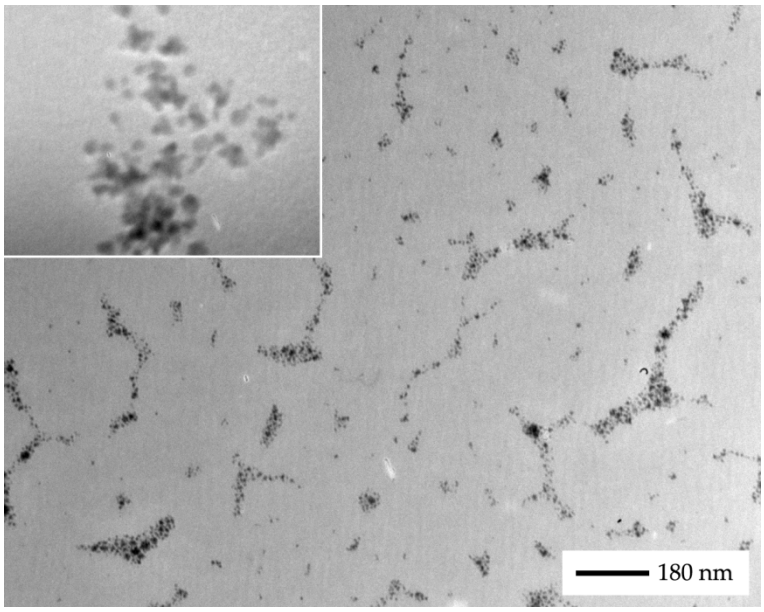

Figure 41: TEM micrograph of a rhodium sol reduced by borohydride and protected by ARG. Inset: magnification of necklaced primary particles.

5.1.3 UV/Vis Data

UV/Vis measurements indicated that the sols with the highest particle density per volume were those protected by ARG, followed by PVP, PVA then PAA. A plot showing the relative sizes of the A_{450} values is shown in Figure 42. As the density can reflect the average particle size in solution, we can conclude that *on average* ARG-protected sols contain the largest particles and PAA contains the smallest. This certainly holds true for PAA, as the sizes of the primary particles measured by TEM were the smallest and showed the least aggregation. For ARG however, the A_{450} value is

approximately twice as high as the other sols but the particle size measured by TEM is not. This probably means that *in situ*, ARG-protected sols had slightly more aggregation than those protected by the other three protecting agents used in this study.

PVA- and PAA-protected sols showed relatively low A_{450} measurements, reflective of both their lighter colour and smaller particle size. This kind of colouration can also be caused by incomplete reduction of the metal precursor salt, however the size of the precursor peaks were small for all preparations and not significantly larger for the PVA- and PAA- protected sols.

The fact that the absorbance measurements for the PVA-protected system were so low also support the idea that the aggregates observed in the TEM micrographs are indeed a result of dehydration, and do not exist in solution.

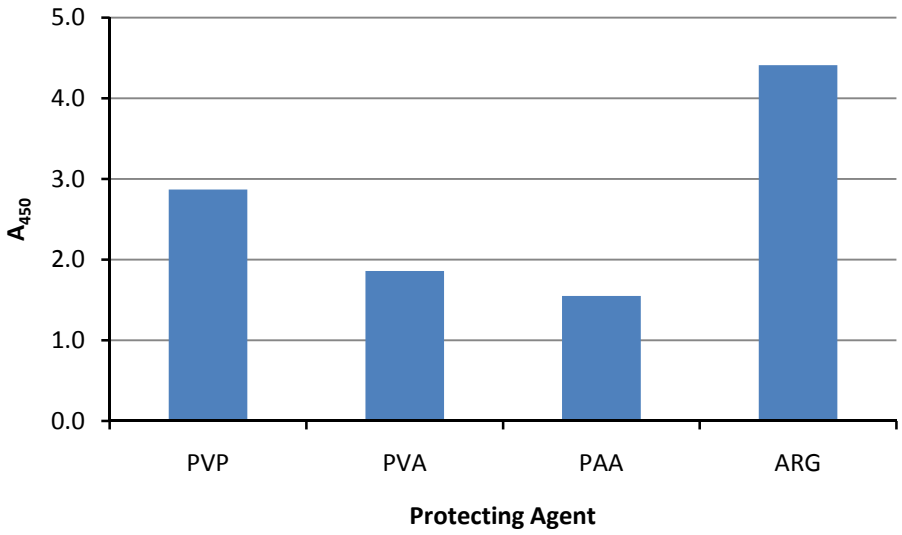

Figure 42: Plot of the dilution-corrected A_{450} values for protected rhodium hydrosols reduced by borohydride in water.

5.1.4 PCS Data

Measurements obtained by PCS are shown in Figure 43. They indicated that *in-situ*, rhodium sols protected by PVA had the largest hydrodynamic size followed by PAA, PVP then ARG. This is unusual given that the PVP chains were so much larger than all the others and the PAA chains were so much smaller, although it was likely an indication of their relative conformations in solution. The sizes *in-situ* were not reflective in any way of the size measured by TEM, again supporting the idea that the PCS measurements are really more of an indication of the hydrodynamic state of the dispersion rather than the 'particle size', per se.

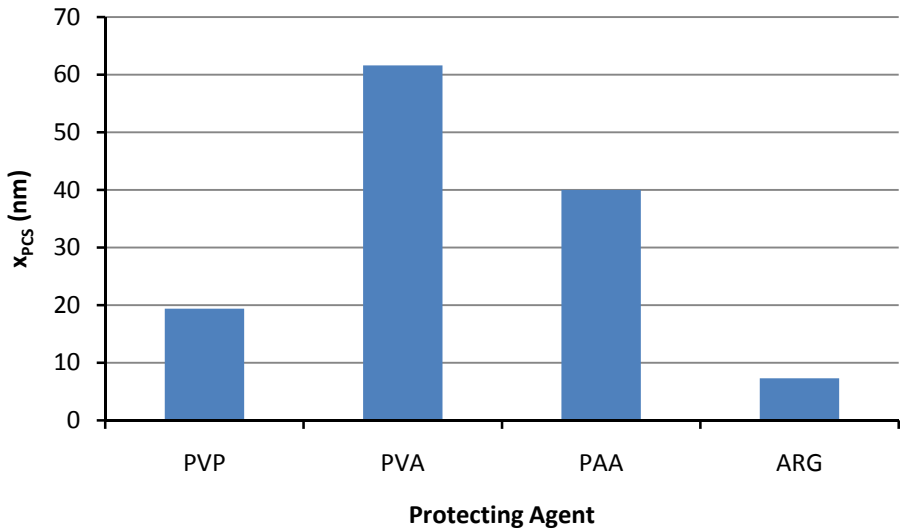

Figure 43: Plot of the x_{PCS} values for protected rhodium hydrosols reduced by borohydride in water.

5.2 Sols in Aqueous Methanol

5.2.1 General Remarks

It was found that mixtures of water and methanol were suitable solvents in which to generate rhodium sols, with the majority of syntheses ending successfully in the production of colloidal Rh^0. Photographs of the sols are shown in Figure 44, and a summary of the data collected is given in Table 11.

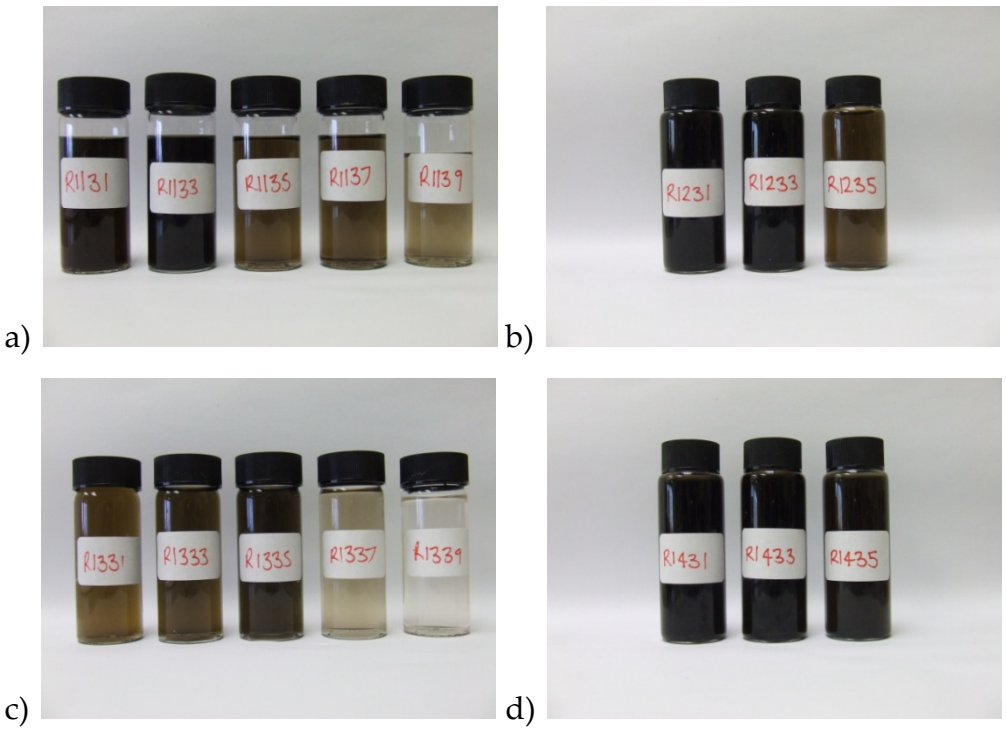

Figure 44: Photographs of rhodium sols reduced by borohydride in mixtures of water and MeOH, protected by a) PVP, b) PVA, c) PAA, d) ARG. The MeOH concentration increases in each photograph from 10% v/v (left) to 30%, 50%, 70% and 90% (right). The labels on the vials refer to their conditions of synthesis, as described in Appendix 1.

The synthesis of both protected and unprotected rhodium sols in the methanolic mixed-media appeared, at least visually, to be similar to the rhodium control sols generated in pure water. Addition of the MeOH to the dilute aqueous solution of $RhCl_3$ caused no obvious changes in the

colour of the solution, possibly indicating that the precursor did not undergo any significant changes in solvation. Addition of the reducing agent slowly caused the solution to darken, indicating the formation of colloidal Rh^0. The time which the solution took to darken was observed to be dependent on the proportion of MeOH it contained; the more MeOH in the dispersion medium the longer this darkening period took. For sols generated in 10% ϕ_{MeOH} it was approximately one minute, while for sols generated in 90% ϕ_{MeOH} it sometimes took upward of several minutes. The resulting sols generated at high MeOH concentrations were often quite light in colour, the PAA-protected sol for example being nearly colourless.

Solubility issues were encountered with two of the protecting agents at high MeOH concentrations. Both PVA and ARG tended to be insoluble in the dispersion medium when the MeOH concentration exceeded 50% v/v, and as a result they were precipitated as a voluminous slime. These precipitates were often orange, which was assumed to be due to adsorption of $RhCl_3$ from solution onto their surfaces. The same precipitation effects were observed in solutions where methanol was added to a solution of the protecting agent in the absence of the metal precursor, although in these cases the precipitates were expectedly white.

Even after the protecting agents had been precipitated, the solutions were still able to be reduced. This resulted in formation of a swirl of black particles in the solution, all of which became adsorbed onto the surface of the precipitate, leaving no particles “free”. Because of this, the samples which suffered from precipitation of protecting agents could not be analysed by the usual means, and were excluded from further analysis.

		TEM		PCS	UV/Vis
Protectant	ϕ_{MeOH}	$\bar{x}$ (nm)	σ (nm)	x_{PCS} (nm)	A_{450}
PVP	10	4.0	1.0	24.8	1.28
	30	2.5	0.6	133.0	1.85
	50	2.0	0.6	25.0	0.80
	70	1.4	0.4	22.0	0.78
	90	1.3	0.3	24.8	0.54
PVA	10	2.6	0.8	90.0	1.52
	30	2.4	0.6	434.0	1.60
	50	2.3	0.6	157.0	0.88
	70	Protecting agent precipitated			
	90	Protecting agent precipitated			
PAA	10	2.0	0.5	48.9	1.95
	30	1.8	0.5	285.0	0.90
	50	1.5	0.4	774.0	0.96
	70	1.0	0.3	58.8	0.37
	90	0.9	0.2	78.0	0.30
ARG	10	2.8	0.8	35.6	1.80
	30	2.6	0.6	38.4	1.79
	50	1.9	0.7	249.8	1.75
	70	Protecting agent precipitated			
	90	Protecting agent precipitated			

Table 11: Summary of the data collected for protected rhodium sols reduced by borohydride in mixtures of water and MeOH.

One possible way to avoid this problem would have been to filter the solutions in which protecting agent precipitation occurred. If the solutions were filtered prior to being reduced, the resulting filtrate would be free of precipitate and could then be reduced to produce a sol. The problem with this would have been that the precipitation and filtration process would have removed a significant portion of the protecting agent and adsorbed precursor metal salt, which would likely have caused significant changes in the particle size once the solution was reduced. This factor would have made these sols invalid for comparison against all the others. For this reason, this was not an avenue which was pursued.

However, on the grounds of curiosity some cursory photographs and SEM micrographs were taken to better understand the nature of these precipitates, which are shown in Figure 45. It appears that once dehydrated the precipitates were quite porous, with many different levels of microstructure. The exact morphology of the precipitates was found to depend on which protecting agent was used and which solvent it was precipitated from. The adsorption of the $RhCl_3$ precursor did not appear to have a significant effect on the morphology of the precipitates, although the adsorption of metallic rhodium particles did.

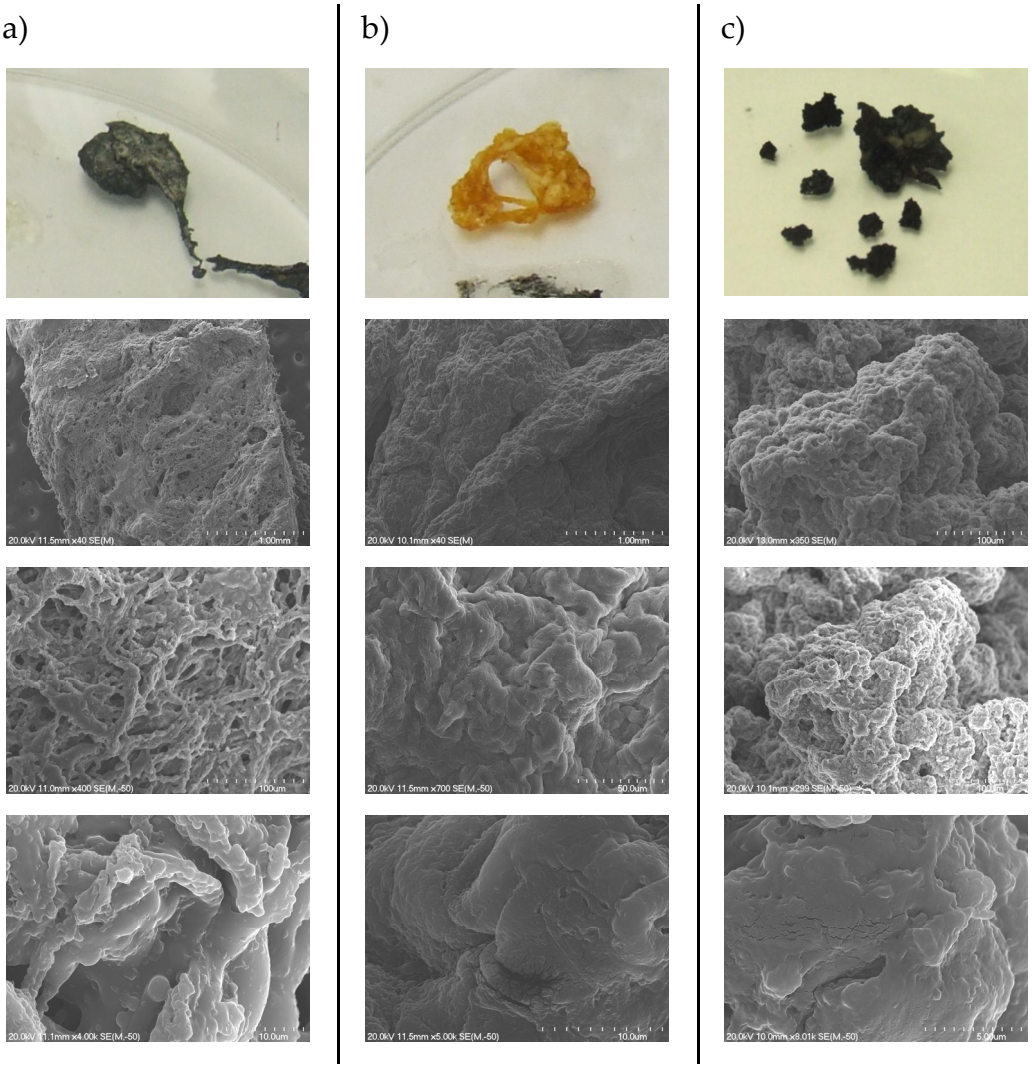

Figure 45: A series of photographs and SEM micrographs at progressively increasing magnifications showing the structures of the precipitated protecting agents. Column a) is an ARG precipitate extracted from a 70% v/v MeOH mixture. b) is a PVA precipitate with adsorbed $RhCl_3$ extracted from a 90% v/v MeOH mixture. c) is precipitate b) after reduction.

5.2.2 TEM Data

As predicted, the size of the primary particles as measured by TEM was significantly influenced by the use of MeOH as a cosolvent. Specifically, $\bar{x}$ was shown to be inversely proportional ϕ_{MeOH}, the proportion of cosolvent in which the sols were generated. The extent to which the size decreased was dependent on the protecting agent used; for example a sharp exponential decrease in $\bar{x}$ was observed for PVP-protected sols, and a slow

linear decrease was observed for PVA-protected sols. A graph showing the change in $\bar{x}$ with ϕ_{MeOH} is shown in Figure 46. Note that due to limitations with Microsoft Excel, the symbol '$\bar{x}$' could not be used in the axis titles, so 'x' is used instead.

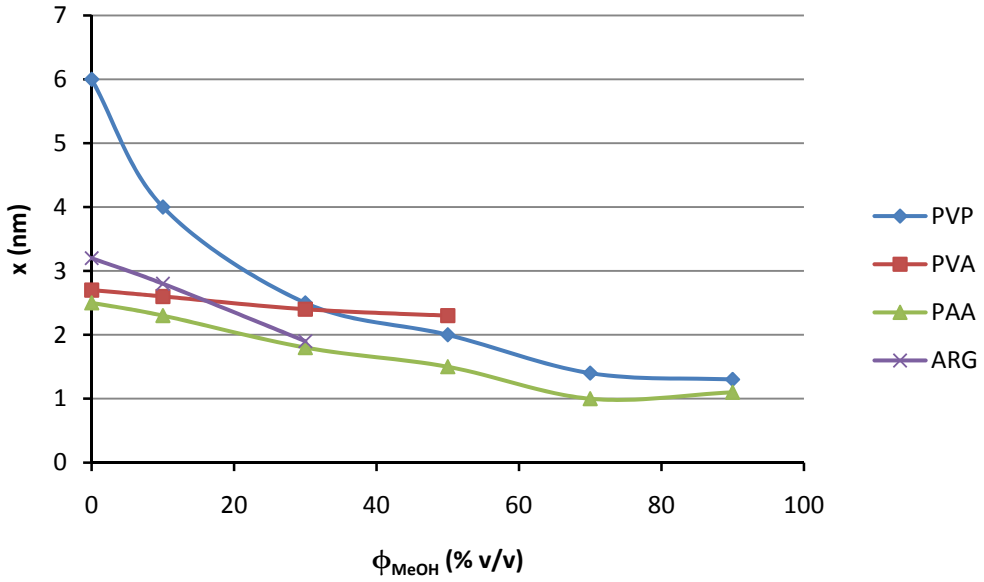

Figure 46: Plot of $\bar{x}$ versus ϕ_{MeOH} for protected rhodium sols reduced by borohydride in mixtures of water and MeOH.

The trends in polydispersity (σ) closely followed the trends in $\bar{x}$. A plot of σ versus ϕ_{MeOH} is shown in Figure 47. It was found that σ generally decreased as ϕ_{MeOH} was increased, the extent to which depended on the protecting agent used.

Despite displaying approximately the same trends, the variation in the plots for σ were much higher than the variation in the plots of $\bar{x}$. This was assumed to be due to the difficulty in *accurately* measuring a large number of particles, which results in anomalously high standard deviations. However, averaging these values provides an adequately *precise* indication of $\bar{x}$, resulting in a smoother plot for $\bar{x}$ versus ϕ_{MeOH} than for σ versus ϕ_{MeOH}.

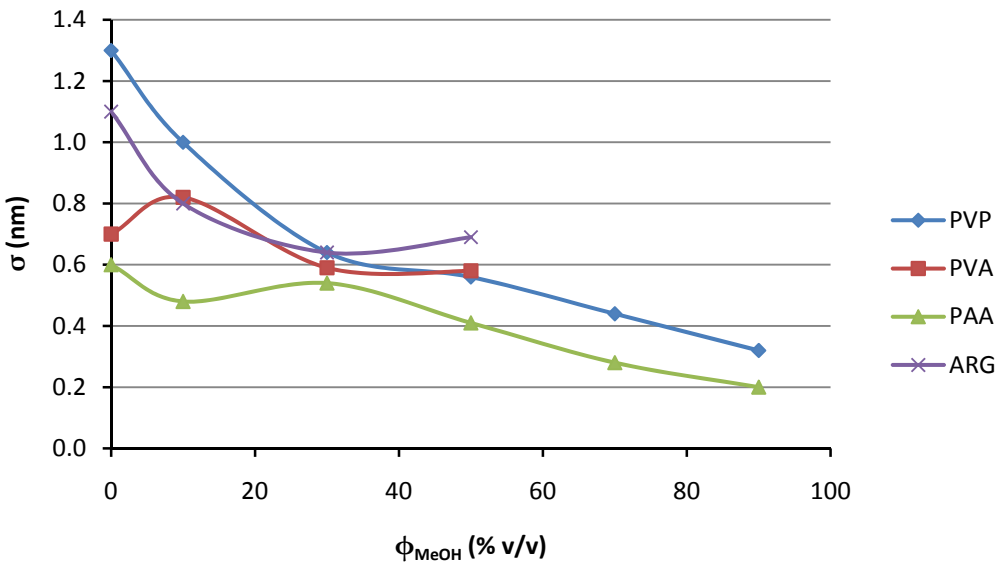

Figure 47: Plot of σ vs ϕ_{MeOH} for borohydride-reduced rhodium sols in mixtures of water and MeOH.

As mentioned previously, increasing ϕ_{MeOH} appeared to cause the reduction to occur more slowly as indicated by the 'darkening time'. Reduction rate has previously been shown to have a strong influence on the particle size, at least for PVP-protected rhodium sols [133]. Decreasing the reduction rate is expected to generate larger particles however, as the generated zero-valent atoms then are more likely to diffuse through the solution to find an existing particle to join to, rather than encountering another atom and creating a new particle. It was therefore probably not the reduction rate which causes the particle size to decrease, however the decreased reduction rate was probably at least partially responsible for the decrease in σ. This possibility is discussed further in Section 6.8.

5.2.1.1 PVP-Protected Sols

TEM micrographs showed that for PVP-protected rhodium sols reduced by borohydride in mixtures of water and MeOH, the presentation of particles on the TEM grids was generally very similar to the PVP-protected hydrosol. No significant changes were observed to either the

morphology of the particles, their aggregates, or their general arrangement. The presentation of the particles in the TEM micrographs was generally very similar to the PVP-protected hydrosol, as no significant changes to morphology of the primary particles or their aggregates or their arrangement on the grids were. A typical micrograph is shown in Figure 48.

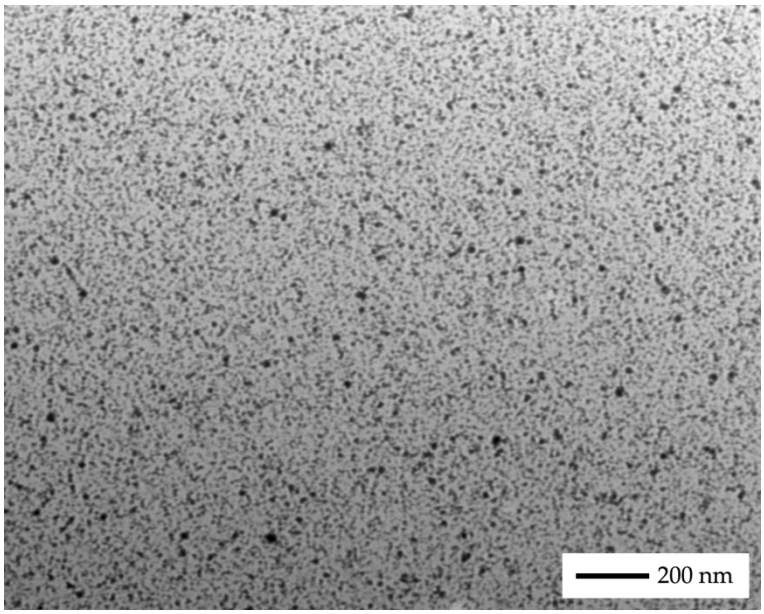

Figure 48: TEM micrograph of a PVP-protected rhodium sol reduced by borohydride in 10% v/v MeOH.

The frequency of the aggregates remained approximately equal throughout all preparations, although their sizes peaked in the middle of the concentration range (30% ϕ_{MeOH} - 50% ϕ_{MeOH}). This was reflected by their darker colour as observed in the photographs, the peak in the A_{450} plot at 30% ϕ_{MeOH}, and by the peak in the PCS plot at the same MeOH concentration, where the major species detected in solution increased in size from *ca.* 35 nm to 134 nm. Since the particle size as measured by TEM in this composition range was certainly not larger the particle size at any other composition, these peaks can only be explained by an increased level of aggregation. We may conclude therefore that for borohydride-reduced

rhodium sols produced in mixtures of water and methanol, the protecting capacity of PVP is decreased between 30% - 50% ϕ_{MeOH} but remains approximately the same as water outside this range, based on the frequency of aggregates observed in the micrographs and the relative flatness of the PCS and A_{450} versus ϕ_{MeOH} plots outside this range. This observation was supported by information from the literature on the conformation of PVP in mixtures of MeOH and water, as described in Section 6.9.

Measurements of the particles indicated that $\bar{x}$ decreased with inverse proportionality to ϕ_{MeOH}, dropping from 6.0 nm in the control experiment with 0% ϕ_{MeOH}, to 4.0 nm with 10% ϕ_{MeOH}, and down to 1.3 nm for 90% ϕ_{MeOH}. This corresponded to a decrease of 78%. A 3D PSD for the particle size data obtained by TEM is shown in Figure 49. Note how the position of the modal size class (the 'mode' in statistical terms is the value which occurs most often) shifted 'left', from 5 nm at 0% ϕ_{MeOH} to 2 nm at 90% ϕ_{MeOH}, mirroring the overall decrease in particle size.

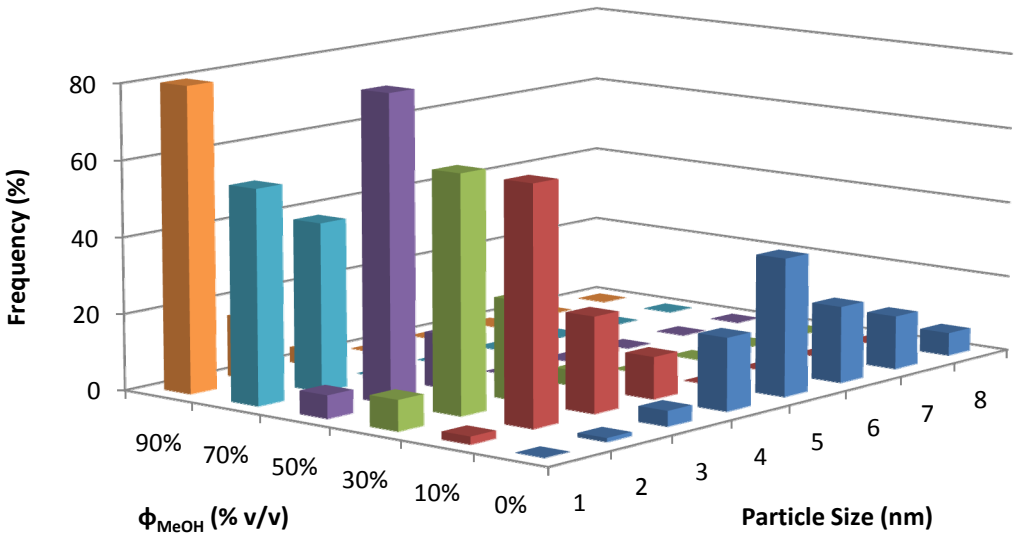

Figure 49: 3D PSD obtained by TEM for PVP-protected rhodium sols reduced by borohydride in mixtures of water and methanol, showing the evolution of the PSD with ϕ_{MeOH}.

5.2.1.2 PVA-Protected Sols

PVA-protected sols generated by borohydride reduction in mixtures of water and MeOH displayed markedly different characteristics to their corresponding aqueous equivalents at all compositions of ϕ_{MeOH}. The most obvious difference was that the dispersions no longer appeared as large aggregates in the TEM micrographs, rather as a well-dispersed homogeneous coating of primary particles or small aggregates thereof. A micrograph showing this is given in Figure 50.

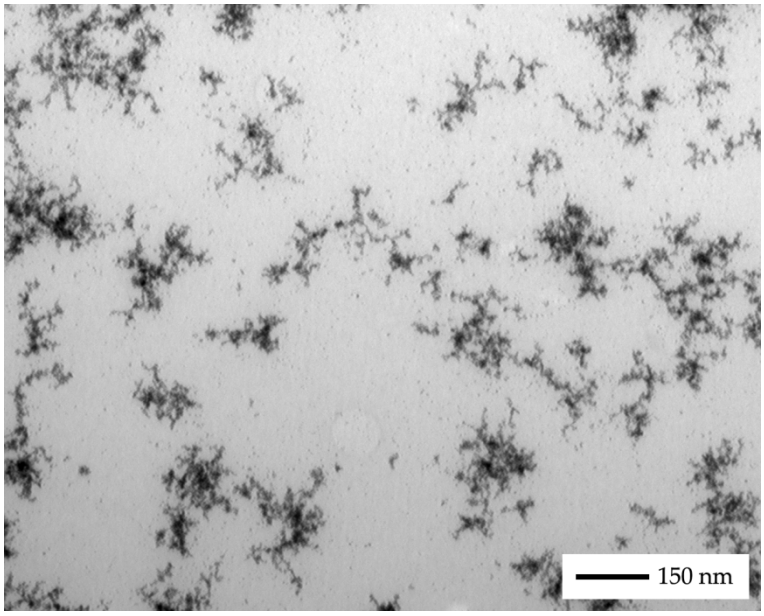

Figure 50: TEM micrograph of a PVA-protected rhodium sol reduced by borohydride in 30% v/v MeOH, illustrating the more open aggregate structure compared to equivalent hydrosols.

As ϕ_{MeOH} was increased the particles became more finely divided and the amount of aggregates decreased, although there were fluctuations observed in the aggregate size and shape. In these preparations discrete primary particles could be found and easily imaged, compared to the PVA-protected hydrosol where they could only be identified by studying the edges of the very large aggregates observed. The size of the aggregates in these sols appeared to vary between 2 - 100 individual particles,

although they were not close-packed aggregates like in the hydrosol, but had a more open structure. These were believed to be an artefact of dehydration rather than existing *in-situ*, as the A_{450} and PCS values were indicative of a much smaller particle size. The exception was the sample generated at 30% ϕ_{MeOH}, where the PCS data appeared to indicate that the aggregates observed via TEM agreed well with the hydrodynamic size *in-situ*. As with the PVP-protected sols, this is supported by the relative conformations of the polymer chains as described in Section 6.9.

The average particle size as measured by TEM appeared to decrease approximately 0.13 nm ± 0.05 nm for every 10% of MeOH in the dispersion medium, dropping from 2.7 nm in the control experiment to 2.3 nm in 50% ϕ_{MeOH}. A 3D PSD is shown in Figure 51. Note how the modal size class did not change; it remained at 3 nm in each case.

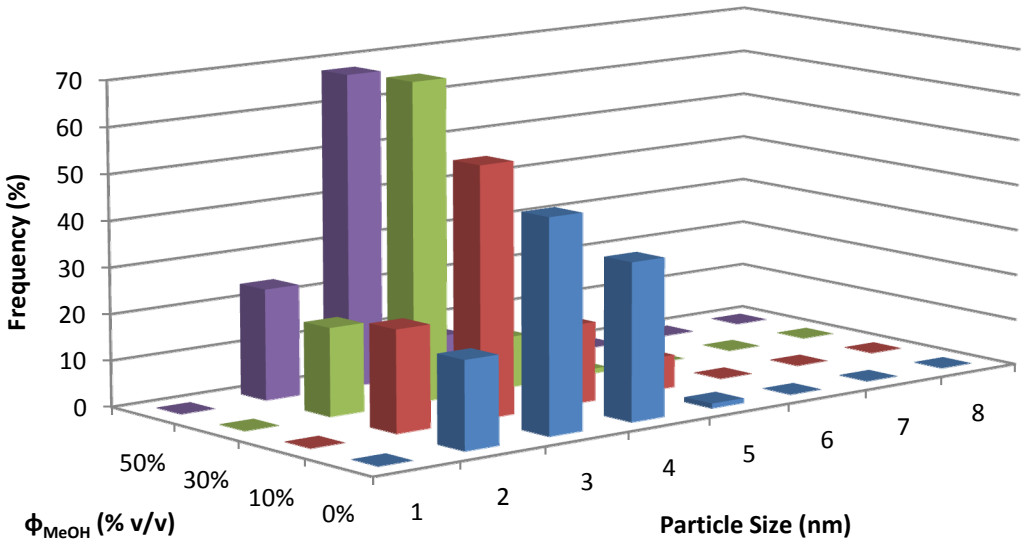

Figure 51: 3D PSD for PVA-protected rhodium sols reduced by borohydride reduction in mixtures of water and methanol, showing the evolution of the PSD with ϕ_{MeOH}.

The change observed in $\bar{x}$ was not a particularly large decrease, and was small enough that it falls within the error limits of the TEM as discussed in Section 4.2. Despite this, the trend was believed to be significant based on

several pieces of data. Firstly, the colour of the sols changed from pitch black to dark brown, indicative of smaller particle sizes at higher MeOH concentrations. The absorbance values also reflected this trend, decreasing from 0% through 50% ϕ_{MeOH}.

Because samples could not be generated above 50% MeOH due to solubility issues discussed previously, the exact trends for PVA-protected sols were harder to rationalise than those for PVP, although a general picture of their behaviour was easily gleaned.

5.2.1.3 PAA-Protected Sols

When PAA was used to protect rhodium sols reduced by borohydride in mixtures of water and MeOH, no problems were encountered with protecting agent precipitation, and the trends exhibited were similar PVP-protected rhodium sols in mixtures of water and MeOH.

All particles were relatively spherical with no unusual morphological traits. No necklacing was observed. A typical micrograph is shown in Figure 52.

Measurements of the sizes of the particles indicated that $\bar{x}$ dropped steadily as ϕ_{MeOH} was increased, from 2 nm in the control experiment with 0% ϕ_{MeOH} to 1.1 nm for the sol generated in 90% ϕ_{MeOH}. This trend was strongly reflected by the colour of the sols, as they were dark brown at low MeOH concentrations and nearly colourless at high MeOH concentrations. Initially it was believed that no sol had been generated for the 90% ϕ_{MeOH} sample because of this, however dispersion on a TEM grid revealed a great number of very small monodisperse particles.

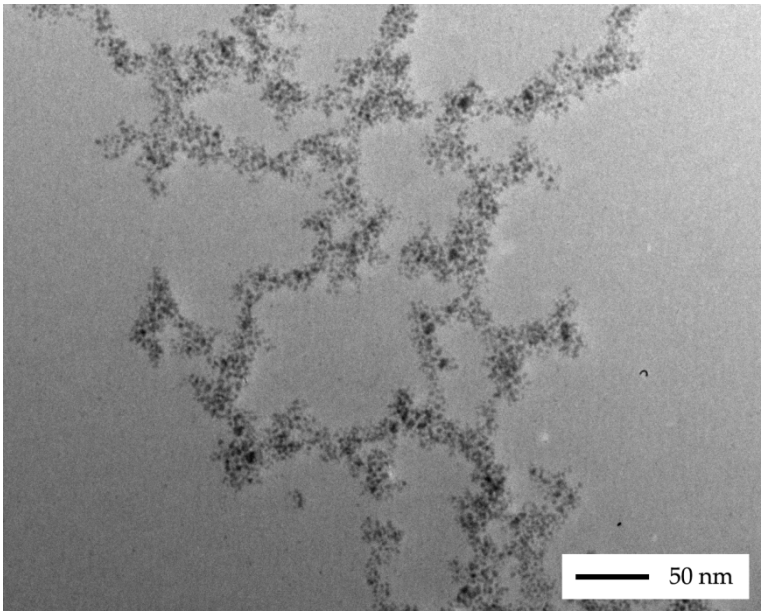

Figure 52: TEM micrograph of a PAA-protected rhodium sol reduced by borohydride 30% v/v MeOH.

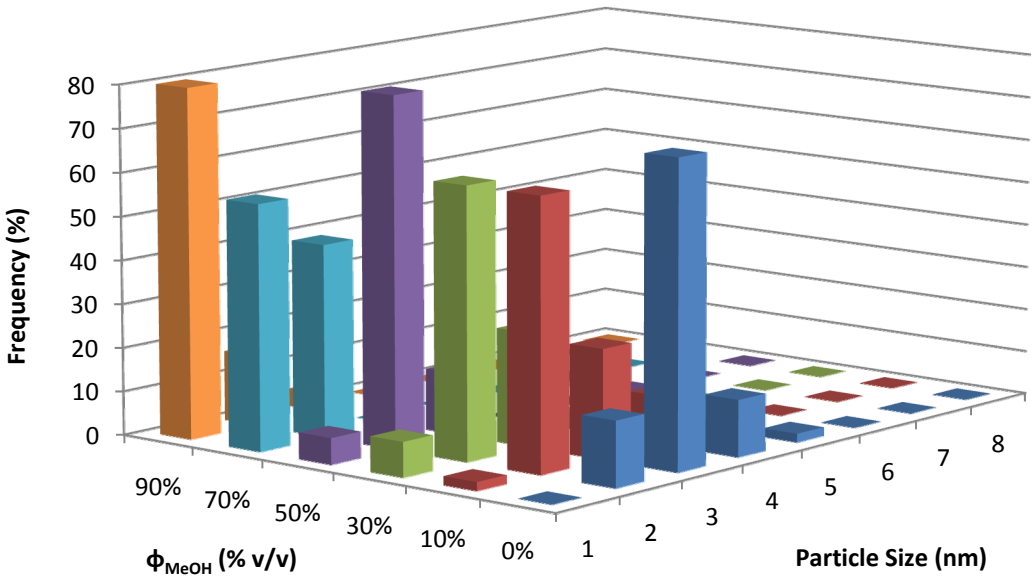

Figure 53: 3D PSD for PAA-protected rhodium sols reduced by borohydride in mixtures of water and methanol, showing the evolution of the PSD with ϕ_{MeOH}.

One may assume that because the sol was not a very dark colour that there must have been a large portion of unreduced precursor salt remaining in solution, however this was deemed unlikely to be the case. Firstly in the absence of large particles to turn the solution a dark colour, the solution should have resembled the colour of the precursor, but it did not. Secondly, large peaks due to the precursor were not observable in the UV/Vis spectra.

At intermediate MeOH concentrations the colour and the absorbance of the sols was found not to be reflective of the primary particle size. This was ascribed to the formation of aggregates during the drying process and in solution. The aggregates observed in the TEM micrographs were long loosely-packed arrays of particles which formed into long cross-linked chains approximately one micron in size. A micrograph illustrating a small section of this structure is shown in Figure 52. These were probably formed in solution to a small extent as the A_{450} and PCS values (discussed in Section 5.2.2 and 5.2.3) showed a peak in this region indicative of aggregation; however neither of the peaks were indicative of aggregates of the size observed in the micrographs. This was supported by the observation that the sols displayed a good level of stability visually and did not visibly aggregate and sediment within several months. It was likely therefore that there was some degree of aggregation in solution, but the majority of the aggregation observed in the micrographs occurred due to dehydration of the sol during sample preparation.

5.2.1.4 ARG-Protected Sols

ARG-protected sols exhibited similar levels of stability to their counterparts generated in water. Aggregation slowly increased as ϕ_{MeOH} was increased toward 30% ϕ_{MeOH}, and decreased again toward 50% v/v. Particle necklacing was progressively suppressed as ϕ_{MeOH} was increased.

A typical micrograph is shown in Figure 54. The particle size exhibited an ϕ_{MeOH}-dependence just as the other protecting agents did, dropping from 3.2 nm at 0% ϕ_{MeOH} steadily downward to 1.9 nm at 50% ϕ_{MeOH}. The polydispersity of the particles was also found to decrease, from 1.1 nm to 0.7 nm, although this is perhaps a result of the decrease in particle size. A 3D PSD is shown in Figure 55 illustrating these points.

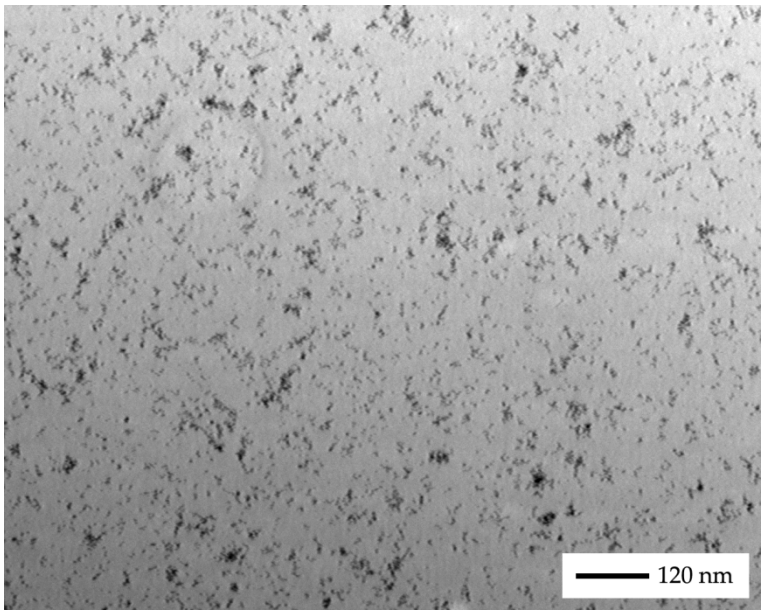

Figure 54: TEM micrograph of an ARG-protected rhodium sol reduced by borohydride in 30% v/v MeOH.

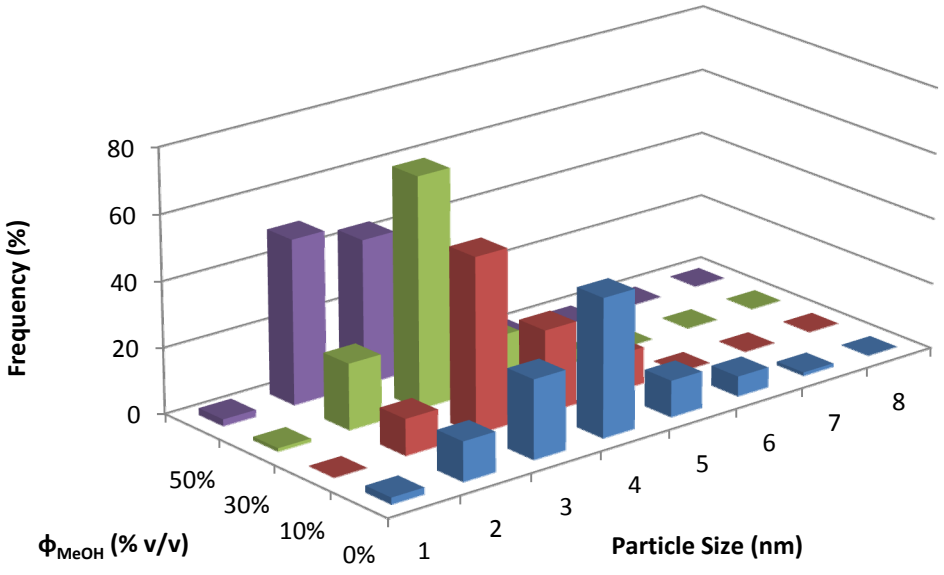

Figure 55: 3D PSD for ARG-protected rhodium sols reduced by borohydride in mixtures of water and methanol, showing the evolution of the PSD with ϕ_{MeOH}.

5.2.2 UV/Vis Data

The UV/Vis data, shown in Figure 56, shows that the A_{450} values for every sol were decreased significantly relative to the control experiment. The most obvious reasons for this are that the particle size was lower and the dielectric of the dispersion medium was higher, so the turbidity would therefore be lower. However, both of these factors change continuously with ϕ_{MeOH}, whereas the turbidity plateaued relatively quickly. However if one considers the aggregates, the behaviour of the plot can be rationalised with relative ease. Taking the PVP-protected rhodium sols for example, initially the turbidity decreased, probably due to the decrease in the primary particle size of the rhodium particles. It then increased slightly, which corresponded with the increase in the size of aggregates observed in the TEM micrographs. It then decreased again sharply as the aggregates disappear, and then proceeded to decrease slowly as the aggregation remained constant but the particle size decreased.

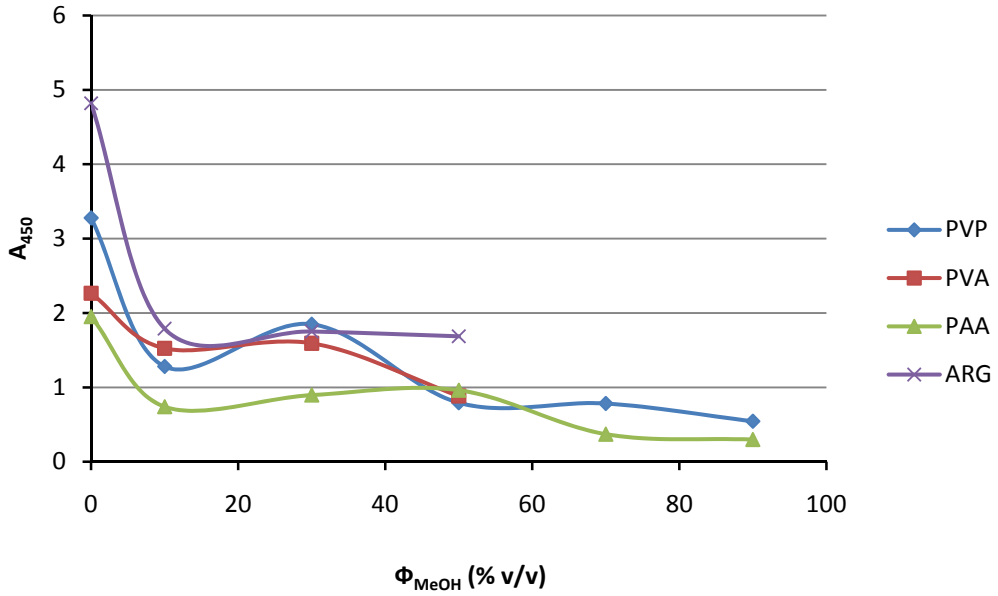

Figure 56: Plot of the dilution-corrected A_{450} values versus ϕ_{MeOH} for protected rhodium sols reduced by borohydride in mixtures of water and MeOH.

The profile of the A_{450} versus ϕ_{MeOH} plots for the other three protecting agents may be rationalised in the same way, indicating that the behaviour of the turbidity plot followed relatively closely the level of aggregation observed in the system by TEM, assuming the total mass of particles in the dispersion remained constant. Based on the UV/Vis spectra which did not show significant changes in the small size of the precursor peak, this assumption holds true.

5.2.3 PCS Data

The PCS data, shown in Figure 57, showed nearly identical trends to the turbidity data. For example, the PCS plot showed the same peaks as the turbidity plot at 30% for PVP and PVA and 50% for PAA, but the peaks were comparatively much larger. The peak in the plot for the PVP-protected sols is approximately 100 nm larger than its surrounding values despite the fact that the aggregates which were responsible for it were only approximately 20 nm larger than the primary particles themselves as

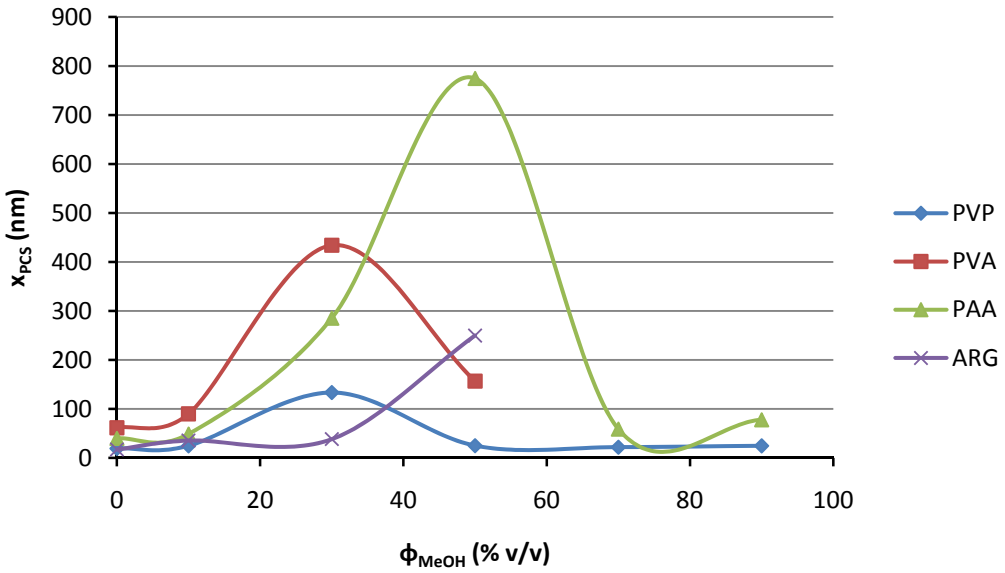

Figure 57: Plot of x_{PCS} versus ϕ_{MeOH} for protected rhodium sols reduced by borohydride in mixtures of water and MeOH.

observed by TEM. One may imagine that the discrepancy could be attributed effects arising from the polymer layers adsorbed to the surface of the particles; however this was probably not the case. At intermediate compositions where the aggregation was observed to be higher, the thickness of the adsorbed layers should have been less, as this is what causes aggregation in the first place. These seemingly excessively large peaks are therefore probably partially due to an inadequacy in the measurement parameters such as the viscosity, and partially due to the fact that light scattering instruments are more sensitive to larger particles, so peaks which do exist become exaggerated in size. In either case the relative increases in aggregation were observed to be real, and backed up by data described in section 6.9.

5.3 Sols in Aqueous Dimethylsulfoxide

All attempts to synthesise rhodium sols in mixtures of water and DMSO were unsuccessful, resulting in canary-yellow solutions rather than the familiar pitch black solutions indicating formation of a rhodium colloid.

When starting with a dilute rose-red $RhCl_3$ solution as the precursor, addition of the DMSO to the solution caused the colour to quickly become *more* red, despite being simultaneously diluted. This was taken to be an indication of some kind of ligand exchange process, where ligands in the $RhCl_3$ aqua-complex were replaced to some extent by DMSO ligands. The vast molar excess of DMSO compared to $RhCl_3$ would probably shift the equilibrium strongly in favour of this occurring. A reaction scheme is shown in Figure 58.

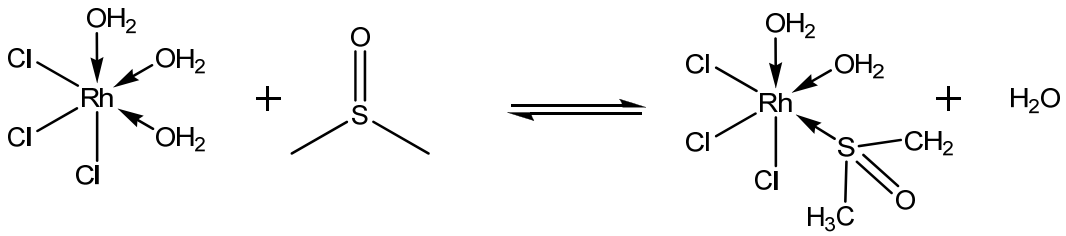

Figure 58: Possible ligand substitution reaction between H_2O and DMSO on $RhCl_3$.

This is likely a simplification of the actual process occurring, as $RhCl_3$ has a quite complex chemistry in aqueous solution. A variety of hydrolysis products are present depending on the age of the solution, among other factors. These are shown in Figure 59.

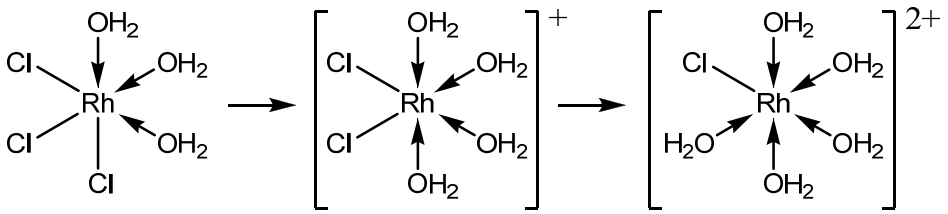

Figure 59: Progressive substitution of the chloride ligands in $RhCl_3$ by aquo ligands.

Secondly, as rhodium(III) is generally 6-coordinate there are up to 6 sites at which ligand exchange could occur, resulting in a wide variety of possible species. It should also be noted that when DMSO replaces aqua ligands it can be either an S-donor or an O-donor; although rhodium *usually* prefers S-donors.

Upon addition of aqueous sodium borohydride, no reaction was initially observed, but the solution slowly turned a canary-yellow colour over a period of half an hour. Since a colour change was caused, it was assumed that some kind of further reaction occurred. Shining a laser-pointer through the solution showed no Tyndall cone, indicating that no particulate matter was formed. This indicated that the reaction produced product(s) which were soluble in aqueous DMSO, which were probably a reduced version of the ligand-substituted complex described earlier. If it is indeed a reduction reaction, it is possible that the rhodium is reduced from Rh(III) to Rh(I), where its +1 state is stabilised by DMSO ligands, a well-documented effect which has been utilised a great many times to synthesise rhodium(I) complexes with coordinating solvents [132]. A reaction scheme showing one possible product is given in Figure 60.

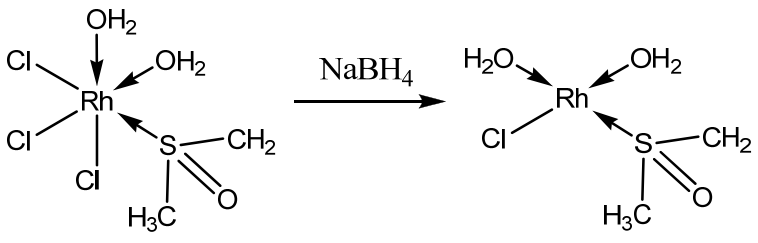

Figure 60: Reaction scheme indicating a possible product formed from the addition of borohydride to a DMSO-substituted $RhCl_3$ complex.

Although not one of the main aims of this project, it was of interest therefore to attempt to determine exactly what complex(es) were formed such that the solution could not be reduced.

Mass spectra of the rhodium solutions were acquired before and after reduction, although their interpretation proved to be challenging. What is clear from the spectra, if they are to be believed, is that there were a variety of species formed in solution, lending credence to the proposal that the aqueous chemistry of the system was not trivial, and was further complicated by the addition of an excess of a coordinating solvent like DMSO. Both positive and negative ion mode ESI-MS spectra of the reduced rhodium solutions are shown in Figure 61 and Figure 62. The negative-ion spectra were relatively simple, containing only one major species at 201 m/z, however the positive ion spectra were more complicated and displayed multiple species with regular isotope patterns, notable at 329 m/z and 407 m/z. All of these peaks were different from the background peaks observed in the spectrometer and different from the unreduced solutions.

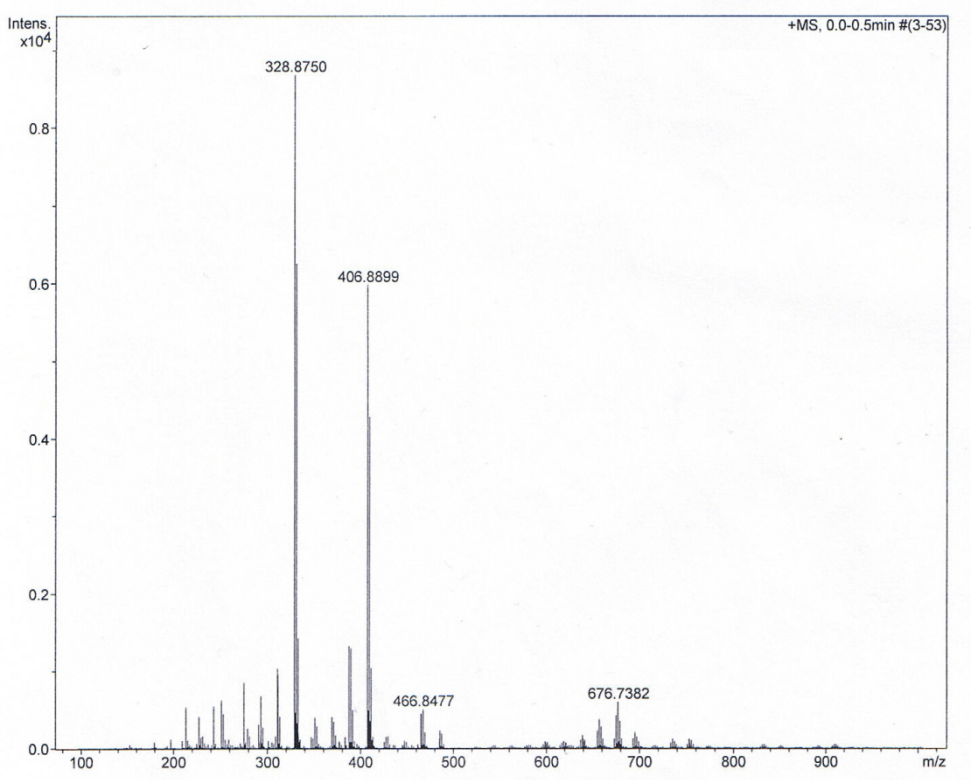

Figure 61: ESI-MS spectrum of a reduced solution of $RhCl_3$ in aqueous DMSO in postive ion mode.

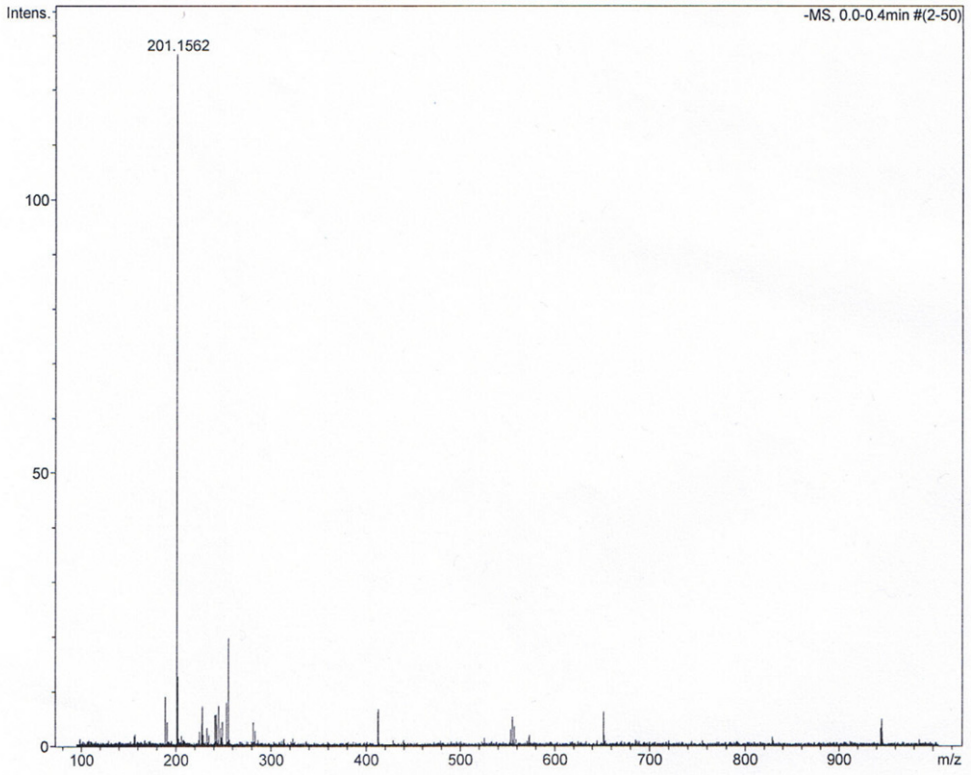

Figure 62: ESI-MS spectrum of a reduced solution of $RhCl_3$ in aqueous DMSO in negative ion mode.

5.4 Sols in Aqueous Dimethylformamide

5.4.1 General Remarks

Surprisingly dimethylformamide proved to be a superb cosolvent for generation of rhodium colloids. Although it appears on first inspection that DMF has the structural characteristics of a strongly coordinating solvent like DMSO, it did not prevent reduction to the Rh^0 state as DMSO did. One may expect the lone pairs on either the oxygen or nitrogen to act as lewis bases, donating electron density to the metal centre. However, the electrons on the nitrogen are unavailable as it is sp^2 hybridised, and the oxygen is not a strong donor as it is relatively hard compared to rhodium. Futhermore, because of its relatively high polarity (ε = 38.25 [131]) it did not cause any precipitation of any of the protecting agents as observed with some other solvents like MeOH. Photographs of the sols generated are given in Figure 63, and a table of data is give Table 12.

One of the most interesting observations to arise from the synthesis of rhodium colloids in DMF was the apparent ability for DMF to act as a protecting agent, stabilising otherwise unprotected colloids against aggregation. Whereas unprotected rhodium sols in water were extremely unstable and completely sedimented within minutes, unprotected rhodium sols synthesised in mixtures of water and DMF appeared to be stable for several weeks, depending on ϕ_{DMF}. DMF was the only solvent observed to do this. This behaviour is perhaps somewhat related to its weakly coordinating nature described previously; it is not such a good electron donor that it bonds to the metal so strongly that it prevents reduction, but it is strong enough to stabilise the particles against aggregation for a significant period of time. It should be mentioned however that this period of time over which DMF exerted a protective action was much less than that 'actual' protecting agents used.

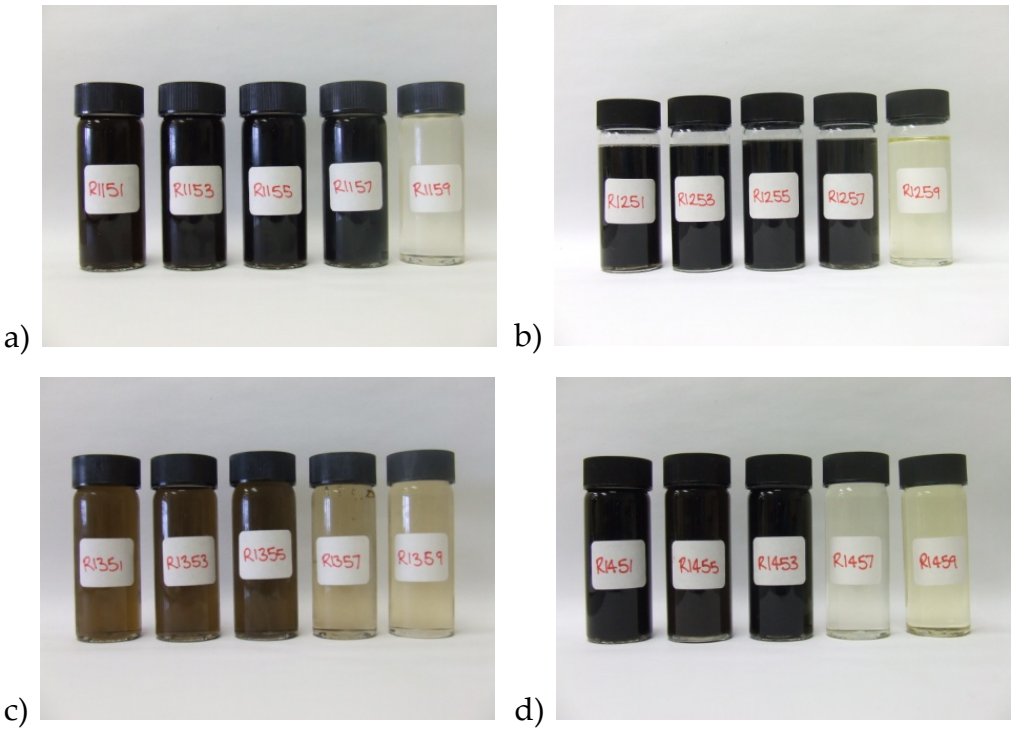

Figure 63: Photographs of rhodium sols reduced by borohydride in mixtures of water and DMF, protected by a) PVP, b) PVA, c) PAA and d) ARG. The MeOH concentration increases from left to right in each photograph, from 10% v/v (left) to 30%, 50%, 70% and 90% (right).

Interestingly, while the majority of syntheses successfully resulted in the production of colloidal rhodium, for each protecting agent there appeared to be a certain DMF concentration past which the generation of Rh^0 ceased and a homogeneous solution was produced instead. This was judged by shining a laser pointer through the solution and by analysing the solutions by TEM. If no Tyndall cone was observed and no particles were found by TEM, the synthesis was deemed to have produced a solution rather than a suspension. This 'cutoff point' varied depending on which protecting agent was used; for PVP, PVA and PAA no colloid was generated past 70% ϕ_{DMF}, for ARG it was 50% ϕ_{DMF}. This could perhaps be explained by a DMF-H_2O ligand-exchange reaction on $RhCl_3$ as shown in Figure 64, similar to the type of reaction which prevented rhodium from being reduced in aqueous DMSO.

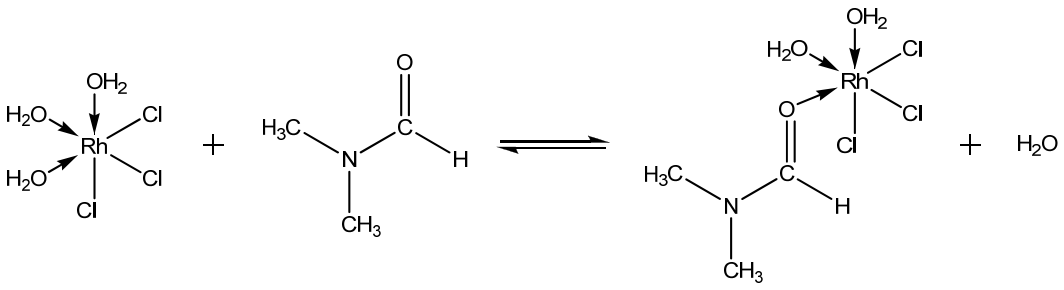

Figure 64: Reaction scheme illustrating the possible ligand exchange between rhodium chloride and DMF.

If this process was an equilibrium, its position could be shifted significantly toward the products at a sufficiently high DMF concentration, rendering the Rh centre too sterically crowded to be reduced. A table which shows for which preparations this occurred, and the other data collected, is shown in Table 12.

		TEM		PCS	UV/Vis
Protectant	ϕ_{DMF}	$\bar{x}$ (nm)	σ (nm)	x_{PCS} (nm)	A_{450}
PVP	10	3.3	0.9	41.1	1.42
	30	2.4	0.6	136	1.54
	50	2.1	0.4	329	1.70
	70	1.8	0.3	225	1.57
	90	Solution produced instead of colloid			
PVA	10	2.1	0.4	131	1.55
	30	2.0	0.4	260	1.60
	50	1.8	0.4	253	1.42
	70	1.5	0.3	660	1.39
	90	Solution produced instead of colloid			
PAA	10	1.5	0.3	123	0.60
	30	1.3	0.3	154	0.64
	50	1.2	0.2	574	0.59
	70	1.1	0.2	511	0.13
	90	Solution produced instead of colloid			
ARG	10	2.8	0.5	64	1.55
	30	2.4	0.4	134	1.13
	50	1.8	0.3	420	1.68
	70	Solution produced instead of colloid			
	90	Solution produced instead of colloid			

Table 12: Summary of the TEM, PCS and UV/Vis data collected for borohydride-reduced rhodium sols in mixtures of water and DMF.

5.4.2 TEM Data

Sols generated in mixtures of water and DMF were not amenable to the usual methods of sample preparation for TEM. The TEM grids used in this study had a thin film of collodion (a nitrocellulose derivative) as the sample support, through which the electron beam passes to image the sample. The application of a drop of a sol containing DMF to these grids appeared to cause the collodion film to dissolve, rendering the grid unusable and any supported sample unable to be imaged. Fortunately this was only a problem with sols containing DMF concentrations equal to or above 50% v/v.

To overcome this problem, an extraction technique was adapted from the literature [136] to remove the DMF from the dispersion medium, which suggested that polar aprotic solvents such as DMF can most easily be removed from aqueous reaction mixtures using a mixture of heptane isomers. As no isomer mixture was available, *n*-heptane was used and found to be sufficiently effective. The procedure used was as follows.

Approximately 1 mL of colloid solution was introduced into a clean glass vial with a volume of *n*-heptane approximately equal to twice the volume of DMF in the colloid to be extracted. For sols generated in 90% v/v a small amount of water (*ca.* 0.5 mL) was added to aid extraction. The vial was shaken for several minutes, and a drop of colloid from the bottom (largely aqueous) layer was deposited onto the grids. In many cases a stable emulsion was created, which was assumed to be a dispersion of heptane in water. Even once the emulsion appeared to have completely separated into its constituent phases, microscopic drops of heptane/cosolvent remained in the aqueous phase. These were observable under a microscope, and it was found that one must wait until they had completely returned to the organic phase before applying a drop of the

extracted colloid onto the grid, otherwise the grid coating would still be dissolved.

The concern using this technique was that the heptane extraction may have affected the size and/or morphology of the particles. It was deemed unlikely that this step would affect the size or morphology of the primary particles however, as this would require that heptane could somehow rearrange the metal lattice of the particles, which seemed unlikely. It was obvious that the heptane extraction affected the characteristics of the aggregates however, based on two main observations. Firstly, micrographs of colloids which have been heptane-extracted showed very unusual structures; at low magnifications it appeared aggregates were arranged in necklaced formations of large (*ca.* 50 nm) particles, however upon closer inspection these particles were themselves aggregates of much smaller particles, whose sizes were much closer to those previously observed.

The morphology of these aggregates indicative of the presence of two-stage aggregation process: a 'slow' process forming the tightly-packed smaller aggregates from which the larger ones were composed, likely a result a compression of the polymer layer due to the cosolvent, and a 'fast' process, forming open necklaced aggregates, likely due to the heptane extraction. This general structure is referred to from here on as the '*compound aggregate*' structure. Consequently, information on the structure of aggregates taken from micrographs of colloids which had been heptane-extracted were interpreted with caution. The second observation was that after extraction, many colloids which were previously stable became destabilised and completely aggregated, sedimenting to the bottom of the extraction vial.

Analysis by TEM of the sols which did not have reduction problems and which had been heptane-extracted indicated that $\bar{x}$ was inversely proportional to ϕ_{DMF}, just as it was for the rhodium sols generated in mixtures of water and MeOH. $\bar{x}$ was shown to decrease sharply from 0% ϕ_{DMF} to 10% ϕ_{DMF}, after which it decreased more gradually. A plot of $\bar{x}$ versus ϕ_{DMF} is shown in Figure 65. Similar trends were observed in other systems studied, such as Pd/DMSO (see Section 6.3).

The origin of this sharp decrease in $\bar{x}$ was perhaps related to temporary stabilisation of the Pd nuclei generated leading to retarded particle growth, as indicated by the apparent ability for DMF to act as a protecting agent. This possibility is discussed further in Section 6.8.

The trends in the polydispersity (σ) of the sols followed fairly closely the trends in $\bar{x}$, as it did with the rhodium sols produced in mixtures of water and MeOH. In all cases σ dropped sharply initially then gradually declined, with the exception of the PVA-protected sols where the polydispersity increased slightly above 10% ϕ_{DMF}. This was probably due to errors in the measurements rather than a real effect however. A plot showing σ versus ϕ_{DMF} is shown in Figure 66.

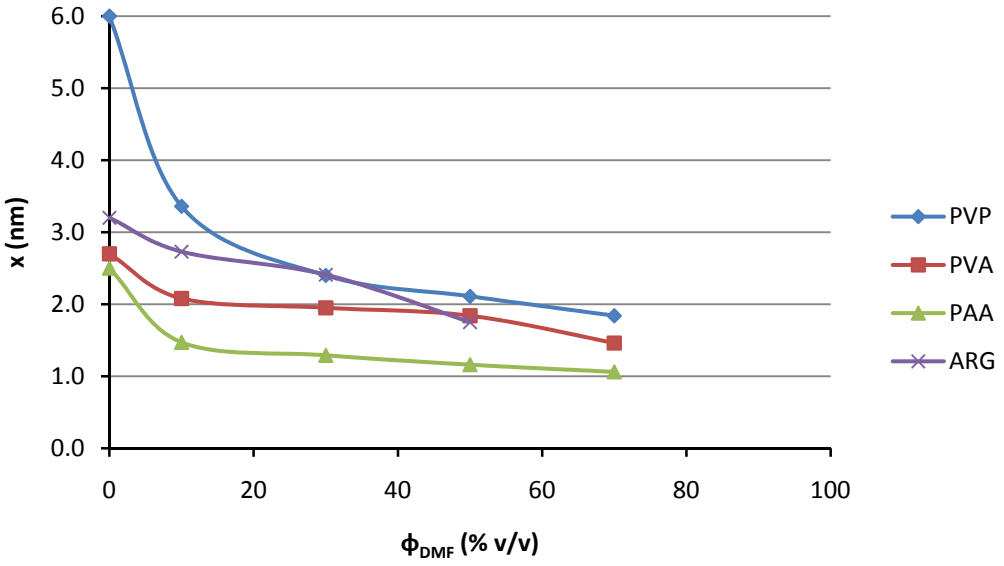

Figure 65: Plot of $\bar{x}$ versus ϕ_{DMF} for protected rhodium sols reduced by borohydride in mixtures of water and DMF.

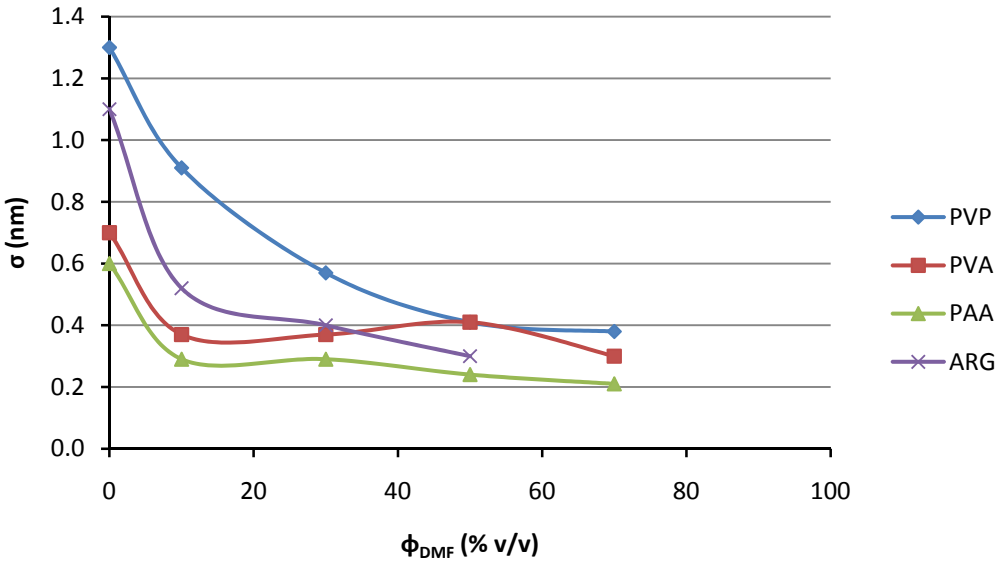

Figure 66: Plot of σ versus ϕ_{DMF} for protected rhodium sols reduced by borohydride in mixtures of water and DMF.

5.4.2.1 PVP-Protected Sols

Analysis of the rhodium sols protected by PVP and reduced by borohydride in mixtures of water and DMF showed that generally the sols were slightly more aggregated than their equivalent hydrosols produced in pure water. The particles existed almost exclusively as small aggregates approximately 5 – 50 primary particles in size. Approximately 90% of the particles existed as these aggregates, with the remainder existing as discrete primary particles. A typical micrograph is shown in Figure 67. The size and morphology of these aggregates was mostly consistent across the composition range studied, although at intermediate DMF concentrations (*ca.* 50% ϕ_{DMF}) there was a shift toward an increased number of primary particles compared to aggregates.

In all cases the primary particles were significantly less spherical than when produced in pure water, exhibiting irregular but rounded morphologies. Their aggregates were even more eccentric, displaying high levels of necklacing which caused their constituent particles to become fused together. These irregularities in the morphologies made the particles somewhat difficult to measure, and those which had become necklaced together were measured as if they had not been necklaced. As measured, $\bar{x}$ decreased 55% across the composition range studied, dropping from 6.0 nm in the control experiment with 0% ϕ_{DMF}, halving to 3.3 nm in 10% ϕ_{DMF} and dropping ultimately to 1.8 nm in 90% ϕ_{DMF}. A 3D PSD showing this evolution is given in Figure 68. Note how the modal size class clearly shifted from 5 nm to 2 nm, reflective of the change in $\bar{x}$.

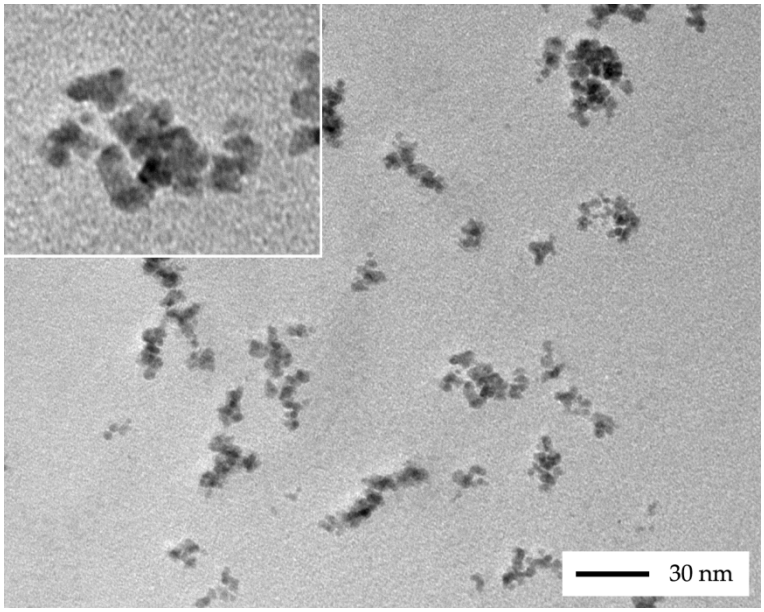

Figure 67: TEM micrograph of a PVP-protected rhodium sol reduced by borohydride in 30% v/v DMF. Inset: higher magnification of the same sol.

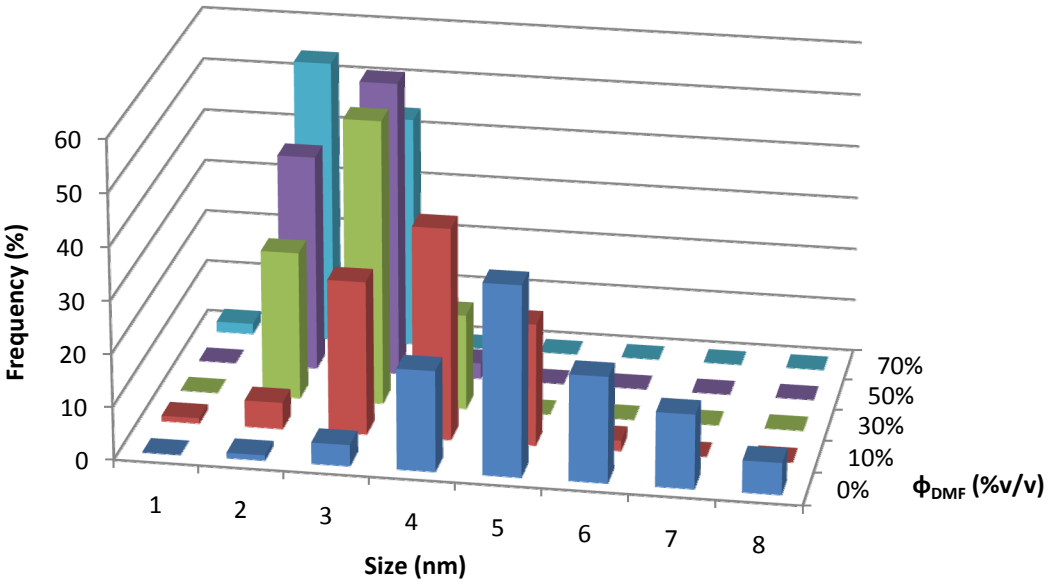

Figure 68: 3D PSD obtained by TEM for PVP-protected rhodium sols reduced by borohydride in mixtures of water and DMF, showing the evolution of the PSD with ϕ_{DMF}.

5.4.2.2 PVA-Protected Sols

PVA-protected rhodium sols reduced by borohydride in mixtures of water and DMF showed large departures in their behaviour from their aqueous equivalents. Rather than existing as densely-packed micron-sized aggregates as their hydrosol equivalents did, at low DMF concentrations particles existed as loosely-packed branched aggregates. An example is shown in Figure 69. As the DMF concentration was increased, the open-branched aggregate structure remained, but became increasingly thicker and more close-packed. An example is shown in Figure 70. Although the aggregates thickened progressively as the DMF concentration was increased, similar effects were observed with palladium sols in MeOH and DMSO (Sections 6.2 and 6.3), so it was believed the changes in morphology were caused by the heptane extraction step rather than existing *in-situ*, a theory which was supported by the UV/Vis and PCS data (Section 5.4.3 and 5.4.4).

At low DMF concentrations the majority of the primary particles had become necklaced together in groups of 5 - 10 particles in random conformations. The few which were not necklaced displayed eccentric rounded morphologies. As the DMF concentration was increased the necklacing became completely suppressed and the particles became increasingly spherical. Their size decreased 44% across the composition range studied, decreasing nearly linearly from 2.7 nm in the control experiment with 0% ϕ_{DMF} to 1.8 nm in 90% ϕ_{DMF}. A 3D PSD showing the changes in the PSD across the composition ranges studied is shown in Figure 71.

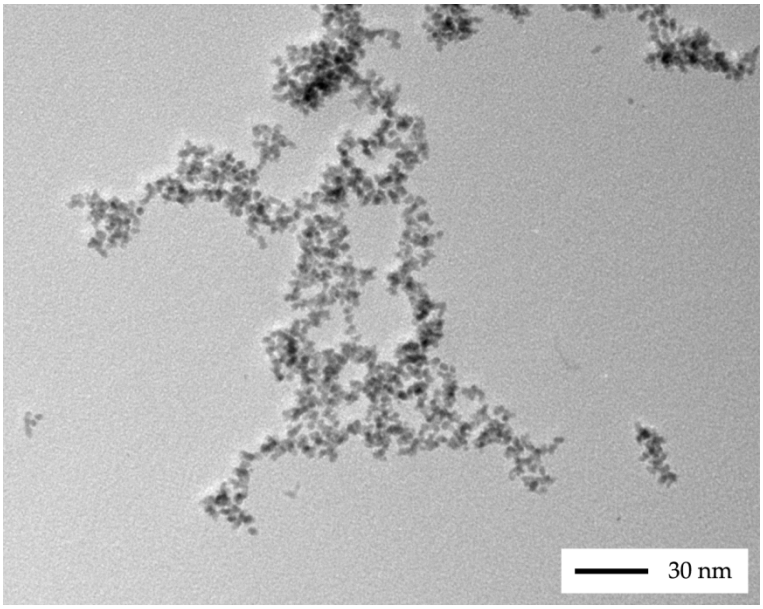

Figure 69: TEM micrograph of a PVA-protected rhodium sol reduced by borohydride in 10% v/v DMF.

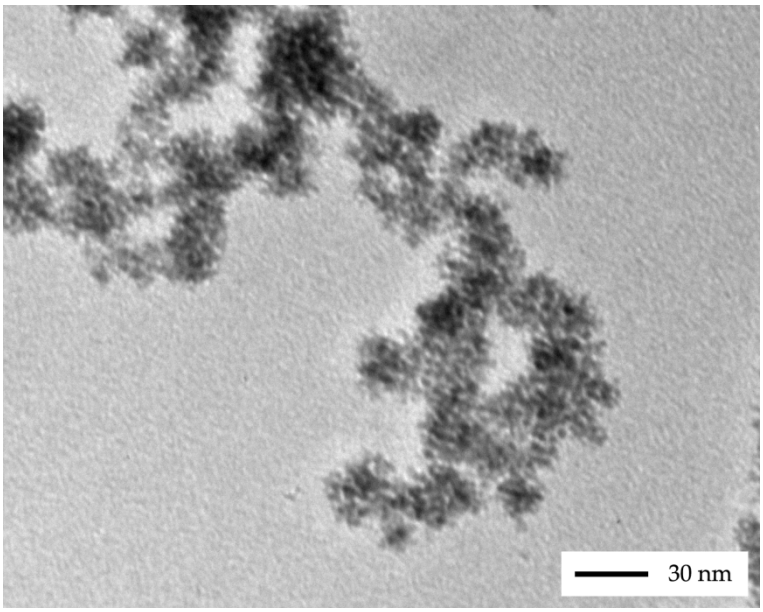

Figure 70: TEM micrograph of PVA-protected rhodium sol reduced by borohydride in 70% v/v DMF.

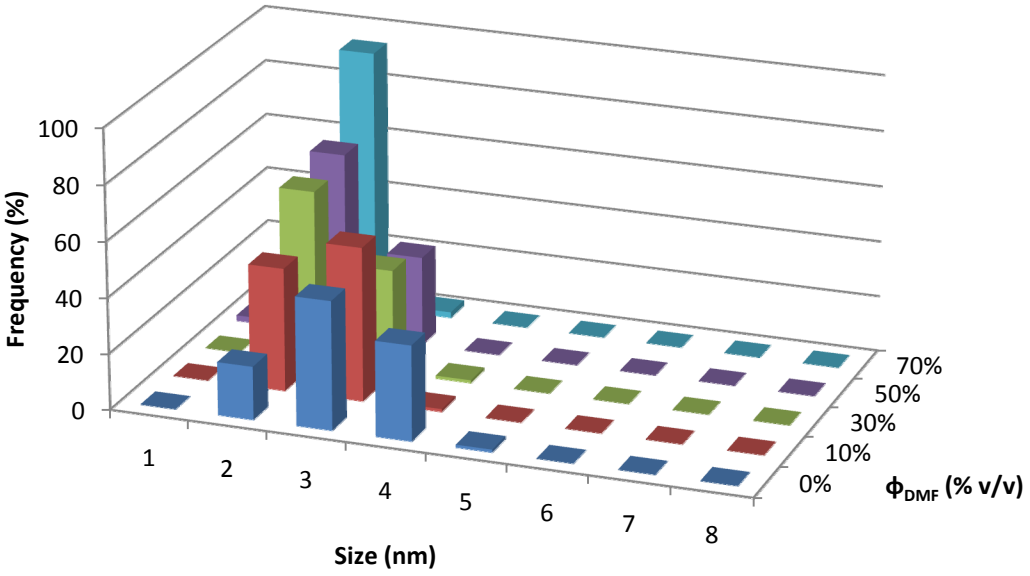

Figure 71: 3D PSD obtained by TEM for PVA-protected rhodium sols reduced by borohydride in mixtures of water and DMF, showing the evolution of the PSD with ϕ_{DMF}.

5.4.2.3 PAA-Protected Sols

At low DMF concentrations the particles in the PAA-protected rhodium sols existed predominantly as aggregates with extensive loosely-associated branched morphologies several particles in width. A typical micrograph is shown in Figure 72. These were similar to the loose associations of particles observed in the PAA-protected hydrosol, where the association was assumed to be due to H-bonding interactions. The presence of DMF probably interrupted the H-bonding network, causing the change in morphology. As the DMF concentration was increased the aggregates became progressively smaller, until at 70% ϕ_{DMF} only primary particles were observed.

The morphology of the primary particles at low DMF concentrations was rounded but eccentric. The majority were necklaced together with other primary particles to create even more irregular morphologies, similar to the primary particles of PVP- and PVA-protected sols in mixtures of water and DMF. As the DMF concentration was increased the necklacing was

suppressed, and the primary particles became more spherical in morphology. The size of the particles decreased 56% across the composition range studied, dropping from 2.5 nm in the control experiment with 0% ϕ_{DMF} to 1.1 nm in 70% ϕ_{DMF}. A 3D PSD showing the change in the PSD with ϕ_{DMF} is shown in Figure 73. As with the PVP-protected rhodium sols in mixtures of water and DMF, the drop in $\bar{x}$ was sharp initially and then slow and linear.

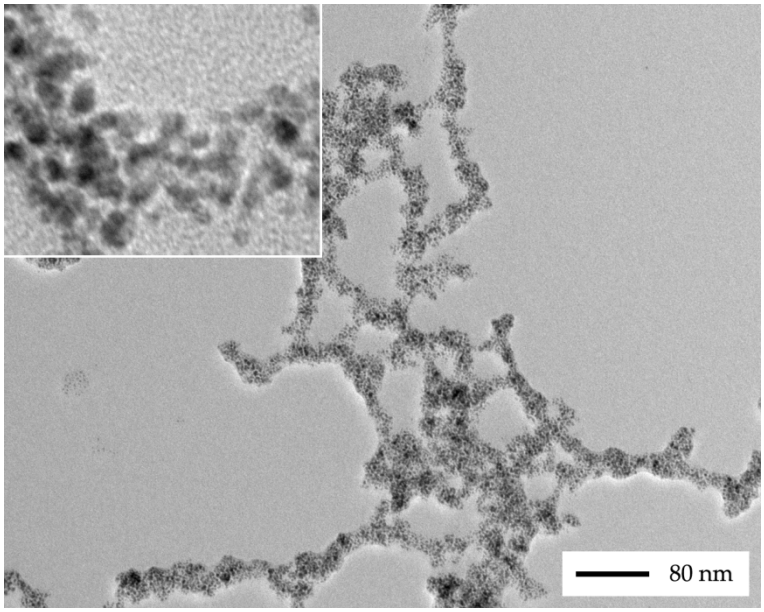

Figure 72: TEM micrograph of a PAA-protected rhodium sol reduced by borohydride in 10% v/v DMF. Inset: higher magnification of the same sol.

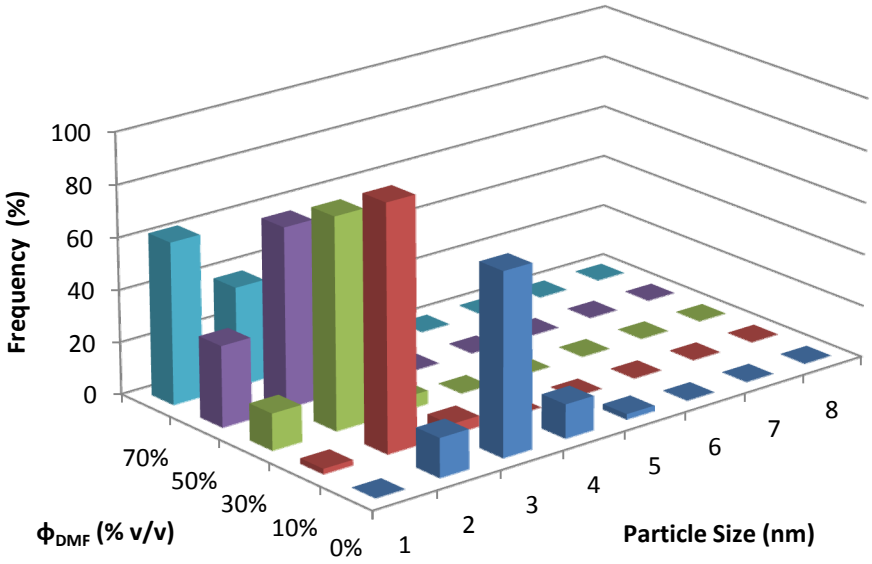

Figure 73: 3D PSD obtained by TEM for PAA-protected rhodium sols reduced by borohydride in mixtures of water and DMF, showing the evolution of the PSD with ϕ_{DMF}.

5.4.2.4 ARG-Protected Sols

For ARG-protected rhodium sols reduced by borohydride in mixtures of water and DMF, at low DMF concentrations the particles existed predominantly as large aggregates several hundred nanometres in size with loosely-associated but 'well-bunched' structures. A micrograph showing an example of a smaller but similarly structured aggregate is given in Figure 74. As the DMF concentration was increased these aggregates remained, but more discrete primary particles were observable.

In all cases the primary particles were heavily necklaced with one another into groups of 2 – 10 particles, producing irregular 'blobby' morphologies. The level of necklacing was the same at all DMF concentrations. The size of the primary particles, measured as if they were not necklaced, decreased 36% across the composition range studied, dropping from 2.8 nm in the ARG-protected hydrosol containing 0% ϕ_{DMF} to 1.8 nm in the sol generated in 50% ϕ_{DMF}. A 3D PSD showing the change

in the PSD with ϕ is shown in Figure 75. Note how the modal size class shifts from 4 nm at 0% v/v DMF to 2 nm at 50% v/v DMF.

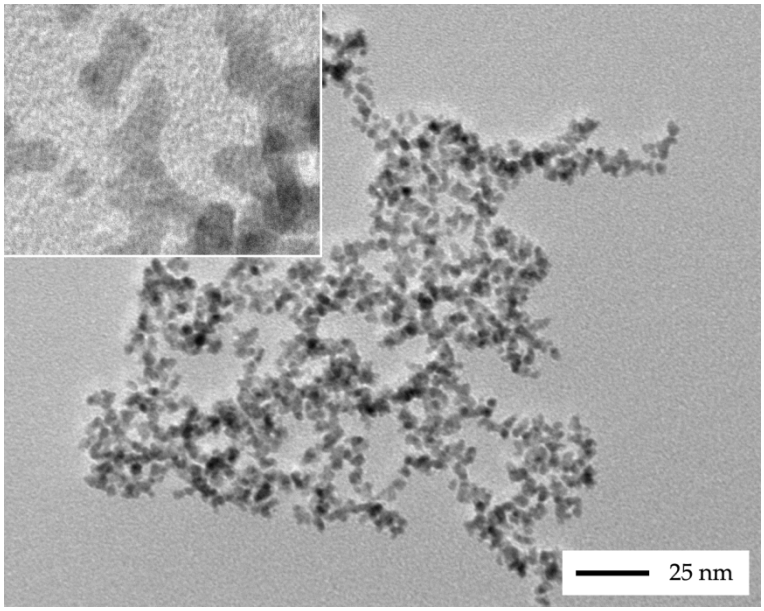

Figure 74: TEM micrograph of an ARG-protected rhodium sol reduced by borohydride in 30% v/v MeOH.

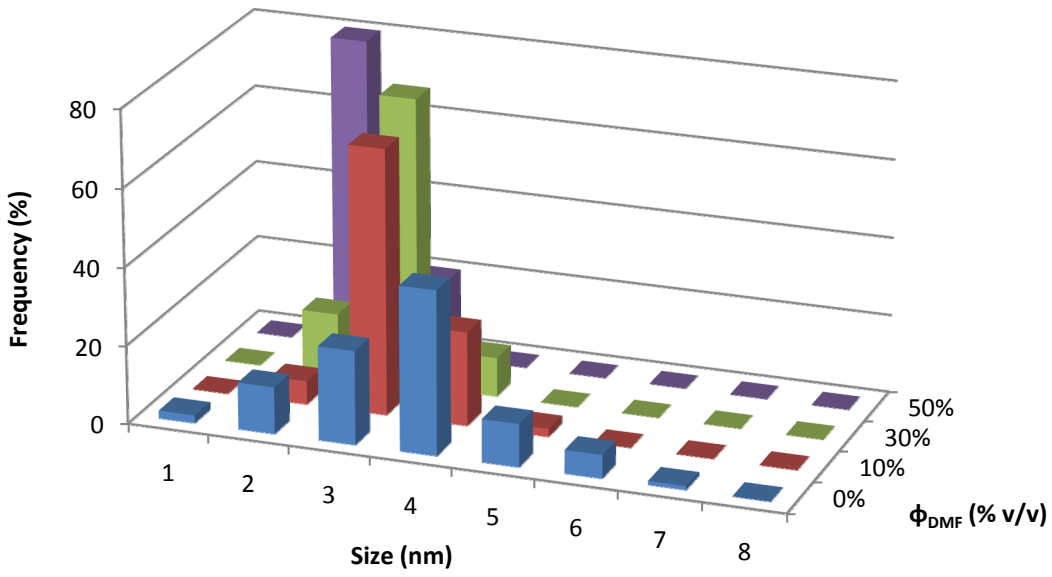

Figure 75: 3D PSD obtained by TEM for ARG-protected rhodium sols reduced by borohydride in mixtures of water and DMF, showing the evolution of the PSD with ϕ_{DMF}.

5.4.3 UV/Vis Data

A plot of the A_{450} values versus ϕ_{DMF}, shown in Figure 76, reveal that the density of borohydride-reduced rhodium sols in mixtures of water and DMF behaved similarly to those of other solvents in that there was a sharp decrease in the sol density upon addition of a small amount of the cosolvent. This can be easily rationalised in terms of the particle size, as $\bar{x}$ was also shown by TEM to have dropped sharply initially. Because the scattering intensity has a dependence to the sixth power on particle size, this initial drop should be much steeper in the A_{450} vs ϕ_{DMF} plot, which is exactly what was observed. Similarly where the PVP-protected sols had the highest particle size they had the largest A_{450} values, and where the PAA-protected sols had the smallest particle size they similarly had the smallest A_{450} values, which further supports the dependence of the A_{450} values on $\bar{x}$.

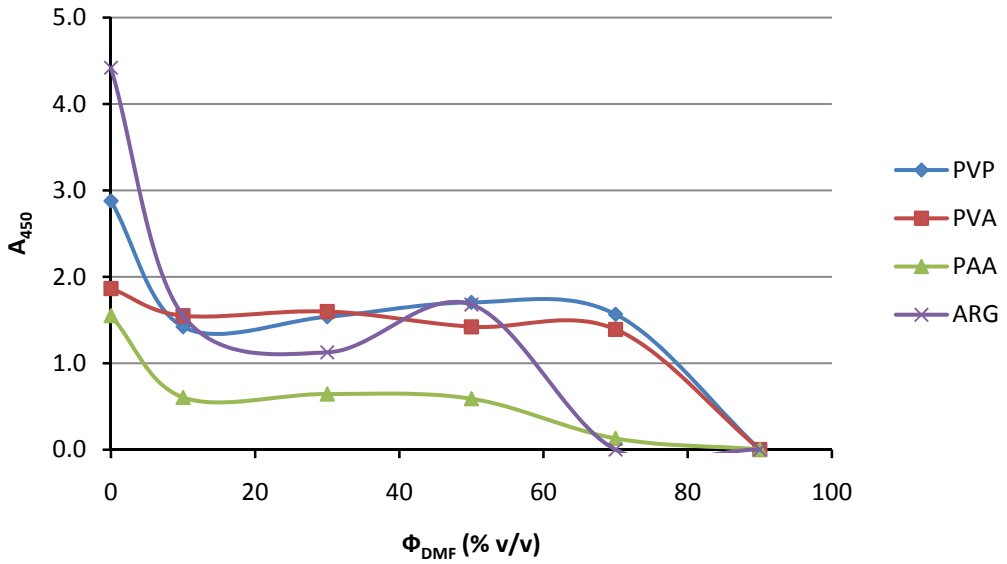

Figure 76: Plot of the dilution-corrected A_{450} values versus ϕ_{DMF} for protected rhodium sols reduced by borohydride in mixtures of water and DMF.

Where the plot differs from other cosolvents however is that the sol density remained relatively stable as ϕ_{DMF} is increased, until the aforementioned point where a colloid ceased to be produced. There were some deviations of *ca.* 0.5, however these were relatively small compared to the deviations observed in other systems. From this data one may reasonably assume that there were no large differences in the state of aggregation of the primary particles with one another, as this would have caused large changes the absorbance. This supports the notion that the majority of the aggregates observed in the TEM micrographs were either formed during the heptane extraction or during dehydration, and were not present *in-situ*. Hydrodynamic data suggests that there are small changes in the radius of gyration of PVP at least, which is perhaps responsible for the small changes in the levels of aggregation observed at intermediate compositions in the TEM micrographs.

5.4.4 PCS Data

The plot of the average hydrodynamic size (x_{PCS}) versus ϕ_{DMF}, shown in Figure 77, also reveals similar behaviour to that observed in other systems, in that there was a mild increase in radius with ϕ_{DMF} until a sharp peak, accompanied by a sudden decrease back to smaller values as ϕ_{DMF} was increased.

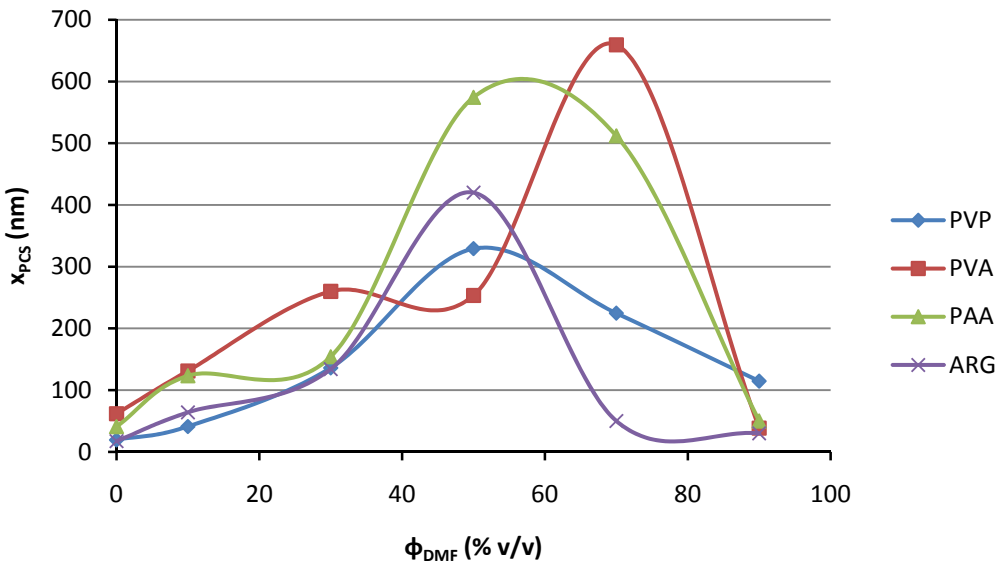

Figure 77: Plot of A_{450} versus ϕ_{DMF} for protected rhodium sols reduced by borohydride in mixtures of water and DMF.

One would expect that if the radius of the particles was to increase to such great of an extent then the A_{450} values would increase proportionally, however this is not observed experimentally. Empirically an increase in particle (or rather, aggregate) size was observed, with colloids generated in intermediate compositions (*ca*. 50% ϕ_{DMF}) typically being darker initially and more precipitated later. We may perhaps assume then that the massive spikes at intermediate compositions in the PCS vs ϕ plots are a result of:

1. Partially a result of small (real) aggregations of particles, which are exaggerated by the increase sensitivity of large particles compared to small ones,

2. Partially a result of the inadequacy of the assumptions used in generating the relevant data parameters required to be input to the Zetasizer (viscosity and refractive index), and:

3. Partially because PCS was always performed after UV/Vis analysis, often days afterward due to its more time-consuming nature, giving particles more time to aggregate.

5.5 Sols in Aqueous Acetonitrile

All syntheses of rhodium colloids in aqueous acetonitrile behaved similarly to those in aqueous dimethylsulfoxide, instead of producing black/brown Rh^0 colloids they yielded homogeneous yellow solutions.

Addition of the aqueous protecting agent to the rose-red dilute aqueous solution of $RhCl_3$ caused a slight darkening of the solution, indicating coordination of the protecting agent to the metal salt precursor, or some similar interaction capable of inducing a colour change. Addition of the MeCN to the solution then caused it to become redder in colour, indicating a reaction between the MeCN molecules and the metal salt precursor. Acetonitrile is known to be an excellent ligand for the 4d transition metals, with Rh-MeCN coordination complexes being prepared easily by refluxing the metal and the acetonitrile in some anhydrous solvent or some similar process [137-138]. In the presence of water it is likely that the resulting complex contains a mixture of acetonitrile and aquo ligands, and in the absence of forcing conditions it is likely that not all of the aquo ligands will be replaced. The reaction is a thus assumed to be a ligand-exchange reaction, illustrated in Figure 78.

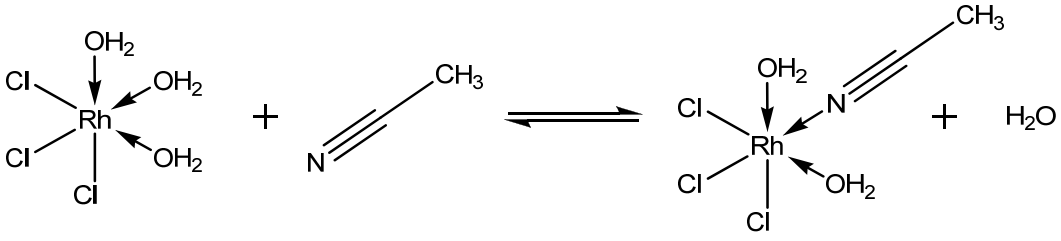

Figure 78: Ligand-exchange reaction between H_2O and MeCN on $RhCl_3$.

Addition of aqueous borohydride caused the solutions to shift gradually from a dilute rose-red to a canary yellow, presumably from a decrease in

oxidation state and loss of chloride ligands as described in previously referenced studies, and as shown in Figure 79.

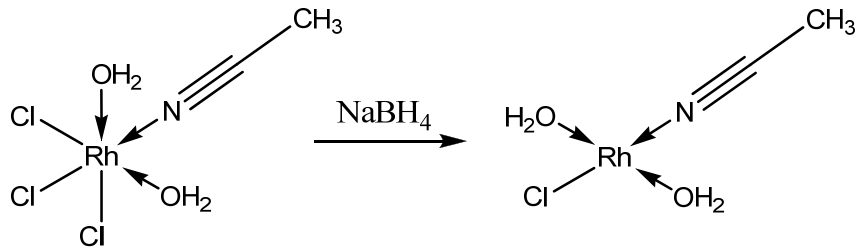

Figure 79: Reduction reaction of a rhodium MeCN complex.

It should be noted that this is purely a hypothetical structure, based on a small amount of empirical observation. Attempts to detect the complex spectroscopically by ESI-MS were met with failure, the resulting spectra being excessively complex and therefore of limited value in interpreting the composition of the solution. Examples of the positive and negative ion mode spectra are shown Figure 80 and Figure 81. As with the DMSO system, the negative ion mode spectra were relatively simple and displayed only one prominent peak at 249 m/z, however the positive ion spectra showed multiple peaks, the most prominent being the 171 m/z and the 237 m/z. What these did indicate however was that there was a wide variety of high-mass species created, the masses of which probably could not be accounted for without invoking the presence of some kind of polynuclear Rh species. A variety of coordinatively unsaturated rhodium complexes have been shown to spontaneously polymerise through weak metallophilic interactions [139], or may perhaps form by chloride-bridging.

Cursory attempts to isolate crystals by volumetric reduction were unsuccessful. Gradual heating eventually yielded crystals, however upon filtering these crystals disappeared by some kind of apparently ‘evaporative process’, and releasing more filtrate. This may have been

because they were unstable in air as they were charged and required a counterion, or were unstable to disproportionation into the free solvent MeCN and the precursor metal salt.

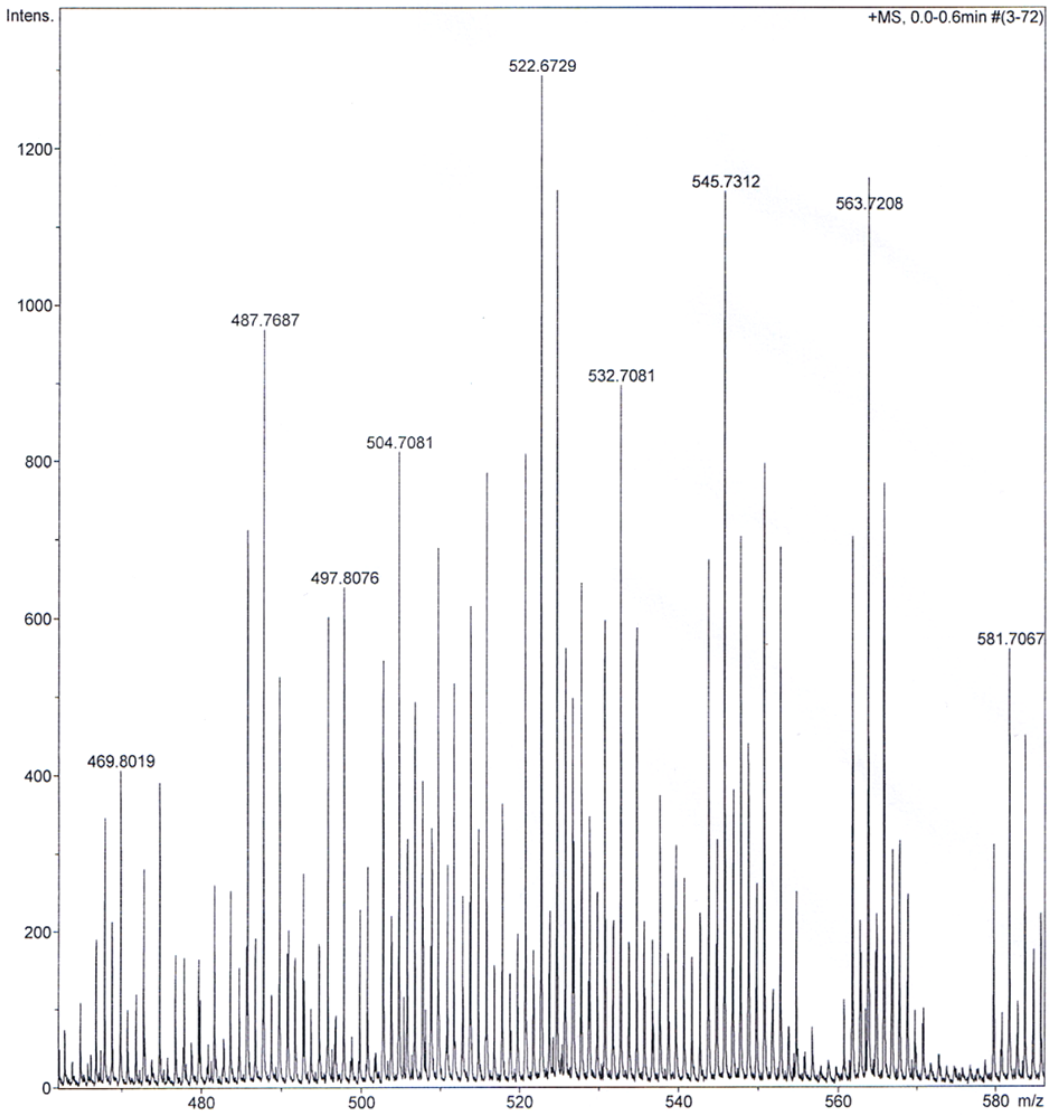

Figure 80: ESI-MS spectra of a reduced solution of $RhCl_3$ in aqueous MeCN in positive ion mode.

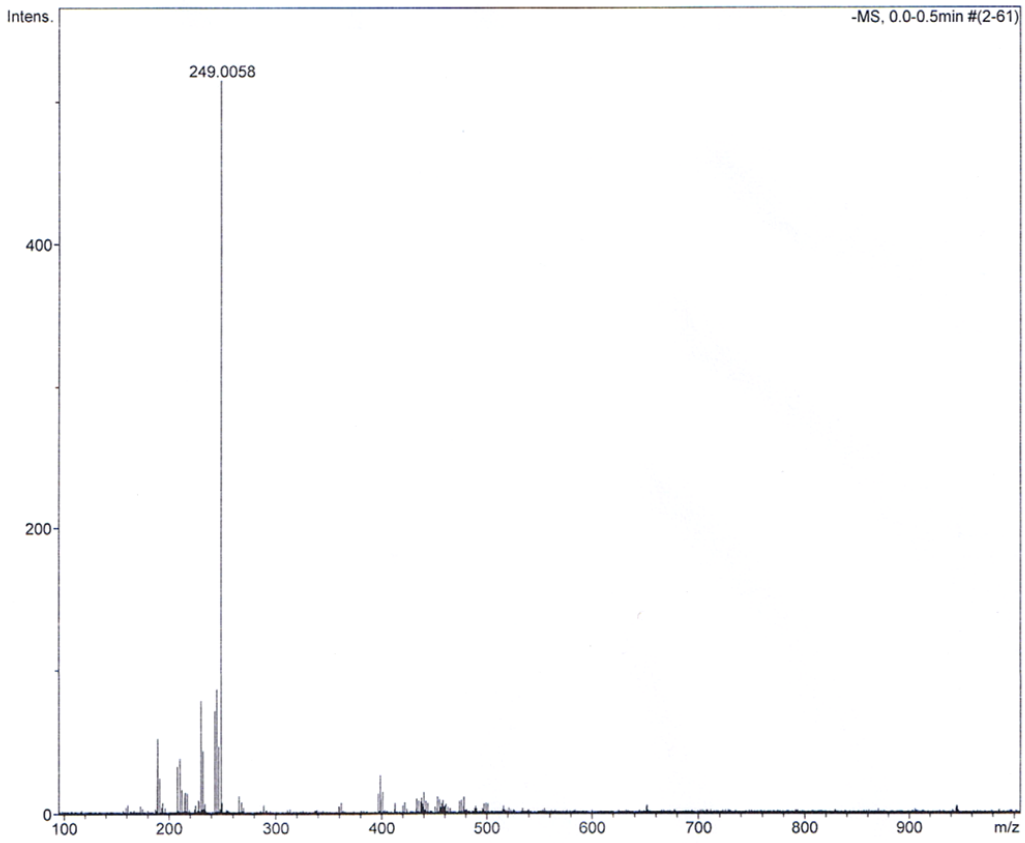

Figure 81: ESI-MS spectrum of a reduced solution of $RhCl_3$ in aqueous acetonitrile in negative ion mode.

5.6 Sols in Aqueous Acetone

The synthesis of protected rhodium sols in aqueous acetone suffered to such a great extent from protecting agent precipitation that it was decided to abandon their characterisation. PVP and PAA became precipitated from solution at 30% v/v acetone, and PVA and ARG were precipitated at 10% v/v acetone. Because of this, so little data could be gathered that any trends formulated would have been statistically insignificant. It should be noted however that unlike MeCN or DMSO, reduction of the precursor metal salt in aqueous acetone was feasible.

5.7 Sols in Aqueous Tetrahydrofuran

Protected rhodium sols in aqueous tetrahydrofuran behaved identically to those in acetone, causing the protecting agent to be precipitated from solution at low THF concentrations. Because of this the characterisation of the sols generated in aqueous THF was abandoned. As with acetone the reduction of the precursor salt was possible, but pointless given the protecting agent precipitation which precluded the formation of many stable colloids.

5.8 Attempts at ^{103}Rh NMR

^{103}Rh NMR of rhodium colloids was attempted, but met with great failure. A 1 mol L^{-1} $RhCl_6^{3-}$ standard was produced by dissolution of the appropriate amount of rhodium chloride in hydrochloric acid. No probe was available with a sufficiently low frequency range, so broad-band probe was used at its lowest allowable frequency on a 300 MHz spectrometer. After 3 days of scanning no signal was found, presumably due to the insensitivity caused by low receptivity and high relaxation time of the ^{103}Rh nucleus. Further rhodium NMR was abandoned.

Chapter 6: Palladium Mixed-Media Sols

Despite the relatively close position of palladium to rhodium in the periodic table, its chemical behaviour with respect to the formation of sols in mixed-media was observed to be radically different. Two obvious disparities were found between the two elements. The first was that the reduction of $[PdCl_4]^{2-}$ in strongly coordinating solvents such as DMSO and MeCN was found to be feasible, unlike the reduction of $RhCl_3$ under equivalent conditions. While the Pd sols in DMSO were relatively stable, the sols generated in MeCN were not stable and consequently were not characterised. The second disparity was that Pd was able to be reduced spontaneously by hydrazine, whereas rhodium was not. Because of these two factors significantly more data was able to be collected for the Pd sols than the Rh sols.

The data collected for the Pd sols generated in mixed-media indicated that their behaviour was otherwise similar to Rh sols generated under equivalent conditions, with $\bar{x}$ and σ both inversely proportional to ϕ. Generally $\bar{x}$ for the palladium sols was larger than for their rhodium counterparts, and generally the changes in $\bar{x}$ as ϕ was increased were larger. The levels of aggregation observed in the TEM micrographs was as unpredictable for the palladium sols as it was for the rhodium sols, however the morphology of the aggregates formed was different between the two elements.

Solubility issues were encountered again with the PVA and ARG protecting agents, which behaved identically to their use in the preparation of Rh sols in mixed media.

6.1 Hydrosols

6.1.1 Borohydride-Reduced Hydrosols

6.1.1.1 General Remarks

When palladium hydrosols were prepared in pure water in the absence of a protecting agent, their behaviour was observed to be similar to rhodium sols produced under equivalent conditions. Addition of the reducing agent instantly caused a swirl of black particles to be formed in solution, indicating reduction of the $[PdCl_4]^{2-}$ precursor from Pd^{II} to Pd^0. The resulting colloid was unstable, aggregating and completely sedimenting within minutes of preparation to form a precipitate of palladium black. A photograph of this sol and the four sols generated using protecting agents is shown in Figure 82.

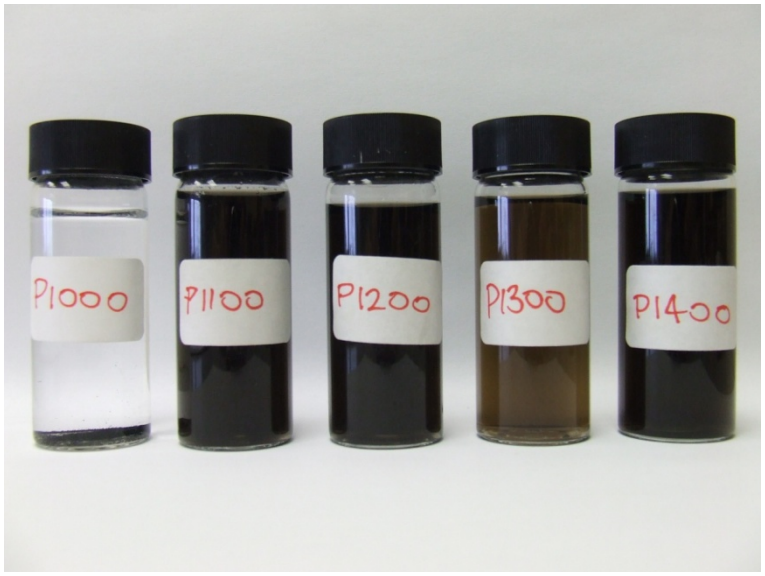

Figure 82: A photograph of five borohydride-reduced palladium hydrosols with different protecting agents. From left to right: no protecting agent, PVP, PVA, PAA, ARG. The labels on the vials refer to their conditions of synthesis, as described in Appendix 1.

When protecting agents were used in the synthesis, all four were shown to be effective in maintaining the state of colloidal dispersion. Sols protected by PVA and PAA remained completely stable for approximately

6 months, while those protected by PVP and ARG were stable for only several weeks. The time taken for the reaction solution to darken indicating reduction of the precursor was observed to be longer than when protecting agents were not used, just as was observed for the equivalent rhodium sols.

The colours of the final sols were similar to those of rhodium, with PVP- and ARG- protected hydrosols appearing pitch black, and PVA- and PAA-protected hydrosols appearing dark and light brown respectively. This was again found to be reflective of the particle size. A summary of the measurements taken supporting this is given in Table 13.

	TEM		PCS	UV/Vis
Protecting Agent	$\bar{x}$ (nm)	σ (nm)	x_{PCS} (nm)	A_{450}
PVP	4.4	1.1	81.5	3.15
PVA	2.5	0.5	42.4	3.03
PAA	2.3	0.6	34.5	1.56
ARG	2.8	0.7	63.6	2.99

Table 13: Summary of the PCS, TEM and UV/Vis data obtained for borohydride-reduced palladium sols.

6.1.1.2 TEM Data

6.1.1.2.1 PVP-Protected Sols

TEM analysis of the PVP-protected palladium hydrosols reduced by borohydride in water showed that they were similar in character to the equivalent rhodium hydrosols. They generally exhibited well-dispersed primary particles which were easily discerned in the micrographs, along with small necklaced strings of 2-10 fused primary particles. Few non-necklaced aggregates were visible, and if present consisted of only 2-3 primary particles. In either case the primary particles were either round or

semi-round, with little deviation from this morphology. They possessed the largest particle size (4.4 nm) and standard deviation (1.1 nm) of the protected palladium hydrosols, similar to rhodium although smaller comparatively. A typical micrograph is shown in Figure 83.

6.1.1.2.2 PVA-Protected Sols

PVA-protected palladium hydrosols generated by borohydride reduction in water behaved similarly to the equivalent rhodium sols, appearing stable macroscopically but exhibiting large micron-sized aggregates in the TEM micrographs which were difficult to image. As with the PVA-protected rhodium sols, these aggregates were assumed to have formed during dehydration rather than existing *in-situ*. This was again supported by the relatively small hydrodynamic size measured by PCS and the low turbidity as indicated by the A_{450} value.

In areas around the edges of these aggregates where primary particles could be discerned, they displayed rounded morphologies with little variation. The average particle size was 2.5 nm and the standard deviation was 0.5 nm (see Table 13), the second smallest of the protected palladium hydrosol group. This is reflective of the sol being the second lightest-coloured of the group, indicative of its relatively smaller particle size. A typical micrograph is shown in Figure 83.

6.1.1.2.3 PAA-Protected Sols

PAA-protected palladium hydrosols generated by borohydride reduction in water did not occur in small groups as per the rhodium equivalents, rather discrete primary particles were dispersed homogeneously across the grid. No particle necklacing was evident, although small amounts of aggregation was present, consisting of clusters of 2-5 primary particles. They were the smallest particles of the hydrosol

control group with an average particle size of 2.3 nm and a standard deviation of 0.6 nm, reflective of the very light colour of the final sol. A typical micrograph is shown in Figure 83.

6.1.1.2.4 ARG-Protected Sols

ARG-protected palladium hydrosols produced by borohydride reduction in water have been prepared and reported previously by Mucalo *et al.* [90] albeit under slightly different synthetic conditions to those used in this study. It was found that arabinogalactan was an excellent protecting agent for palladium sols, as reported in previous studies. The dispersion of particles observed in the TEM micrographs appeared similar, grouping into small non-necklaced chains of particles approximately 50 nm – 100 nm in length. The primary particles themselves were smaller and less eccentric in their morphologies than previously reported [90]. Very little aggregation was observed, and those aggregates which did exist were very small, consisting of a maximum of 2 - 3 non-necklaced particles. ARG-protected sols exhibited the second-largest particle size of the protected palladium hydrosol group, with an average size of 2.8 nm and a standard deviation of 0.7 nm. A typical micrograph is shown in Figure 83. Unfortunately the micrographs collected for this preparation were not of the highest possible quality, again due to the poor condition of the TEM column used and the quality of its alignment, factors which were out of control of the users of the instrument.

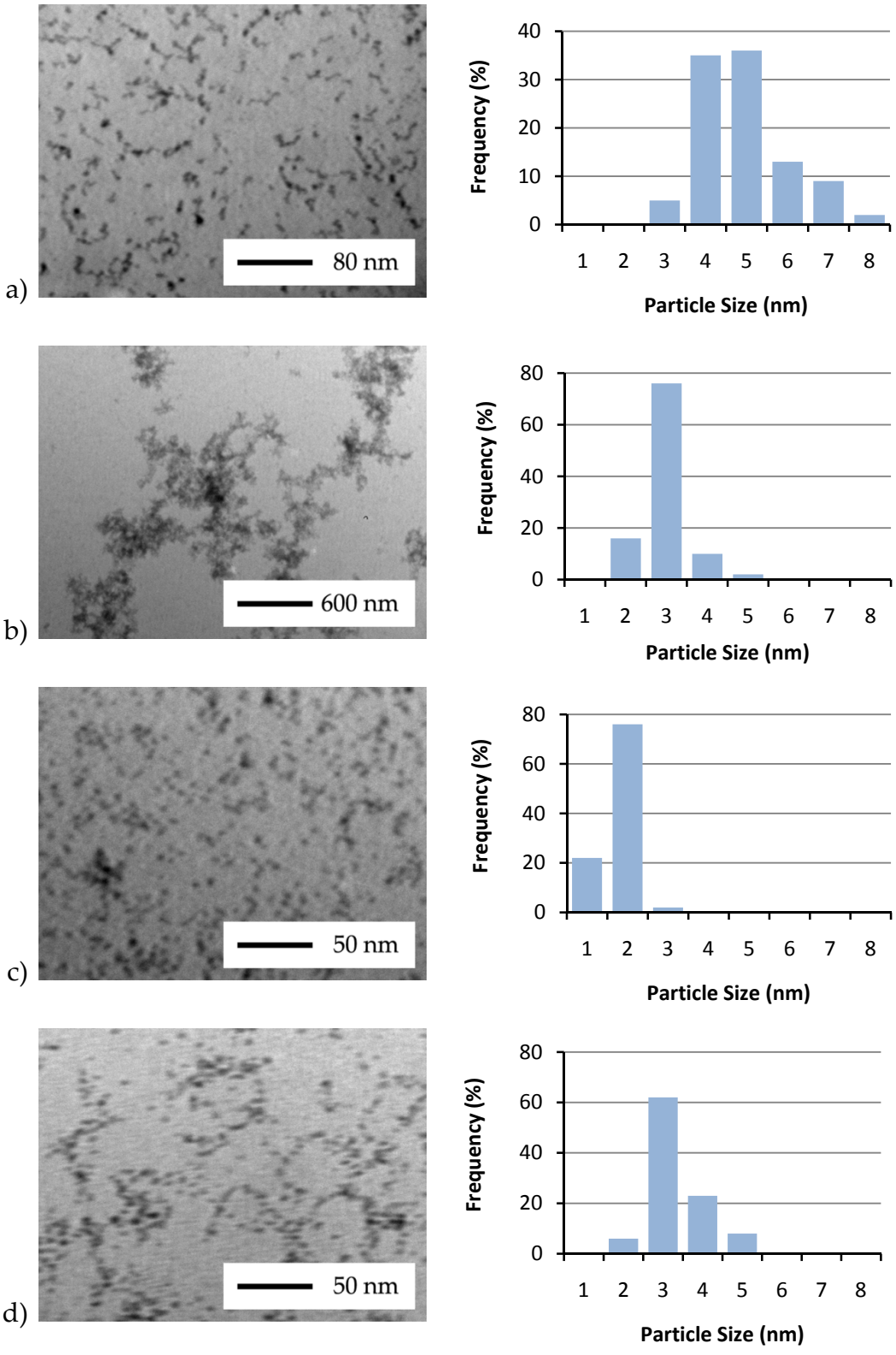

Figure 83: TEM micrographs and their accompanying particle size distributions for palladium colloids reduced by borohydride in water and protected by a) PVP, b) PVA, c) PAA and d) ARG.

6.1.1.3 UV/Vis Data

The UV/Vis data obtained for protected palladium hydrosols indicated that they all possessed similar A_{450} values (≅ 3), except for the PAA-protected sol whose value was approximately half of this. Given the significantly larger size of the PVP-protected particles (4.4 nm) compared to the PVA- or ARG- protected particles (2.5 nm and 2.8 nm respectively), the similarity in the A_{450} values indicates that the PVP-protected sol must have had significantly less aggregation *in-situ* compared to the PVA- or ARG- protected sols. This data also supports the idea that the large aggregates which were observed in the TEM micrographs for the PVA-protected palladium hydrosol were formed during dehydration and did not exist in situ. Because the A_{450} value of the PAA-protected sol was even lower, this was taken to indicate that it possessed even less aggregation *in-situ* than the others. This is supported by the PCS data (see later). A plot showing the relative size of the A_{450} values for each preparation is shown in Figure 84.

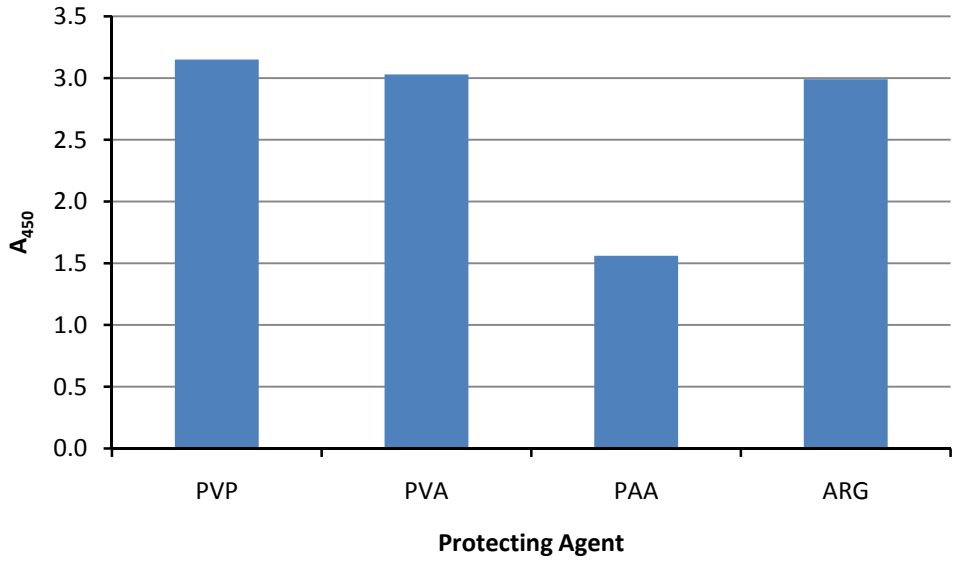

Figure 84: Plot of the dilution-corrected A_{450} values for protected rhodium hydrosols reduced by borohydride in water.

Although the colour of the sols and the A_{450} values are theoretically a good indicator of particle size when little aggregation exists *in-situ*, this did not completely exclude the possibility that the size of the particles generated when the different protecting agents were used was caused by differences in the level of reduction. For the PVA- and PAA- protected sols this was probably a factor, as the UV/Vis spectra indicated the presence of a small amount of unreduced precursor, however the size of the precursor peaks were not sufficiently large to explain the relatively smaller particle sizes, hence the smaller size of the PVA- and PAA- protected sols is probably a combination of decreased reduction levels and 'real' effects caused by the specific characteristics of the protecting agents used. For example the PAA used had a smaller molecular mass than the other protecting agents of approximately 2000 g mol^{-1}, therefore as the protecting agent is added by mass, more chains were be added. Because there were more chains, there were more sites for nucleation of particles, hence particles would have been generated in larger numbers but would have been smaller in size.

6.1.1.4 PCS Data

The PCS data indicated that the hydrodynamic sizes of the protected palladium hydrosols ranged from approximately 35 nm to 80 nm. A plot comparing the values is shown in Figure 85.

The largest value was exhibited by the PVP-protected sol, which was probably attributable to its much larger molecular mass, which would limit its hydrodynamic mobility. ARG-protected sols had the next lowest hydrodynamic diameter (63.6 nm), followed by the PVA-protected sols (42.4 nm) and PAA-protected sols (34.5 nm). This data is consistent with both the decreasing particle size as observed by TEM and the levels of aggregation observed, with the relative molecular masses of the protecting

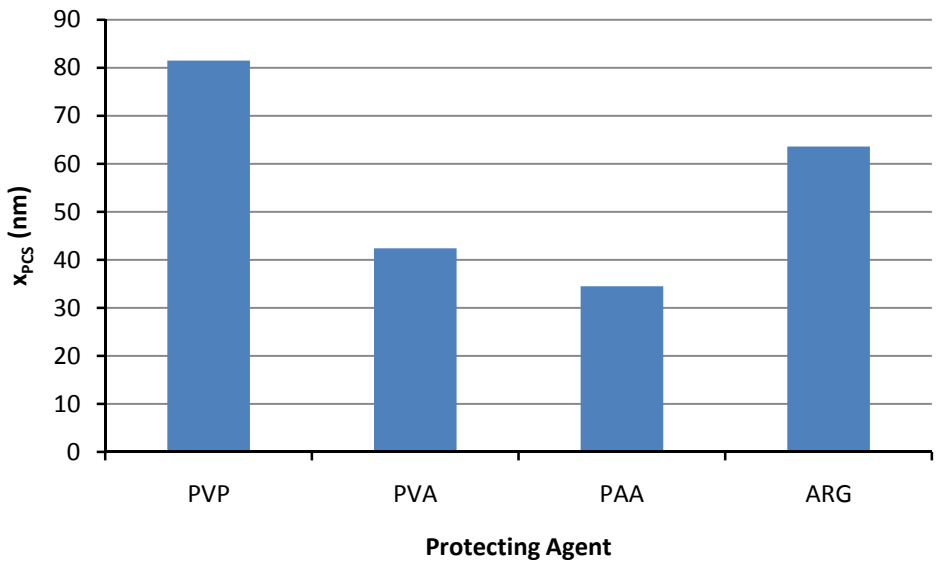

Figure 85: Plot of the x_{PCS} values for protected palladium hydrosols reduced by borohydride in water.

agents used (PVP nominally being 700,000 g mol^{-1} and PAA being 2000 g mol^{-1}), and with the colours of the sols being an indicator of the relative particle size *in-situ*.

6.1.2 Hydrazine Reduced Hydrosols

6.1.2.1 General Remarks

Compared to $RhCl_3$, it was found that $[PdCl_4]^{2-}$ could spontaneously be reduced to colloidal palladium by hydrazine reduction in pure water. In general the resulting sols possessed both smaller particle sizes and smaller standard deviations than the corresponding borohydride-reduced palladium sols, although they were less stable and their aggregates were larger. No comparisons could be drawn with the equivalent rhodium sols because rhodium could not be reduced by hydrazine, as mentioned earlier. A summary of the data collected for these sols is shown in Table 14.

	TEM		PCS	UV/Vis
Protecting Agent	$\bar{x}$ (nm)	σ (nm)	x_{PCS} (nm)	A_{450}
PVP	2.5	0.6	27.0	0.93
PVA	2.7	0.7	65.0	0.60
PAA	No colloid formed			
ARG	2.7	0.7	28.2	1.15

Table 14: Summary of the PCS, TEM and UV/Vis data obtained for hydrazine-reduced palladium sols.

Their synthesis was much the same as the borohydride-reduced Pd and Rh sols, except for one major factor. Hydrazine reduction of $[PdCl_4]^{2-}$ yielded colloidal palladium in all cases *except* when PAA was used as a protecting agent. Upon addition of hydrazine to a reaction mixture containing PAA no darkening of the solution was observed, *viz.*, reduction to Pd^0 did not occur. Evolution of gas was also observed. Addition of a large excess (*ca.* 10 mL) of 99% hydrazine eventually yielded a colloidal Pd, however it was unstable and sedimented within minutes. Attempts to produce a palladium sol protected by PAA pre-treated with hydrazine yielded a similarly unstable colloid. This indicates that the hydrazine molecules were probably reacting preferentially with the PAA molecules and deactivating their protective ability, which is why the colloid generated after an excess of hydrazine was added was unstable.

A possible mechanism for this phenomenon is a condensation reaction between the two molecules, specifically nucleophilic acyl substitution. The hydrazine nitrogens were presumed to have attacked the carbonyl carbons in the PAA molecules, forming a poly(acrylic acid hydrazide) (PAAH), or similar derivative. There are reports in the literature of monoacrylic acid hydrazides synthesised by direction combination of the two reagents;

although these are generally performed under different synthetic conditions. A reaction scheme is shown in Figure 86.

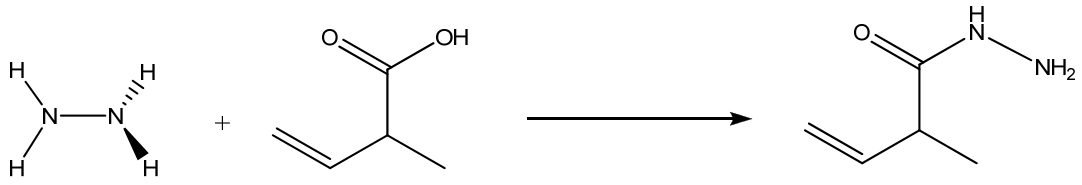

Figure 86: Reaction of acrylic acid with hydrazine.

It was hypothesised that although PAA does not possess an identical structure to acrylic acid (polymerisation is present in lieu of the double bond), the key functional group (carboxylic acid) is present, allowing the reaction to proceed in an analogous fashion. It is possible that this reaction consumed all added hydrazine, rendering the metal precursor unreduced, accounting for the failure of the synthesis of hydrazine-reduced PAA-protected sols. The proposed reaction is shown in Figure 87. If all hydroxyl groups were replaced by bulkier R-NH-NH_2 groups then this also accounts for the loss of colloidal stability when eventually reduction was induced, as there would have been no hydroxyl functionalities to interact with the metal.

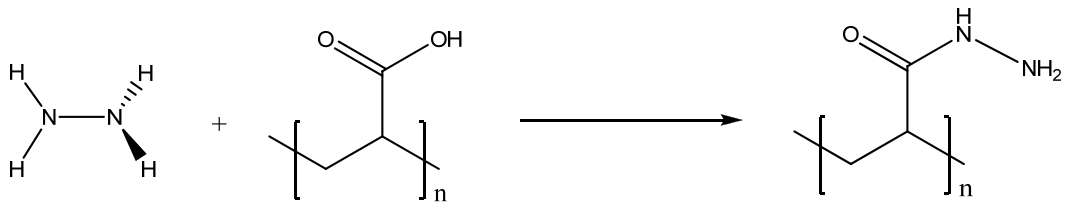

Figure 87: Hypothetical reaction of poly(acrylic acid) with hydrazine

6.1.2.2 TEM Data

6.1.2.2.1 PVP-Protected Sols

Palladium sols reduced by hydrazine protected by PVP were more difficult to image by TEM than their corresponding borohydride-reduced counterparts, exhibiting more densely packed particles in the micrographs, with more extensive particle necklacing. Few discrete primary particles were observable; rather they were all in the form of necklaced aggregates up to approximately 50 nm in length, composed of between 5 to 20 primary particles. Because of the extensive necklacing, significant difficulty was encountered in discerning and measuring exactly what constituted a primary particle. Those that were measured had an average particle size of 2.5 nm and a standard deviation of 0.6 nm, displaying rounded but eccentric morphologies, indicative of the necklacing process observed. A typical TEM micrograph is shown in Figure 88, along with micrographs showing the sols protected by the other two protecting agents.

6.1.2.2.2 PVA-Protected Sols

PVA-protected colloids formed similarly large aggregates to their borohydride-reduced equivalents, although they were much easier to image due to their more open structure. All particles appeared to possess some level of necklacing, with approximately half existing as small necklaced aggregates of 2-5 particles, and the other half existing as part of the much larger aforementioned aggregates, whose size appeared to be range from 200 nm - 1000 nm. The average particle size was measured to be 2.7 nm with a standard deviation of 0.7 nm. Although no discrete primary particles were observable, the shape of the aggregates indicates they would have been semi-rounded with no unusual morphological traits. A micrograph is shown in Figure 88.

a)

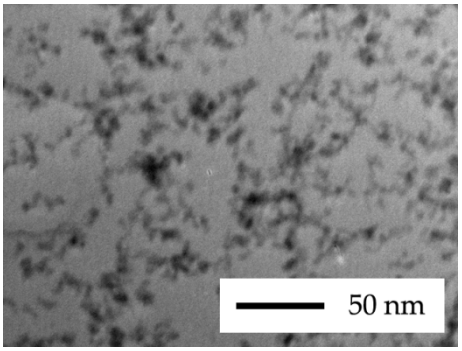

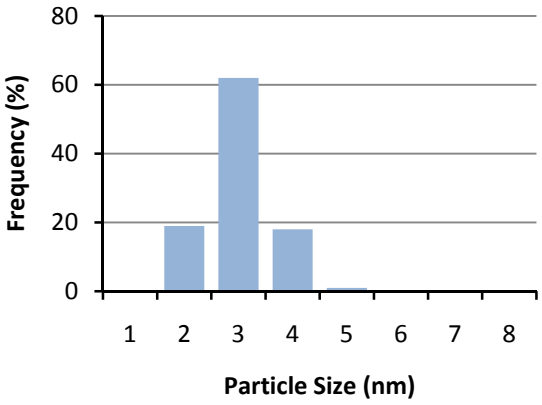

b)

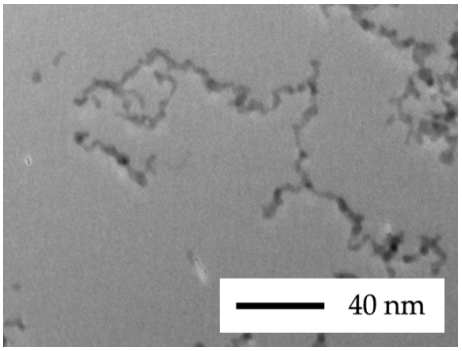

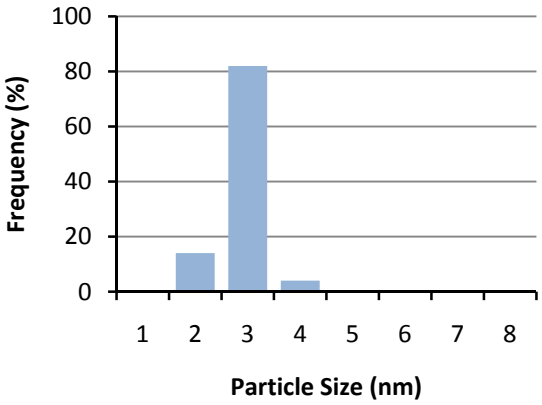

c)

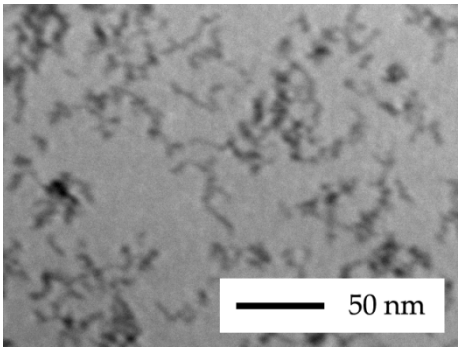

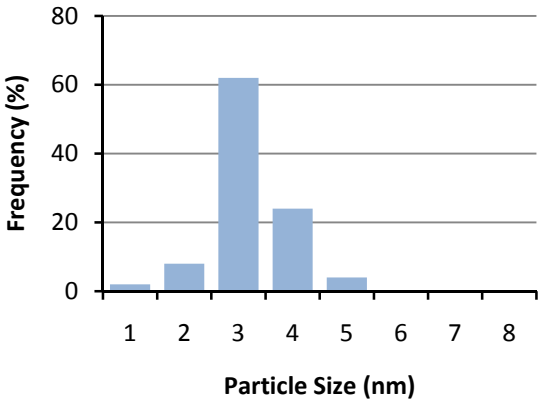

Figure 88: TEM micrographs and accompanying particle size distributions of palladium hydrosols reduced by hydrazine, protected with a) PVP, b) PVA, c) ARG.

6.1.2.2.3 ARG-Protected Sols

ARG-protected palladium hydrosols reduced by hydrazine in water exhibited similar morphological characteristics to their equivalents protected by PVP. It was observed that the particles occurred more densely than for the equivalent sols generated by borohydride reduction, making imaging more difficult. Few discrete primary particles were evident, with the majority of particles being necklaced into small strings of 2 - 10 particles. Measurements taken from the micrographs indicated that the particles were of the same size as those protected by PVA, with an average size of 2.7 nm and a standard deviation of 0.7 nm. A micrograph is shown in Figure 88.

6.1.2.3 UV/Vis Data

The UV/Vis data indicated that the hydrazine-reduced protected rhodium sols had a much lower turbidity than their corresponding borohydride-reduced equivalents, by a factor of approximately four-fold, with A_{450} values ranging from 0.6 for the PVA-protected sol to 1.15 for the ARG-protected sol. These values were curiously low, indicating that there was less aggregation *in-situ* compared to the borohydride-reduced sols, assuming similar levels of chemical reduction. The UV/Vis spectra did not indicate that there was any radical different between the hydrazine and borohydride-reduced sols in this respect, so the differences in the turbidity values were perhaps a result of the extensive necklacing of the particles combined with the smaller relative particle sizes, causing them to scatter light as if they were individual primary particles rather than large aggregates. A plot of the values is shown in Figure 89.

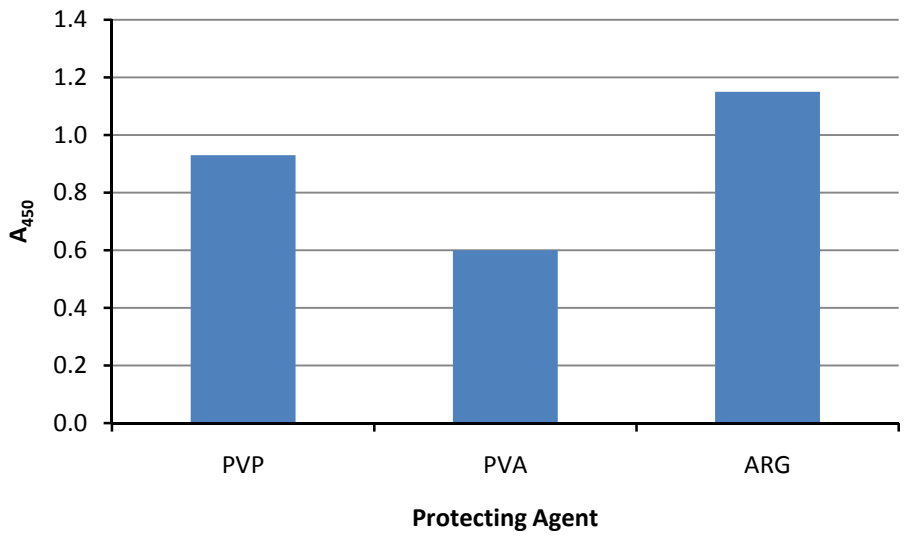

Figure 89: Plot of the dilution-corrected A_{450} values for protected palladium sols reduced by hydrazine in water.

6.1.2.4 PCS Data

The hydrodynamic diameters of the hydrazine-reduced protected palladium sols were similar in magnitude to those of their borohydride-reduced equivalents, falling between 27 nm for the PVP-protected sol and 65 nm for the PVA-protected sol. The hydrodynamic size of the PVP-protected sol was significantly smaller when reduced by hydrazine compared to borohydride, probably a result of the smaller primary particle size. The PVA-protected sol was significantly larger than the equivalent borohydride-reduced sol, reflective of the significant number of large necklaced aggregates as observed in the TEM micrographs. The ARG-protected sol was approximately half the size of its borohydride-reduced equivalent, which was surprising given the number of small necklaced aggregates observed in the TEM micrographs. This was perhaps a result of the comparative lack of the more densely-packed non-necklaced aggregates present in the borohydride-reduced sol, which may have shifted the hydrodynamic size upward. A plot illustrating the relative sizes is given in Figure 90.

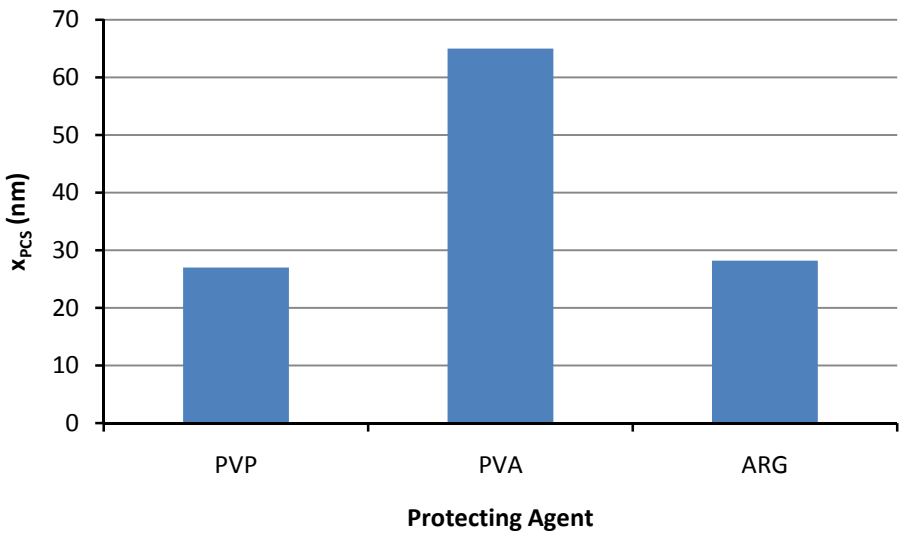

Figure 90: Plot of x_{PCS} for protected palladium hydrosols reduced by hydrazine in water.

6.2 Sols in Aqueous Methanol

6.2.1 Borohydride-Reduced Sols

6.2.1.1 General Remarks

Methanol was found to be as good a cosolvent for the synthesis of palladium mixed-media sols as it was for rhodium. Its behaviour as a cosolvent was similar to when it was used for rhodium sols, exhibiting all the same general trends. For those syntheses which successfully resulted in the production of colloidal palladium, $\bar{x}$ was clearly shown to be inversely proportional to ϕ_{MeOH}, which was easily reconciled with both the PCS and UV/Vis data collected. A summary of all the data collected for these sols is given in Table 15. Only a quarter of the preparations suffered from protecting agent precipitation due to the decreased solubility of the polymers in the mixed media, PVA above ϕ_{MeOH} values of 70% v/v and ARG above 50% v/v. Both PVP and PAA remained in solution at all times. It is of importance to note however that as one approaches the limits of solubility with a given protecting agent in the mixed-media (specifically ones like methanol with lower polarities), the cosolvent must be added slowly and carefully so as to avoid localised increases in cosolvent concentration in the reaction vessel which may prematurely precipitate the protecting agent.

When sols were synthesised in the mixed-media in the absence of a protecting agent, they were unstable and sedimented rapidly, just as they did for the unprotected palladium hydrosols. This indicates that the methanol molecules were neither large enough nor strongly enough binding that they could provide effective steric protection, nor were they more effective than water at providing a sufficiently large EDL to stabilise

		TEM		PCS	UV
Protectant	ϕ_{MeOH}	$\bar{x}$ (nm)	σ (nm)	x_{PCS} (nm)	A_{450}
PVP	10	4.4	0.9	24.8	3.65
	30	3.7	0.7	133.6	2.80
	50	2.9	0.5	25.0	2.50
	70	2.5	0.5	22.0	1.97
	90	2.1	0.4	48.3	1.87
PVA	10	1.8	0.3	90.0	3.10
	30	1.5	0.5	434.2	3.32
	50	1.4	0.4	156.8	2.35
	70	Protecting agent precipitated			
	90	Protecting agent precipitated			
PAA	10	2.0	0.6	48.8	1.90
	30	2.0	0.4	235.4	2.08
	50	1.9	0.5	774.5	1.76
	70	1.9	0.7	63.4	1.72
	90	1.5	0.4	77.9	1.70
ARG	10	2.5	0.6	35.6	3.14
	30	2.1	0.5	38.4	3.10
	50	Protecting agent precipitated			
	70	Protecting agent precipitated			
	90	Protecting agent precipitated			

Table 15: Summary of the mean and standard deviations in the particle size for palladium colloids reduced by sodium borohydride in the presence of methanol.

the resulting particles against aggregation, unsurprising given the low dielectric constant of MeOH ($\varepsilon = 33.0$) relative to water ($\varepsilon = 80.1$) [131].

As previously described with rhodium sols, the time taken for the solution to darken indicating reduction of the $[PdCl_4]^{2-}$ precursor was proportional to ϕ_{MeOH}. This was the case with all four protecting agents used without exception. The synthesis of this class of sols was otherwise without any remarkable physical differences from palladium hydrosols in pure water.

6.2.2.2 TEM Data

The average size of the primary particles as observed by TEM, $\bar{x}$, was observed to be inversely proportional to ϕ_{MeOH}, the same trend that was observed for rhodium sols generated in the same kind of mixed media. The particle size for sols protected by PVP and PVA decreased by approximately 50% over the composition range studied, whereas the changes in the particle size for the PAA-protected sols and ARG-protected sols were much less. In the case of the ARG-protected sols this was probably a result of the limited composition range over which the sols could be measured due to protecting agent precipitation, however for the PAA-protected sols the full composition range was studied but the change in $\bar{x}$ was simply not very big. A plot of $\bar{x}$ versus ϕ_{MeOH} is shown in Figure 91 which illustrates these points.

The trends in σ were similar to the trends in $\bar{x}$, decreasing as ϕ_{MeOH} increased. The plot of σ versus ϕ_{MeOH} is shown in Figure 92. The profile of this plot was not as smooth as it was for the $\bar{x}$ versus ϕ_{MeOH} plot, exhibiting a number of peaks and troughs. It is believed that these were not a real effect, but rather were anomalous measurements caused by difficulties in measuring the particle size from the TEM micrographs, leading to unnecessarily high or low σ values. These difficulties resulted exclusively

from poor image quality, whether caused by misalignment of the TEM column or samples which were too thick to image clearly. These problems manifested mostly for the PVA and PAA protected sols, whereas the trend for the PVP and ARG protected sols clearly mimicked the trend in $\bar{x}$.

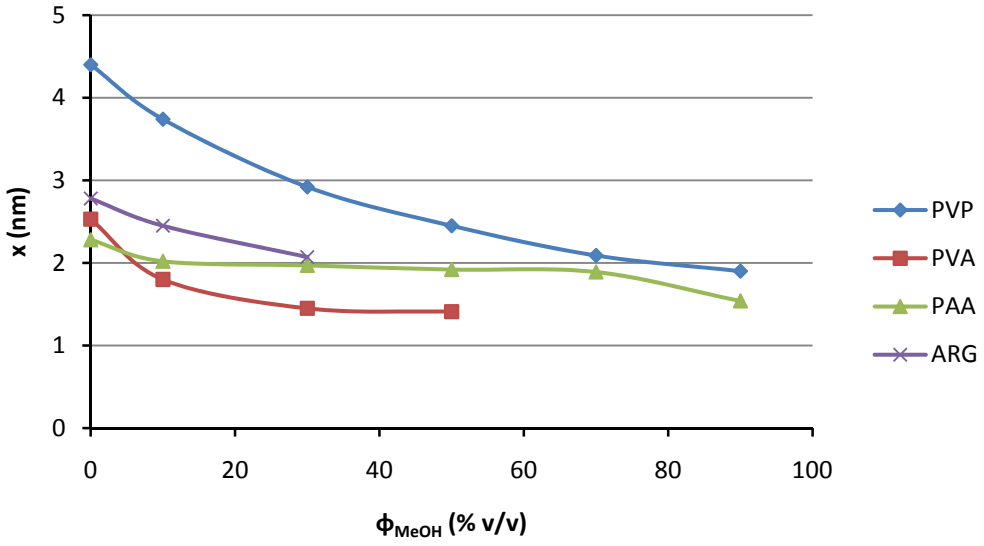

Figure 91: Plot of $\bar{x}$ versus ϕ_{MeOH} for protected palladium sols reduced by borohydride in mixtures of water and MeOH.

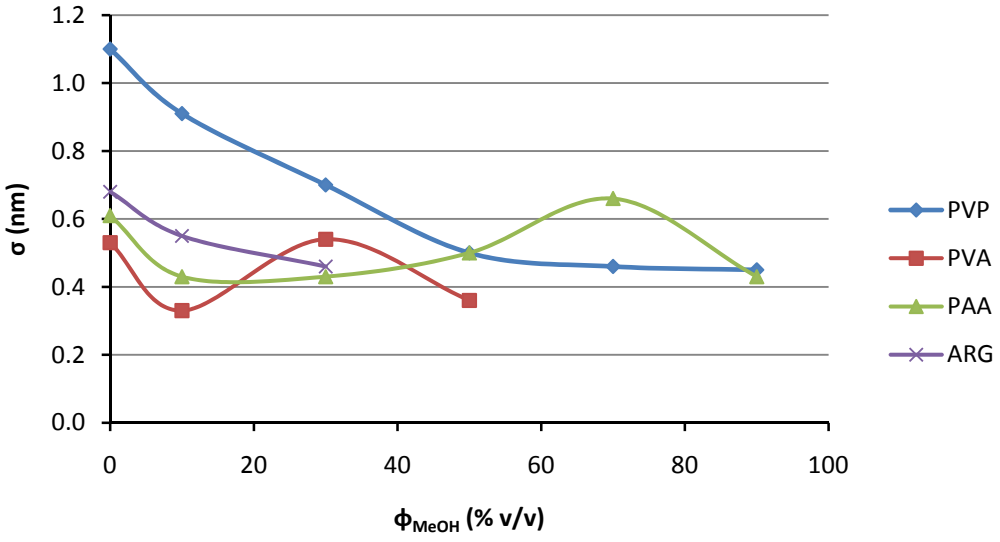

Figure 92: Plot of σ versus ϕ_{MeOH} for protected palladium sols reduced by borohydride in mixtures of water and MeOH.

6.2.2.2.1 PVP-Protected Sols

TEM micrographs revealed that for PVP-protected palladium sols reduced by borohydride in mixtures of water and methanol, altering ϕ_{MeOH} had very little effect on the organisation of the particles on the grids. All micrographs were similar to those of the corresponding hydrosol in pure water, so much so that they could not be readily distinguished from one another. There were no obvious changes in the morphology of the primary particles as ϕ_{MeOH} was altered, existing largely as discrete semi-round primary particles with a small number of small aggregates consisting of 2 - 5 individual particles. Neither their shape changed, nor the amount of necklacing, nor the size or frequency of any non-necklaced aggregates.

The particle size decreased 57% across the composition range studied, dropping from 4.4 nm in 0% ϕ_{MeOH} to 1.9 nm in 90% ϕ_{MeOH}. A 3D PSD is shown in Figure 93. The mode shifted from 5 nm to 3 nm as ϕ_{MeOH} was increased, and the distributions became taller and narrower, indicative of the decrease in both $\bar{x}$ and σ.

The only perceivable difference between the PVP-protected palladium sols prepared in aqueous methanol compared to those produced in pure water was the presence of a number of unusual spherical formations observable in the micrographs. In some occasions these were darker than the background collodion film, in which case they were assumed to be concentrated deposits of dehydrated PVP. In some cases however they were lighter than the background support film, in which case they were assumed to be due to pitting in the collodion sample support, caused by the action of MeOH. An example of such formations is shown in Figure 94.

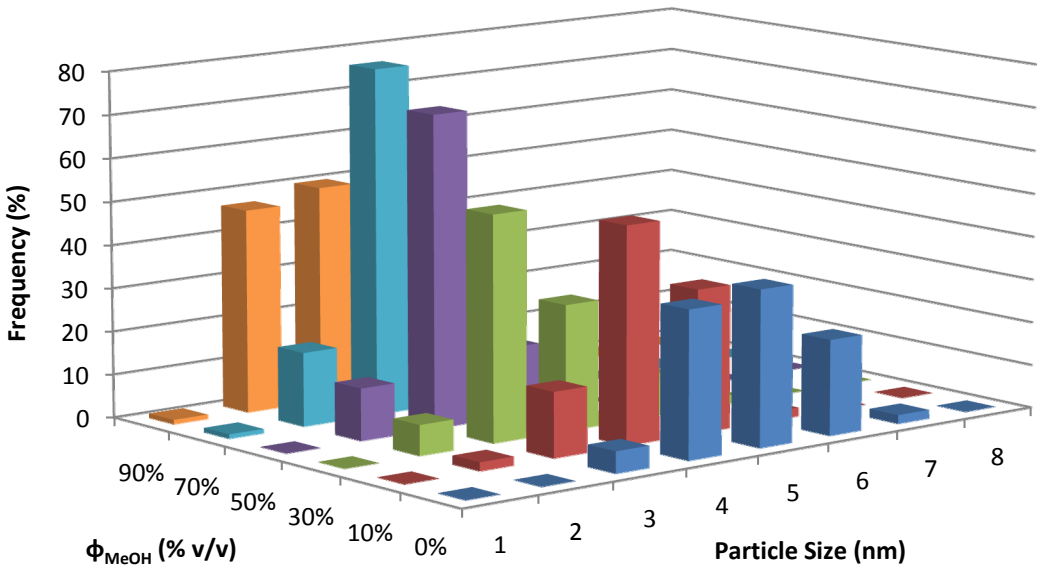

Figure 93: 3D PSD obtained by TEM for PVP-protected palladium sols reduced by borohydride mixtures of water and methanol, showing the evolution of the PSD with ϕ_{MeOH}.

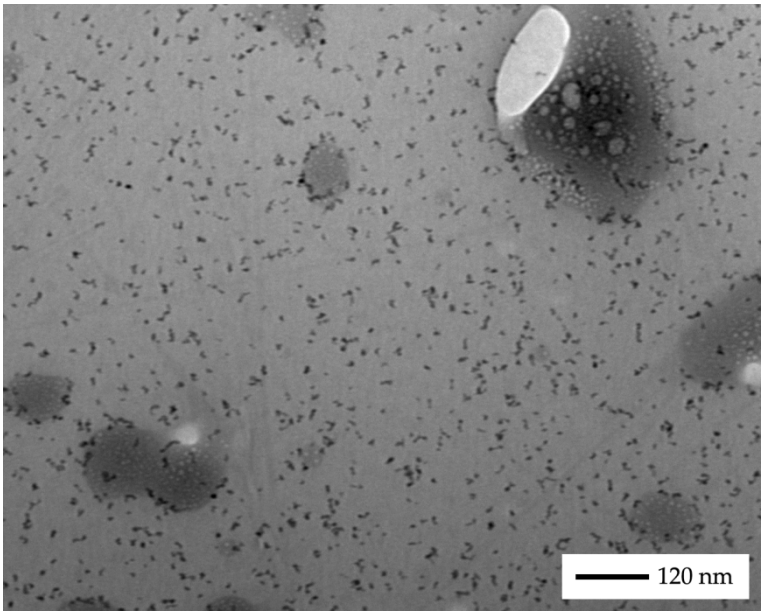

Figure 94: TEM micrograph of a PVP-protected palladium colloid reduced by borohydride in 10% v/v MeOH, showing unusual dark and light spots.

6.2.2.2.2 PVA-Protected Sols

As with rhodium, sols protected by PVA in aqueous MeOH were significantly easier to image than their purely aqueous counterparts. Instead of the large micron-sized aggregates typical of PVA protected hydrosols, a large proportion of discrete primary particles were observable, along with an equal proportion of small necklaced aggregates composed of 2 - 20 primary particles. These necklaced aggregates were similar to the typical borohydride necklacing pattern observed in previous works by Mucalo *et. al.*. A micrograph showing a typical sol is given in Figure 95. Adding methanol to a PVA-protected sol post-synthesis was also observed to have prevented the formation of these aggregates.

The particle size exhibited a 44% decrease across the composition range studied, dropping from 2.5 nm to 1.4 nm across the limited range studied. Ignoring any irregular morphologies arising from particles becoming necklaced together, the primary particles were all semi-round. A 3D PSD is shown in Figure 96 illustrating the data collected. The decrease in polydispersity and particle size were more difficult to observe than they were for PVP, as the system suffered from protecting agent precipitation above 50% v/v ϕ_{MeOH} so the range of data collected was relatively small. Despite this, the modal size class obviously shifted from 3 nm to 2 nm, and the breadth of the distributions changed from being 4 size classes wide to only 3.

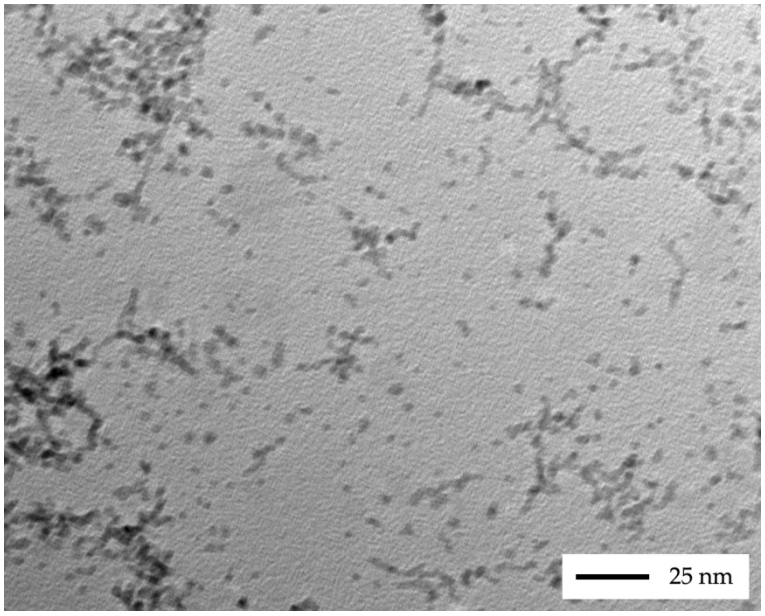

Figure 95: TEM micrograph of a PVA-protected palladium colloid generated by borohydride reduction in 50% v/v MeOH

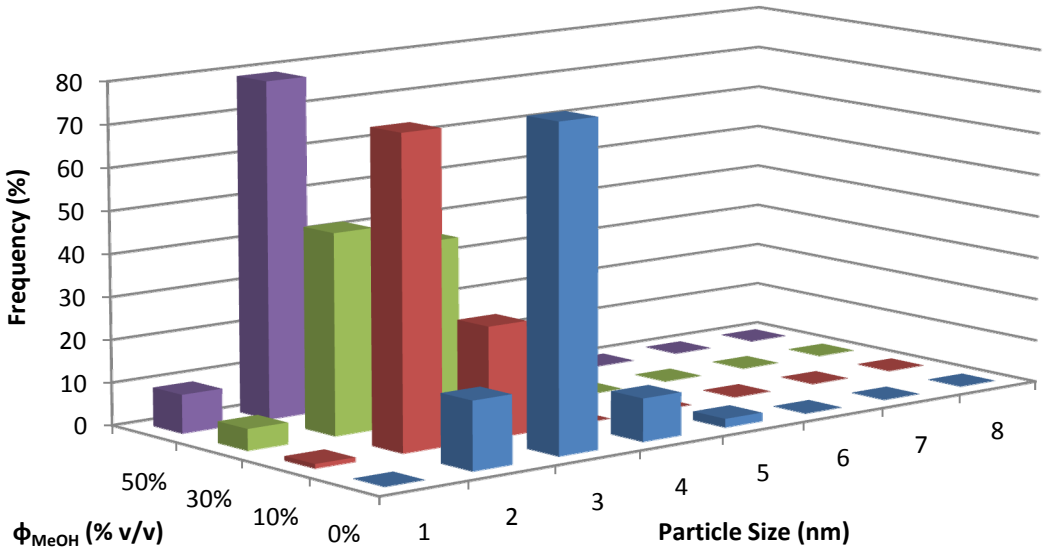

Figure 96: 3D PSD obtained by TEM for PVA-protected palladium sols generated by borohydride reduction in mixtures of water and methanol, showing evolution of PSD with ϕ_{MeOH}.

6.2.2.2.3 PAA-Protected Sols

PAA-protected sols were the only ones which did not show near-perfect exponential decreases in $\bar{x}$ with ϕ_{MeOH}. Instead, $\bar{x}$ dropped suddenly with the addition of the cosolvent, plateaued at intermediate compositions, and then dropped again toward the end. This is clearly evident in Figure 91.

The morphology and arrangement of particles in the TEM micrographs was significantly affected by the presence of MeOH when compared to the equivalent hydrosols produced in water. At low ϕ_{MeOH} values particles existed solely as discrete primary particles, and no aggregation was observed. As ϕ_{MeOH} was increased large necklaced aggregates began to form, the size and frequency of which increased with ϕ_{MeOH}. A micrograph illustrating this is shown in Figure 97.

The size of the primary particles showed only a 32% decrease across the composition range studied, dropping from 2.3 nm in 0% ϕ_{MeOH} to 1.5 nm in 90% ϕ_{MeOH}. This relatively smaller decrease was reflected in the 3D PSD, which appears to remain relatively constant across all composition ranges. It is shown in Figure 98. The modal size class remained at 2 nm across all ϕ_{MeOH} values, and the breadth of the distribution remained at 3 classes in width.

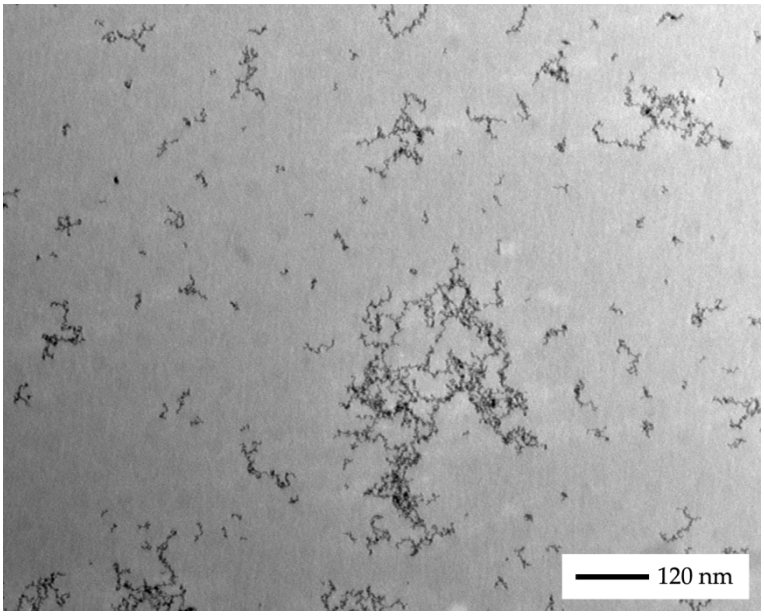

Figure 97: TEM micrograph of a PAA-protected palladium sol reduced by borohydride in 70% v/v MeOH.

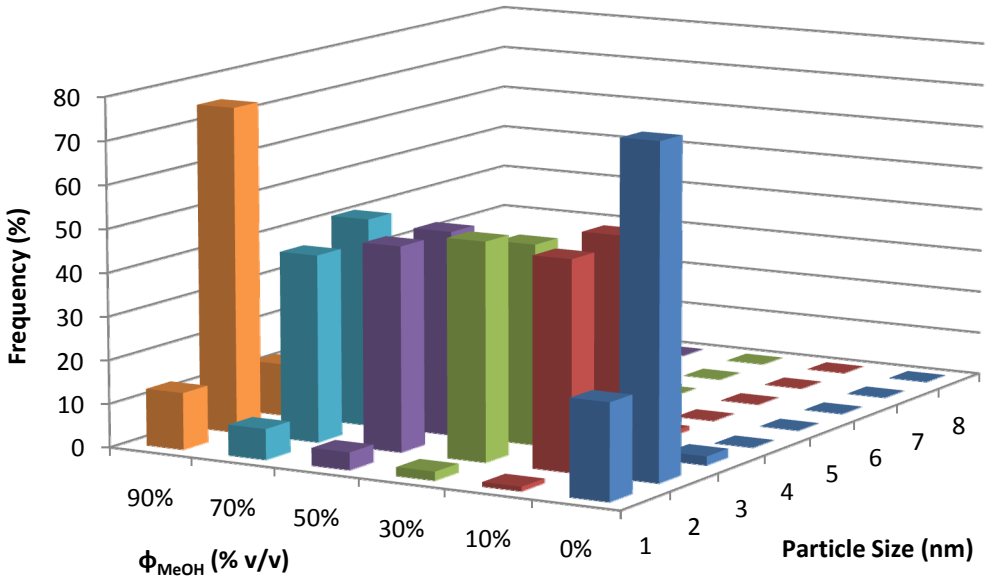

Figure 98: 3D PSD obtained by TEM for PAA-protected palladium sols generated by borohydride reduction in mixtures of water and methanol, showing the evolution of the PSD with ϕ_{MeOH}.

6.2.2.2.4 ARG-Protected Sols

Sols protected by ARG were difficult to image by TEM, as the particles tended to pack together into a very tight but thin layer dispersed homogeneously across the grid. A typical micrograph is shown in Figure 99. Despite this, they were sufficiently separated that judgements could be made on their size and shape.

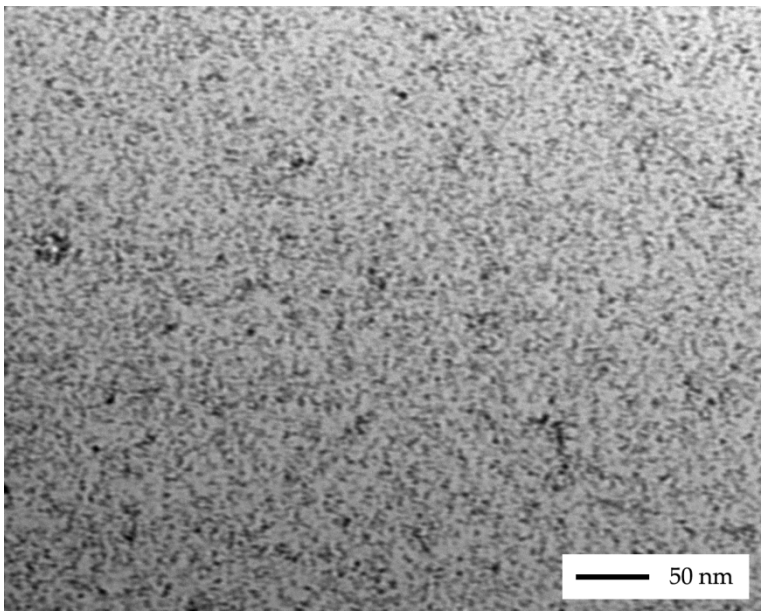

Figure 99: TEM micrograph of an ARG-protected palladium sol reduced by borohydride in 10% v/v MeOH.

The presence of MeOH did not significantly alter the morphology of the primary particles; they remained well-rounded with no necklacing or other unusual morphological traits, just as they were when generated in pure water. This behaviour was independent of ϕ_{MeOH}, occurring at all compositions.

The particle size showed a 29% decrease from 2.8 nm in 0% ϕ_{MeOH} to 2.1 nm in 30% ϕ_{MeOH}, with precipitation of the ARG molecules resulting at higher MeOH concentrations. A 3D PSD is shown in Figure 100.

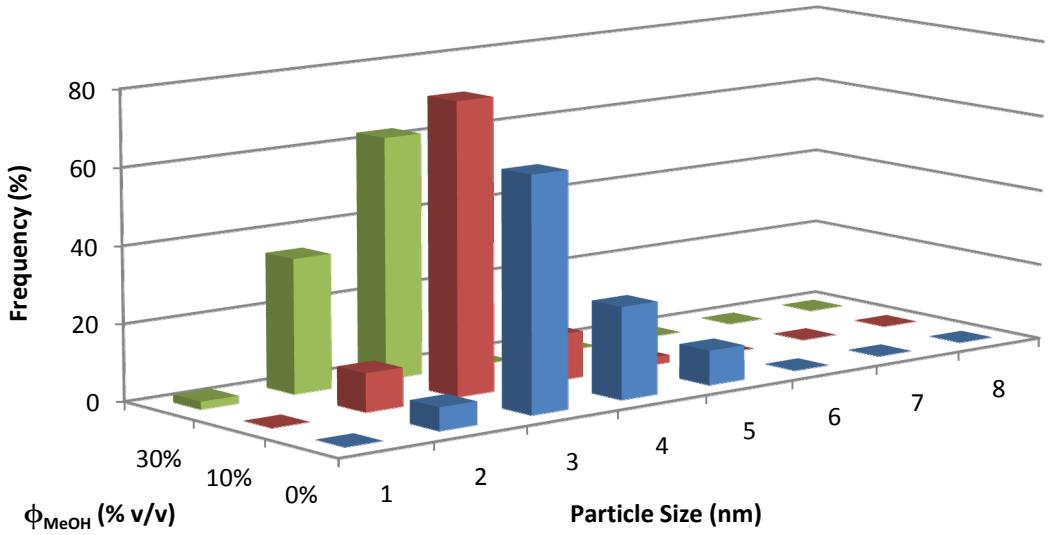

Figure 100: 3D PSD obtained by TEM for ARG-protected palladium sols generated by borohydride reduction in mixtures of water and methanol, showing the evolution of the PSD with ϕ_{MeOH}.

6.2.2.3 UV/Vis Data

The A_{450} values, plotted in Figure 101 against ϕ_{MeOH}, could be easily reconciled with the average particle size and the levels of aggregation observed in the TEM micrographs, indicating that to a good approximation the observations made *ex-situ* by TEM are a good indication of the state of the dispersion *in-situ*.

For example, with sols protected by PVP, the particle size has already been shown to decrease as ϕ_{MeOH} was increased. No drastic changes in the size or morphology of the aggregates were observed in the TEM micrographs, therefore one would expect that the A_{450} values would decrease as the particle size does, which is exactly what was observed experimentally. For the PVA-protected sols, the particle size was shown to decrease as it does for PVP, but it is observed in the micrographs that the level of aggregation increases slightly. It should be noted that for PVA there are two 'types' of aggregates in this case; those formed *in-situ* and

those formed during dehydration, so PVA is not a 'cut and dry' case. Not all of the particles were aggregated however, but enough to raise the absorbance of the system progressively as ϕ_{MeOH} was increased.

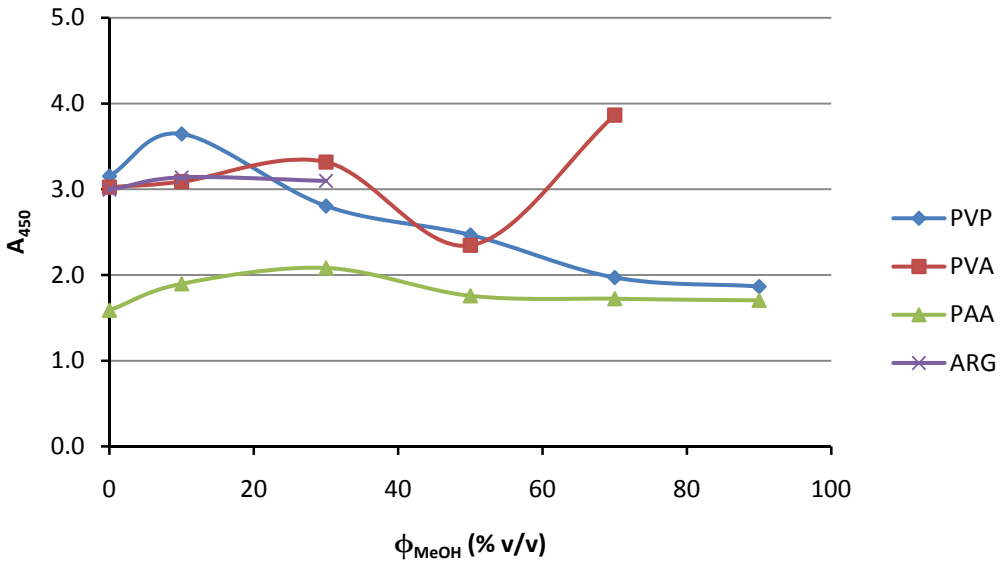

Figure 101: Plot of the dilution-corrected A_{450} values versus ϕ_{MeOH} for protected palladium sols reduced by borohydride in mixtures of water and MeOH.

For the PAA-protected sols, their A_{450} values could be easily reconciled with observations made by TEM. When no cosolvent was used there was little aggregation observed, consequently the A_{450} value was relatively low. As aggregates began to appear at 10% ϕ_{MeOH}, the A_{450} values increased correspondingly, coming to a peak at 30% ϕ_{MeOH} which coincided with the highest observed levels of aggregation in the TEM micrographs. As the MeOH concentration was increased further the level of aggregation decreased, as did the A_{450} values.

For ARG-protected sols there was a very small amount of aggregation which increased with ϕ_{MeOH}, although not enough to outweigh the decrease in particle size. Consequently there was little change in the A_{450} values.

6.2.2.4 PCS Data

The PCS data obtained was slightly harder to interpret, as it has been previously described to be. A plot of the average hydrodynamic size versus ϕ_{MeOH} is given in Figure 102.

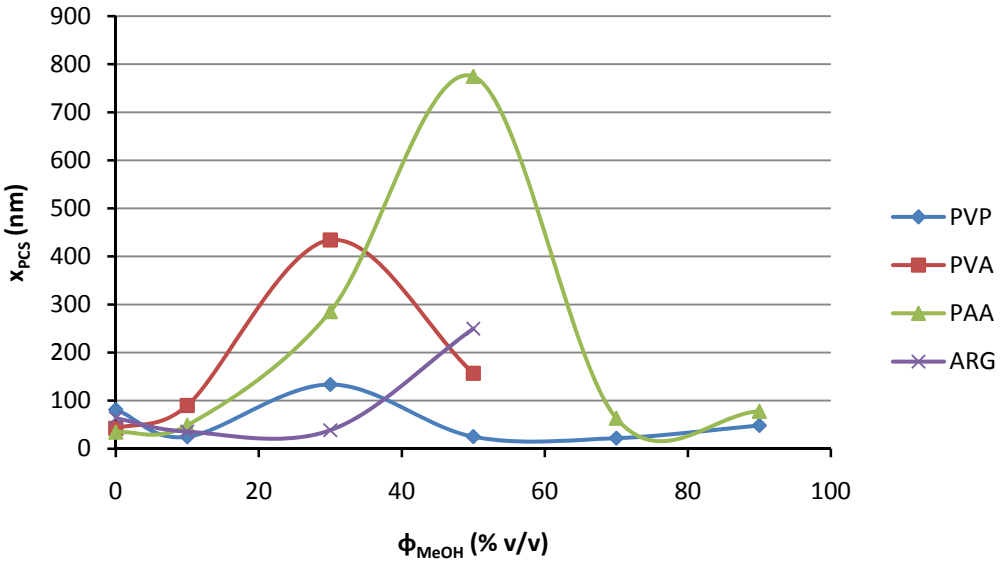

Figure 102: Plot of x_{PCS} versus ϕ_{MeOH} for protected palladium sols reduced by borohydride in mixtures of water and MeOH.

At the extremes of the composition range the hydrodynamic size was measured to be approximately 50 nm for each of the systems measured, results which agree well with data obtained from the few other research groups which have employed similar techniques [140-141].

At intermediate compositions the measured hydrodynamic radii were in the order of ten times larger than at either end of the composition range. As per rhodium, it was similarly observed that those sols with intermediate compositions were the least stable, forming deposits of palladium black within a week of synthesis, while those at the ends of the composition range proved to be more stable. This effect was also observed for all protecting agents, assumedly due partially to changes in the radius

of gyration of the protecting agents used in mixed-media, and partially due to the way in which the data was collected, as per the rhodium sols.

6.2.2 Hydrazine-Reduced Sols

6.2.2.1 General Remarks

Methanol was found to be an equally as effective cosolvent for the generation of hydrazine-reduced palladium sols in mixtures of water and methanol as it was for the borohydride-reduced equivalents. The synthesis of this class of sols was similar to those reported previously in this study. In the absence of a protecting agent the sols were unstable; conversely when protecting agents were used the sols were stable for extended periods of time. The time taken for the solutions to darken following addition of the reducing agent was against found to be proportional to ϕ_{MeOH}. All preparations eventually yielded pitch black sols.

Precipitation of the protecting agents was problematic once again, causing the PVA and ARG molecules to be precipitated in preparations where ϕ_{MeOH} was equal to or greater than 70% v/v and 50% v/v respectively. PVP remained in solution at all times, and preparations using PAA yielded homogeneous solutions rather than dense black solutions indicating the formation of palladium sols. A summary of the data collected is shown in Table 16.

		TEM		PCS	UV/Vis
Protectant	ϕ_{MeOH}	$\bar{x}$ (nm)	σ (nm)	x_{PCS} (nm)	A_{450}
PVP	10	2.4	0.7	5.1	1.54
	30	2.2	0.6	88.4	1.64
	50	2.0	0.4	53.9	1.73
	70	1.7	0.3	18.4	1.64
	90	1.4	0.4	12.8	1.65
PVA	10	2.5	0.7	67.9	1.45
	30	2.2	0.5	100.9	1.57
	50	1.9	0.3	73.9	1.59
	70	Protecting agent precipitated			
	90	Protecting agent precipitated			
PAA	10	Homogeneous solution formed			
	30	Homogeneous solution formed			
	50	Homogeneous solution formed			
	70	Homogeneous solution formed			
	90	Homogeneous solution formed			
ARG	10	2.0	0.5	29.3	1.56
	30	1.9	0.6	5.4	1.29
	50	Protecting agent precipitated			
	70	Protecting agent precipitated			
	90	Protecting agent precipitated			

Table 16: Summary of the data collected for hydrazine-reduced palladium sols in aqueous MeOH.

6.2.2.2 TEM Data

TEM measurements showed that palladium sols reduced by hydrazine in mixtures of water and methanol exhibited the same trends as observed with the previously described systems, a decrease of $\bar{x}$ with ϕ_{MeOH}. A plot of $\bar{x}$ versus ϕ_{MeOH} is shown in Figure 103.

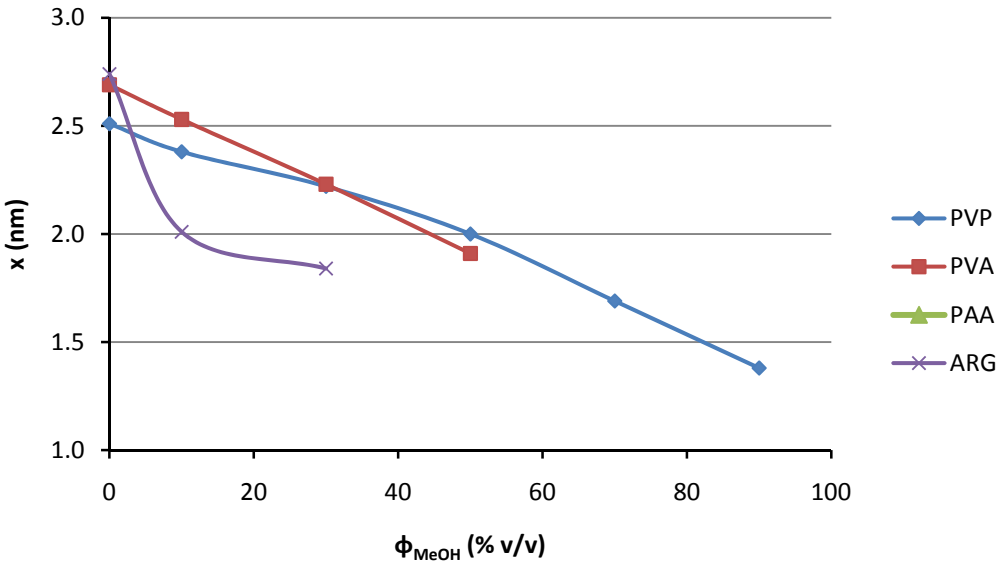

Figure 103: Plot of $\bar{x}$ versus ϕ_{MeOH} for protected palladium sols reduced by hydrazine in mixtures of water and MeOH.

The PVP-protected and PVA-protected sols behaved similarly to one another, with the average particle size as measured by TEM ($\bar{x}$) decreasing approximately linearly at a rate of approximately 0.25 nm per 20% ϕ_{MeOH} increase. The average particle size of the ARG-protected sols dropped more quickly, although little data could be collected as the ARG molecules were precipitated from solution at relatively low MeOH concentrations.

The polydispersity (σ) approximately mirrored the trends in $\bar{x}$, decreasing as ϕ_{MeOH} was increased. A plot illustrating this is shown in Figure 104.

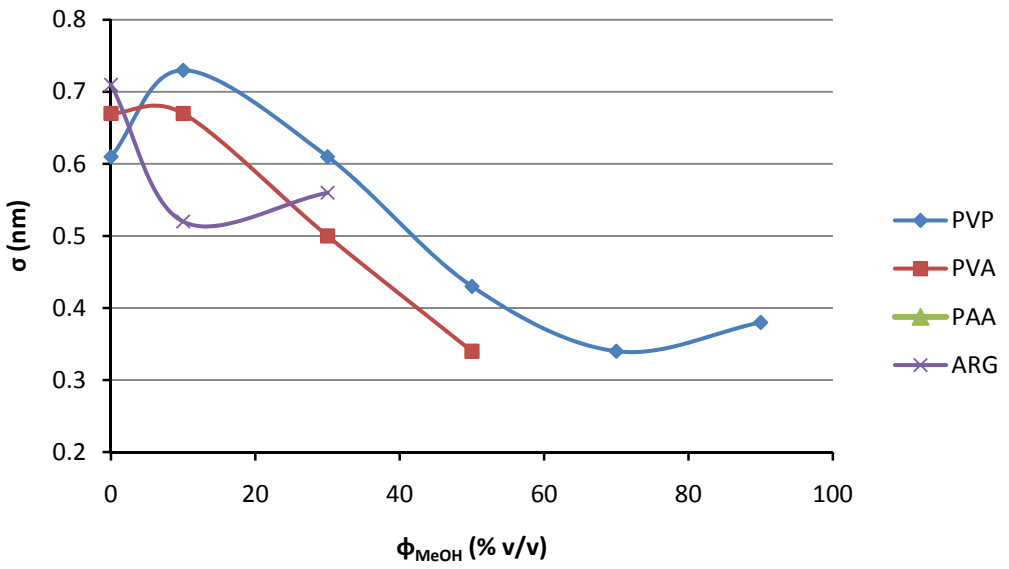

Figure 104: Plot of σ versus ϕ_{MeOH} for protected palladium sols reduced by hydrazine in mixtures of water and MeOH.

6.2.2.2.1 PVP-Protected Sols

Observation by TEM showed that PVP-protected sols existed on the grids primarily as discrete primary particles, with a small proportion of necklaced aggregates of 2 - 10 particles. As ϕ_{MeOH} was increased, there were several effects observed. Firstly, the size and frequency of the aggregates present increased with ϕ_{MeOH}, to the point where tightly-packed 50 nm aggregates were relatively common at 90% ϕ_{MeOH}. Secondly, the level of necklacing appeared to decrease ϕ_{MeOH} was increased, tending toward none at 90% ϕ_{MeOH}. The tendency for particles to gather together during evaporation also decreased with ϕ_{MeOH}. In this respect methanol changed the *type* of aggregation, shifting from necklaced aggregates to close-packed aggregates. A typical micrograph is shown in Figure 105.

The particle size was shown to decrease 44% across the composition range studied, dropping from 2.5 nm in 0% ϕ_{MeOH} to 1.4 nm in ϕ_{MeOH}. In all cases the primary particles were well-rounded when not necklaced. A 3D PSD is shown in Figure 106.

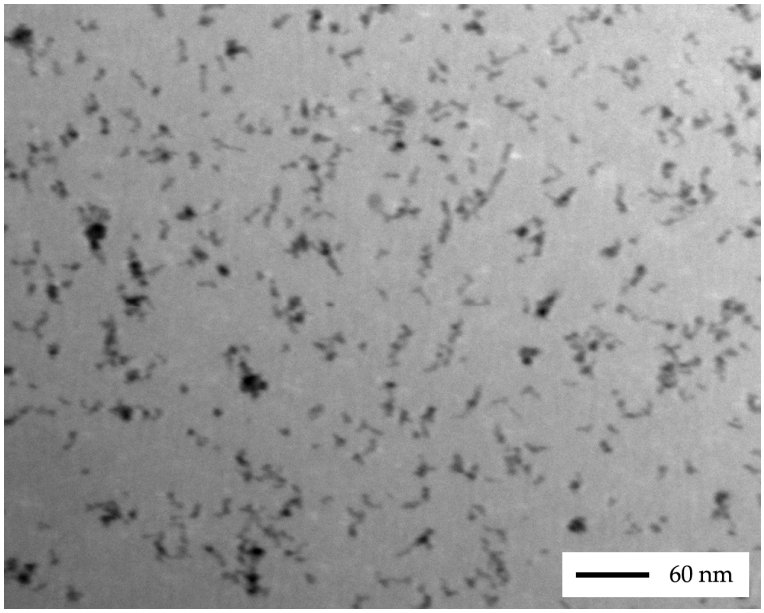

Figure 105: TEM micrograph of a PVA-protected palladium sol reduced by hydrazine in 50% v/v MeOH.

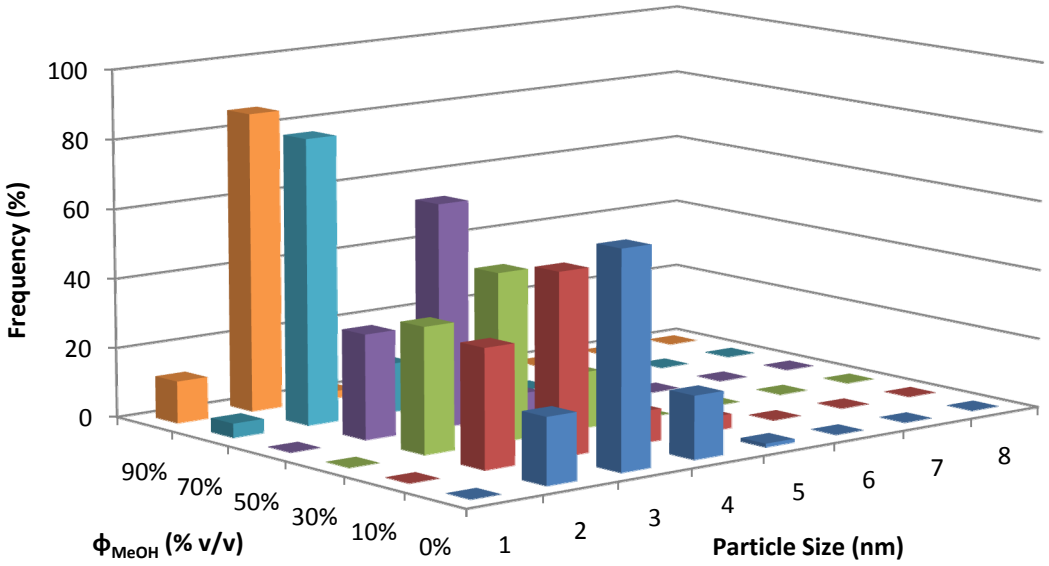

Figure 106: 3D PSD obtained by TEM for PVP-protected palladium colloids generated by hydrazine reduction in mixtures of water and methanol, showing the evolution of the PSD with ϕ_{MeOH}.

Although it is initially unclear that the PSD supports the fact that the particle size decreases, it can be observed that the modal size class dropped from 3 nm to 2 nm, and the lower size classes increased in frequency as ϕ_{MeOH} was increased.

6.2.2.2.2 PVA-Protected Sols

PVA-protected sols displayed similar trends to those protected by PVP. As ϕ_{MeOH} was increased the level of necklacing between particles decreased, changing from extended chain-like aggregates in the control experiment with no cosolvent to well-dispersed collections of primary particles and small necklaced aggregates thereof at high MeOH concentrations. In this sense, MeOH acted to break up the PVA aggregates in the same way that it did for borohydride-reduced palladium and rhodium sols. A typical micrograph is shown in Figure 107.

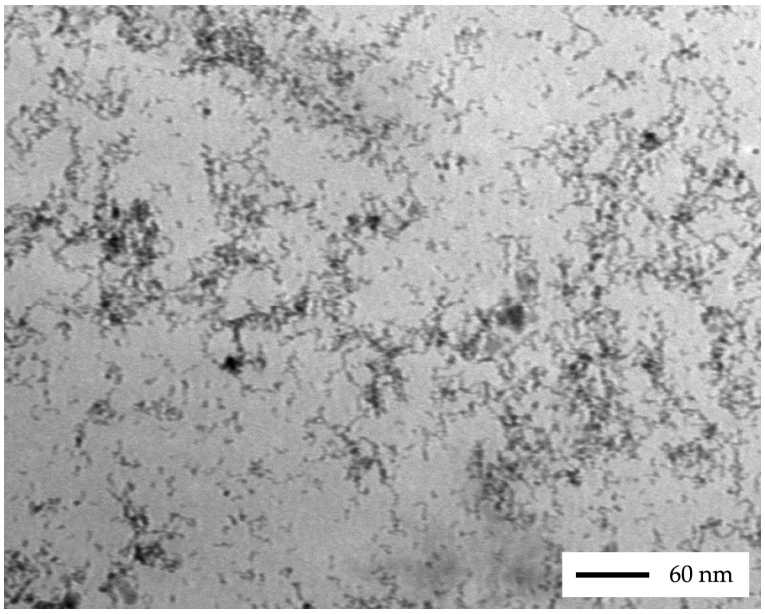

Figure 107: TEM micrograph of a PVA-protected palladium sol reduced by hydrazine in 10% v/v MeOH.

The size of the primary particles was shown to have decreased 30% from 2.7 nm in the control experiment in 0% ϕ_{MeOH} to 1.9 nm in 90% ϕ_{MeOH}. The polydispersity of the particles decreased simultaneously, as observed with

all the systems described previously. A 3D PSD is shown in Figure 108. The modal size class decreased from 3 nm to 2 nm over the composition range, reflecting the relatively small change in $\bar{x}$ and the relatively small composition range studied.

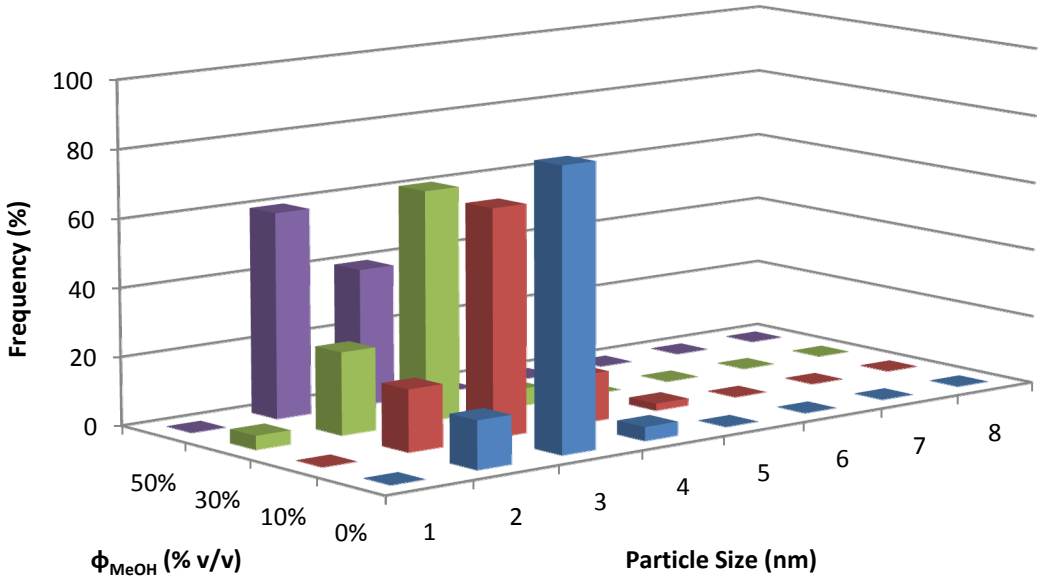

Figure 108: 3D PSD obtained by TEM for PVA-protected palladium colloids generated by hydrazine reduction in mixtures of water and methanol, showing the evolution of the PSD with ϕ_{MeOH}.

6.2.2.2.3 ARG-Protected Sols

ARG-protected sols behaved similarly to the PVA-protected sols. The formations into which particles assembled on the grids were dispersed with increasing homogeneity as ϕ_{MeOH} was increased, to the point where at 30% ϕ_{MeOH} they existed exclusively as discrete primary particles with no aggregation and no necklacing. A typical micrograph is shown in Figure 109. Because the ARG molecules were precipitated from solution by 50% v/v ϕ_{MeOH}, little data could be collected, although the data which was collected provided an observable trend. The size of the primary particles decreased 32% from 2.7 nm in 0% ϕ_{MeOH} to 1.9 nm in 30% ϕ_{MeOH}, past

which sols were not characterised due to protecting agent precipitation. A 3D PSD is shown in Figure 110.

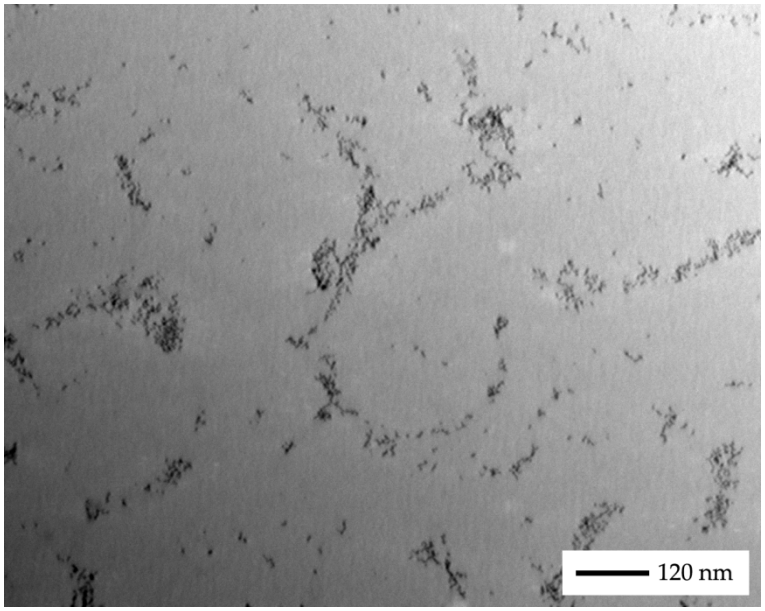

Figure 109: TEM micrograph of an ARG-protected palladium sol reduced by hydrazine in 10% v/v MeOH.

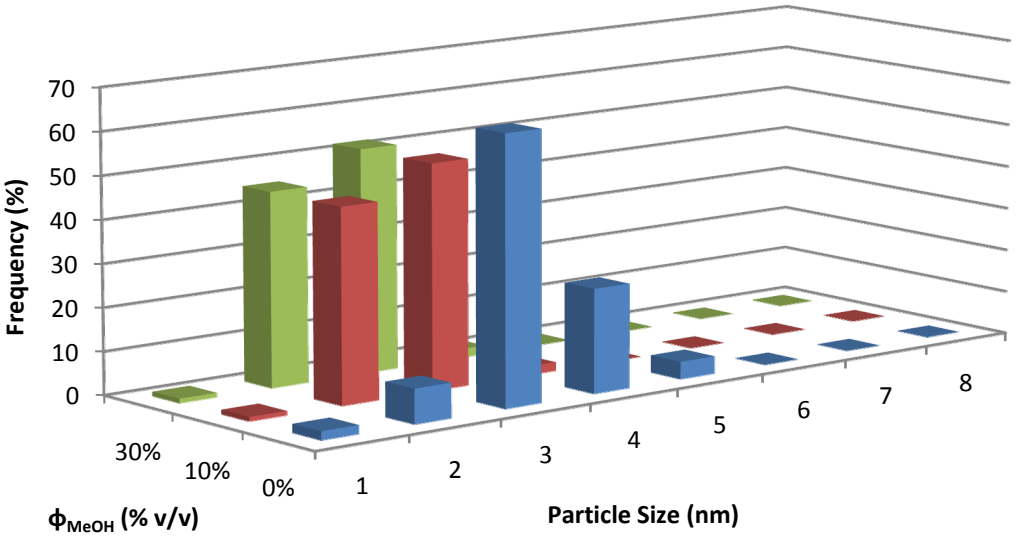

Figure 110: 3D PSD obtained by TEM for ARG-protected palladium sols generated by hydrazine reduction in mixtures of water and methanol, showing the evolution of the PSD with ϕ_{MeOH}.

6.2.2.3 UV/Vis Data

The UV/Vis data showed that in all cases the A_{450} values of each preparation were *approximately* the same as the control experiment containing 0% ϕ_{MeOH}, with variations of only 20%. A plot of the A_{450} values is shown in Figure 111.

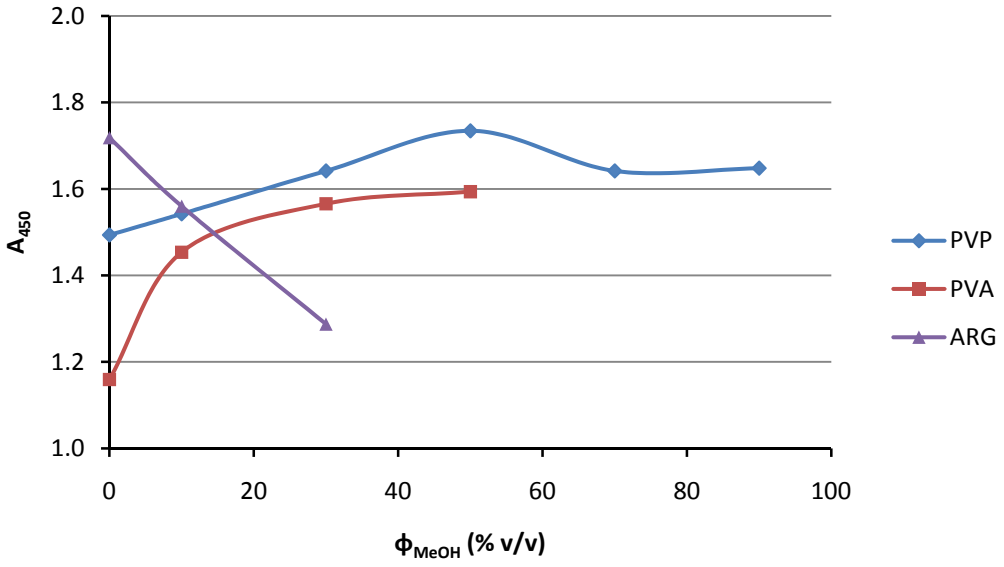

Figure 111: Plot of the dilution-corrected A_{450} values versus ϕ_{MeOH} for protected palladium sols reduced by hydrazine in mixtures of water and MeOH.

This data indicates that the average level of aggregation increased *in-situ* as ϕ_{MeOH} was increased, so hydrazine-reduced palladium sols became progressively less stable as MeOH was added, compared to the borohydride-reduced sols where the changes were much less predictable. The PCS data corroborates these measurements by displaying the same trends, so they are assumed to be real. This means that the ability of the particles to scatter light is outweighed by the increase in the increase in the size and frequency of any aggregates formed.

In the case of the PVP- and ARG-protected sols this data compares favourably with the level of aggregation observed in the TEM

micrographs. However, for the PVA-protected sols the trend is the opposite of what was observed. This is unsurprising given the observed propensity for PVA to display markedly different characteristics *ex-situ* compared to *in-situ*, as described previously.

6.2.2.4 PCS Data

The PCS data displayed similar trends to the UV/Vis data, as mentioned in the previous section. A graph showing the x_{PCS} values for each sol plotted against ϕ_{MeOH} is shown in Figure 112.

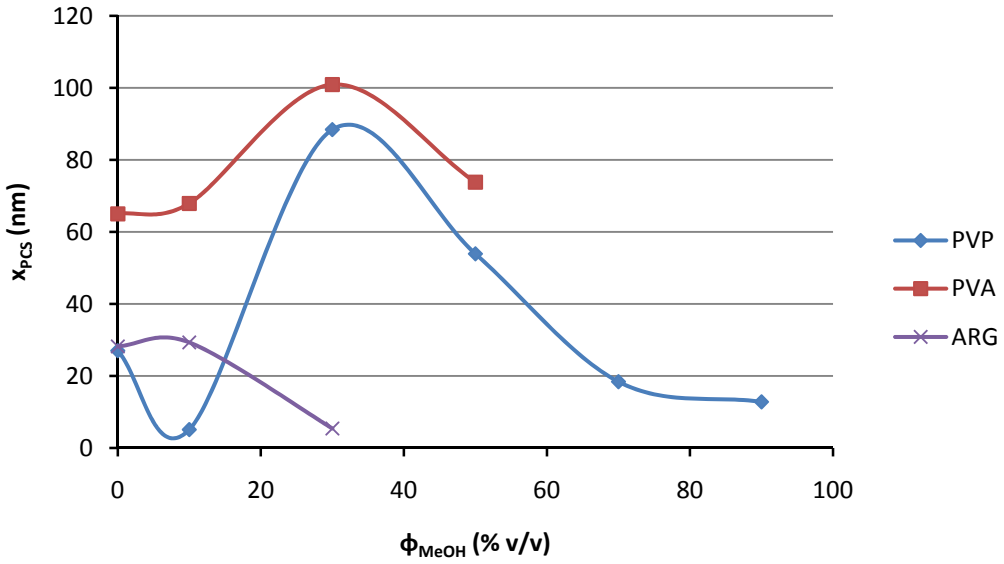

Figure 112: Plot of x_{PCS} versus ϕ_{MeOH} for protected palladium sols reduced by hydrazine in mixtures of water and MeOH.

Interestingly the changes in the average hydrodynamic sizes were comparable with the size of the aggregates observed in the TEM micrographs, as opposed to some other PCS plots where the average size was greatly exaggerated at intermediate compositions. For the PVP-protected sols the changes were likely to be due largely to the frequency of the aggregates as overall their size did not change significantly; for the PVA- and ARG- protected sols the average hydrodynamic radius

increased and decreased respectively, reflective of the sizes of the aggregates observed by TEM.

6.3 Sols in Aqueous Dimethylsulfoxide

6.3.1 Borohydride-Reduced Sols

6.3.1.1 General Remarks

DMSO was shown to be a suitable cosolvent for the generation of colloidal palladium. Unlike methanol there were no problems with precipitation of the protecting agents, with even arabinogalactan remaining in solution in 90% ϕ_{DMSO} solutions. This was assumed to be due to the relatively higher polarity of the DMSO molecules (ε = 47.2) compared to MeOH (ε = 33.0). A summary of the data collected is given in Table 17.

When beginning the reduction reaction required to produce colloidal palladium, the addition of the first drop of the borohydride always resulted in the formation of a deep blood-red solution. The addition of the rest of the reducing agent then caused the solution to become black, typifying the formation of a palladium colloid. The number of drops required to cause the solution to turn black was shown to be proportional to ϕ_{DMSO}; at 10% ϕ_{DMSO} the solution remained red for only a few drops, in contrast at 90% ϕ_{DMSO} it remained for almost the entirety of the addition of the reducing agent. It is believed that this phenomenon was due to the formation of low-oxidation state DMSO solvation complexes of palladium, analogous to those formed for rhodium.

The resulting colloids generated displayed unusual trends in stability. Those protected by PVP remained stable for an indefinite amount of time, possibly as the particularly large molecular mass (700,000 g mol^{-1}) of the PVP means that even under compression by an antisolvent, the polymer layer surrounding the colloidal particles is too thick for the free energy of two closely-separated particles to fall below zero and the system to

aggregate, on a macroscopic state at least. Samples at low cosolvent compositions were slightly lighter in colour than the relevant control sample, those at intermediate compositions similar, and those at high compositions much lighter. Photographs of the sols are shown in Figure 113.

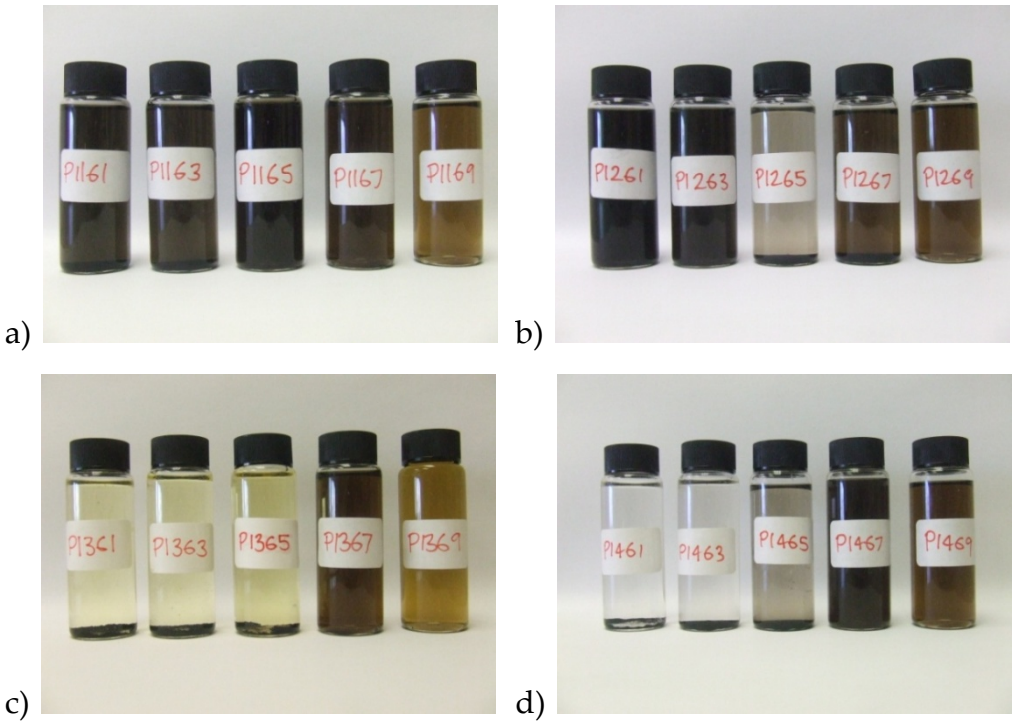

Figure 113: Photographs of palladium colloids generated by borohydride reduction in aqueous DMSO protected by a) PVP, b) PVA, c) PAA, d) ARG. ϕ_{DMSO} increases from left to right in each photo. Refer to Appendix 1 for a full explanation of the vial labels.

The sols protected by PVA were unstable at intermediate composition ranges, fully aggregating to form a precipitate of palladium black. At lower compositions the colloids were dark; at higher compositions they were light. The light colour was shown (later) to be due to relatively smaller particle sizes.

Those protected by PAA were unstable in the ranges 10% ϕ_{DMSO} through to 50% ϕ_{DMSO}, with nearly all of the suspended particles aggregating and

		TEM		PCS	UV/Vis
Protectant	ϕ_{DMSO}	$\bar{x}$ (nm)	σ (nm)	x_{PCS} (nm)	A_{450}
PVP	10	3.7	0.8	32.5	1.05
	30	2.6	0.5	69.5	1.13
	50	1.6	0.4	326.0	1.79
	70	1.1	0.3	125.0	1.27
	90	0.8	0.2	39.8	0.86
PVA	10	2.5	0.7	38.7	1.79
	30	2.0	0.4	127.0	1.60
	50	1.4	0.3	498.0	0.63
	70	1.0	0.3	237.0	1.07
	90	0.8	0.2	45.0	1.29
PAA	10	1.8	0.4	184.0	0.35
	30	1.6	0.6	202.0	0.41
	50	1.4	0.4	168.0	0.47
	70	1.3	0.3	124.0	1.05
	90	1.3	0.3	62.0	0.91
ARG	10	2.0	0.6	458.0	0.39
	30	1.6	0.3	568.0	0.40
	50	1.5	0.3	357.0	0.73
	70	1.1	0.4	124.6	1.59
	90	0.7	0.2	24.8	1.37

Table 17: Summary of TEM, PCS and UV data obtained for palladium sols reduced by borohydride in aqueous DMSO.

subsequently precipitating. It was uncertain whether the light yellow retained by the dispersion medium was due to unreduced metal salt precursor, or the persistence of a small number of small particles causing the light to be scattered. The UV/Vis spectrum did not exhibit any large precursor peaks, although this is not diagnostic for a two reasons. Firstly, the region where λ_{max} was located, around 200 nm, was obscured by a strong absorption from both the protecting agents and the solvent. Secondly, the colour of the metal precursor salt was observed to change as the cosolvent was added, so the profile of the UV/Vis spectrum must therefore have changed also. From 70% ϕ_{DMSO} above samples were stable although light coloured. This information is summarised in the "stability maps" in Section 6.10.

Arabinogalactan, which has never been used to protect palladium colloids in DMSO, did not give stable colloids at low DMSO concentrations, forming Pd black up to and including 50% ϕ_{DMSO}. However above this point the colloids were stable.

6.3.1.2 TEM Data

Attempts to prepare samples for TEM analysis in the fashion described previously (see Section 3.3.3) were unsuccessful, as the DMSO present in the dispersion medium caused the collodion sample supports on the grids to dissolve, just as they did for the rhodium colloids prepared in aqueous DMF (see Section 5.4). To overcome this problem the previously-devised heptane extraction method (see section 5.4.2) was utilised for all samples.

Once samples were prepared using the heptane extraction method, TEM analysis revealed similar trends to the other systems studied, with $\bar{x}$ decreasing as ϕ_{DMSO} was increased. The extent to which this occurred was much greater however, with colloids protected by PVP, PVA and ARG all

reaching the sub-nanometre level at high DMSO concentrations, converging at around 0.8 nm (or 8 Å). This is near the resolution limit of the TEM used, although with the aid of the magnification provided by the digital camera, particles of this size could be detected with sufficient care. Previous works calculate palladium clusters of this size to contain as few as seven atoms, also stating that they are extremely rare and possess high catalytic efficiencies [142], something which may be useful for future works. A plot of $\bar{x}$ versus ϕ_{DMSO} is shown in Figure 114. The polydispersity was found to generally decrease with ϕ_{DMSO} as it did for all previous systems, with one standard deviation generally being 20% - 25% of the average particle size. A plot of σ versus ϕ_{DMSO} is shown in Figure 115.

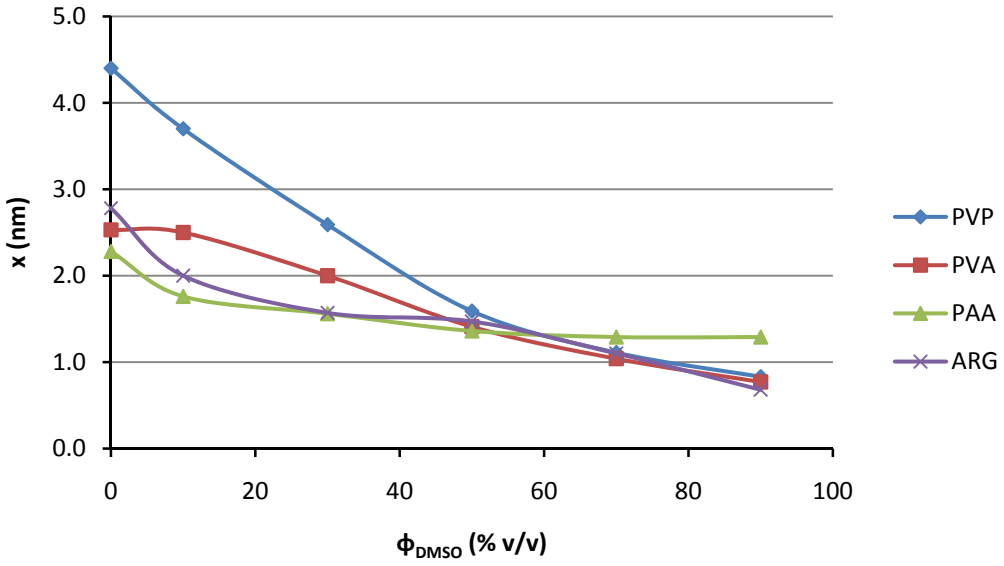

Figure 114: Plot of $\bar{x}$ versus ϕ_{DMSO} for protected palladium sols reduced by borohydride in mixtures of water and DMSO.

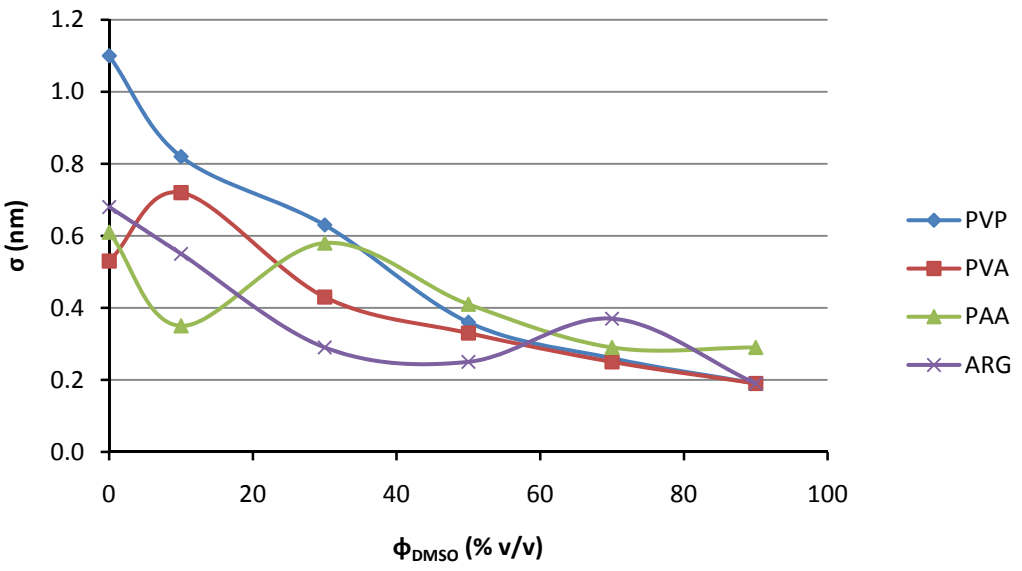

Figure 115: Plot of σ versus ϕ_{DMSO} for protected palladium sols reduced by borohydride in mixtures of water and MeOH.

6.3.1.2.1 PVP-Protected Sols

TEM analysis showed that for PVP-protected sols, the compound aggregates as previously described existed predominantly at low DMSO concentrations, but became increasingly less frequent as ϕ_{DMSO} was increased. At intermediate compositions the compound aggregate structure was completely replaced by individual 'bundles' of particles. As ϕ_{DMSO} was increased further these 'bundles' disappeared and the level of aggregation decreased to the point where at 90% ϕ_{DMSO} the particles existed largely as discrete primary particles. Some micrographs illustrating this change are given in Figure 116. The level of necklacing between particles also decreased significantly, and was completely absent by approximately 30% ϕ_{DMSO}.

Ignoring those particles which had become necklaced into strings, primary particles were in all cases mostly rounded, becoming less irregular and more spherical as ϕ_{DMSO} was increased. They decreased in size from 4.4 nm in the control experiment with 0% ϕ_{DMSO} to 0.8 nm in 90%

v/v ϕ_{DMSO}, an 81% decrease in particle size over the composition range studied. This may be of use in the future for producing ultra-fine particles, for example, raising the proportion of DMSO to 95% or 99% may hopefully produce even smaller clusters, such as Pd_3 or Pd_4. Unsurprisingly the polydispersity decreased as ϕ_{DMSO} was increased. A 3D PSD is given in Figure 117 which illustrates these observations. Note the narrowing of the particle size distribution from 5 size classes to just 2, and the shift in the modal size class from 5 nm to 1 nm

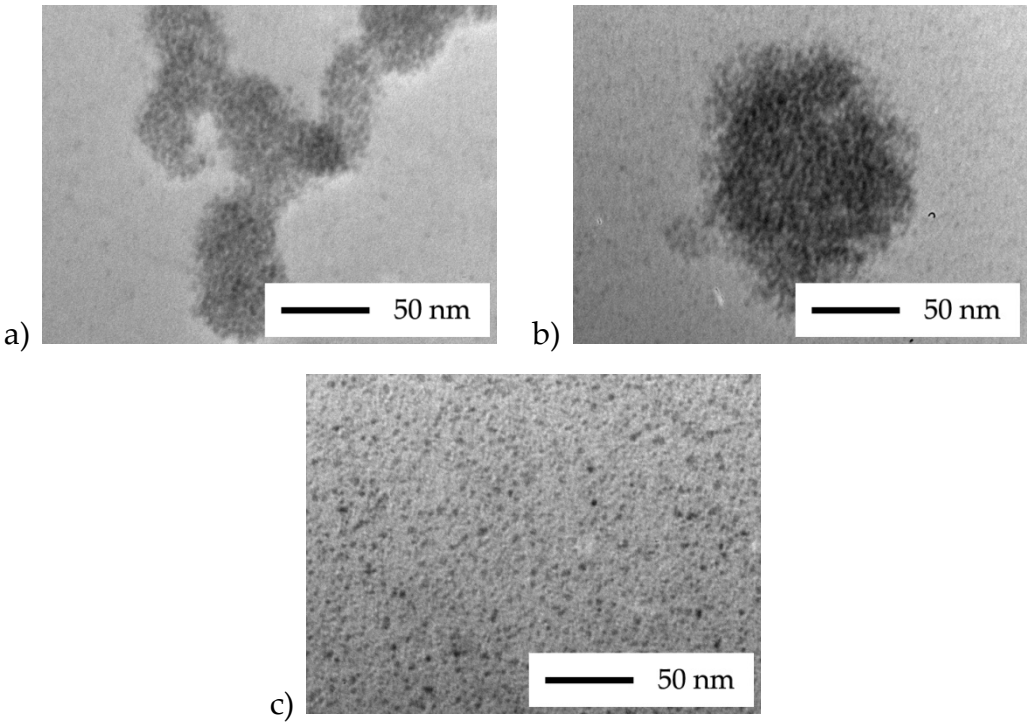

Figure 116: TEM micrographs of PVP-protected palladium sols reduced by borohydride in aqueous DMSO showing how the aggregate structure changed with ϕ_{DMSO}, from the compound aggregate structure (a) to the bundle structure (b) to complete dispersion (c).

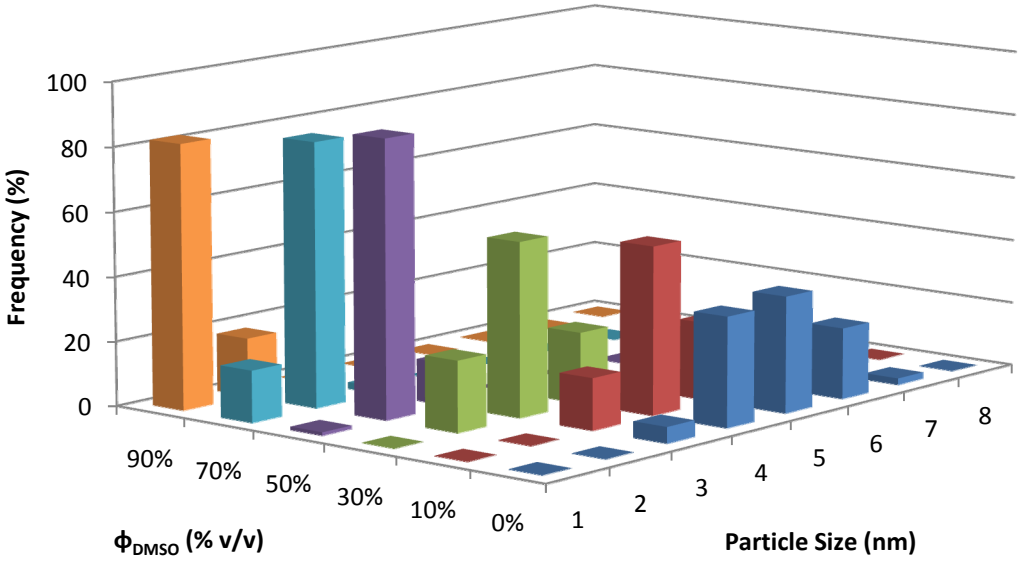

Figure 117: 3D PSD obtained by TEM for PVP-protected palladium sols reduced by borohydride in mixtures of water and DMSO, showing the evolution of the PSD with ϕ_{DMSO}.

6.3.1.2.2 PVA-Protected Sols

For the PVA-protected sols, the behaviour of the aggregates observed was even more complicated than for the PVP-protected sols. At low DMSO concentrations, the compound aggregate structure *would* have existed, but because of the strong tendency for particles to necklace together the primary particles which would have constituted these aggregates had become formed into larger irregular particles, as shown in Figure 118. As the proportion of DMSO was increased toward 50%, the necklacing became increasingly suppressed, and the irregular necklaced morphologies of the compound aggregates transformed back into their usual 'compound aggregate' structure. As the DMSO concentration was increased further the compound aggregates were broken up into smaller and smaller portions forming the 'bundles' of particles as seen with the PVP-protected sols.

In cases where primary particles were visible and were not necklaced together they appeared to be well-rounded, with their sizes decreasing 68% from 2.5 nm in the control experiment with 0% ϕ_{DMSO} to 0.8 nm in 90% ϕ_{DMSO}. As with the other systems observed, the polydispersity decreased simultaneously. A 3D PSD is shown in Figure 119 illustrating these trends. Note the shift of the modal size class from 3 nm to 1 nm, and the narrowing of the distributions as ϕ_{DMSO} was increased.

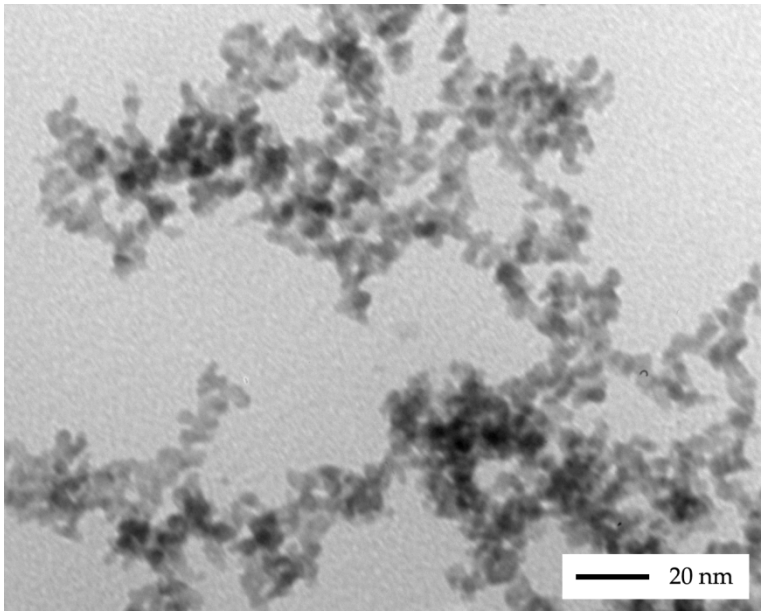

Figure 118: TEM micrograph of a PVA-protected palladium sol reduced by borohydride in 10% v/v DMSO.

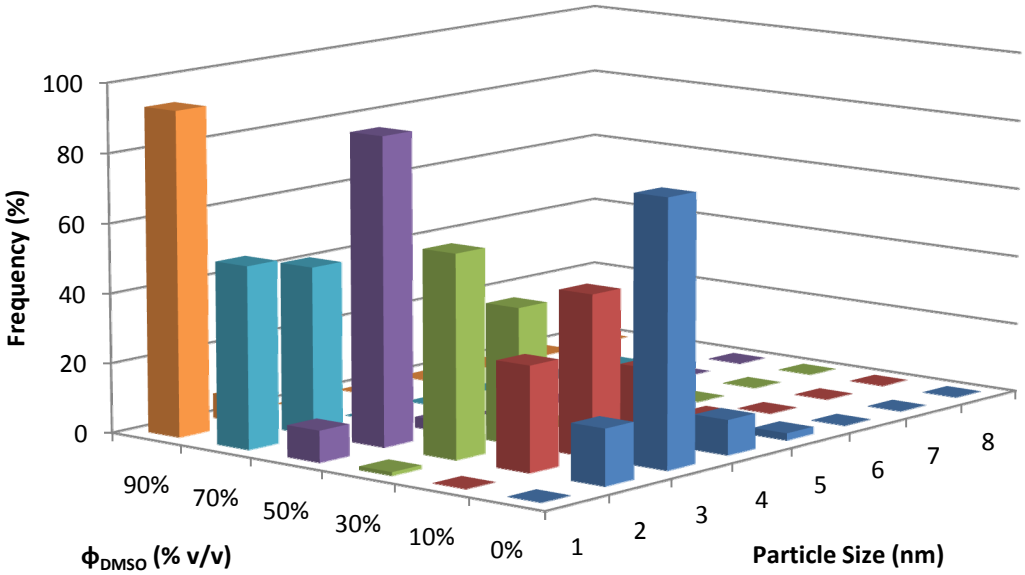

Figure 119: 3D PSD obtained by TEM for PVA-protected palladium sols reduced by borohydride in mixtures of water and DMSO, showing the evolution of the PSD with ϕ_{DMSO}.

6.3.1.2.3 PAA-Protected Sols

For PAA-protected sols the presentation of particles on the TEM grids was dominated by the presence of large aggregates and few discrete primary particles. At low DMSO concentrations the aggregates were large and irregular, typical of any other unstable colloidal system. At higher DMSO concentrations particles began to assemble into extensive web-like networks, an example of which is shown in Figure 120. The size of the primary particles in these aggregates was shown to decrease 43% over the composition range studied, dropping from 2.3 nm in the control sol with 0% ϕ_{DMSO} to 1.3 nm in the sol generated in 90% ϕ_{DMSO}. This was the smallest size decrease of all the protecting agents studied, a fact which is reflected in the nature of the 3D PSD presented in Figure 121, showing no change in the modal size class from 2 nm across the entire composition range. In all cases the primary particles were spherical, with no evident necklacing.

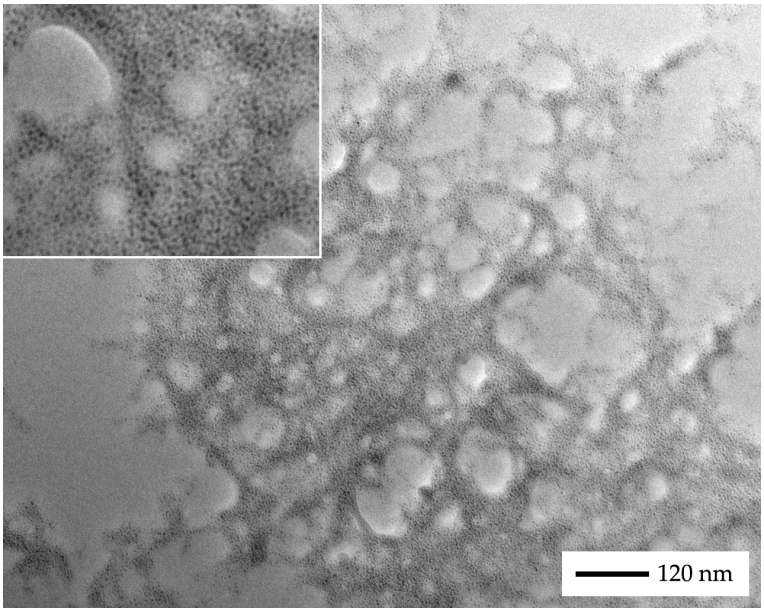

Figure 120: TEM micrograph of a PAA-protected palladium sol reduced by borohydride in 70% v/v DMSO. Note the formation of the web-like networks. Inset: higher magnification of the same sol.

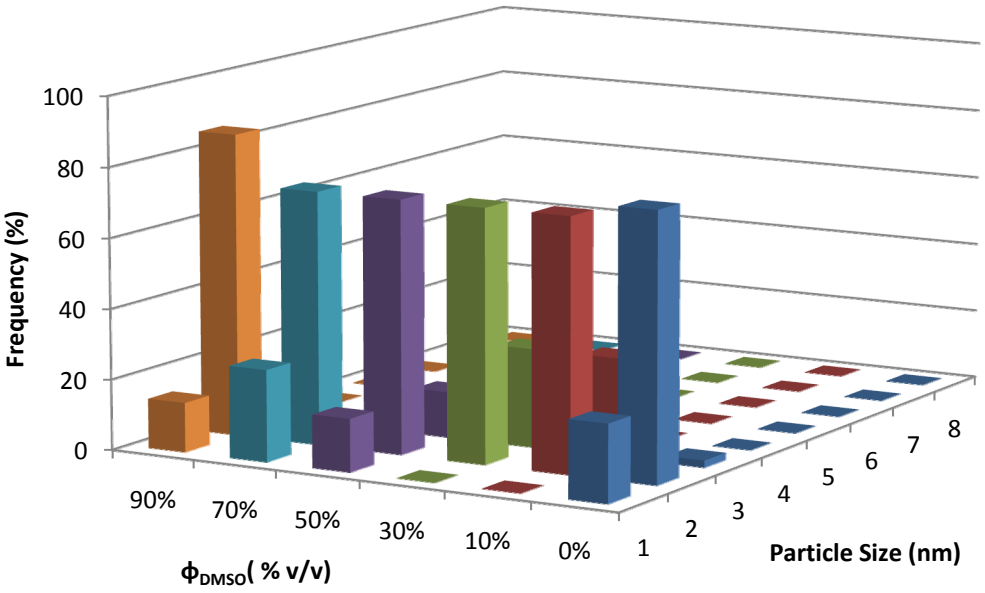

Figure 121: 3D PSD obtained by TEM for PAA-protected palladium sols reduced by borohydride in mixtures of water and DMSO, showing the evolution of the PSD with ϕ_{DMSO}.

6.3.1.2.4 ARG-Protected Sols

For ARG-protected sols, the nature of the aggregates and the primary particles was similar to that of the PVP-protected sols. At low DMSO concentrations particles existed *ex-situ* primarily in the compound aggregate form, at intermediate compositions the aggregate structures began to break down and form bundles rather than networks, and at high DMSO concentrations the particles were almost completely dispersed in a uniform fashion across the grid with no observable aggregation. A typical micrograph is shown in Figure 122.

In no cases was any kind necklacing effect observed, and all particles were generally semi-rounded although slightly eccentric. This made measuring the primary particles relatively easy and unambiguous, the measurements showing that over the composition range there was a 75% decrease in particle size. The average particle size dropped from 2.8 nm in the control sol generated 0% ϕ_{DMSO} to 0.7 nm for the sol generate in 90% ϕ_{DMSO}. A 3D PSD is shown in Figure 123. This clearly shows the progression to smaller particles sizes as ϕ_{DMSO} was increased, with the mode shifting exponentially downward from 3nm to 1 nm, and the breadth of the distribution changing from 4 size classes to just 2.

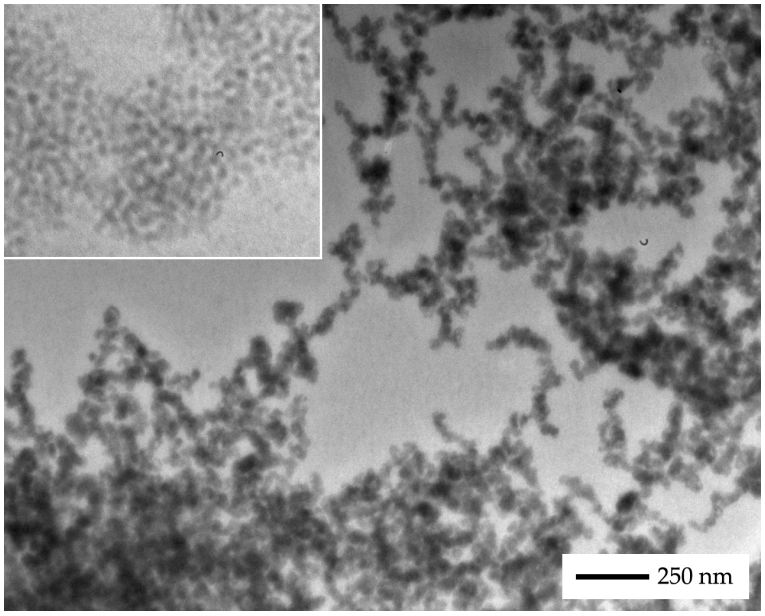

Figure 122: TEM micrograph of an ARG-protected palladium sol reduced by borohydride in 50% v/v MeOH.

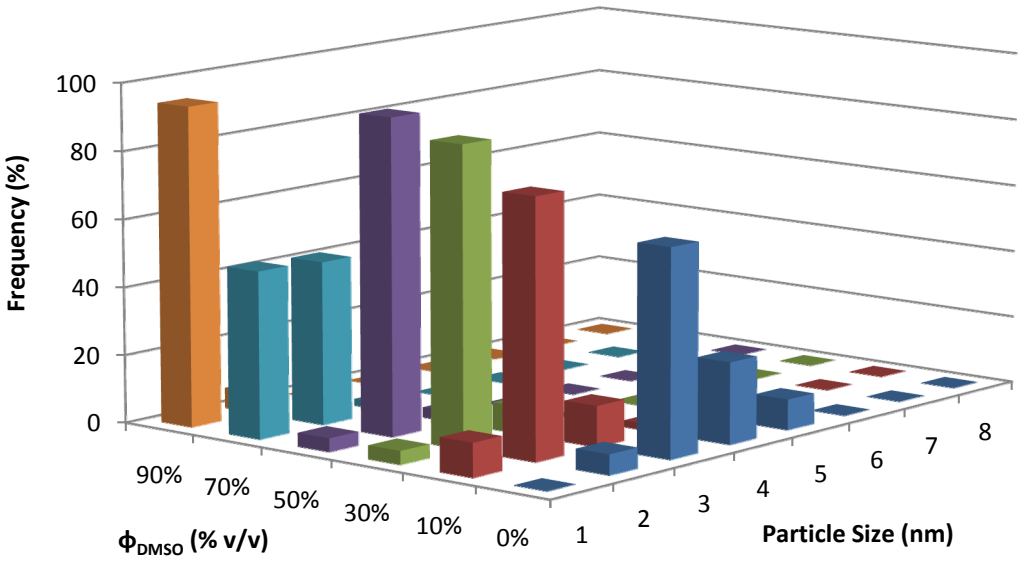

Figure 123: 3D PSD obtained by TEM for ARG-protected palladium sols reduced by borohydride reduction in mixtures of water and DMSO, showing the evolution of the PSD with ϕ_{DMSO}.

6.3.1.3 UV/Vis Data

The A_{450} measurements showed a net decrease in sol density as ϕ_{DMSO} was increased, dipping sharply at low DMSO concentrations but increasing as the DMSO concentration was increased. A plot of the A_{450} values versus ϕ_{DMSO} is shown in Figure 124.

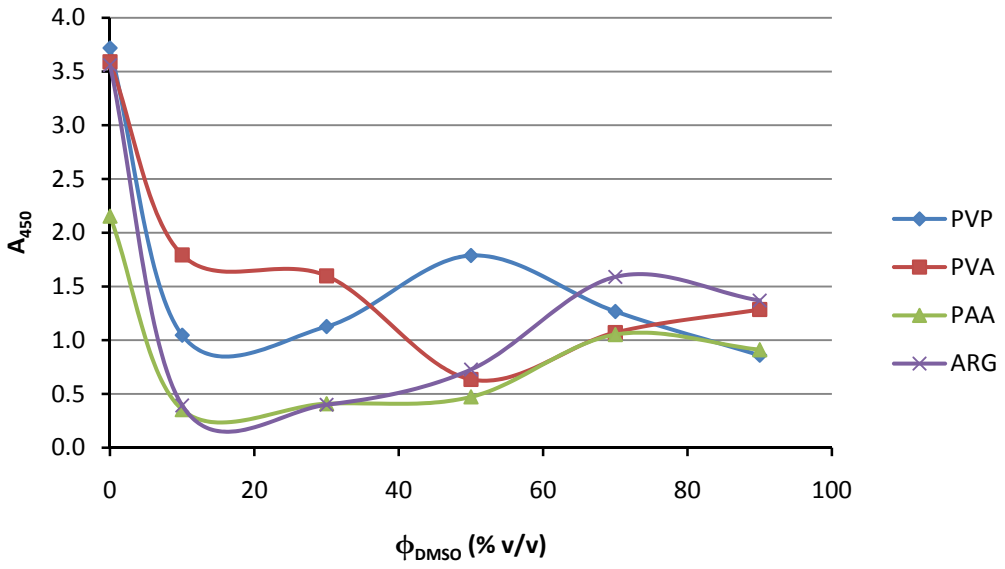

Figure 124: Plot of the dilution-corrected A_{450} versus ϕ_{DMSO} for protected palladium sols reduced by borohydride in mixtures of water and DMSO.

These measurements were somewhat difficult to completely rationalise, although several important points can be made. The sols generated in mixed-media containing low DMSO concentrations had larger particle sizes, and consequently the A_{450} values were relatively high. Conversely, the sols generated in mixed-media containing high DMSO concentrations had smaller particle sizes, and consequently the A_{450} values were relatively low. The relationship between these two measurements was clearly evident at these compositions because they displayed relatively little aggregation, however at intermediate compositions the aggregation was generally observed to be higher, and consequently the A_{450} values displayed more complex trends dependent on the size and morphology of

the aggregates present. The exact morphology of these aggregates was expected to alter the way in which they scattered light, giving rise to the unpredictability observed at these compositions.

Despite these difficulties, the trends were found to mirror the levels of aggregation observed by TEM to a reasonable approximation, indicating that generally the aggregates observed *ex-situ* were also present *in-situ*. When the levels of aggregation were sufficiently large to cause sedimentation of the suspended particles the A_{450} values were relatively low, but in cases where the aggregates were the aggregates were large enough to remain suspended colloidally, the A_{450} values were observed to be relatively higher.

6.3.1.4 PCS Data

The PCS measurements, plotted against ϕ_{DMSO} in Figure 125, show similar trends to the A_{450} measurements, with the average hydrodynamic size approximating the levels of aggregation in the system. As stated in the Section 6.2, this is expected to be a combination of real changes in aggregate sizes and inadequacies in the measurement parameters. Regardless, PCS indicates that the largest aggregates *in-situ* were formed at intermediate compositions, as previously observed.

The PVP-protected sols showed a maximum at 50% ϕ_{DMSO} as did the PVA-protected sols; PAA shows a broad increase over all composition ranges although slowly decreasing as ϕ_{DMSO} was increased, again consistent with its general lack of stability. ARG appeared to be least stable at low DMSO concentrations, becoming more stable although possessing aggregates of several hundred nanometres at intermediate compositions and small aggregates at high concentrations. This data was consistent with both the UV/Vis measurements and the levels of stability

observed macroscopically, and also agreed well with observations made *ex-situ* by TEM.

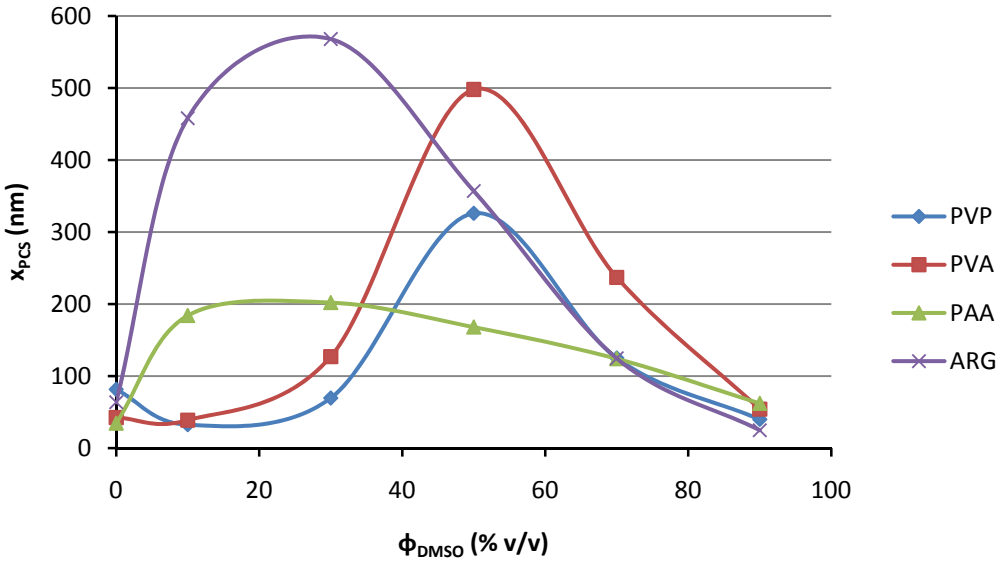

Figure 125: Plot of x_{PCS} versus ϕ_{DMSO} for protected palladium sols reduced by borohydride in mixtures of water and DMSO.

6.3.2 Hydrazine-Reduced Sols

6.3.2.1 General Remarks

Palladium colloids generated by hydrazine reduction in mixtures of water and DMSO displayed similar trends to those reduced by borohydride. Macroscopically they appeared to be more stable, with only 20% displaying visible signs of aggregation, compared to 40% for the borohydride-reduced sols. Microscopically however, they appeared to be more prone to aggregation. Photographs of the sols produced are shown in Figure 126, and a summary of the data collected is given in Table 18.

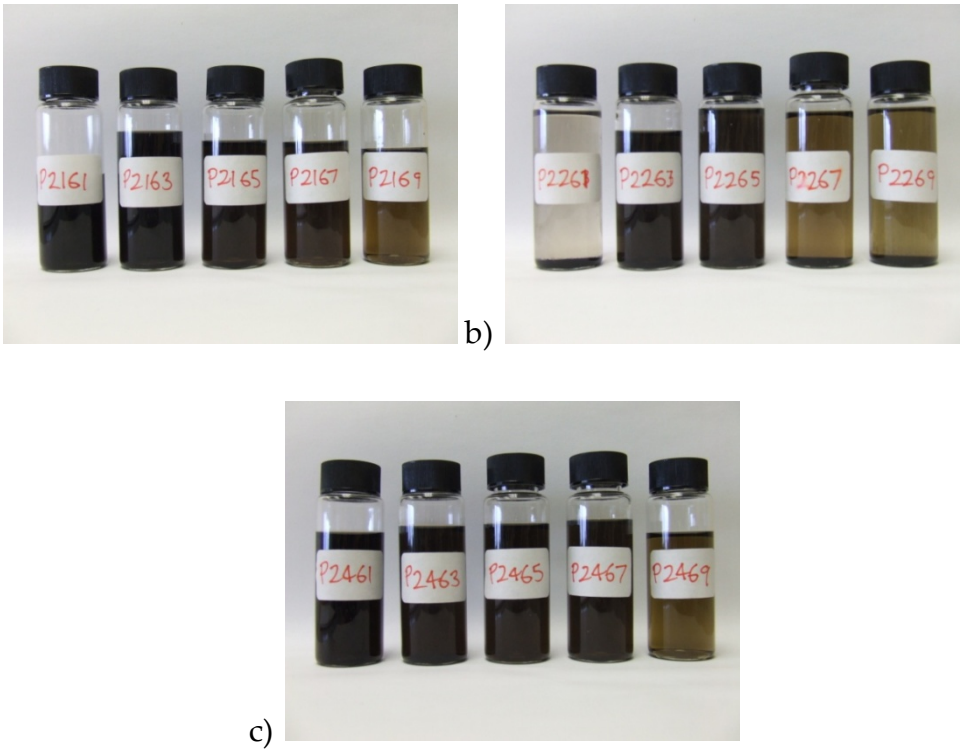

Figure 126: Photographs of palladium sols reduced by hydrazine in mixtures of water and DMSO, and protected by a) PVP, b) PVA, c) ARG. The DMSO concentration increases in each photo from 10% v/v left, to 30%, 50%, 70%, and 90% right. The labels on the vials refer to the conditions of their synthesis as described in Appendix 1.

Their synthesis was similar to those reduced by borohydride, with all generated sols displaying the 'red phase', with no obvious changes in either its persistence of its colour with the use of hydrazine rather than

borohydride as the reducing agent. As with previous preparations the PAA-protected sols were unsuccessful and resulted in a solution rather than colloidal palladium. Similar problems were encountered with precipitation of the protecting agents.

		TEM		PCS	UV/Vis
Protectant	ϕ_{DMSO}	$\bar{x}$ (nm)	σ (nm)	x_{PCS} (nm)	A_{450}
PVP	10	2.4	0.7	406.0	1.25
	30	2.2	0.6	171.0	0.18
	50	2.0	0.4	99.0	0.85
	70	1.7	0.3	290.0	0.88
	90	1.4	0.4	155.0	0.54
PVA	10	2.0	0.3	68.0	0.37
	30	1.7	0.3	303.0	0.80
	50	1.4	0.3	457.0	0.80
	70	1.3	0.3	178.0	0.50
	90	1.2	0.3	67.0	0.67
PAA	10	Solution generated instead of colloid			
	30	Solution generated instead of colloid			
	50	Solution generated instead of colloid			
	70	Solution generated instead of colloid			
	90	Solution generated instead of colloid			
ARG	10	2.1	0.5	95.0	1.10
	30	1.8	0.4	116.0	0.01
	50	1.7	0.3	101.0	0.80
	70	1.5	0.3	203.0	0.95
	90	1.3	0.2	79.0	0.42

Table 18: Summary of the TEM, PCS and UV/Vis data collected for palladium sols reduced by hydrazine in aqueous DMSO.

6.3.2.2 TEM Data

The average particle size, $\bar{x}$, was shown to be inversely proportional to ϕ_{DMSO}, similar to the other systems studied. The percentage decrease in $\bar{x}$ when hydrazine was used as the reducing agent was shown to be smaller compared to the borohydride-reduced equivalents, typically around 40%. Plots of $\bar{x}$ versus ϕ_{DMSO} are given in Figure 127. The polydispersity of the sols, σ, was also inversely proportional to ϕ_{DMSO}. A plot of σ versus ϕ_{DMSO} is given in Figure 128.

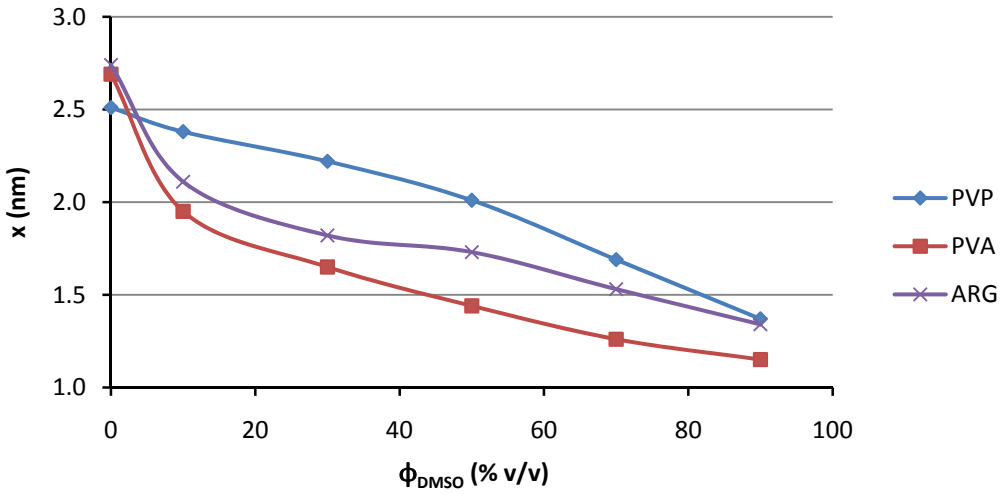

Figure 127: Plot of $\bar{x}$ versus ϕ_{DMSO} for protected palladium sols reduced by hydrazine in mixtures of water and DMSO.

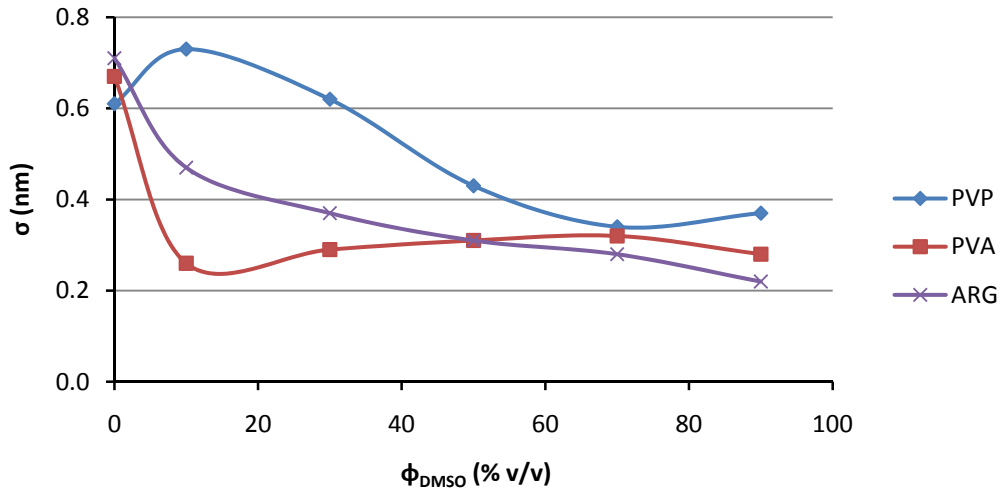

Figure 128: Plot of σ versus ϕ_{DMSO} for protected palladium sols reduced by hydrazine in mixtures of water and DMSO.

6.3.2.2.1 PVP-Protected Sols

For PVP-protected sols the nature of the aggregates observed in the TEM micrographs changed almost linearly with ϕ_{DMSO}. At low DMSO concentrations, particles assumed morphologies typical of those in the control experiment with 0% ϕ_{DMSO}, giving small (10 nm – 50 nm) irregular aggregates. As the concentration of DMSO was increased further these aggregates became progressively less irregular and assumed nearly spherical 'bundles' of particles, similar to those described in previous sections. Micrographs illustrating these two extremes are shown in Figure 129. While the shapes of the aggregates changed significantly, the morphologies of the primary particles did not change at all over the composition range, all being well-rounded with no necklacing between particles.

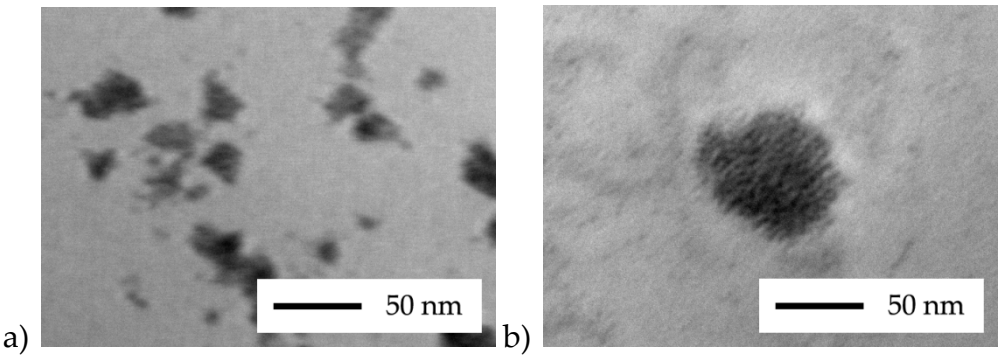

Figure 129: TEM micrographs of PVP-protected palladium sols reduced by hydrazine in aqueous DMSO, illustrating the change from the typical aggregate structure (a) to the atypical bundle structure (b).

The size of the primary particles was shown to decrease almost linearly from 2.5 nm in the control experiment with 0% ϕ_{DMSO} to 1.7 nm in 90% ϕ_{DMSO}, a decrease of 45% across the composition range studied. The polydispersity also decreased simultaneously. A 3D PSD is shown in Figure 130 illustrating these trends.

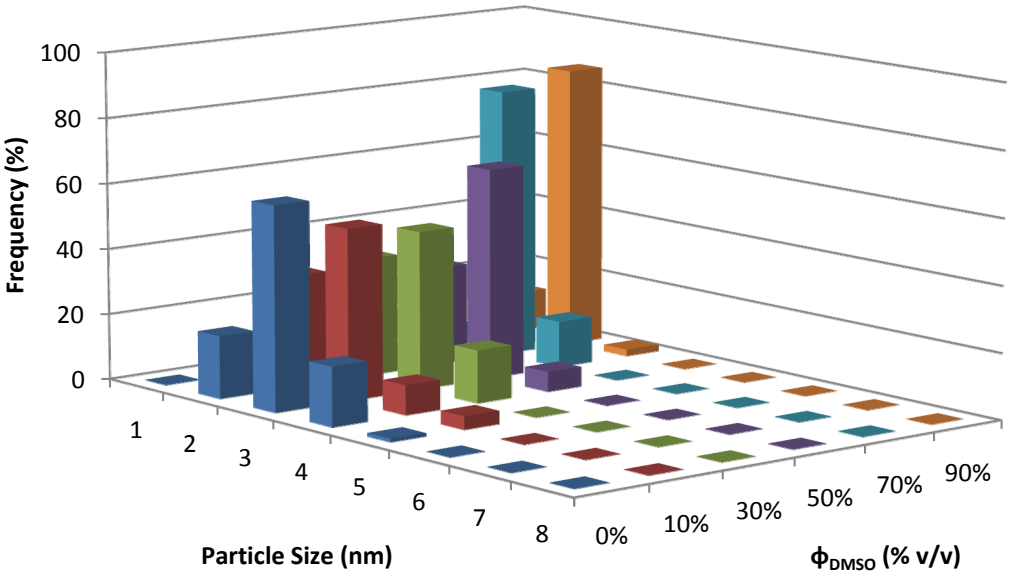

Figure 130: 3D PSD obtained by TEM for PVP-protected palladium sols reduced by hydrazine in mixtures of water and DMSO, showing the evolution of the PSD with ϕ_{DMSO}.

6.3.2.2.2 PVA-Protected Sols

For PVA-protected sols, at lower DMSO concentrations the aggregates as observed by TEM tended to exist in large densely-packed morphologies, similar to those which occur with PVA hydrosols in water. As the DMSO concentration was increased these aggregates slowly branched out and became more open, and began to resemble the compound aggregate structure described previously. As the DMSO concentration was increased further they began to exist as closely-associated 'bundles' toward 90% ϕ_{DMSO}. At low DMSO concentrations the particles were also heavily necklaced, but increasing the DMSO concentration suppressed this tendency, becoming completely absent by approximately 50% ϕ_{DMSO}. Some micrographs illustrating these transitions are shown in Figure 131.

When they were not necklaced together, the primary particles were well-rounded with no unusual morphological traits. Their sizes were observed to decrease 57% across the composition range studied, dropping from

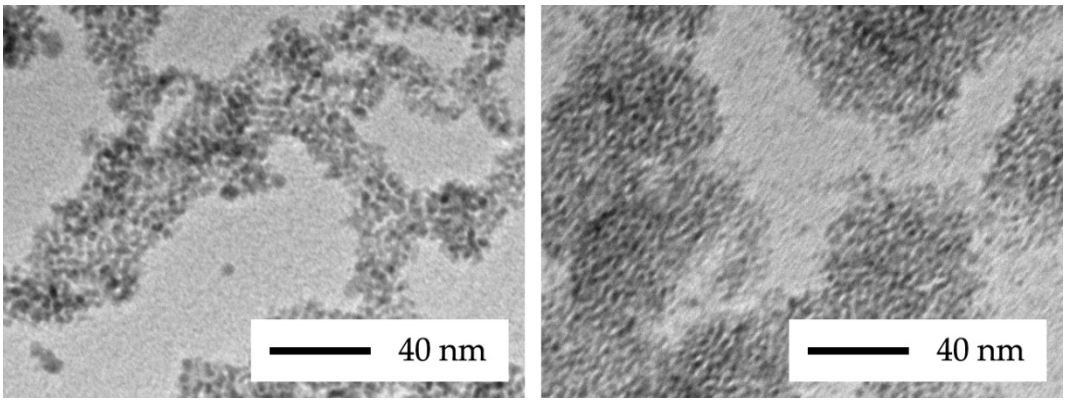

Figure 131: TEM micrographs of PVA-protected palladium sols reduced by hydrazine reduction in aqueous DMSO. Left is generated at low DMSO concentration with high levels of necklacing, right is at high concentration with no necklacing.

2.7 nm for the sol generated in 0% ϕ_{DMSO} to 1.2 nm for the sol generated in 90% ϕ_{DMSO}. This decrease was not as linear as it was for the PVP-protected sol, dropping sharply at low concentrations and decreasing linearly from then onward. The polydispersity of the system unusually did not decrease linearly with ϕ_{DMSO} as observed with other systems, rather it dropped quickly initially before levelling off thereafter. A 3D PSD is shown in Figure 132 illustrating these points. The modal size class shifted from 3 nm to 2 nm, but the breadth of the distributions did not change over all.

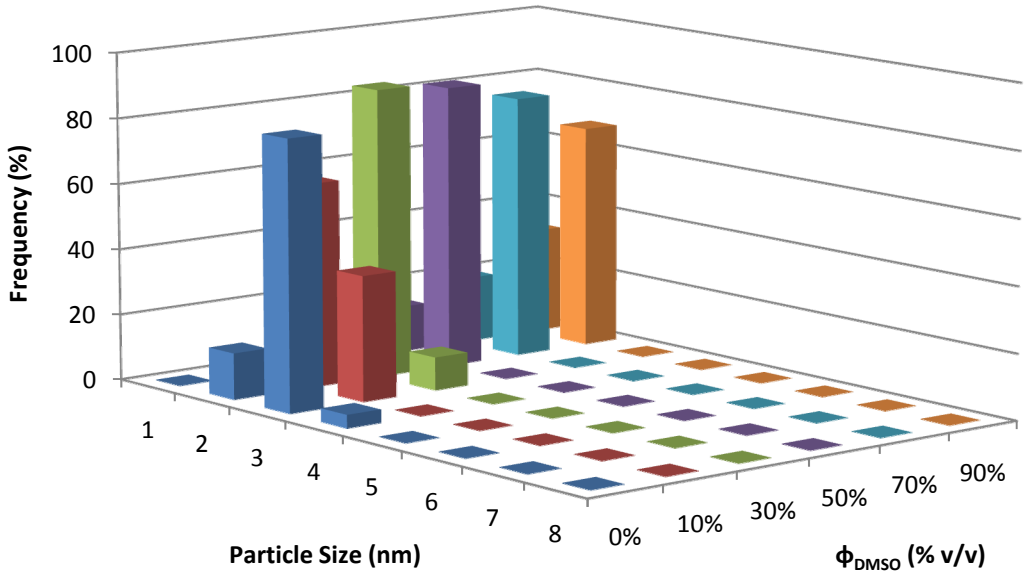

Figure 132: 3D PSD obtained by TEM for PVA-protected palladium sols reduced by hydrazine in mixtures of water and DMSO, showing the evolution of the PSD with ϕ_{DMSO}.

6.3.2.2.3 ARG-Protected Sols

For ARG-protected sols $\bar{x}$ decreased in a manner similar to the PVA-protected sols, dropping 51% from 2.8 nm for those produced in the 0% ϕ_{DMSO} to 1.3 nm for those produced in 90% ϕ_{DMSO}. A 3D PSD is shown in Figure 133 illustrating this. There did not appear to be any observable necklacing between particles at any composition, all particles being relatively spherical. The size of the aggregates was largest at intermediate compositions, decreasing again toward the extremes of the composition range. The morphology of the aggregates was typical of that of colloids generated by reduction with hydrazine, being generally semi-round existing in discrete groups. A micrograph is shown in Figure 134. No 'compound aggregates' were observed at any composition.

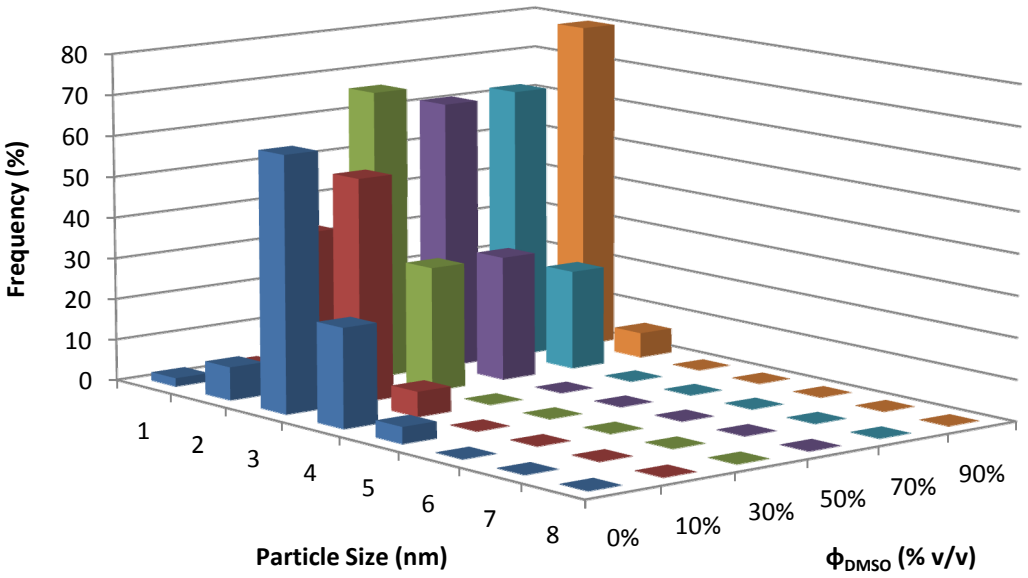

Figure 133: 3D PSD obtained by TEM for ARG-protected palladium sols reduced by hydrazine in mixtures of water and DMSO, showing the evolution of the PSD with ϕ_{DMSO}.

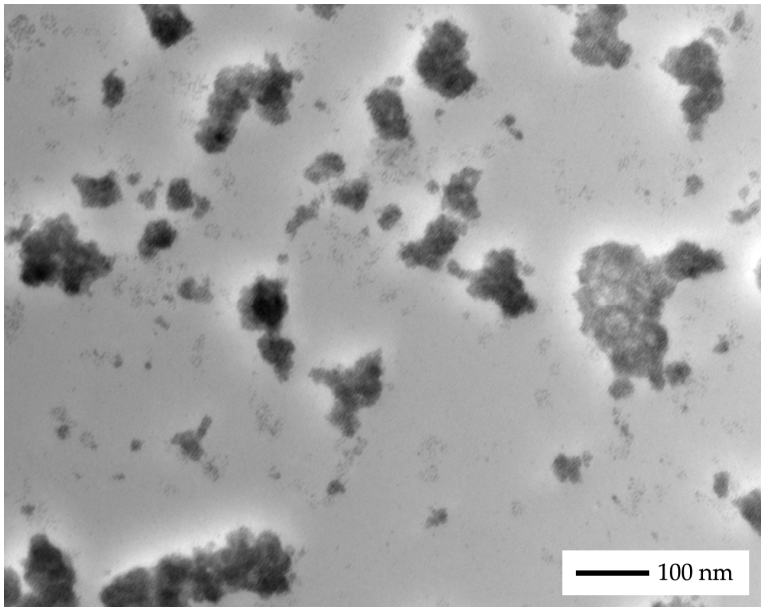

Figure 134: TEM micrograph of an ARG-protected palladium sol reduced by hydrazine in 30% ϕ_{DMSO}.

6.3.2.3 UV/Vis Data

The A_{450} data obtained by UV/Vis closely followed the trends in the sizes of the aggregates observed in the TEM micrographs. A plot of the A_{450} values versus ϕ_{DMSO} is shown in Figure 135.

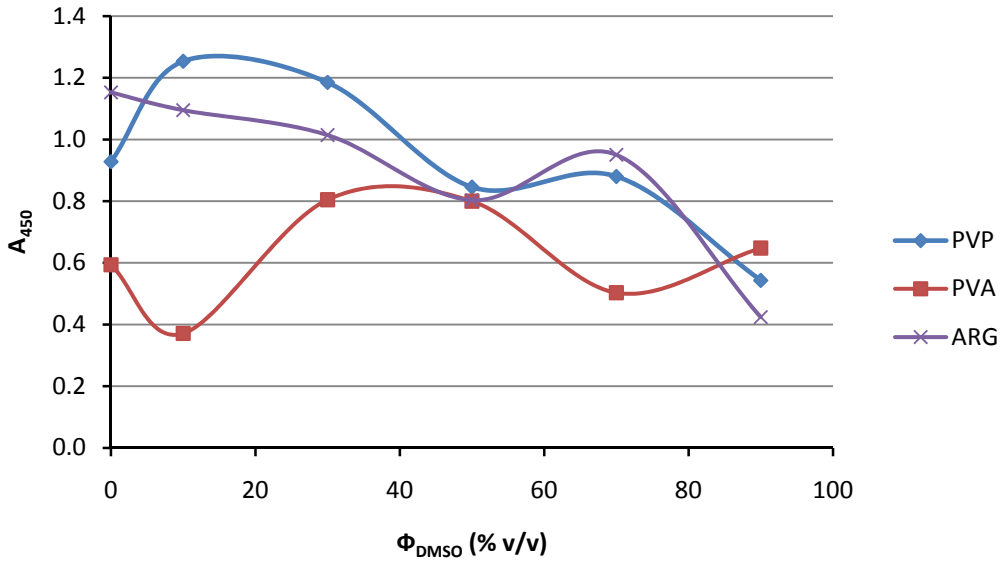

Figure 135: Plot of the dilution-corrected A_{450} values versus ϕ_{DMSO} for protected palladium sols reduced by hydrazine in mixtures of water and DMSO.

The PVP-protected sols showed increased levels of aggregation in the TEM micrographs in the ranges of 10% - 30% ϕ_{DMSO}, consequently the A_{450} values were higher in this range. At intermediate compositions the levels of aggregation between primary particles remaining suspended in solution was observed to be lower than in the control experiment, and as a consequence the A_{450} values decreased correspondingly, dropping to below 1. As ϕ_{DMSO} was increased further $\bar{x}$ decreased but the aggregation remained constant, and as a consequence the A_{450} values decreased. The PCS data (Section 6.3.2.4) also mirrored these trends, confirming that they were real.

TEM and UV/Vis measurements were much harder to reconcile with one another for the PVA-protected sols, as the sols suffered extensively from

formation of compound aggregates during the extraction process at low concentrations of DMSO. At intermediate compositions the A_{450} values were significantly higher than at either end of the composition range, indicating that the average particle size must have been larger. This was observed in the micrographs, where frequently 20 nm - 40 nm aggregates were observed which decreased in size as the DMSO concentration was increased. This was consistent with the extraction process only having affected the morphology of the aggregates at low DMSO concentrations. The presence of these aggregates prior to extraction is further supported by the PCS data which indicates an increase in particle size *in-situ* at intermediate compositions. Again the increase observed was far in excess of what is observed by TEM.

The UV data for the ARG-protected sols showed that the turbidity generally decreased as ϕ_{DMSO} was increased, with only a brief increase at 70% ϕ_{DMSO}. This peak was also present in the PCS data, which showed that the average hydrodynamic radius increased relative to the control experiment at this composition. The increase in diameter detected by PCS was approximately 100 nm at intermediate compositions, which was approximately the increase in the size of the aggregates as seen in the TEM micrographs, therefore was assumed to be real.

6.3.2.4 PCS Data

As mentioned previously, the PCS data collected was similar to the UV/Vis data. A plot of the x_{PCS} values versus ϕ_{DMSO} is shown in Figure 136. As with previous systems, the changes in the average hydrodynamic size appear to be much larger than the changes observed in the A_{450} plots, which was probably due to the way the data for PCS was collected and analysed by the instrument.

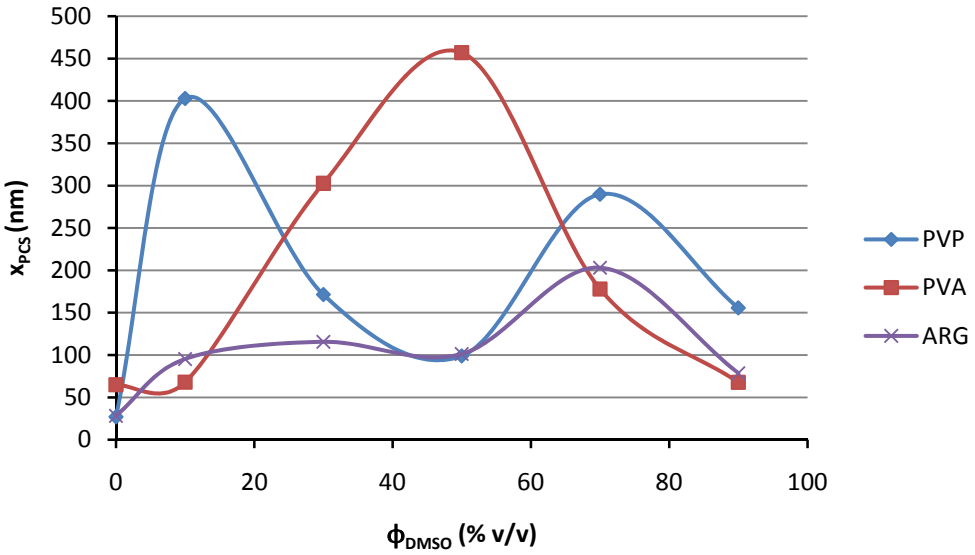

Figure 136: Plot of A_{450} versus ϕ_{DMSO} for protected palladium sols reduced by hydrazine in mixtures of water and DMSO.

For PVP and ARG protected sols, the plots were "M-shaped", with peaks at 10% ϕ_{DMSO} and 70% ϕ_{DMSO}. As stated previously this supports the observation of increased levels of aggregation in the TEM micrographs at these concentrations. For the PVA-protected sol, the average hydrodynamic size increased steadily from 56 nm to 457 nm at 50% ϕ_{DMSO}, supporting the formation of aggregates *in-situ* at intermediate DMSO concentrations but not at either end of the composition range.

6.4 Sols in Aqueous Dimethylformamide

Dimethylformamide was found to be even better a cosolvent when mixed with water for the formation of palladium sols than it was for rhodium sols. No preparations suffered from the prevention of reduction as found with rhodium, or from precipitation of the protecting agents as found with other less polar solvents. The majority of sols were stable for at least a year.

The synthesis of the sols otherwise exhibited similar characteristics to those described previously, with an increase in ϕ_{DMF} causing a decrease in the darkening time, although eventually becoming the dark colour indicating formation of colloidal palladium.

Unfortunately at the time of writing TEM micrographs had not been acquired for all of the following sols due to an unknown operational fault in the TEM used to collect them, hence only PCS and UV data are available.

6.4.1 Borohydride-Reduced Sols

6.4.1.1 General Remarks

The vast majority of borohydride-reduced sols were found to be stable over the period during which they were studied, with only a few sols at intermediate compositions displaying signs of aggregation many weeks after their synthesis. The notable exception to this rule was the PVA-protected sol in 50% v/v ϕ_{DMF}, which was completely unstable and completely aggregated within hours of preparation. Photographs of the sols are shown in Figure 137. All other sols were a dark black colour, and remained this way for many months.

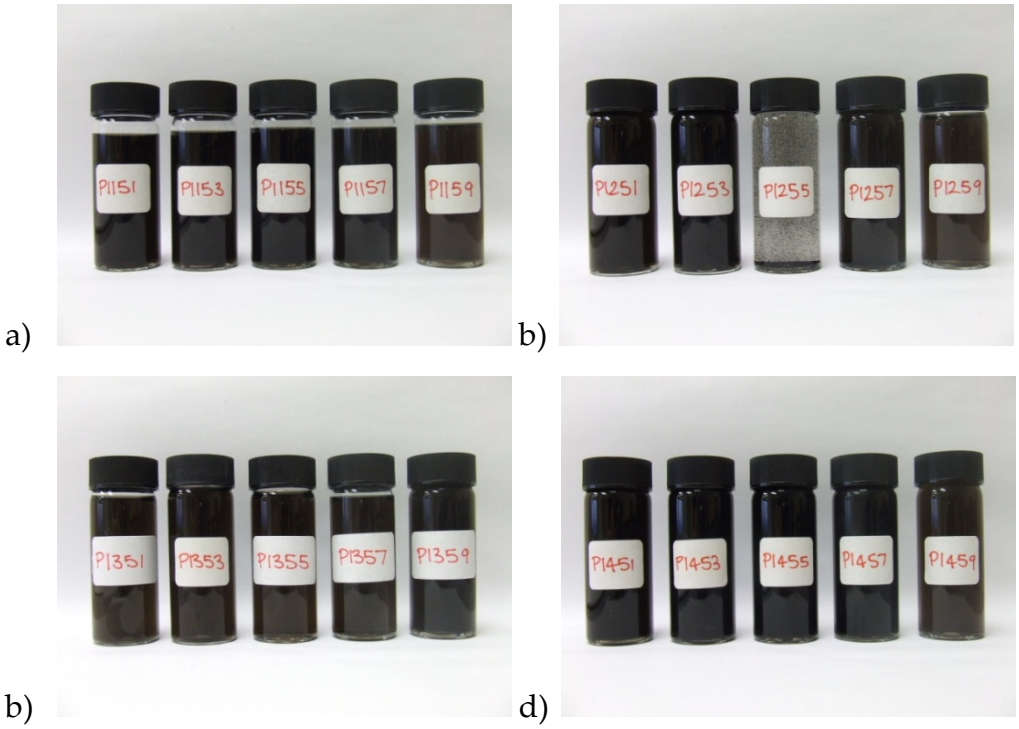

Figure 137: Photographs of palladium colloids generated by borohydride reduction in aqueous DMF, protected by a) PVP, b) PVA, c) PAA, d) ARG. The concentration of DMF increases in each photo from 10% v/v (left), to 30%, 50%, 70%, to 90% (right). The labels on the vials refer to the conditions of their synthesis as described in Appendix 1.

6.4.1.2 TEM Data

As mentioned previously no TEM micrographs could be collected for these sols. Samples were prepared for TEM analysis regardless, using the previously described heptane extraction technique. While it could not be confirmed that the extraction method worked as well for this set of sols as it did for the others, under an optical microscope no signs were observed indicating that the collodion sample supports on the copper grids were dissolved.

6.4.1.3 UV/Vis Data

The A_{450} values collected supported the visual appearance of the sols insofar as that they were relatively large, compared to previously

described sols with light colours which had A_{450} values below 1. A plot of the A_{450} values versus ϕ_{DMF} is shown in Figure 138.

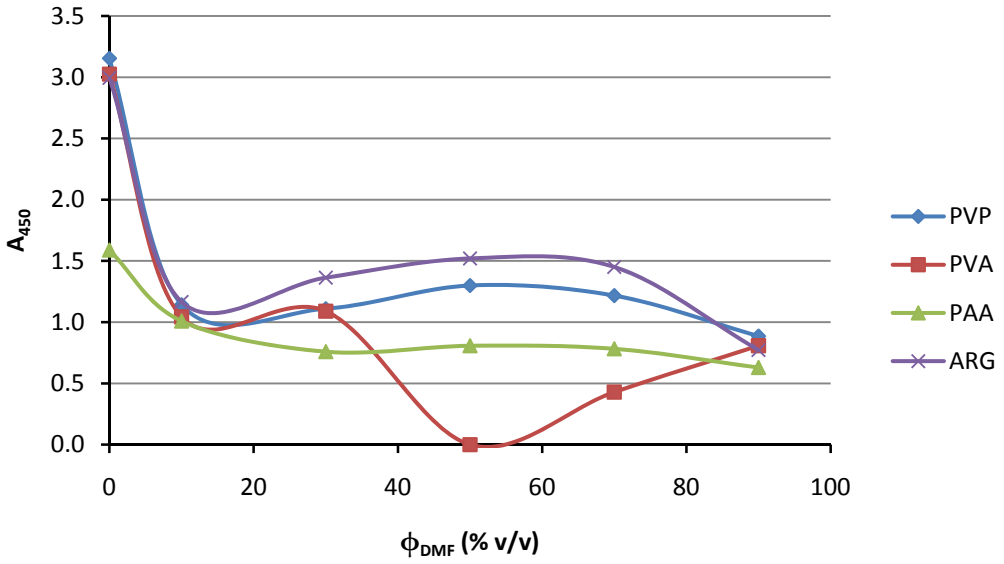

Figure 138: Plot of the dilution-corrected A_{450} values versus ϕ_{DMF} for protected palladium sols reduced by borohydride in mixtures of water and DMF.

Where sols protected by PVP, PAA, and ARG all appeared to be exactly the same colour, their A_{450} values were all similar when generated in mixtures of water and DMF, with broad peaks at intermediate compositions. All values were lower relative to the control sols. In the absence of any particle size data obtained by TEM, no comparisons could be made surrounding the correlation between the levels of aggregation and the A_{450} values, although several inferences were made based on previously discussed systems. The sharp decrease in the A_{450} values at 10% ϕ_{DMF} had been observed previously in the Pd/DMSO system, where it was caused by a sudden decrease in $\bar{x}$ coupled with a small increase in the levels of aggregation. Because the A_{450} values remained relatively constant thereafter, it was deemed reasonable to assume that there were no large changes in the size of the aggregates, but the aggregate size probably reached a peak at approximately 50% ϕ_{DMF}. This theory was supported by

measurements of the radius of gyration of the various protecting agents in mixtures of water and DMF as discussed in Section 6.9. The PVA-protected sols showed similar trends to the sols protected by the other three protecting agents, except for a region of instability around 50% ϕ_{DMSO}, where the levels of aggregation were obviously much larger, as the particles were observed to aggregate and sediment macroscopically.

6.4.1.4 PCS Data

The PCS data collected corroborated the trends in the UV/Vis data, although the increases in the hydrodynamic size were disproportionately large once again, consistent with the reasons described previously. A plot of the average hydrodynamic radius, x_{PCS}, versus ϕ_{DMF} is shown in Figure 139.

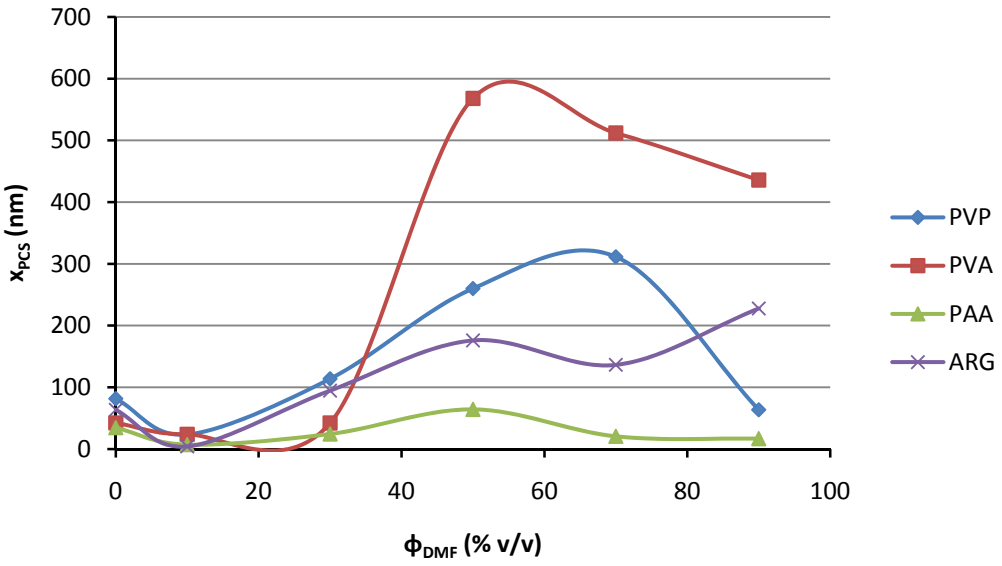

Figure 139: Plot of x_{PCS} versus ϕ_{DMF} for protected palladium sols reduced by borohydride in mixtures of water and DMF.

The hydrodynamic size of the sols protected by all four of the protecting agents was shown to decrease initially as ϕ_{DMF} was increased, coming to a peak size at approximately 50% - 70% ϕ_{DMF}. The unusual feature of this was this trend was also observed for the PVA-protected sol, which was

observed to have a very low A_{450} value and high levels of aggregation. The origins of this are unclear, however it is possible that the trend was reversed because PCS is sensitive to large aggregates. A second possibility is that because the UV/Vis instrument relies on transmission of light through the sample (i.e. the scattering angle is 180° relative to the incident beam) whereas PCS collects scattered light (collected at 90° to the incident beam), the specific morphologies of the aggregates dictated that the isotropy in their scattering intensity disposed them to detection more easily by PCS than UV/Vis.

If the DMF system displayed at least remote similarities to the other mixed-media sols described previously, then several hypothesis could be postulated surrounding the microscopic (or "nanoscopic", perhaps more accurately) behaviour of the sols. Firstly, the size of the primary particles probably decreased as ϕ_{DMF} was increased, and correspondingly the polydispersity probably decreased simultaneously. No hypothesis could be made on the levels of necklacing between particles. Due to the use of the heptane extraction method however, the particles would probably have appeared on the TEM grids in the 'compound aggregate structure'. Since the colour of the sols did not change significantly from pitch-black, there was probably some level of aggregation *in-situ* for each preparation, as discussed previously. If in any of the sols the particles existed as discrete primary particles *in-situ*, then it could be expected that the sols would be a lighter colour, as observed with previous mixed-media systems. As the data indicates that the turbidity and hydrodynamic radius are lower at 10% ϕ_{DMF}, this probably means there is less aggregation at this point in concentration. The aggregation probably slowly increases in very small amounts with ϕ_{DMF}, which would account for the mild increases in the turbidity and the increase in the PCS data.

6.4.2 Hydrazine Reduced Sols

6.4.2.1 General Remarks

When hydrazine was used as the reducing agent instead of borohydride, the behaviour of the sols was not as consistent across the composition range as when borohydride was used. Not all sols were black as when generated by borohydride reduction, but became dark brown in media containing high DMF concentrations, assumed to be a sign of mild size-dependence on ϕ_{DMF}, an effect especially evident for ARG-protected sols. A photograph of the sols is shown in Figure 140.

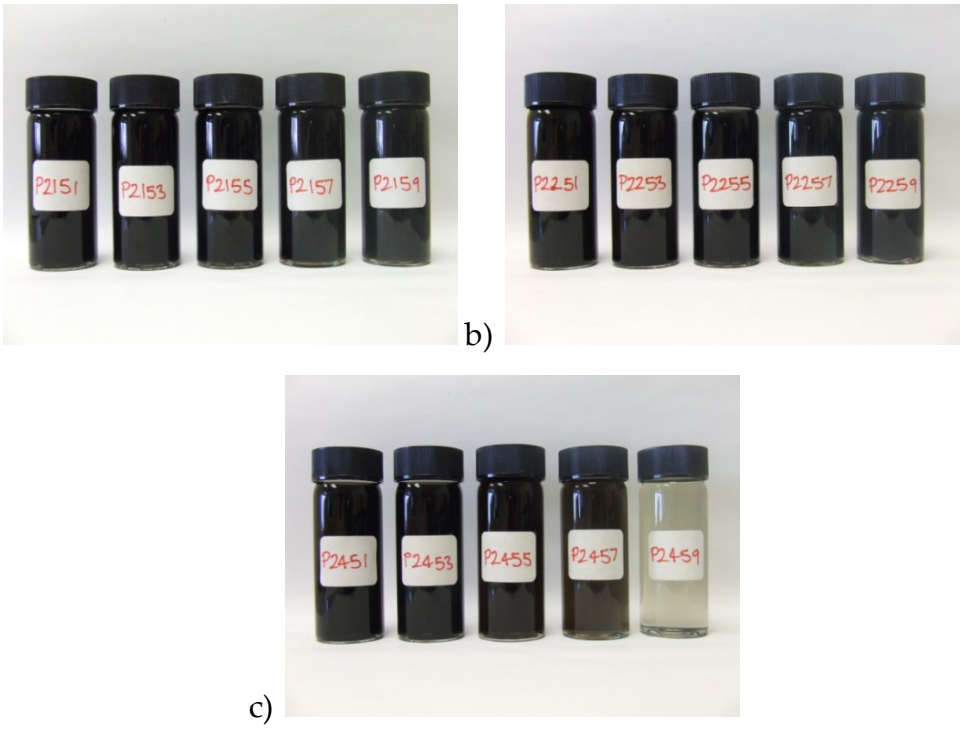

Figure 140: Photographs of palladium colloids reduced by hydrazine in aqueous DMF, protected by a) PVP, b) PVA, c) ARG.

6.4.2.2 TEM Data

As with the borohydride-generated sols, no TEM data could be collected. The heptane extraction technique was also assumed to work with the hydrazine-reduced sols, as no dissolution of the collodion sample support was evident under an optical microscope.

6.4.2.3 UV/Vis Data

The A_{450} data indicated that for the sols protected by PVP and PVA there was an overall increase in turbidity. This was taken to be a sign of an increase in the levels of aggregation occurring in the system. As with previous mixed-media systems, it is likely that the decrease in the average primary particle size was not as significant with the hydrazine-reduced sols as for the borohydride-reduced equivalents, thus the changes in aggregation probably contributed more to the A_{450} values than the changes in the particle size detracted from the turbidity. A plot of the A_{450} values versus ϕ_{DMF} is given in Figure 141.

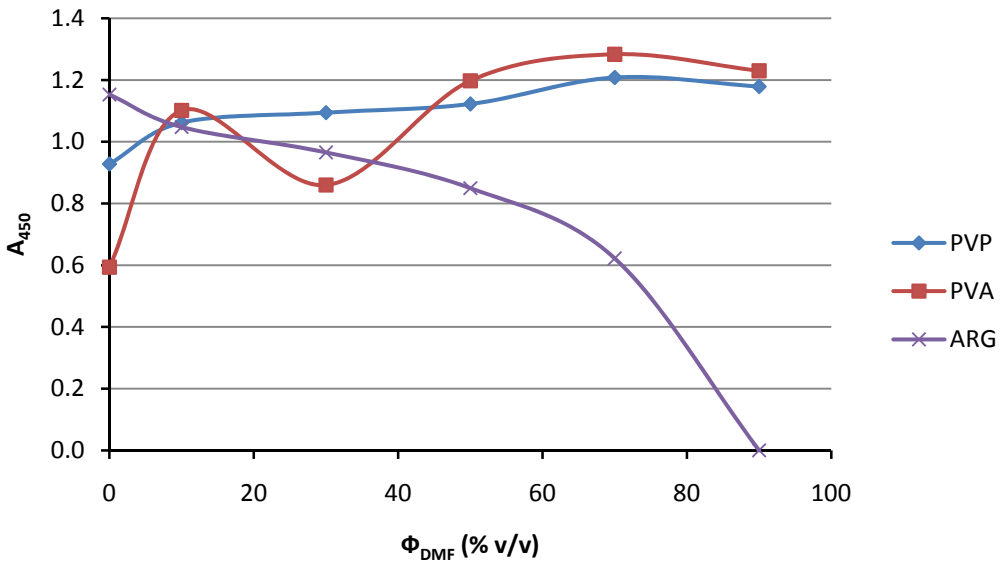

Figure 141: Plot of the dilution-corrected A_{450} values versus ϕ_{DMF} for protected palladium sols reduced by hydrazine in mixtures of water and DMF.

The changes in the A_{450} values for the PVP-protected system are only mild; increasing from 0.85 to 1.2 over the composition range studied. The PCS data loosely supports this, showing a net increase in the hydrodynamic radius of approximately 500 nm.

Also observed with borohydride, the behaviour of the PVA-protected sol appeared to vary widely with composition. Overall the turbidity

increased, although there were significant fluctuations in the A_{450} value. The sols all appeared visually to be pitch black, so the fluctuations in the turbidity were likely a result of significant changes in the morphology of the aggregates present in the system. In previous mixed-media systems using PVA as a protecting agent this has been shown to be quite significant.

The data collected for the ARG-protected sols showed a continuous net decrease in the turbidity of the system. Similarly the colours of the sols decreased from black to nearly clear, indicating that there is likely very little aggregation in this system, and the change in both the colour and the A_{450} value are due predominantly to the particle size.

6.4.2.4 PCS Data

Unexpectedly the PCS data collected for ARG-protected sols displayed the opposite trend to the UV/Vis data, giving a large net increase in particle size. A plot of the x_{PCS} values versus ϕ_{DMF} are given in Figure 142.

This trend was observed for the sols protected by all three protecting agents. This seemingly contrary set of data perhaps arose due to the change in the conformation of the polymers in solution. As discussed further in section 6.9, the changes in the radius of gyration of some polymers in mixtures of water and DMF can be rather complicated. This probably lead not only to changes in the levels of aggregation, but also changes in the hydrodynamic mobility of the particles, the combination of which may have given rise to the apparently complicated trends in the PCS data.

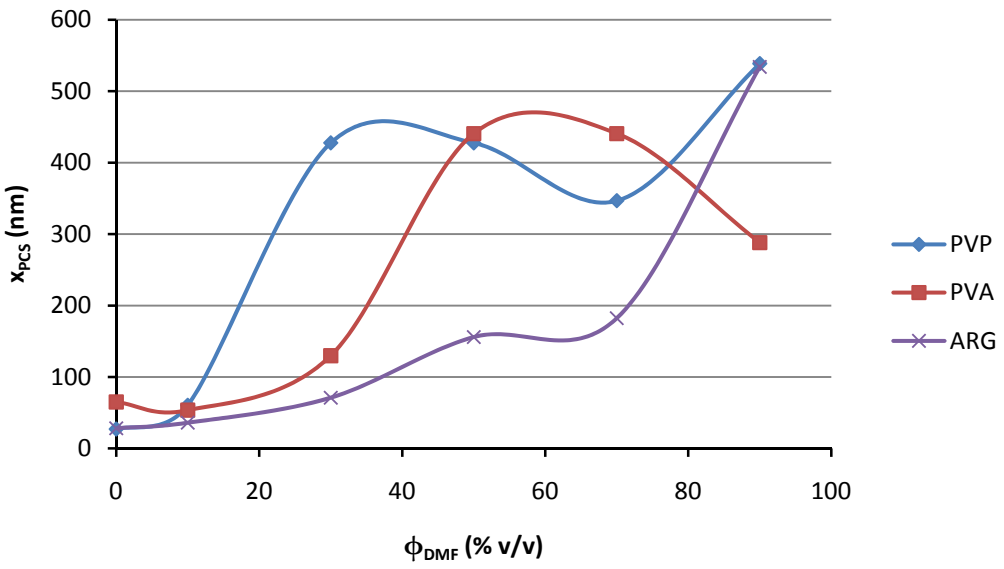

Figure 142: Plot of x_{PCS} versus ϕ_{DMF} for protected palladium sols reduced by hydrazine in mixtures of water and DMF.

6.5 Sols in Aqueous Acetonitrile

The synthesis of palladium sols in mixtures of water and acetonitrile appeared to be feasible, although no attempts were made to fully characterise the resulting sols. The majority of syntheses ended in either protecting agent precipitation, or a precipitate of palladium black. In few cases was a stable dark black colloid produced successfully.

With respect to the precipitation of the protecting agent, acetonitrile behaved similarly to methanol, although the solubility of both PVP and PAA was less in acetonitrile mixtures than in any of the other solvents.

For those preparations which did not result in the precipitation of the protecting agent, the colloids which resulted from these were very often highly unstable. This was presumed to be an indication of MeCN acting as an antisolvent for the protecting agents used, compressing the polymer layers adsorbed to the particle surfaces to such an extent that particles could approach one another with sufficient distance that aggregation could occur. This was found to be especially problematic for PVA, which formed large aggregates almost instantaneously after the addition of the reducing agent during synthesis.

For the aforementioned reasons, characterisation of the colloids generated in aqueous acetonitrile was abandoned, as they were too unstable to run either PCS or UV/Vis scans of. In addition the aggregates formed were too large to place onto TEM grids, and could not be broken up by sonication for a sufficiently long period to prepare the samples. These problems were encountered for almost all combinations of all protecting agents, using either borohydride or hydrazine as a reducing agent.

6.6 Sols in Aqueous Acetone

Syntheses of palladium colloids in acetone were abandoned for the same reasons as rhodium colloids described in Section 5.6, dissolution of the protecting agent. All syntheses attempted displayed similar characteristics, with the formation of a stable palladium colloid feasible in mixtures with low $\phi_{acetone}$ values (high water contents), but not in mixed-media with compositions greater than approximately 30% v/v acetone where precipitation of the protecting agent occurred.

6.7 Sols in Aqueous Tetrahydrofuran

Syntheses of palladium colloids in THF were abandoned for the same reasons as rhodium colloids in THF, where attempts to synthesise colloids in mixtures containing even relatively low proportions of THF resulted in precipitation of the protecting agent.

6.8 Explanations for the Decrease in the Primary Particle Size

The foremost question to be asked given the results presented until this point is what caused the average primary particle size ($\bar{x}$) of all systems investigated to decrease as the cosolvent proportion (ϕ) was increased. There are two possible general reasons for this.

The first possible reason is that as ϕ was increased, the level of reduction in the sols was decreased. If the level of reduction was decreased then less metal salt would be reduced to form metal particles, therefore the resulting particles would ultimately be smaller. Note that this assumption is only valid for relatively monodisperse sols, where all seed nuclei are generated nearly simultaneously.

The second possible reason is that increasing ϕ caused more seed nuclei to be formed during the nucleation period, delaying the growth period, and subsequently causing the fixed amount of metal salt precursor introduced into the system at the beginning of the synthesis to be distributed over a larger number of smaller particles.

Initially it was suspected that the first option, incomplete reduction, was the source of the decrease in particle size, as the brown colour of the sols were believed to be due to unreduced metal precursor. However, this does not explain why the rhodium sols with very small particle sizes were light brown rather than light red.

The usual route for determining incomplete reduction in such cases is analysis of the UV/Vis spectrum, however this proved unsuccessful due to several factors. The first factor was that the protecting agents and the cosolvents all displayed electronic transitions in the ultraviolet region which gave rise to strong adsorption peaks which coincided with the absorption peaks from the precursor salts. This made the presence of unreduced precursor in any of the sols hard to detect. The second factor was that it had already been shown that adding a cosolvent influenced the speciation of the precursor and changed its colour, hence attempting to identify incomplete reduction by comparison against the precursor in aqueous solution was not considered prudent.

In the absence of data from the UV/Vis spectra, it was decided that it would be useful to determine the concentration of the metal salt precursor remaining in the dispersion medium by either Atomic Absorption Spectroscopy (AAS) or Inductively Coupled Plasma Mass-Spectrometry (ICP-MS). This was the concentration of metal which remained dissolved in the dispersion medium but which had *not* been converted to zero-valent

metal particles. Alternatively this may be thought of as a way to determine 'how reduced' a colloid is, allowing one to make unequivocal claims such as 'this colloid is only 65% reduced.' If the decrease in particle size was purely due to a decrease in the level of reduction, then a plot of the percentage of reduction (or the absolute metal concentration) versus ϕ would yield a plot with a strongly positive slope. If the decrease in particle size was due to some other effect such as the nucleation process being altered, then the plot should theoretically be flat.

In order to do this analysis, the colloidal particles and any sedimented matter had to be removed completely from the dispersion medium. This was a task which proved difficult, as there was little information in the literature surrounding how to completely flocculate sterically-protected colloidal precious metal sols, and to the author's knowledge there was no literature pertaining to the same task in mixed-media. A variety of usual techniques were attempted to induce flocculation, including the addition of concentrated acids and bases, cooling, heating and bubbling with various gasses and addition of ligands to displace the protecting agents, however none proved reliable. In the end the method chosen was adapted from an effect observed earlier in the research project: precipitation of the protecting agent and associated particles using MeCN. It had been shown previously that MeCN was of sufficiently low polarity to precipitate out the protecting agents, but, most importantly, was sufficiently polar to retain the unreduced precursor salt in solution without causing it to become co-precipitated, so it remained amenable to analysis. The procedure used was as follows:

To a 15 mL Falcon tube, 4.00 mL of MeCN was added to 1.00 mL of colloid solution. A proportion of water and cosolvent was then added such that the final concentration of cosolvent in the mixture was consistent

across the samples. For example, for a sample which was originally 30% v/v DMSO, 0.7 mL of DMSO was added with 0.3 mL of water. This step was performed so that the final solvent composition was the same for all samples, as having different levels of different solvents in each sample could affect the efficiency with which the Pd was ionised and detected in the spectrometer. Samples were then filtered (0.45 μm) and submitted for analysis. Unfortunately not all samples could be analysed due to constraints of time, and additionally many samples had not been kept.

Unfortunately the results of ICP-MS analysis were inconclusive, with unpredictably varying levels of Pd in the samples due to incomplete ionisation in the instrument. It was observed after analysis that a black material had condensed onto the skimmer cones of the mass spectrometer, which was believed to be reduced Pd. This did not mean that the samples were unreduced however, as spiked samples were introduced throughout the run. The Pd standards used gave sufficiently accurate results, so the inability for the instrument to reproducibly ionise the Pd samples was assumed to be a result of the specific sample preparation method used.

In the absence of any quantitative evidence to indicate the level of reduction of the sols, qualitative evidence was used instead. Firstly, despite the non-diagnostic nature of the UV/Vis spectra, there was not ever any overwhelming presence of a precursor peak or any other unexplainable peaks, thus it was probably likely that similar levels of reduction were present in all of the sols analysed. Secondly, in the TEM micrographs it appeared as though there were more particles present in the micrographs of sols generated with high ϕ values, although this is obviously very subjective. While this evidence is far from concrete, it indicates that the decrease in $\bar{x}$ was *probably* not caused by incomplete reduction.

If the incomplete reduction theory is discounted, then the remaining option is that the decrease in $\bar{x}$ was caused by some modification of the nucleation and growth process of the particles. This was perhaps related to the observation that the time taken for the reaction medium to darken upon addition of the reducing agent was proportional to ϕ. If the solution did not darken as quickly then the particles were not growing as quickly, indicating that the system spent longer in the nucleation phase than the growth phase, resulting in smaller particles in larger numbers.

In order for the growth of the nuclei to be slowed so the system spent longer in the nucleation phase, the ability for nuclei to diffuse to and aggregate with one another must have been hindered in some fashion. This could be influenced by transport phenomena such as viscosity, however this was deemed unlikely as it would result in smaller particles when the viscosity was higher, rather than a continuous decrease in $\bar{x}$ as was observed experimentally.

It was also considered that the ability for the particles to grow was in some fashion influenced by the physical conformation of the protecting agents in solution. For example under θ-solvent conditions the polymers would adopt the random coil conformation in solution, providing little barrier for the very small nuclei to adjoin to existing particles. This was also deemed unlikely though, as this would have resulted in the trends in the particle sizes following the trends in the levels of aggregation, which was not observed experimentally. However, this was deemed likely to be the cause of the observed changes in the levels of aggregation observed in the sols (see Section 6.9).

A third possibility, which was theorised to be the most likely, was that the cosolvent preferentially adsorbed to the surface of the metal nuclei

which were formed, temporarily stabilising them against becoming ensconced upon the surface of an existing particle. This would increase the tendency for new particles to form rather than for existing particles to grow. It has been shown in this study that the relative proportion of cosolvent adsorbed to the surface of colloidal particles is proportional to ϕ, at least in the case of attempts to adsorb CO to the surface of the particles (see Chapter 7). Similarly it has been shown by other groups that in mixtures of water and an organic cosolvent that the cosolvent competitively adsorbs to the surface of various metals [143]. It has also been shown that for hydrophobic substrates immersed in mixtures of water and DMSO, the surface is preferentially wetted by the DMSO molecules across a wide composition range [144]. Palladium colloids fall into this category of hydrophobic substrates, as their categorisation as lyophobic sols dictates this by definition. For some systems this interaction was so strong that the metal precursor could not even be reduced to the metallic state, at least in the case of Rh/DMSO/H_2O. As molecules are free to adsorb and desorb from the surface it is an equilibrium process, thus as the concentration of cosolvent was increased more cosolvent molecules were forced to adsorb to the particle surfaces. In this case, increasing the proportion of cosolvent would increase the likeliness with which the cosolvent molecules adsorbed to the surface of the metal nuclei generated, thereby decreasing the particle size.

Another possibility that may explain the change in $\bar{x}$ is that the redox properties of the reducing agents were modified in some way by the presence of the cosolvent. For example, it is widely known that the reaction rate of borohydrides is faster in MeOH than it is in water [145-147]. It is possible therefore that for borohydride-reduced sols generated in mixtures of water and MeOH, as ϕ_{MeOH} was increased the reduction rate

increased simultaneously. As discussed in Chapter 5 it is accepted that increasing the rate at which a metal salt precursor is reduced, other factors aside, leads to smaller particle sizes. It was expected therefore that this may have played a factor in the observed decrease in $\bar{x}$ as ϕ was increased. Other solvents are known to affect the reductive capacity of various borohydrides, thus it is expected that they may incite similar changes in the reduction rate as MeOH is known to. Unfortunately there is little information specifically detailing the changes in reduction rate in different solvents.

6.9 Explanations for the Change in the Levels of Aggregation

Until this point, little time has been given in this study to discussing the reasons for the unpredictable levels of aggregation observed in the sols generated in mixed-media. There are two general reasons that a sterically-protected sol becomes destabilised and aggregation is induced. The first is that the protecting agent is not bound strongly enough to the surface of the suspended particles, and the second is that the protecting agent is not physically large enough to provide adequate steric protection. The later of these two options was expected to be most pertinent to the sols generated in this study.

The classically cited mechanism by which sterically protected sols become destabilised is due to compression of the adsorbed polymer layer in the presence of an antisolvent for the polymer in question, as discussed in Section 1.3.2.2. It is of interest therefore to examine the hydrodynamic size (‘*radius of gyration*’) of the polymers used in the cosolvent mixtures used.

For PVP there is an abundance of information in the literature pertaining to its conformation in solutions comprised of binary mixtures of water and various organic cosolvents. Studies, experimental and theoretical, have shown that the conformation of PVP molecules in solution is sensitive to both the dielectric constant of the medium in which they are dispersed [148]. Several structural transitions are observed in the ternary system PVP/MeOH/H_2O, where at the intermediate composition range ($0.3 \leq X_{MeOH} \leq 0.6$) the mixed-media acts as an antisolvent for PVP, and the morphology of the chains in solution changes from the random coil arrangement to a 'globular' morphology [149]. This was consistent with the observed increase in aggregation at intermediate compositions in the Pd and Rh sols protected by PVP in aqueous MeOH, although the effect was not striking probably due to the very large size of the PVP molecules to some extent preventing aggregation.

In the ternary system PVP/DMSO/H_2O, the viscosity of the solutions was observed to decreased at intermediate compositions, which is believed to be due to contraction of the polymer into the globular morphology [150-151]. Outside this range the solutions act more like θ-solvents. This is consistent with the observed increase in the size of the aggregates observed by TEM for the PVP-protected Pd sol in aqueous DMSO, and also with the relative increases in the A_{450} values and hydrodynamic radii. It is also consistent with the observation that the sols generated at intermediate compositions were darker in colour due to the increase in aggregation.

In the ternary system PVP/DMF/H_2O, it was found that the radius of gyration (R_g) decreases toward 18% v/v ϕ_{DMF}, increases toward 60% v/v ϕ_{DMF}, and decreases again toward 100% v/v ϕ_{DMF}. This is consistent with the increased levels of aggregation at 50% v/v $\leq \phi_{DMF} \leq$ 70% v/v observed

by TEM and PCS in the Rh sols protected by PVP in aqueous DMF, although it is harder to observe by UV/Vis as it is less sensitive to change in aggregation than the other two techniques, as described previously. It is also consistent with observations made by PCS and UV/Vis for the equivalent Pd sols.

For PVA there appeared to be less data available than for PVP pertaining to the hydrodynamic state of the chains in mixed-media. The size of unperturbed PVA chains in the ternary system PVA/MeOH/H_2O was observed to be higher at intermediate compositions than in either of the pure solvents [152], which is reflected by all the data collected for the PVA-protected Pd sols in aqueous DMSO.

Data was available on the ternary system PVA/DMSO/H_2O however, which indicated that when PVA is dissolved in mixtures of DMSO and water, at low DMSO concentrations the PVA chains are preferentially solvated by water molecules, but at high DMSO concentrations the chains are preferentially solvated by DMSO molecules, however at intermediate compositions the formation of H-bonded DMSO$\cdots$$(H2O)_2$ complexes decrease the affinity of the mixed solvent for the PVA molecules, giving rise to a contraction of the chains [153-155]. This is consistent with the observed decrease in stability of the Pd sols protected by PVA in aqueous DMSO at intermediate compositions.

No data was found which gave indications of the hydrodynamic state of PAA chains in mixed-media, however measurements of the swelling of PAA membranes in mixed-media indicate that PAA expands in mixtures of water and DMSO at low to intermediate compositions [156], which correlates well with the levels of aggregation observed. Theoretical and experimental studies also indicate that water is not a θ-solvent for PAA

[157], thus it is expected that the stability of the sols would increase as ϕ was increased, which again supports the observations made in this study.

At the time of writing there were few studies of which the author was aware which gave any insight into the hydrodynamic state of arabinogalactan in solution. Several give indications of its size and morphology in water, but none in non-aqueous or mixed solvents. It was decided therefore to investigate the hydrodynamic size of ARG molecules in mixed-media by PCS. Solutions were made comprised of 1 mL of a 5% w/v solution of ARG containing 0.1% w/v NaN_3 and made up with water and an organic cosolvent as described in Section 3.2.2. A plot showing x_{PCS} versus ϕ for ARG in mixtures of water and MeOH, DMSO or DMF is shown in Figure 143. The data indicates that in mixtures of water and MeOH the average hydrodynamic size remains steady until 30% v/v MeOH, upon which it increases rapidly before becoming precipitated from solution. Because of the obvious insolubility of ARG at this composition range, the increase in hydrodynamic size was believed to be due to aggregation of the ARG molecules in solution rather than expansion of the dimensions of the chain, which explains the increase in the levels of aggregation observed in ARG-protected sols in aqueous MeOH at high MeOH concentrations. When ARG was measured in mixtures of water and DMSO or water and DMF, the plots were "M-shaped", exhibiting two large maxima, which cannot be readily reconciled with the levels of aggregation observed by TEM due to the use of the heptane extraction process, nor do they obviously reflect the changes in the hydrodynamic radius of the sols or their A_{450} values. The discrepancy between the observed levels of aggregation and these hydrodynamic measurements probably originates from the assumptions used in the PCS measurements, or from the formation of aggregates of polymer molecules

in solution which cause peaks to be shown when in fact the mixed-media is acting as an anti-solvent.

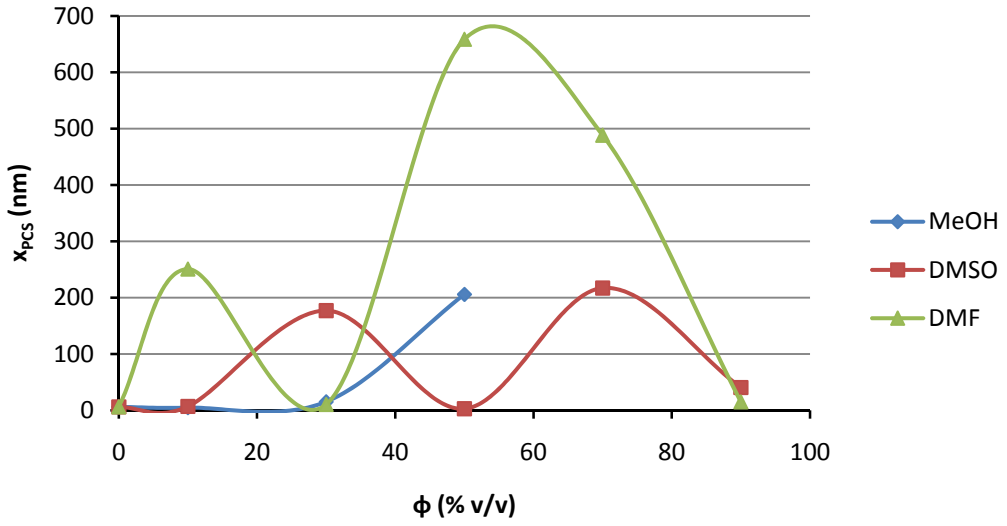

Figure 143: PCS measurements showing the hydrodynamic radius of ARG in the ternary systems ARG/H_2O/Cosolvent.

6.10 Stability Maps

No serious attempts have been made so far in this work to systematically describe the *long-term* stability of the sols generated. What follows is a series of "stability maps" to address this, in Figure 144 - Figure 151. The maps are presented as a scatter plot of the time taken for visible signs of aggregation to appear in a sol (t_{agg}) versus the cosolvent proportion (ϕ). The ordinate axis is given in log scale due to the large time differences involved in the observed behaviours. Table 19 lists each t_{agg} value and the time it corresponds to.

Note that these maps are purely qualitative and are based largely on empirical observations. As such they are not wholly accurate, but give a good indication of the approximate behaviour of each system and attempt to visualise a large amount of data in a relatively simplistic fashion. The upper limit is also defined not by the actual stability of the sol, but by the

time before publishing that it was produced. Where a colloid was observed to be stable and little aggregation was observed in the micrographs or inferred from PCS or UV/Vis values, the t_{agg} value was increased slightly to compensate for this. Protecting agent precipitation is depicted as a sharp drop to zero.

log(t_{agg})	Aggregation time	Approximate Timeframe
1	1 minutes	Instantly
2	10 minutes	10 minutes
3	100 minutes	1 hour
4	1000 minutes	1 day
5	10000 minutes	1 week
6	100000 minutes	2 months
7	1000000 minutes	2 years

Table 19: List of tagg values and their corresponding times in minutes, along with a nominal value related most closely to a 'real' time period.

6.10.1 Rhodium

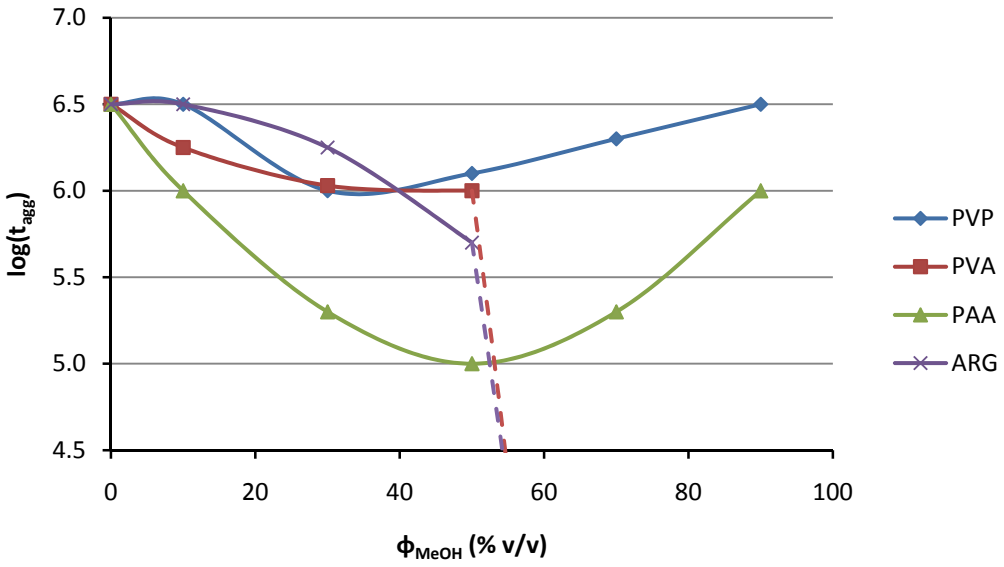

Figure 144: Stability map for rhodium sols reduced by borohydride in mixtures of water and methanol.

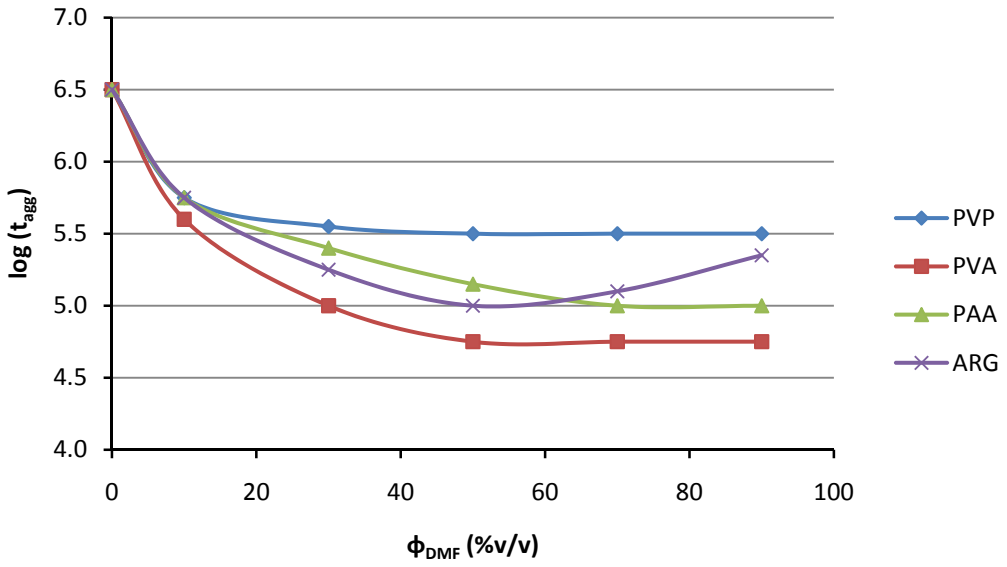

Figure 145: Stability map for rhodium sols reduced by borohydride in mixtures of water and DMF.

6.10.2 Palladium

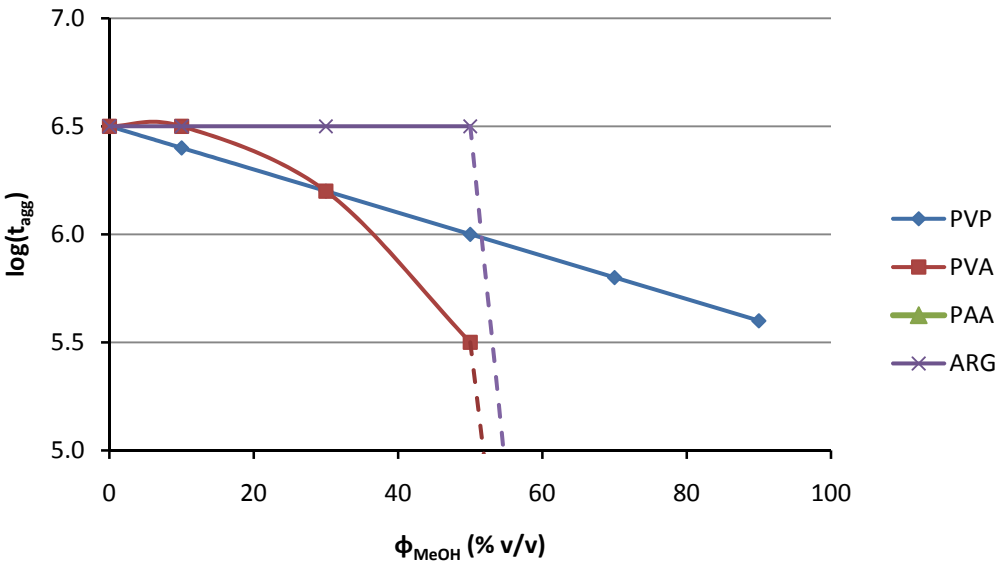

Figure 146: Stability map of palladium sols reduced by borohydride in mixtures of water and MeOH.

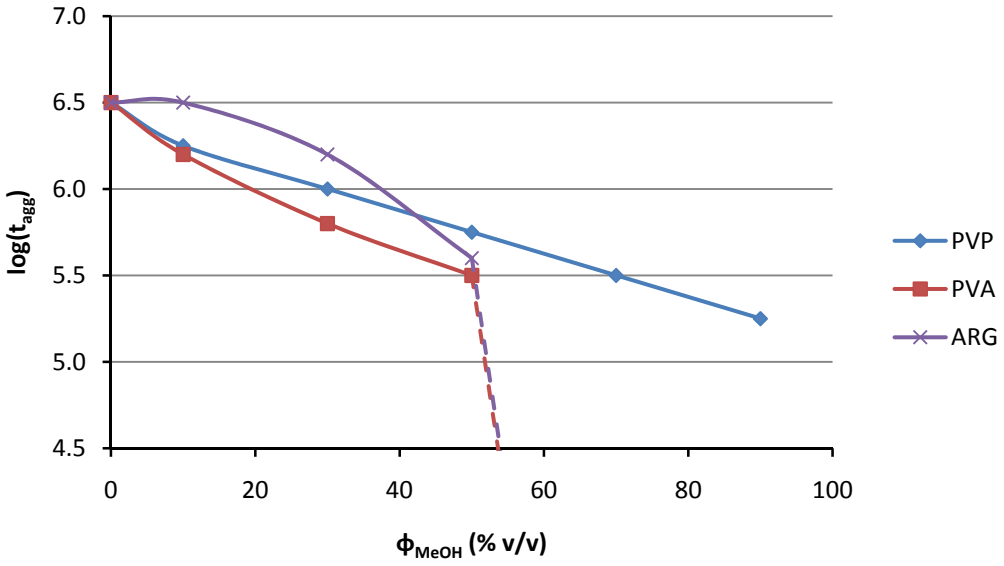

Figure 147: Stability map of palladium sols reduced by hydrazine in mixtures of water and MeOH.

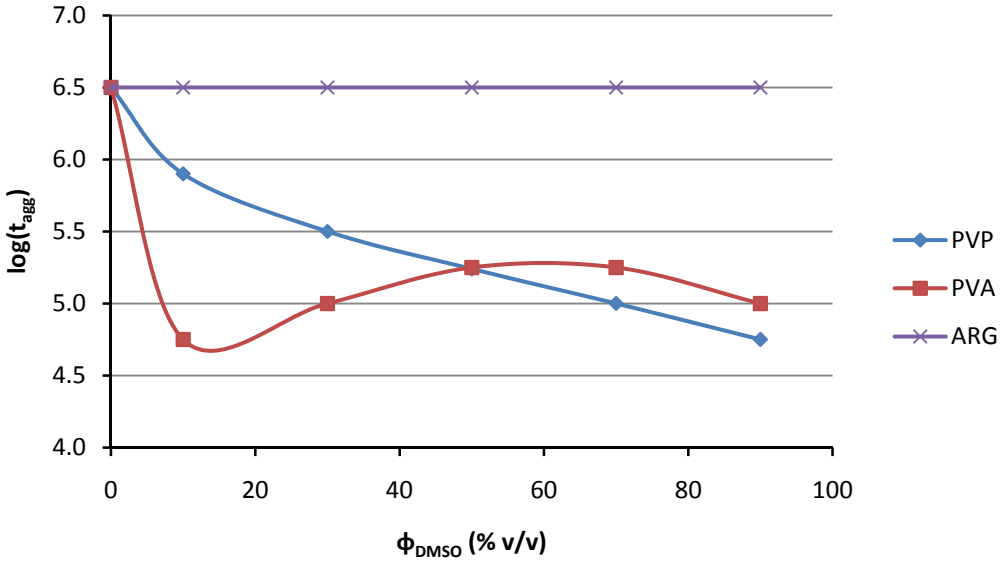

Figure 148: Stability map of palladium sols reduced by hydrazine in mixtures of water and DMSO.

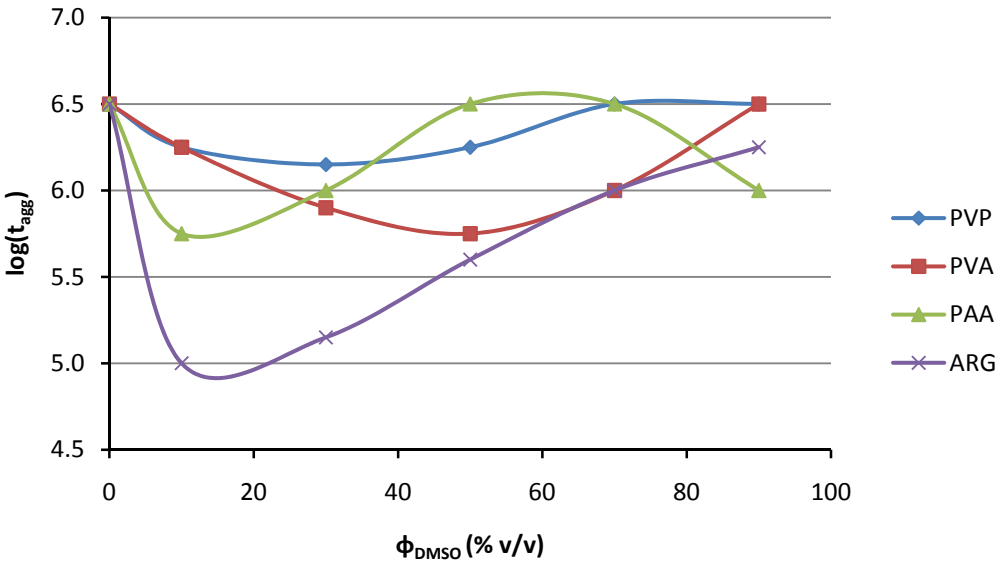

Figure 149: Stability map of palladium sols reduced by borohydride in mixtures of water and DMSO.

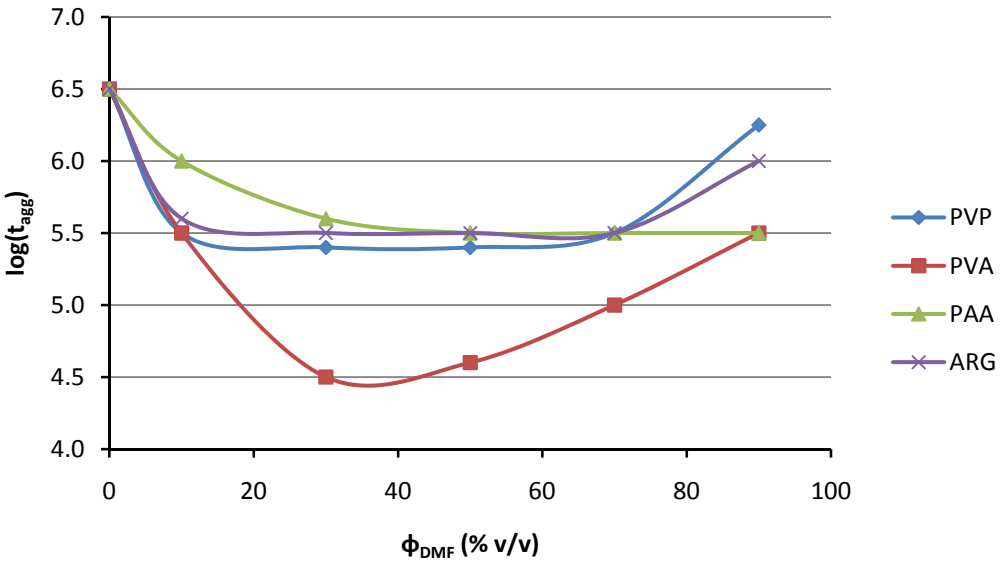

Figure 150: Stability map of palladium sols reduced by borohydride in mixtures of water and DMF.

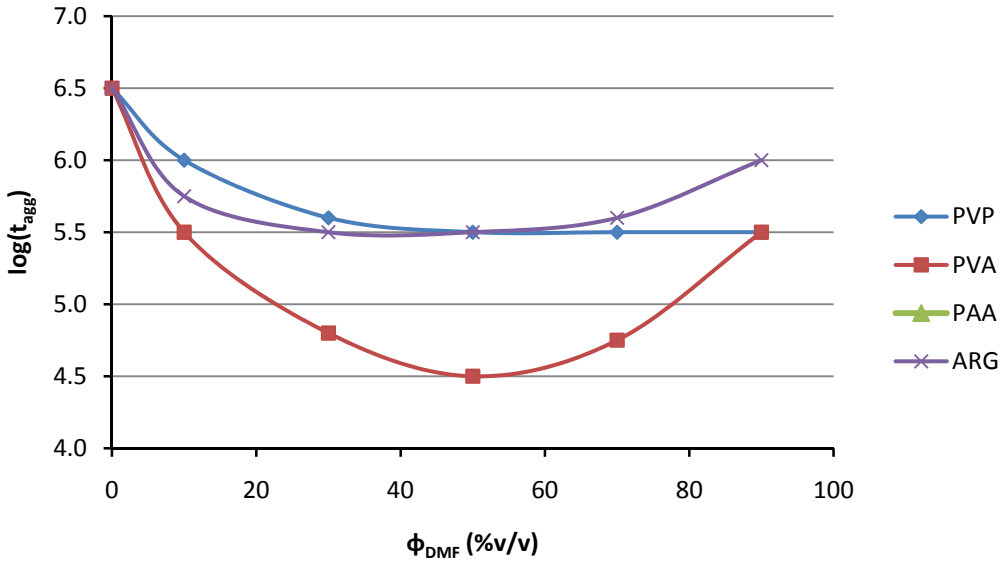

Figure 151: Stability map of palladium colloids reduced by hydrazine in aqueous DMF.

Chapter 7: FTIR Studies of CO-Treated Sols in Mixed-Media

As mentioned in Section 1.3.7, carbon monoxide adsorbed to the surface of colloidal particles can be used as a highly sensitive spectroscopic probe. By measuring $\nu(CO)_{ads}$, insights can be acquired into the chemical environment of the surface on which the CO molecules are adsorbed.

Practically speaking, the intensity of the spectra of surface-adsorbed CO is limited not only by the amount of colloidally suspended material, but also by the solubility of CO in the solvent from which the dispersion medium is composed. Previous works [3, 112] have had great difficulty in the detection of adsorbed CO in non-aqueous solvents, thus it is hoped that using sols in mixed-media may overcome this problem, and also provide an insight into the chemistry occurring when sols are generated in mixed-media.

7.1 General Results and Issues

Shortly after the beginning of the work described in this section, it was discovered that the particular CO cylinder used was dispensing significant proportions of $Fe(CO)_5$ in addition to CO. It is a well-documented phenomena [158] that some iron cylinders containing pressurised carbon monoxide undergo a spontaneous reaction to form $Fe(CO)_5$, indeed the synthetic route to $Fe(CO)_5$ is a simple room-temperature reaction exposing finely-divided Fe to CO. Under ambient conditions $Fe(CO)_5$ is an amber-coloured liquid with a low viscosity and a relatively high vapour pressure (it is more volatile than methanol), which was a concern because of its extreme toxicity. It is insoluble in water but readily soluble in organic solvents. This meant that it would not dissolve in the hydrosols which

were used in this study, but when treating the mixed-media sols with CO it may. Because of this significant contamination issue, it was deemed necessary to use a cold trap between the cylinder and the sol being treated. An acetone slush bath (-78 °C) with a cold finger submerged in it was found to be sufficiently effective for this purpose.

FTIR spectra of the protecting agents used to stabilise the colloids against aggregation were taken to determine whether their carbonyl groups would appear in the spectral region under examination. Fortunately no bands were observed. Curiously however, in the spectra of PVP, PVA and PAA a moderate band was observed at approximately 2146 cm^{-1} with little variance. This was assigned to the asymmetric stretching mode of the azide ion, N_3^-, used to protect the solutions against microbial growth, and was in good agreement with the literature [159], and with the collected spectrum of free azide. In the spectrum of arabinogalactan the peak was shifted higher and significantly weakened, along with the appearance of a broad absorbance at lower wavenumbers.

In order to remove this spectroscopic interference, colloids were prepared using protecting agents which did not have NaN_3 added, which was shown to be effective. It also prevented the possibility that the azide ion could react with other chemicals in the system, which was of concern. The most likely reaction to occur in the presence of azide was the conversion of the adsorbed carbon monoxide ligands (-C≡O) to isocyanate ligands (-N=C=O). This side reaction is spontaneous and fast under standard conditions, often being exploited for the conversion of small metal carbonyl clusters to metal isocyanate clusters [160]. By extension it is possible this reaction may occur with colloidal particles.

It was found that the sols generated which had been generated described previously were of insufficient density to successfully detect $\nu(CO)_{ads}$, so a series of sols with much higher densities were created specifically for this purpose. Because it was discovered that changing ϕ influenced the size and morphology of particles generated in mixed-media, if CO was to be adsorbed to particles generated in mixed-media then multiple variables would likely influence $\nu(CO)_{ads}$, so any trends observed would be of little use. In order to eliminate this problem it was decided to prepare hydrosols in water of sufficient density that they could be diluted *post-synthesis* with a sufficient volume of water and cosolvent such that the entire composition range could be studied, and the only variable which would then influence $\nu(CO)_{ads}$ would be ϕ.

In order to cover this wide of a composition range, the sols had to have densities as measured by the A_{450} value of approximately 100, so that when diluted they could reach compositions of 90% v/v cosolvent and $\nu(CO)_{ads}$ would still be detectable. It was found that a good concentration at which to prepare these sols was 80x the concentration of those described in Section 3.2.2. PAA was chosen to protect these high-density sols, as PVP was of too higher viscosity to be manageable at such a concentration, and PVA and ARG were found previously to be too easily precipitated from solution. Unfortunately at this higher a concentration, the colloids were not stable for extended periods of time, so it is perhaps more accurate to think of the spectra recorded as belonging to a 'suspension of large aggregates' rather than a truly stable colloidal dispersion.

The dilution scheme was as follows. 100 μL of colloid solution was placed in a vial. If the percentage of cosolvent in the final diluted colloid is

called *n*, then 900-10*n* μL of water was added. Finally 10*n* μL of cosolvent was added, the mixture was stirred and treated with CO.

After preparing these high-density sols, diluting them and treating them with CO, FTIR spectra were recorded. The resulting spectra for both the rhodium and palladium sols were typical of surface-adsorbed CO, and were in good agreement with the literature. Slight broadening of the peaks was evident, although this was attributed to the wide variety of sizes and shapes of aggregates present in solution, giving rise to similarly wide varieties of electronic environments which caused the strength of the M-CO bond to be altered.

When FTIR spectra were recorded of the rhodium and palladium sols in mixed-media, at low cosolvent proportions the spectra were similar to those recorded in pure water; however as the cosolvent proportion was increased the μ_2 bridging mode quickly became unobservable by approximately 30% v/v – 50% v/v cosolvent, and was replaced by water vapour spikes. The terminal stretching mode was generally replaced shortly afterwards by an unidentified but reproducible peak (or peaks, Section 7.2.3-7.2.5).

7.2 Adsorption of CO to Rhodium Sols

7.2.1 Rhodium in Water

The collected infrared spectra of CO adsorbed to rhodium agreed well with those in the literature [85], despite arising from adsorption to unstable colloidal particles rather than a stable sol. Intense peaks were observed at 2039.6 cm^{-1} and 1900 cm^{-1}, assigned to the terminal and doubly-bridging modes of CO respectively. A typical spectrum is shown in Figure 152.

To determine if indeed the peaks were due to surface-adsorbed species, the sample was left in the beam for a period of time with spectra collected once every five minutes. The stretching frequency was shown to decrease

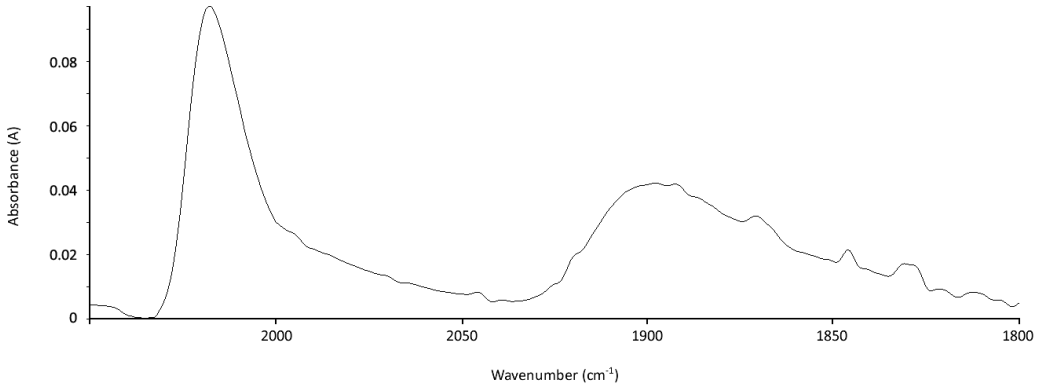

Figure 152: IR spectrum of CO adsorbed to a rhodium sol.

with time, arising from surface desorption of the CO ligands. This has been shown previously to be due to a loss of dipolar coupling between molecules, responsible for the changes in stretching frequency with surface coverage [161]. The CO (terminal) stretching frequency was observed to drop to around 2029 cm^{-1} over a period of 40 minutes. A graph of $\nu(CO)_{ads}$ is shown in Figure 153.

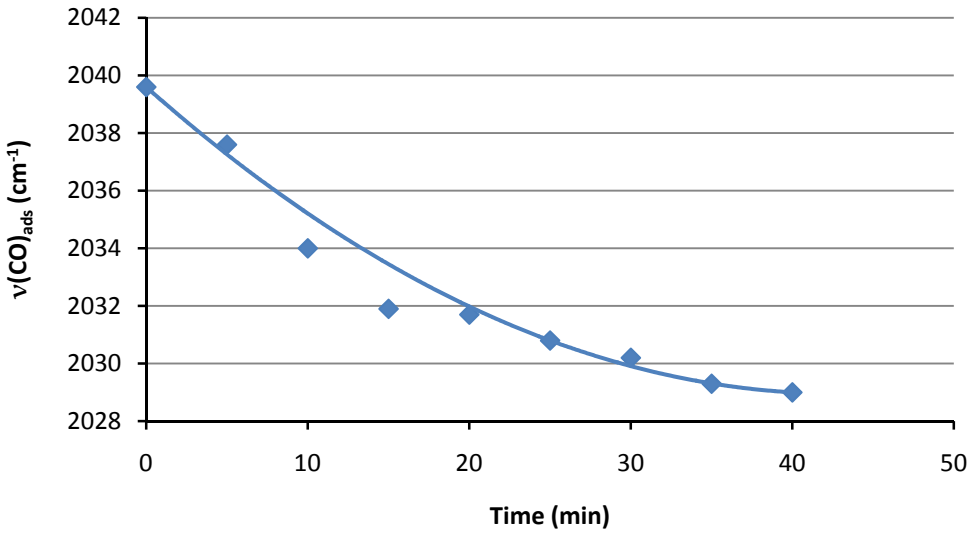

Figure 153: Graph of $\nu(CO)_{ads}$ versus time for CO adsorbed on a rhodium sol.

7.2.1 Rhodium in Methanol

Methanol proved to be a particularly bad cosolvent for the detection of surface-adsorbed CO. Spectra which were recorded displayed no peaks reminiscent of $\upsilon(CO)_{ads}$ at any value of ϕ_{MeOH}, instead displaying a flat spectrum with water vapour spikes of very low intensity. It has been shown previously that neat $_n$-alcohols are less desirable solvents for the adsorption of CO than water for various noble metals [3, 112], and indeed it appears that for rhodium sols, the mixing of water and methanol in any proportion does not change these findings. The mechanism usually cited is that the alcohol molecules competitively adsorb to the surface of the particles, directly precluding carbon monoxide ligands from being adsorbed. Because the spectrum of surface-adsorbed CO could not be observed at any MeOH concentration whereas with the other solvents (DMSO, MeCN) it could, this perhaps indicates that the strongly coordinating solvents are better at coordinating to Rh in nonzero oxidation states, whereas MeOH adsorbs more strongly to metallic rhodium. It has been shown previously that MeOH has a strong affinity for Rh^0 [162].

7.2.3 Rhodium in Dimethylsulfoxide

Dimethylsulfoxide proved to be a much more successful solvent for the adsorption of CO than methanol, although no enhancement in the spectral intensity was obtained, despite CO being significantly more soluble in DMSO than water.

In a 10% DMSO solution the spectrum of CO adsorbed to the surface of rhodium particles was still recognisable as surface adsorbed CO, with both $\upsilon(CO)$ and $\upsilon(\mu_2\text{-}CO)$ observable. The intensity of both modes decreased quickly with the addition of DMSO, and the contribution of uncompensated water vapour spikes became relatively larger. By

approximately 50% ϕ_{DMSO} the recorded spectra were no longer recognisable as CO adsorbed to colloidal rhodium. This is assumed to be an effect of the increased concentration of DMSO forcing the equilibrium between 'free' DMSO and 'adsorbed' DMSO toward the latter, and progressively precluding the adsorption of CO to Rh to the extent that none can be observed. A plot of the stretching frequency of the terminal mode and its intensity is given in Figure 155. Note that due to limitations with Microsoft Excel, the 'ads' in the chart legend could not be made subscript, indicating surface-adsorbed CO. Actual spectra are given in Figure 154.

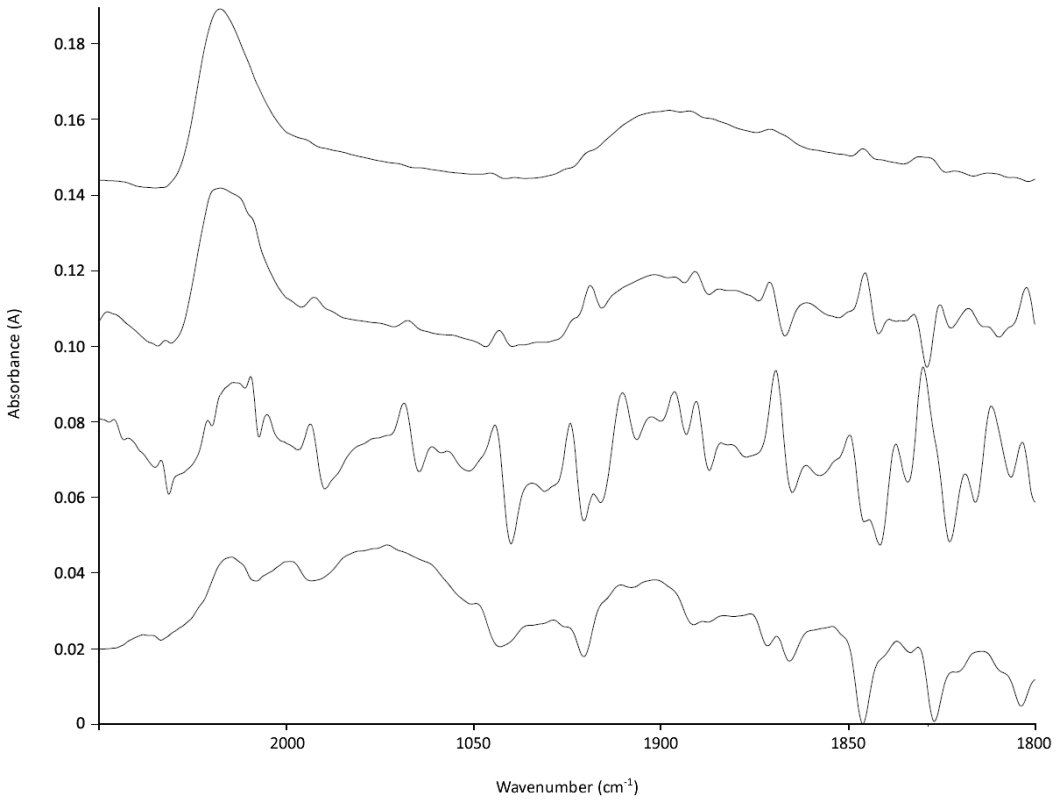

Figure 154: IR spectra of CO adsorbed to colloidal rhodium in 0% ϕ_{DMSO} (top), 10%, 30%, and 50% (bottom).

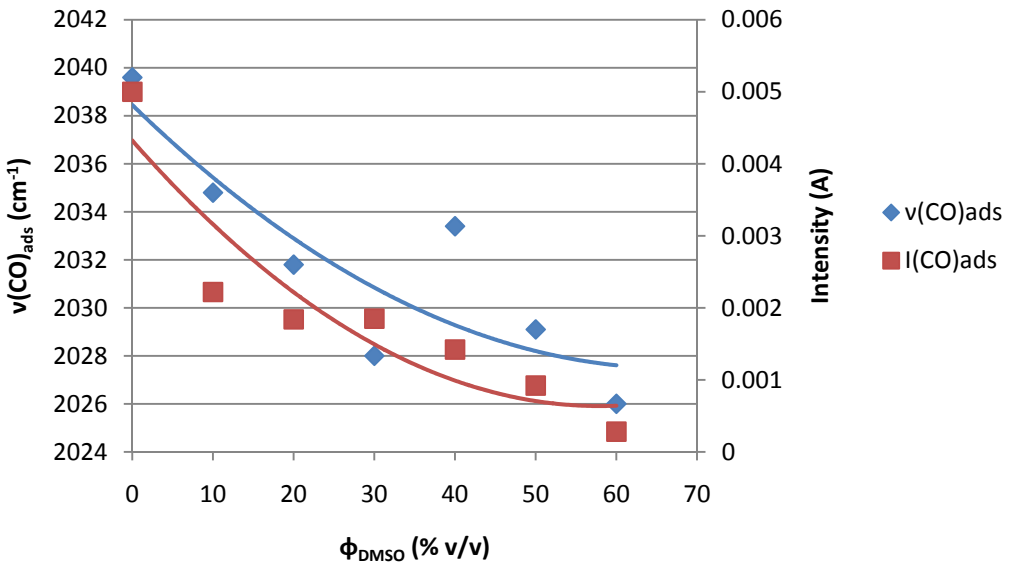

Figure 155: Graph of $\upsilon(CO)_{ads}$ and $I(CO)_{ads}$ for CO adsorbed to colloidal rhodium in mixtures of water and DMSO.

7.2.4 Rhodium in Acetonitrile

Acetonitrile displayed far different characteristics to DMSO, although still showed no merits over water as a solvent for the adsorption of CO. Above 70% ϕ_{MeCN} the protecting agent and the particles adsorbed to it were precipitated from solution, so the system could not be studied above this ϕ_{MeCN} value. However the ranges which were studied, the stretching frequency decreased overall in a linear fashion, although the intensity decreased toward intermediate compositions then increased again as ϕ was increased. At the intermediate compositions the μ_2 mode was more or less completely supressed, although it appeared to re-appear at higher ϕ_{MeCN} values. Similar trends have been observed with other systems, such as Pt/EtOH [112]. A graph of the CO stretching frequency (terminal mode) and its intenity is given in Figure 156.

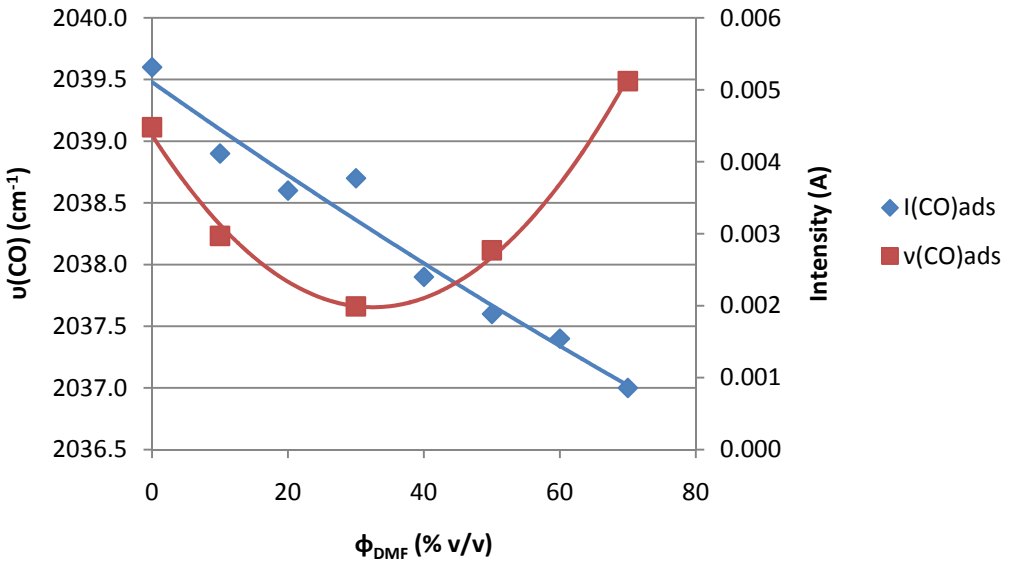

Figure 156: Graph of υ(CO)ads and I(CO)ads for CO adsorbed to colloidal rhodium in mixtures of water and MeCN.

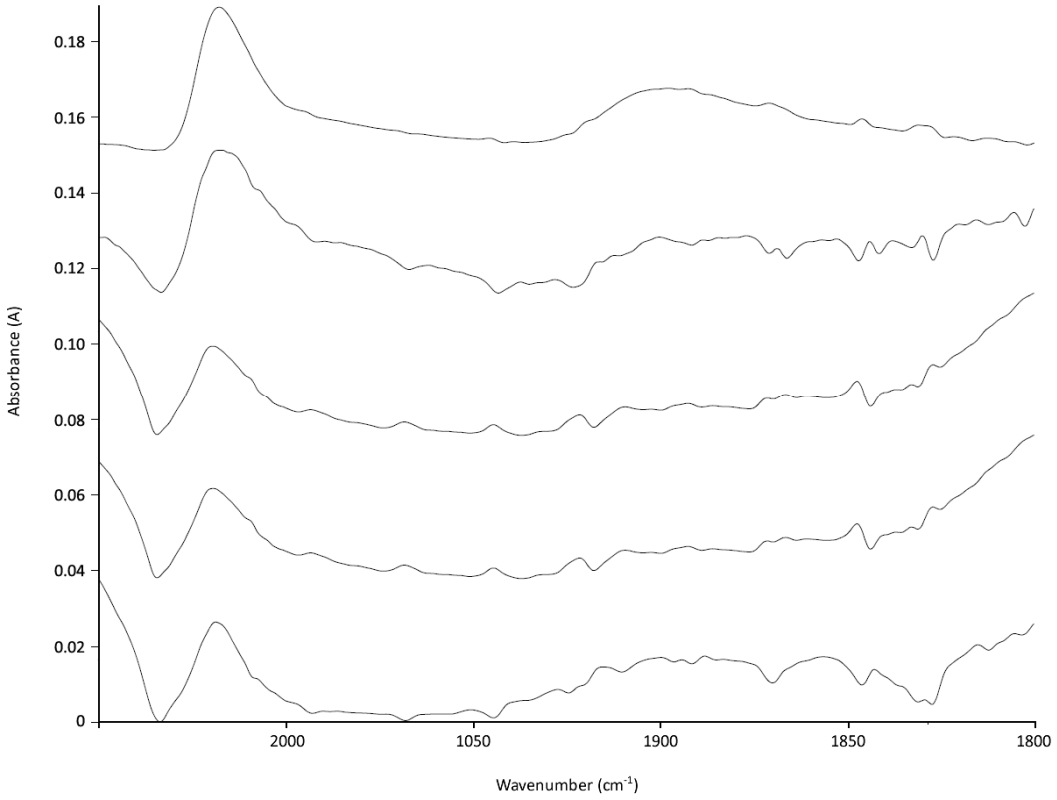

Figure 157: IR spectra of CO adsorbed to colloidal rhodium in 0% ϕ_{MeCN} (top), 10%, 30%, 50%, and 70% (bottom).

7.2.5 Rhodium in N,N-dimethylformamide

Dimethylformamide was shown to be somewhat more capricious in its behaviour than the other solvents studied, with both the stretching frequencies and their intensities varying to a wider extent. Whether or not this was simply a result of differences in the loading of rhodium onto the IR windows or whether it was a 'real' effect is not completely known.

The $\upsilon(CO)_{ads}$ stretching frequency was shown overall to decrease as ϕ_{DMF} was increased, although as mentioned there appeared to be much variation in its position, even when repeated in triplicate. Similar variations were observed in its intensity. The most unusual point was the anomalously low intensity and stretching frequency of the sample measured in 20% v/v DMF, which occurred at approximately 2025 cm^{-1} in each replicate. Unsurprisingly the bridging mode always disappeared before the terminal mode. A plot of the stretching frequency and intensity of the linear mode is given in Figure 158, spectra are shown in Figure 159.

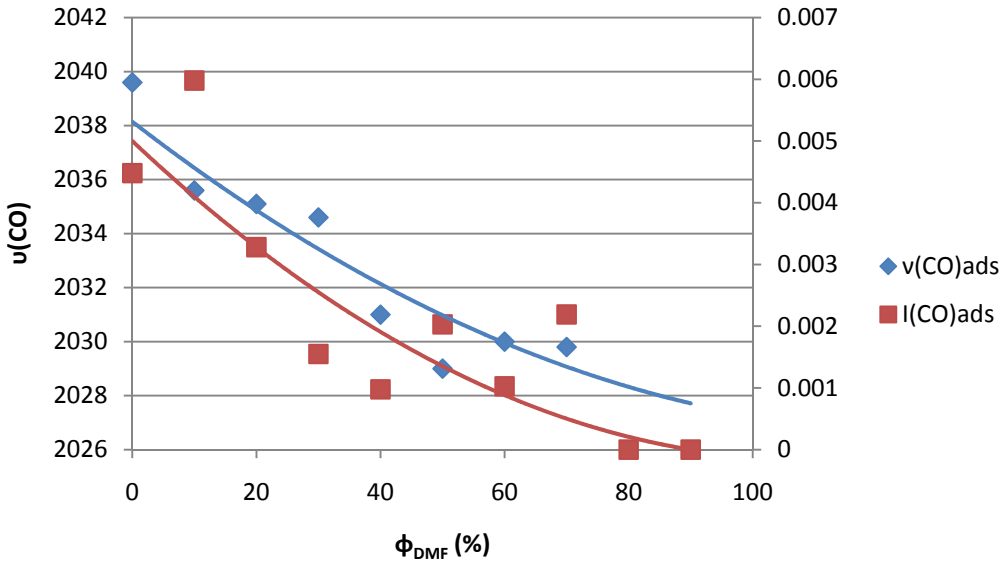

Figure 158: Graph of u(CO) and I versus ϕ for CO adsorbed to colloidal rhodium in DMF.

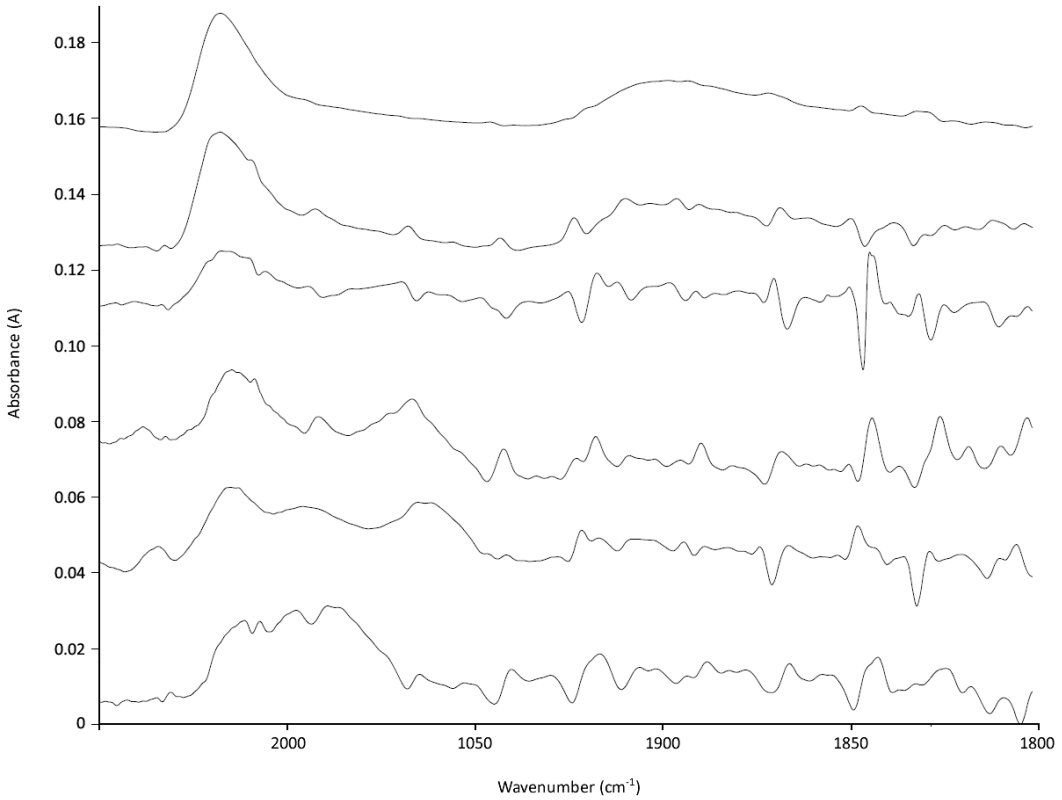

Figure 159: IR spectra of CO adsorbed to colloidal rhodium in 0% ϕ_{DMF} (top), 10%, 30%, 50%, 70%, and 90% (bottom).

7.3 Adsorption of CO to Palladium Sols

Palladium sols could not be prepared with sufficient density to undergo the ten-fold dilution required for the procedure used. Because of this no results could be obtained for palladium.

When rhodium sols were prepared at the required concentration, an unstable colloid was generated which led ultimately to a precipitate of Rh black, although the resulting particles were still small enough to be dispersed and gassed. With palladium, syntheses under analogous conditions led to a solid deposit of Pd black in the reaction vessel which could not be redispersed by shaking, stirring or sonication.

7.4 Attempts at Isocyanation of Adsorbed CO

Brief attempts were made at isocyanation of adsorbed CO ligands using sodium azide, although these were unsuccessful. The reaction of CO with N_3 is spontaneous under ambient conditions for metal carbonyls, so it was possible by extension that it may occur for CO adsorbed to colloidal particles. General methods were taken from a paper on metal carbonyls by McIndoe and Nicholson [160]. Sodium azide was added pre-synthesis and post-synthesis in both acetonitrile and water. IR spectra were recorded in the region 1600 cm^{-1} to 2200 cm^{-1} using the same technique which was used for CO detection. One possible reason no appropriate IR modes were observed is that the N_3^- ion preferentially attacked the carbonyl groups in the PAA protecting group instead of the adsorbed CO molecules, which would be unsurprising given their (supposed) role as a steric barrier. This could perhaps be circumvented by the use of a different protecting agent or by the use of a metal which does not require steric protection, and can achieve stability by electrostatic stabilisation.

7.5 Attempts at NO Adsorption

Attempts were also made to adsorb nitric oxide to palladium and rhodium sols, which also were unsuccessful. As no commercial-grade NO was available it had to be synthesised *ad-hoc*, using a variety of basic syntheses from the literature [163]. Special difficulty was found keeping the systems free from oxygen, which otherwise resulted in production of the brown NO_2. When collected over water the gas was colourless; when exposed to the atmosphere it turned brown, taken to be a sign of the production of NO_2. When purged through a palladium colloid the particles dissolved and the sol turned green, when purged through a rhodium colloid no changes were observed. The palladium sol turning

green was assumed to be due to oxidation of the Pd by NO/NO_2 dissolving to form nitric acid; this could perhaps be circumvented by heating the dispersion medium mildly, as NO is insoluble in warm water. Observation by IR in the region 1600 cm^{-1} to 2200cm^{-1} showed no characteristic M-NO or N-O stretches.

Chapter 8: Conclusion

A series of rhodium and palladium sols were prepared in mixed-media composed of water and an organic cosolvent. Four different protecting agents were used to maintain the state of stable colloidal dispersion, and whose properties were shown to strongly influence the properties of the sols, representing a significant original aspect of the study. The resulting sols were characterised by TEM, UV/Vis and PCS.

For those syntheses which successfully resulted in the generation of the appropriate colloidal metal, there was shown to be a strong dependence of $\bar{x}$ on ϕ. The extent of this dependence was influenced by the specific protecting agent used, the cosolvent used and the proportions in which it was used, as well as the reducing agent used. Sols protected by PVP typically showed the greatest dependence, exhibiting decreases in $\bar{x}$ of up to 70% in some cases. PVA- and ARG- protected sols showed similar size-composition dependencies although to a lesser extent, and PAA-protected sols were frequently the least responsive to the composition of the reaction medium. These trends were valid for both rhodium and palladium sols. In several cases for palladium sub-nanometer particles (0.8 nm) were produced, specifically when generated in mixed-media with high DMSO concentrations, which have been previously identified as containing as few as 7 individual palladium atoms, a relatively rare synthetic occurrence.

To determine that the decrease was not simply due to incomplete reduction of the metal precursor, an investigation was carried out to determine the concentration of residual unreduced metal in the dispersion medium. A method was successfully developed for the removal of the

colloidally suspended material. However, ICP-MS analysis was inconclusive due to inefficient ionisation of the Pd contained in the samples. In lieu of any quantitative data, it was inferred from other data that the level of reduction did not significantly change as ϕ was increased.

Several theories were proposed to explain the decrease in $\bar{x}$ as ϕ was increased. The first was based on stabilisation of the generated metal nuclei by specific adsorption of the cosolvent molecules. Stabilisation of the metal nuclei generated was proposed to have suppressed particle growth in favour of the formation of extra particles which ultimately grew to a smaller size. The second theory was based on modification of the redox properties of the reducing agents by the presence of a cosolvent, giving rise to changes in the reduction kinetics.

The apparent macroscopic stability of the colloidal systems *in-situ* and the size of its comprising aggregates, two inextricable characteristics, showed a much more complex dependence on ϕ as shown by all three techniques used. One may expect that linearly altering the composition of the medium, the stability would be affected in a linear fashion, analogous to the concept of ideality in physical chemistry. This was categorically not the case. Many systems displayed unusual characteristics such as extreme instability at intermediate compositions, as judged by direct observation, TEM micrographs, and comparisons with the UV/Vis and PCS data. The changes were rationalised based on the changes in the radius of gyration of the polymers in the mixed-media. Stability maps were created to show the long-term macroscopic stability of the dispersions.

Analysis by UV/Vis and PCS generally gave data which supported the levels of aggregation observed in TEM micrographs, and generally both were in relatively good agreement with each other.

There were a variety of phenomena which interfered with the synthesis of many of the sols which prevented the successful production of colloidal metal. Rhodium could not be reduced by hydrazine under any circumstances, although this was later discovered to be because it required heating. Because of this the reduction of rhodium by hydrazine was not pursued.

Rhodium could also not be reduced in the presence of the strongly coordinating solvents DMSO and MeCN, presumable due to the formation of solvent complexes which stabilised the Rh^{I} oxidation state.

In a many cases when low-polarity solvents were used, the protecting agents adsorbed to the particles were precipitated from solution, presumably due to the decrease of the polarity of the reaction medium. This resulted in slurries in the reaction vessel which would strongly adsorb and remove the metal precursor from the solution, or would co-precipitate the adsorbed colloidal particles from the dispersion medium if reduction was attempted. For this reason syntheses where this was a problem were not characterised further. This occurred with nearly all syntheses in THF and acetone, and to a small extent with methanol and acetonitrile. Where syntheses in acetonitrile did not result in protecting agent precipitation the colloids were very unstable, hence analysis of acetonitrile colloids was also abandoned.

The effect of cosolvent on the adsorption of CO was also investigated. It was found the sols generated previously were of insufficient particle density for υ(CO) to be detected, so special "high-density" sols were synthesised. These were diluted with appropriate volumes of water and cosolvent such that the effect of ϕ alone could be investigated, without the additionally observed effects of variations in particle size and aggregate

structure. When CO was adsorbed to the colloids in pure water the resulting spectra agreed well with those in the literature. As a cosolvent was introduced the ability to detect adsorbed CO was progressively suppressed as ϕ was increased, assumed to be due to competitive adsorption of the cosolvent molecules. This effect was observed for mixtures of water and DMSO, DMF or MeCN. In mixtures of water and MeOH no peaks due to adsorbed CO were present in any of the collected IR spectra. These results were used to support the theory for the decrease in $\bar{x}$ observed, as described previously.

8.1 Recommendations for Future Study

Of all the observations made in this study, perhaps the most striking was the decrease in the average particle size as the concentration of cosolvent was increased. Whether this was a legitimate effect or was simply the result of incomplete reduction remains unproven, but could easily be solved by analysing the dispersion medium of various sols for unreduced metal content. This would require the development of a sound method for the removal of the particles while the chemical composition of the dispersion medium remains unchanged. These may include precipitation methods, extraction methods, size-exclusion methods, magnetic separation or ultracentrifugation.

As this study has shown, the behaviour of the sols in mixed-media depends to a large extent on which protecting agent is used. Therefore it may be of interest to investigate metals which do not require protecting agents, such as gold, silver, or platinum. The absence of the protecting agent which acts as a site for nucleation and anchoring of particles may give rise to different behaviour.

A second advantage to using metals which to not require protecting agents is that problems encountered with the solubility of the protecting agents would not occur. It may, however, be of interest to fully investigate and characterise the nature of these precipitates when they do occur.

Additionally it may be of interest to investigate other cosolvents with higher polarities than those investigated in this study, in which case it may be expected that the precipitation of the protecting agents may not occur to such a great extent. Possible examples include formic acid or formamide. If indeed the origin of the particle size decrease is due to surface-adsorption of the cosolvent, it may be of specific interest to find a solvent which has a lesser affinity for either of the metals than water, in which case it may be expected that increases in particle size could be produced. Cosolvents of interest include glycerol, nitromethane, hexamethylphosphoramide, dimethylacetamide, polyols, dioxanes and pyrrolidones. It may also be of interest to perform experiments to evaluate the kinetics of reduction in mixed-media, to determine if this contributed to the decrease in $\bar{x}$ at all.

Because of the very small size and therefore very high surface area of some of the particles generated, it may be of interest to test their catalytic activities in any of a variety of reactions. It may also be of use to determine if, *in-situ,* they have catalytically oxidised, reduced, or otherwise transformed the cosolvent in which they were generated.

To ensure the accuracy of the PCS characterisation of future work, it would be of substantial benefit to develop a more accurate method for the analysis of sols in mixed-media. This would specifically involve accurate determinations of the refractive index and viscosity of various sols, and would specifically benefit from determining the relative contribution to

each of these properties of each of the species (polymer, ions, cosolvent, etc) in the sol.

Appendix 1: Sample Nomenclature

For the purposes of sample identification, a labelling system was employed by the researcher. These labels are visible on the outside of sample vials, photos of which appear throughout this thesis. The system employs a 5-character code, such as R1135 or P2000. These are explained below.

- The first character, a letter, denotes which metal the colloid is produced from.

R. Rhodium

P. Palladium

- The second character, a number, denotes which reducing agent was used to reduce the metal.

1. Sodium borohydride
2. Hydrazine hydrate

- The third character, also a number, denotes which protecting agent was used to stabilise the system against aggregation.

0. None
1. PVP (poly(vinyl pyrrolidone))
2. PVA (poly(vinyl alcohol))
3. PAA (poly(acrylic acid))
4. ARG (arabinogalactan)

- The fourth character, another number, denotes which cosolvent was used.

0. None
1. THF (tetrahydrofuran)
2. Acetone
3. MeOH (methanol)
4. MeCN (acetonitrile)
5. DMF (dimethylformamide)
6. DMSO (dimethylsulfoxide)

- The fifth and final character, a number, denotes in what proportion (v/v) the cosolvent denoted by the previous number is used in.

0. 0%
1. 10%
3. 30%
5. 50%
7. 70%
9. 90%

To illustrate, the previously mentioned "R1135" sample therefore is rhodium colloid, reduced by sodium borohydride, protected by PVP, and generated in a 1:1 (50%) mixture of water and methanol. "P2000" therefore refers to a control sample; a palladium colloid reduced by hydrazine, with no protecting agent and no cosolvent.

Appendix 2: NICOMP Laser Particle Size Data for SpheroTech 70 nm Latex Standard

Particle Sizing Systems, Inc.
Santa Barbara, Calif., USA

530-1001A;082009
Menu File: C:\Particle Sizing Systems\ZPW388\zpw388.tbl 11:2:24 9/17/2009

INTENSITY-Weighted NICOMP DISTRIBUTION Analysis (Solid Particle)

NICOMP SUMMARY:
Peak #1: Mean Diam.= 80.2 nm, S.Dev.= 14.7 nm (18.3%) Intens.= 100.0 %

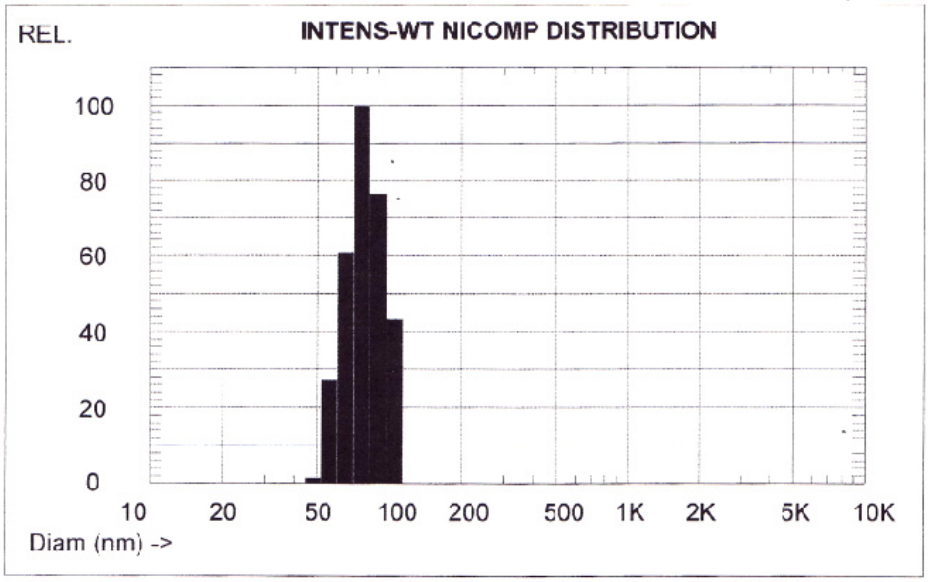

Run_Sample

Mean Diameter = 80.0 nm Fit Error = 5.810 Residual = 3.653

Ref. No. 3K-200
Lot No. 35426

M. Hdo.
9.17.09

NICOMP SCALE PARAMETERS:
Min. Diam. = 10 nm Plot Size = 45
Smoothing = 3 Plot Range = 1000

GAUSSIAN SUMMARY:

Mean Diameter	*= 78.7 nm*	*Variance (P.I.)*	*= 0.004*
Stnd. Deviation	*= 5.3 nm (6.7 %)*	*Chi Squared*	*= 0.616*
Norm. Stnd. Dev. (Coeff. of Var'n)	*= 0.067*	*Baseline Adj.*	*= 0.193 %*
		Z-Avg. Diff. Coeff.	*= 5.90E-008 cm2/s*
Run Time	*= 0 Hr 10 Min 22 Sec*	*Wavelength*	*= 639.0 nm*
Count Rate	*= 302 KHz*	*Temperature*	*= 23 deg C*
Channel #1	*= 312.2 K*	*Viscosity*	*= 0.933 cp*
Channel Width	*= 9.3 uSec*	*Index of Ref.*	*= 1.333*

References

[1] A.D. McNaught, A. Wilkinson, *Compendium of Chemical Terminology, 2nd ed. (the "Gold Book")* (Blackwell Scientific Publications, Oxford, **1997**)

[2] D.H. Everett, *Basic Principles of Colloid Science* (Royal Society of Chemistry Paperbacks, London, **1988**)

[3] K. Babu, MSc Thesis, University of Waikato, **2003**

[4] K.S. Birdi, *Handbook of Surface and Colloid Chemistry, Second Edition* (CRC Press, Florida, **2003**)

[5] P.C. Hiemenz, *Principles of Colloid and Surface Chemistry* (Marcel Dekker, New York, **1987**)

[6] R.J. Hunter, *Foundations of Colloid Science* (Oxford University Press, New York, **2001**)

[7] E.A. Hauser, *J. Chem. Educ.*, 29(9), **1952**, 456-458

[8] F. Antonii, *Panacea Aurea-Auro Potabile* (Bibliopolio Frobeniano, Hamburg, **1618**)

[9] M. Faraday, *Phil. Trans. R. Soc. Lond*, 147, **1857**, 145-181

[10] S. Claesson, K.O. Pedersen, *Biogr. Mems Fell. R. Soc.*, 18, **1972**, 595-627

[11] R.A. Zsigmondy, *Nobel Lectures, Chemistry 1922-1941* (World Scientific Publishing Co., Singapore, **1999**)

[12] H.B. Weiser, *Inorganic Colloid Chemistry Volume I: The Colloidal Elements* (Chapman & Hall, Limited, London, **1933**)

[13] H.B. Weiser, *Inorganic Colloid Chemistry Volume II: The Hydrous Oxides and Hydroxides* (Chapman & Hall, Limited, London, **1935**)

[14] H.B. Weiser, *Inorganic Colloid Chemistry Volume III: The Colloidal Salts* (Chapman & Hall, Limited., London, **1938**)

[15] J. Turkevich, P.C. Stevenson, *Discuss. Faraday. Soc.*, 11, **1951**, 55-75

[16] J. Chen, T. Herricks, M. Geissler, Y. Xia, *J. Am. Chem. Soc.*, 126(35), **2004**, 10854-10855

[17] S. Komarneni, D. Li, B. Newalkar, H. Katsuki, A.S. Bhalla, *Langmuir*, 18(15), **2002**, 5959-5962

[18] M. Tsuji, M. Hashimoto, Y. Nishizawa, T. Tsuji, *Mater. Lett.*, 58(17-18), **2004**, 2326-2330

[19] A. Roucoux, J. Schulz, H. Patin, *Chem. Rev.*, 102(10), **2002**, 3757-3778

[20] H. Hirai, Y. Nakao, N. Toshima, *J. Macromol. Sci. A*, 12(8), **1978**, 1117-1141

[21] H. Hirai, Y. Nakao, N. Toshima, *J. Macromol. Sci. A*, 13(6), **1979**, 727-750

[22] W. Wang, S. Efrima, O. Regev, *Langmuir*, 14(3), **1998**, 602-610

[23] K. Esumi, M. Shiratori, H. Ishizuka, T. Tano, K. Torigoe, K. Meguro, *Langmuir*, 7(3), **1991**, 457-459

[24] M.R. Mucalo, R.P. Cooney, *J. Chem. Soc. Faraday T.*, 87, **1991**,

[25] J.B. Perrin, *Les Atoms* (Constable & Company Ltd, London, **1916**)

[26] Malvern, *Colloidal Stability and colloidal dispersion*, **2009**, http://www.malvern.com/LabEng/industry/colloids/colloids_stability.htm

[27] J. Lykelma, *Fundamentals of Interface and Colloid Science Volume II: Solid-Liquid Interface* (Academic Press, London, **1995**)

[28] H. Helmholtz, *Pogg. Ann.*, LXXXIX, **1853**, 211

[29] L.G. Gouy, *Comt. Rend.*, 149, **1909**, 654

[30] L.G. Gouy, *J. Phys.*, 4(9), **1910**, 457

[31] D.L. Chapman, *Philos. Mag.*, 25(6), **1913**, 475

[32] O. Stern, *Z. Electrochem*, 30, **1924**, 508

[33] A.V. Delgado, F. González-Caballer, R.J. Hunter, L.K. Koopal, J. Lykelma, *Pure Appl. Chem.*, 77(10), **2005**, 1753-1805

[34] E.D. Schukin, A.V. Pertsov, E.A. Amelina, A.S. Zelenev, *Colloid and Surface Chemistry* (Elsevier, Amsterdam, **2001**)

[35] J. Goodwin, *Colloids and Interfaces with Surfactants and Polymers* (Wiley, Chichester, **2004**)

[36] P.J. Flory, *Principles of Polymer Chemistry* (Cornell University Press, Ithaca, New York, **1953**)

[37] B. Derjaguin, L. Landau, *Prog. Surf. Sci.*, 43(1-4), **1993**, 30-59

[38] E. Verwey, J. Overbeek, *Theory of the stability of lyophobic colloids* (Elsevier, Amsterdam, **1948**)

[39] Malvern, *Derjaguin, Landau, Verwey and Overbeek theory (DLVO theory)*, **2009**, http://www.malvern.com/LabEng/industry/colloids/dlvo_theory.htm

[40] L. Rayleigh, *Phil Mag.*, 12(73), **1881**, 81-101

[41] G. Mie, *Ann. Phys.*, 25(3), **1908**, 377-445

[42] A. Nel, T. Xia, L. Madler, N. Li, *Science*, 311(5761), **2006**, 622-627

[43] Scientific Committee on Emerging and Newly Identified Health Risks, *The Appropriateness of Existing Methodologies to Assess the Potential Risks associated with Engineered and Anventitious Products of Nanotechnologies*, **2006**

[44] D. Vollath, *Nanomaterials* (Wiley, Weinheim, **2008**)

[45] T.F. Tadros, *Colloids in Cosmetics and Personal Care* (Wiley, Weinheim, **2008**)

[46] M. Pagliaro, *Nano-Age* (Wiley, Weinheim, **2010**)

[47] J. Mongillo, *Nanotechnology 101* (Greenwood Press, Westport, **2007**)

[48] L.N. Lewis, *Chem. Rev.*, 93(8), **1993**, 2693-2730

[49] G. Schmid, *Nanoparticles: From Theory to Application* (Wiley-VCH, Weinheim, **2004**)

[50] G. Cao, *Nanostructures & Nanomaterials: Synthesis, Properties & Applications* (Imperial College Press, London, **2004**)

[51] Institute for Surface Chemistry, Royal Institute of Technology, *SKB Technical Report: Study of groundwater colloids and their ability to transport radionuclides*, **1987**

[52] W. Yu, W. Tu, H. Liu, *Langmuir*, 15(1), **1998**, 6-9

[53] G. Frens, *Colloid Polym. Sci.*, 250(7), **1972**, 1435-1536

[54] H. Hiramatsu, F.E. Osterloh, *Chem. Mater.*, 16(13), **2008**, 2509-2511

[55] A. Taleb, C. Petit, M.P. Pileni, *Chem. Mater.*, 9(4), **1997**, 950-959

[56] F. Bonet, V. Delmas, S. Grugeon, R. Herrera Urbina, P.-Y. Silvert, K. Tekaia-Ehlsissen, *Nanostruct. Mater.*, 11(8), **1999**, 1277-1284

[57] P. Jiang, J.-J. Zhou, R. Li, Y. Gao, T.-L. Sun, X.-W. Zhao *et al.*, *J. Nanopart. Res.*, 8(6), **2006**, 927-934

[58] J.-E. Park, M. Atobe, T. Fuchigami, *Ultrason. Sonochem.*, 13(3), **2005**,

[59] A. Guerrero-Martínez, J. Pérez-Juste, E. Carbó-Argibay, G. Tardajos, Luis M. Liz-Marzán, *Angew. Chem. Int. Edit.*, 48(50), **2009**, 9484-9488

[60] A. Swami, A. Kumar, P.R. Selvakannan, S. Mandal, R. Pasricha, M. Sastry, *Chem. Mater.*, 15(1), **2002**, 17-19

[61] Y. Sun, Y. Xia, *Science*, 298(5601), **2002**, 2176-2179

[62] Y. Nagata, Y. Mizukoshi, K. Okitsu, Y. Maeda, *Radiat. Res.*, 146(3), **1996**, 333-338

[63] R.A. Salkar, P. Jeevanandam, S.T. Aruna, Y. Koltypin, A. Gedanken, *J. Mater. Chem.*, 9(6), **1999**, 1333-1335

[64] Y. Mizukoshi, K. Okitsu, Y. Maeda, T.A. Yamamoto, R. Oshima, Y. Nagata, *J. Phys. Chem. B*, 101(38), **1997**, 7033-7037

[65] K.S. Suslick, M. Fang, T. Hyeon, *J. Am. Chem. Soc.*, 118(47), **1996**, 11960-11961

[66] W. Tu, H. Liu, *Chem. Mater.*, 12(2), **2000**, 564-567

[67] W. Tu, H. Liu, *J. Mater. Chem.*, 10(9), **2000**, 2207-2211

[68] H. Remita, J. Khatouri, M. Tréguer, J. Amblard, J. Belloni, *Z. Phys. D*, 40(1-4), **1997**, 127-130

[69] A. Henglein, *Langmuir*, 15(20), **1999**, 6738-6744

[70] A. Henglein, B.G. Ershov, M. Malow, *J. Phys. Chem.*, 99(38), **1995**, 14129-14136

[71] L. Bronstein, D. Chernyshov, P. Valetsky, N. Tkachenko, H. Lemmetyinen, J. Hartmann *et al.*, *Langmuir*, 15(1), **1998**, 83-91

[72] H.H. Huang, X.P. Ni, G.L. Loy, C.H. Chew, K.L. Tan, F.C. Loh *et al.*, *Langmuir*, 12(4), **1996**, 909-912

[73] F. Kim, J.H. Song, P. Yang, *J. Am. Chem. Soc.*, 124(48), **2002**, 14316-14317

[74] K. Esumi, K. Matsuhisa, K. Torigoe, *Langmuir*, 11(9), **1995**, 3285-3287

[75] K. Esumi, T. Tano, K. Torigoe, K. Meguro, *Chem. Mater.*, 2(5), **2002**, 564-567

[76] I.R. Collins, S.E. Taylor, *J. Mater. Chem.*, **1992**, 1277-1281

[77] T. Svedberg, *Colloids Chemistry, Wisconsin Lectures* (Chemical Catalog Company, New York, **1924**)

[78] M.R. Mucalo, C.R. Bullen, *J. Mater. Sci. Lett.*, 20(20), **2001**, 1853-1856

[79] D.F. Shriver, P.W. Atkins, *Inorganic Chemistry, Third Edition* (Oxford University Press, Oxford, **1999**)

[80] H. Arai, H. Tominaga, *J. Catal.*, 43(1-3), **1976**, 131-142

[81] T.E. Hoost, K. Otto, K.A. Laframboise, *J. Catal.*, 155(2), **1995**, 303-311

[82] B. Wichterlová, P. Sazama, J.P. Breen, R. Burch, C.J. Hill, L. Capek *et al.*, *J. Catal.*, 235(1), **2005**, 195-200

[83] J.-L. Freysz, J. Saussey, J.-C. Lavalley, P. Bourges, *J. Catal.*, 197(1), **2001**, 131-138

[84] L.N. Lewis, N. Lewis, *J. Am. Chem. Soc.*, 108(23), **1986**, 7228-7231

[85] M.R. Mucalo, R.P. Cooney, *Chem. Mater.*, 3(6), **1991**, 1081-1087

[86] D.d. Caro, J.S. Bradley, *New J. Chem.*, **1998**, 1267-1273

[87] M.R. Mucalo, R.P. Cooney, *Can. J. Chem.*, 69(11), **1991**, 1649-1655

[88] M.R. Mucalo, R.P. Cooney, *J. Colloid Interf. Sci.*, 150(2), **1992**, 486-491

[89] M.R. Mucalo, K.M. Babu, K.S.W. Wu, *J. Colloid Interf. Sci.*, 310(1), **2007**, 184-189

[90] M.R. Mucalo, C.R. Bullen, M. Manley-Harris, T.M. McIntire, *J. Mater. Sci.*, 37, **2002**, 493-504

[91] J.H. Prescott, E.V. Groman, G. Gulyas, *Carbohyd. Res.*, 301, **1997**, 89-93

[92] G.R. Ponder, *Carbohyd. Polym.*, 36(1), **1998**, 1-14

[93] J.A. Creighton, D.G. Eadon, *J. Chem. Soc. Faraday T.*, 87, **1991**, 3881-3891

[94] D.H. Melik, H.S. Fogler, *J. Colloid Interf. Sci.*, 92(1), **1982**, 161-180

[95] E.J. Meehan, W.H. Beattie, *J. Phys. Chem.*, 64(8), **1960**, 1006-1016

[96] M.L. Wallach, W. Heller, *J. Phys. Chem.*, 68(4), **1964**, 924-930

[97] J.M. Irache, C. Durrer, G. Ponchel, D. Duchêne, *Int. J. Pharm.*, 90(3), **1993**, R9-R12

[98] T. Kourti, F. MacGregor John, in *Particle Size Distribution II.* (American Chemical Society, Washington, DC, 1991), pp. 34-63.

[99] R.J. Gledhill, *J. Phys. Chem.*, 66(3), **1962**, 458-463

[100] L.D. Maxim, A. Klein, M.E. Meyer, C.H. Kuist, *J. Polym. Sci. Pol. Sym.*, 27(1), **1969**, 195-205

[101] W. Haiss, N.T.K. Thang, J. Aveyard, D.G. Fernig, *Anal. Chem.*, 79, **2007**, 4215-4221

[102] D.N. Furlong, A. Launikonis, W.H.F. Sasse, *J. Chem. Soc. Faraday T.*, 80(3), **1984**, 571-587

[103] C. Bullen, MSc Thesis Thesis, University of Waikato, **2000**

[104] J. Turkevich, *Anal. Chem.*, 21(4), **1949**, 475-485

[105] M. Knoll, E. Ruska, *Z. Phys. A-Hadron. Nucl.*, 78(5), **1932**, 318-339

[106] C. Kisielowski, *Microsc. Microanal.*, 14(05), **2008**, 469-477

[107] R. Erni, M.D. Rossell, C. Kisielowski, U. Dahmen, *Phys. Rev. Lett.*, 102(9), **2009**, 096101

[108] Philips, *Philips CM30 Mechanic Manual* (Philips, Amsterdam, **1984**)

[109] A. Gomez, K. Tang, *Phys. Fluids*, 6(1), **1994**, 404-414

[110] K.-Y. Li, H. Tu, A.K. Ray, *Langmuir*, 21(9), **2005**, 3786-3794

[111] J.J.v.d. Klink, J. Buttet, *Phys. Rev. B*, 29(11), **1984**, 6352-6355

[112] M.R. Mucalo, PhD Thesis Thesis, University of Auckland, **1991**

[113] M.R. Mucalo, R.P. Cooney, *J. Chem. Soc. Chem. Comm.*, 94, **1989**,

[114] M.R. Mucalo, R.P. Cooney, J.B. Metson, *Colloid Surface.*, 60, **1991**, 175-197

[115] E.A. Hyde, R. Rudham, *J. Chem. Soc. Faraday T.*, 80(3), **1984**, 531-547

[116] K.K. Chih-ting F. Lo, Boyd R. Davis, *Ind. Eng. Chem. Res.*, 46(17), **2008**, 5478-5484

[117] R.G. LeBel, D.A.I. Goring, *J. Chem. Eng. Data*, 7(1), **1962**, 100-101

[118] S. Song, C. Peng, *J. Disper. Sci. Technol.*, 29(10), **2008**, 1367-1372

[119] J. Herráez, R. Belda, *J. Solution Chem.*, 35(9), **2006**, 1315-1328

[120] J. Acosta, A. Arce, E. Rodil, A. Soto, *Fluid Phase Equilibr.*, 203(1-2), **2002**, 83-98

[121] J.W. Thompson, T.J. Kaiser, J.W. Jorgenson, *J. Chromatogr. A*, 1134(1-2), **2006**, 201-209

[122] T.M. Aminabhavi, B. Gopalakrishna, *J. Chem. Eng. Data*, 40(4), **1995**, 856-861

[123] S.S. Kurtz, A.E. Wikingsson, D.L. Camin, A.R. Thompson, *J. Chem. Eng. Data*, 10(4), **1965**, 330-334

[124] P. Laven, *MiePlot*, **2010**, http://www.philiplaven.com/mieplot.htm

[125] P. Laven, *Appl. Opt.*, 44(27), **2005**, 5675-5683

[126] P. Laven, *Appl. Opt.*, 42(3), **2003**, 436-444

[127] P. Laven, *Appl. Opt.*, 44(27), **2005**, 5667-5674

[128] M.A. Martins, S. Fateixa, A.V. Girão, S.r.S. Pereira, T. Trindade, *Langmuir*, 26(13), **2010**, 11407-11412

[129] S.S. Kinge, M. Crego-Calama, D.N. Reinhoudt, *Langmuir*, 23(17), **2007**, 8772-8777

[130] S.T. Gentry, M.W. Bezpalko, *J. Phys. Chem. C*, 114(15), **2010**, 6989-6993

[131] *CRC Handbook of Chemistry and Physics (Digital Edition)* (CRC Press, **2010**)

[132] B.R. James, R.H. Morris, *Can. J. Chem.*, 58, **1980**, 399-408

[133] G.W. Busser, J.G.v. Ommen, J.A. Lercher, *J. Phys. Chem. B*, 103(10), **1999**, 1651-1659

[134] W.B. Retallick, United States Patent and Trademark Office, *Washcoat for a Catalyst Support*, 4762567 (**1988**) 1-9

[135] H. Hirai, N. Yakura, *Polym. Adv. Tecnol.*, 12(11-12), **2001**, 724-733

[136] L. Delhaye, A. Ceccato, P. Jacobs, C. Köttgen, A. Merschaert, *Org. Process Res. Dev.*, 11(1), **2006**, 160-164

[137] B.D. Catsikis, M.L. Good, *Inorg. Chem.*, 8(5), **1968**, 1095-1099

[138] O. Renn, H. Rüegger, L.M. Venanzi, J. Gallus, V. Gramlich, A. Martelletti, *Inorg. Chim. Acta*, 240(1-2), **1995**, 575-580

[139] E.M. Gussenhoven, Thesis, University of California, **2008**

[140] T. Thurn-Albrecht, G. Meier, uuml, P. ller-Buschbaum, A. Patkowski, W. Steffen *et al.*, *Phys. Rev. E*, 59(1), **1999**, 642

[141] T. Thurn-Albrecht, W. Steffen, A. Patkowski, G. Meier, E.W. Fischer, Gr *et al.*, *Phys. Rev. Lett.*, 77(27), **1996**, 5437

[142] K. Okamoto, R. Akiyama, H. Yoshida, T. Yoshida, S. Kobayashi, *J. Am. Chem. Soc.*, 127(7), **2005**, 2125-2135

[143] V.M. Gun'ko, *Theor. Exp. Chem.*, 43(3), **2007**, 139-183

[144] J. Vieceli, I. Benjamin, *Langmuir*, 19(13), **2003**, 5383-5388

[145] V.R. Fernandes, A.M.F.R. Pinto, C.M. Rangel, *Int. J. Hydrogen Energ.*, In Press, Corrected Proof, **2009**,

[146] B.R. Davis, Chih-ting F. Lo, K. Karan, *Ind. Eng. Chem. Res.*, 46(17), **2008**, 5478-5484

[147] D.E. Ward, C.K. Rhee, *Can. J. Chem.*, 67(7), **1989**, 1206-1211

[148] M.P. Tarazona, E. Saiz, L. Gargallo, D. Radic, *Macromol. Theor. Simul.*, 2(5), **1993**, 697-710

[149] M. Guettari, A. Gharbi, *J. Macromol. Sci. B*, 49(3), **2010**, 592-601

[150] L.A. Bimendina, V.V. Roganov, Y.A. Bekturov, *Polym. Sci. USSR*, 16(12), **1974**, 3274-3279

[151] L.A. Bimendina, E.A. Bekturov, G.S. Tleubaeva, V.A. Frolova, *J. Polym. Sci. Pol. Sym.*, **1979**,

[152] J.N. Mohanty, P.L. Nayakh, S. Lenka, *Colloid Polym. Sci.*, 2654(11), **1987**, 982-985

[153] S.-J. Hong, H.-T. Huang, P.-D. Hong, *J. Appl. Polym. Sci*, 92(5), **2004**, 3211-3217

[154] S.-J. Hong, P.-D. Hong, J.-C. Chen, K.-S. Shih, *Eur. Polym. J.*, 45(4), **2009**, 1158-1168

[155] J.C.J.F. Tacx, H.M. Schoffeleers, A.G.M. Brands, L. Teuwen, *Polymer*, 41(3), **2000**, 947-957

[156] T. Tamura, N. Kawabata, M. Satoh, *Polym. Bull.*, 44(2), **2000**, 209-214

[157] D. Reigh, B. Müller, F. Müller-Plathe, S. Wiegand, *J. Chem. Phys.*, 116(20), **2002**, 9100-9106

[158] J. Sendroy, H.A. Collison, H.J. Mark, *Anal. Chem.*, 27(10), **1955**, 1641-1645

[159] E. Lieber, C.N.R. Rao, T.S. Chao, C.W.W. Hoffman, *Anal. Chem.*, 29(6), **1957**, 916-918

[160] J.S. McIndoe, B.K. Nicholson, *J. Organomet. Chem.*, 573(1-2), **1999**, 232-236

[161] H. Nichols, R.M. Hexter, *J. Chem. Phys.*, 73(2), **1980**, 965-974

[162] J.E. Parmeter, J. Xudong, D.W. Goodman, *Surf. Sci.*, 240(1-3), **1990**, 85-100

[163] M.G. Suryaraman, A. Viswanathan, *J. Chem. Educ.*, 26(11), **1949**, 594-596